# Fluid-Structure Instability in an Internal Flow Energy Harvester

Thesis by

Luís Phillipe Costa Ferreira Tosi

In Partial Fulfillment of the Requirements for the
Degree of
Doctor of Philosophy

Caltech

CALIFORNIA INSTITUTE OF TECHNOLOGY
Pasadena, California

2019
Defended July 20th, 2018

*Pela memória do meu pai e inspiração do meu avô,*
*que me levou à engenharia.*

# ACKNOWLEDGEMENTS

I am indebted to a lot of people for making my work and this thesis possible. First and foremost, I would like to thank my advisor, Tim Colonius, for taking a not-so-young-oil-field engineer and doing his best to shape him into a researcher. His effort was relentless and I hope that this dissertation will show he was at least partly successful. I am equally thankful for his off-the-field advice, his lessons on skepticism and optimism (superimposed), his lightheartedness, and the incredibly tight-nit and fostering group environment that challenged me to think and develop as an engineer.

As it so happens, my computational flow physics group colleagues were the core to that environment, where little would have happened without their support. I would like to first thank the PDU: Georgios Rigas for our discussions on stability and nonlinear analyzes, Oliver Schmidt for his guidance on jet dynamics, global stability, and SPOD, and Gianmarco Mengaldo for his guidance on programming and data structures. I would like to thank Kazuki Maeda and Andre da Silva, who were instrumental in compressible flow discussions, and Marcus Lee, Ke Yu, and Ethan Pickering for making our office a great, fluid-centric habitat. Most notably in this thesis, I would like to thank Andres Goza for being the ultimate fluid-structure interaction comrade.

As additions to CFPG, I would also like to thank Guillaume Blanquart and Mory Gharib for their guidance and support over my time at Caltech.

I would like to thank the Advanced Actuators Technologies group at the NASA Jet Propulsion Laboratory, particularly Yosi Bar-Cohen, for allowing us to partake in their facilities and knowledge of structures and piezoelectricity. I would like to thank Jake Chesin and Tyler Wynn for their many hours in the lab helping to get some vibration going. I would especially like to thank Stewart Sherrit and Hyong Jae Lee for their guidance, ingenuity, and creativity.

I would like to thank Jeff Hall for his support in finding the unknown about an unproven technology, and his guidance on how to do it. I would like to thank Dean Wiberg and Larry Bergman for their endless wisdom and encouragement.

I would like to thank Kris Maskos and Al Arrazola for their unwavering support for flow energy harvesting, and their incredible project management abilities. I would like to thank Manny Gonzalez, Dave Charlesworth, Solomon Lekia, Chip

Claiborne, Dennis McHugh, Waqar Qureshi, Steven Christian, and George Buck for making it viable for me to pursue a doctorate on my own terms.

I would like to thank Damian Hirsch, Nicholas Burali, Nikola Georgiev, and Victor Miller for their on- and off- the-field help with fluid mechanics, robots, software, math, and bikes. I would like to thank my friends and family for the support over a lifetime, and for constantly pushing me in the right direction, especially when winds were not favorable.

Lastly, I would like to thank Paula Henzel for her strength and faith, support and help, and for being the best partner in crime someone could have. You have taught me about myself and the world, and challenged me to think outside the room.

# ABSTRACT

Access to reliable power sources in remote locations is a recurring engineering challenge for both large and small applications. The developing world struggles with power connectivity in remote villages, while sensor networks strain with power limitations of batteries or short-lived turbines. Energy harvesting based on fluid-induced vibration provides a potential robust alternative for in-situ power generation, furnishing means for a decades long supply of power. Yet, one of the main challenges in the design of flow energy harvesters is understanding the mechanisms that drive their motion. Fluid-structure interaction problems often span a large parametric space and require considerable computational resources to resolve the necessary dynamic details for reliable designs.

This thesis aims to address this challenge for a piezoelectric internal flow energy harvester developed in conjunction with NASA Jet Propulsion Laboratory for in-well, deepwater sensor and actuator systems. Through exploratory experimentation, a configuration consisting of a piezoelectric beam within a converging-diverging channel in axial flow generated considerable power at moderate flow velocities when compared to other devices of the same size. The current device, though adapted to a more robust configuration based on flextensional actuators, still maintains the same fluid-structure interaction: the instability that ensues forces the system into self-sustained oscillations that produces consistent power output for flow rates above a critical threshold.

To understand and quantify this behavior, we develop an analytical framework based on a leakage-flow type instability, which curtails the shortcomings of expensive numerical simulations once verified. The formulation consists of a quasi one-dimensional simplification of coupled fluid-structure equations, which are linearized for classical stability analysis. The stability boundary and critical property predictions are verified through a set of fully coupled fluid-structure immersed boundary direct numerical simulations. Experiments are carried out in tandem to quantify the dynamics of the harvester, specifically targeting the critical flow rate threshold. The analytical framework is expanded to include flow in the spanwise direction of the beam, and results to a simplified geometry of the harvester compared with those from experiments. Agreement between predicted critical values suggest that leakage-flow may be the principal mechanism for fluid-induced vibration within our device. The model can serve as the foundation of initial exploration

of design parameters, and perhaps more powerful devices in future endeavors.

# PUBLISHED CONTENT AND CONTRIBUTIONS

[1] L. P. Tosi and T. Colonius. “Experimental Study and Modeling of a Flextensional Flow-Energy Harvester.” In: (2018). *In Preparation*.
LPT performed the experimental campaign, processed the data, and is currently writing the manuscript. This material is part of chapters 2, 3, and 5 in this thesis.

[2] L. P. Tosi and T. Colonius. “Modeling and Simulation of Elastic Member in Two-Dimensional Viscous Channel Flow.” In: (2018). *In Preparation*.
LPT performed the simulation campaign, processed the data, and is currently writing the manuscript. This material is part of chapters 2, 3, and 4 in this thesis.

[3] H. J. Lee et al. “Design and experimental evaluation of flextensional-cantilever based piezoelectric transducers for flow energy harvesting.” In: *SPIE Smart Structures and Materials + Nondestructive Evaluation and Health Monitoring*. 2016. DOI: `10.1117/12.2219269`.
LPT contributed to experimental design and data analysis of the flextensional flow-energy harvester presented. He partly contributed to the writing of the manuscript.

[4] S. Sherrit et al. *Flow energy piezoelectric bimorph nozzle harvester*. US Patent 9,531,303. Dec. 2016.
LPT contributed to the primary claim.

[5] H. J. Lee et al. “Piezoelectric Energy Harvesting in Internal Fluid Flow.” In: *Sensors* 15.10 (2015). DOI: `10.3390/s151026039`.
LPT contributed in experimental design and in processing experimental data to obtain dynamics of bimorph and flextensional flow-energy harvesters. He contributed equally to the writing the manuscript.

[6] S. Sherrit et al. “Flow energy piezoelectric bimorph nozzle harvester.” In: *SPIE Smart Structures and Materials + Nondestructive Evaluation and Health Monitoring*. 2014. DOI: `10.1117/12.2084574`.
LPT contributed with stress analysis and experimental video data processing to estimate fatigue level on the piezoelectric material. He partly contributed to the writing of the manuscript.

# CONTENTS

# LIST OF FIGURES

# LIST OF TABLES

# NOMENCLATURE

$(\cdot)'$. $\frac{\partial}{\partial x}(\cdot)$.

$(\cdot)^*$. Non-dimensional parameter, unless otherwise noted.

$(\hat{\mathbf{u}}_1)_i$. SPOD mode 1 shape at discrete frequency i.

$\alpha_m$. Effective separation angle for quasi-1D experimental simplified geometry.

$\delta$. Beam transverse displacement.

$\dot{(\cdot)}$. $\frac{\partial}{\partial t}(\cdot)$.

$\gamma_g$. Ratio of specific heats.

$\hat{c}_{\mathrm{bc}}$. Boundary to fluid damping ratio.

$\hat{h}$. gap to length ratio.

$\hat{k}$. Beam to fluid stiffness ratio.

$\hat{k}_{\mathrm{bc}}$. Boundary to fluid stiffness ratio.

$\hat{m}$. Beam to fluid mass ratio.

$\hat{m}_{\mathrm{bc}}$. Boundary to fluid mass ratio.

$\lambda$. Eigenvalue corresponding to structural response.

$\mathcal{M}_{\mathrm{STP}}$. Mach number.

$\mu_f$. Fluid dynamic viscosity.

$\nu$. Poisson's ratio.

$\phi_i$. Euler-Bernoulli beam in-vacuum eigenfunction at index $i$.

$\rho_f$. Fluid density.

$\rho_s$. Solid density.

$\xi_x$. Profile factor for definition of non-linear advection term in quasi-1D model.

$\zeta_{\mathrm{in}}$. Inlet loss coefficient.

$\zeta_{\mathrm{out}}$. Outlet loss coefficient.

$b$. Beam width.

$c_0$. Flexure damping.

$E$**.** Young's modulus.

$f$**.** Fanning friction factor, unless otherwise noted.

$f_s^*$**.** Non-dimensional structural frequency response normalized by structural properties.

$g_i$**.** Expansion function at index $i$.

$h_b$**.** Beam thickness.

$h_e$**.** Equilibrium channel shape.

$h_t$**.** Channel throat size.

$k_0$**.** Flexure stiffness.

$L$**.** Beam length.

$L_e$**.** Entry length.

$M^*$**.** Fluid to solid mass ratio.

$m_0$**.** Flexure mass.

$P_{\text{in}}$**.** Stagnation pressure upstream of channel in quasi-1D model.

$P_{\text{out}}$**.** Constant flowing pressure downstream of channel in quasi-1D model.

$q_{x0}$**.** Steady axial flow rate.

$R_{\text{g}}$**.** specific gas constant.

$Re_h$**.** Throat size/channel gap based Reynolds number.

$Re_L$**.** Length based Reynolds number.

$U^*$**.** Solid-centric non-dimensional velocity.

$U_c$**.** Characteristic flow velocity.

$V$**.** Piezoelectric voltage.

$x_t$**.** Axial throat position.

**Bimorph.** Piezoelectric actuator comprised of two thin piezoelectric sheets bonded to form a cantilever beam.

**FIV.** Fluid-induced vibration.

**Flextensional actuator.** Piezoelectric actuator comprised of piezoelectric stacks within a mechanical flexure that amplifies small axial motion into large transverse motion.

**Flutter.** Fluid-structure instability due to positive feedback between natural modes of a vibrating structure and aerodynamic forces.

**FSI.** Fluid-structure interaction.

**FSI DNS.** Fluid-structure interaction direct numerical simulation. Refers to the two-dimensional strongly-coupled fluid-structure immersed boundary numerical algorithm that solves the incompressible Navier-Stokes equations and a co-rotational formulation of structural equations for a thin elastic beam.

**LFI.** Leakage-flow instability.

**Quasi-1D model.** Reduced order model based on leakage-flow primarily in the axial direction. Model may include flow in the spanwise direction if specified as spanwise quasi-1D.

## *Chapter 1*

# INTRODUCTION

### 1.1 Motivation

Access to reliable electricity in remote locations has been a global challenge since the inception of the power grid. Lack of infrastructure, cost, and low reliability often prohibit the connection of rural areas, secluded villages, and scientific monitoring stations to centralized power; the developing world being disproportionally affected by the former two [1]. As of recent, decentralized power generation has become a strong candidate to bridge this gap, especially as hydrokinetic technologies become viable. Turbines designed for either wind or river operation, along with tidal energy harvesting represent are a few technologies that can [2] or have been implemented in the Amazon, Africa, and Alaska to either replace old or provide new power sources to communities [3].

Similarly, environmental energy harvesting has become a feasible alternative for sensor networks as electronics come to be more efficient [4]. The landscape of relevant applications tackled by decentralized power can be broken down into power requirements and reliability. Sensor networks may have power budgets $O(10^{-3} - 10^{1})$ [W] dependent on data rates and system architecture [5]; but likely require maintenance-free operations for decades due to access costs (i.e. excessive number of sensors or inaccessible locations). Small rural villages, on the other hand, often require $O(10^{3} - 10^{5})$ power generation, but reliability is perhaps more flexible contingent on available resources (i.e. local repair expertise and access to replacement parts) [3, 6].

A more immediate application can be found in the vein of distributed sensing: in-situ power generation would enable the combination of remote sensing and control to optimize the delivery of hydrocarbons. The deployment of inflow control valves (ICVs) with integrated sensors for pressure, temperature, flow rate, and composition in deepwater wells has been shown to increase the amount of recoverable hydrocarbons in place [7–9] and to impact not only financials, but the environment. By decreasing the number of wells drilled to develop a reservoir, along with increasing the reservoir's hydrocarbon recovery efficiency, such a system has the ability to wholly decrease drilling activities globally. The step-change in technology conversion from cabled to in-situ power generation systems bypasses the reliability shortcomings of leaking or shorted control-lines, their connections, and operational costs associated with their deployment. Benefits also include increase in the reliability of other well equipment that are safety critical (i.e. pressure containment) by reducing feed-throughs and leak paths necessary for cabled connections, for example. More importantly, it allows the deployment of multiple independent actuator-sensing systems such that production can be optimized for reservoirs, where production intervals are appropriately discretized, monitored, and controlled. The power budget for this application, which includes sensing, actuation, and communication is as low as $O(1)$ [W] when coupled with power management electronics. The longevity requirement of any power generation device, however, is the same as other downhole equipment: it must survive a minimum of 20 years without maintenance. Costs associated with well hardware repair and upkeep is equivalent to those of drilling a new well, which makes system reliability requirements as critical as those of power generation.

Ensuring devices robustly generate power over decades of maintenance-free functionality remains as large a challenge as meeting the power budget itself. Turbine designs alone, for example, can generate from fraction to thousands of watts individually [10]. However, the most reliable turbines to date fall well short of the 20 year desired lifetimes [10, 11], with wear and friction central to their failures [12]. Moreover, turbine devices are often miniaturized in applications discussed, which makes them even more susceptible to these failure mechanisms [13].

## 1.2 Fluid-Induced Vibration Energy Harvesting

Fluid-induced vibration based energy harvesting refers to a structure or series of structures that are placed in a flowing fluid to extract energy from the ensuing vibration and/or deformation. Steming from the spurt of efficient electronics, FIV energy harvesting research has been especially active since the early 2000's. Harvesting concepts range from flow driven magnets to forced piezoelectric elements for energy transduction, with power outputs $O(10^{-7} - 10^{4})$, though largely dependent on device length scales [14, 15]. Piezoelectric elements are particularly attractive for solid-state transduction since structural vibration can be converted into electricity without the wear of moving mechanical parts [13, 16]. By coupling the structure with a piezoelectric transducer, direct energy conversion can be achieved without the use of rotating machinery, bearings, or gears. This shifts the primary failure mechanism from wear to structural fatigue. Thus, unlike conventional turbines, these devices may enable decades of reliable electricity generation in remote locations with minimal maintenance.

The power output fundamentally necessitates that the flow exert an oscillating force onto the structure [17]. Large oscillating fluid forces are often associated with flow instabilities. When these forces constructively couple with the motion of a structure, large structural displacements can ensure and achieve a regime favorable to flow-energy extraction. This describes the essence of fluid-structure interaction (FSI) instabilities, which occur regularly in many engineering applications, though most designs vehemently seek to avoid them. FSI instabilities often lead to noise, vibration, and failure of structures, vehicles, and devices [18]. Of particular interest to this work, is the flutter type FSI , which relies on a positive feedback between the natural modes a vibrating structure and aerodynamic forces. The well known failure of the Tacoma bridge represents a drastic case of *single degree-of-freedom torsional flutter* due to the separated flow-structure coupling [19]. Flutter can be manifested in axial flows over flexible structures, also known as flag instability. This has been explored as an energy harvesting mechanism for the *Flutter-Mill* by Tang, Païdoussis, and Jiang [20]. Other specific configurations include cross-flow instabilities [21], which has been responsible for a number deepwater risers failures [22], but also used as a concept for large scale FIV power generation [14]. Similarly, coherent vortex shedding from diffusers in transitory stall is another flow instability that may have direct application in power harvesting given its geometrical simplicity [23].

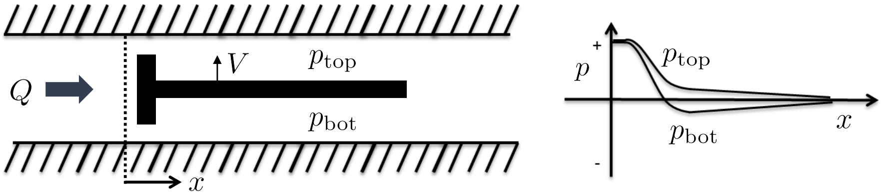

Figure 1.1: Leakage-flow instability illustration. The pressure profile as flow with flow rate $Q$ bypasses a structure moving with velocity $V$ induces a net force in the direction of the structure's motion [24].

FSIs can also be amplified when they occur in confined flow paths. When the flow paths are narrow in nature and surround an elastic body, the instability is known as a leakage-flow type instability (LFI). LFIs are likely to occur in the configuration illustrated in figure 1.1. These small passages are susceptible to instabilities because of the significant impact a small area change has on local velocities and pressures

[24]. They have been identified as the cause of fatigue failures in nuclear reactor cooling systems in the late 1960s. LFI remains largely unexplored in the context of flow-energy harvesting, and is ultimately where we will focus our effort in this thesis.

## 1.3 Flextensional Flow-Energy Harvester

In a joint effort with the Advanced Actuators Technologies group at the NASA Jet Propulsion Laboratory (JPL), we designed flow-energy harvesters to power sensors and actuators within an oil well [25–27]. The design philosophy we implemented is based on a trade-off between eliciting strong fluid-electro-mechanical coupling and avoiding the device's dominant failure mode.

In our initial study, a bimorph transducer mounted as a cantilever within a nozzle-diffuser channel geometry proved to be exceptional at extracting electricity from the flow [25]. The device generated ~ 0.02 W [28] and a factor of 5 times more power than that of flow-energy harvesting devices of similar volume [15]. Through further testing, however, the device failed due to fatigue at flow rates that would otherwise yield peak power production. Specifically, the same stresses responsible for the increase in power relative to other devices also exceeded the fatigue limit of the piezoelectric material. Even after ruggedization of the transducer and decreasing the total power output, failure occurred in the span of hours [26].

To increase the robustness of the structure, a flextensional actuator-based device was proposed [27]. Two main ideas motivated this design change to combat fatigue and degradation limitations: moving piezoelectric materials out of the flow path, and ensuring that the piezoelectric materials are sustained in compression only, as opposed to failure-inducing tension seen during bending.

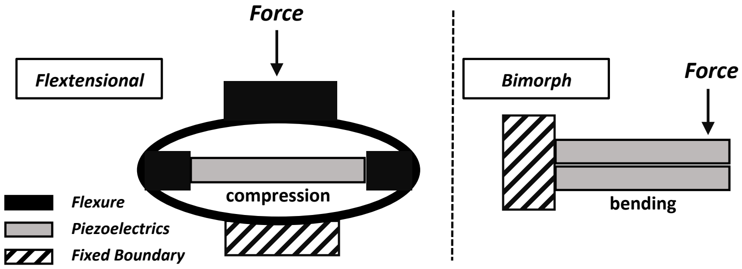

Figure 1.2: Flextensional actuator illustration (left), and bimorph actuator illustration (right).

Figure 1.2 illustrates the two actuator types. In the flextensional actuator , the piezoelectric material is comprised of PZT ceramic stacks that are located inside a flexure and pre-stressed in compression. As the top of the flexure moves up and down, the motion is converted into compression of the PZT at its core. In contrast, the bimorph forcing places a bending load on the two piezoelectric sheets, which alternate in compression and tension (where brittle ceramics are known to fail). Different choices of piezoelectric materials, such as polyvinylidene fluoride (PVDF), were considered in the bimorph configuration, but this caused unacceptably large decreases in electromechanical conversion efficiency. By comparison, the flextensional actuator is approximately twice as electromechanically efficient as the PZT-based bimorph.

The evolution of the flextensional flow-energy harvester can be seen in figure 1.3 by contrasting the original, double flextensional armature to the most recent single flexure design (tested in this chapter).

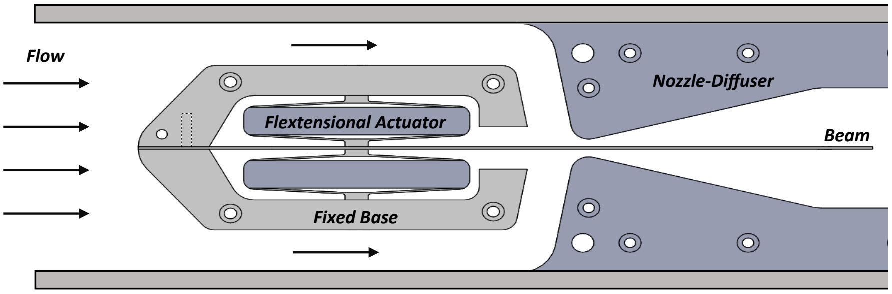

(a) Original flextensional flow-energy harvester with commercially available actuators.

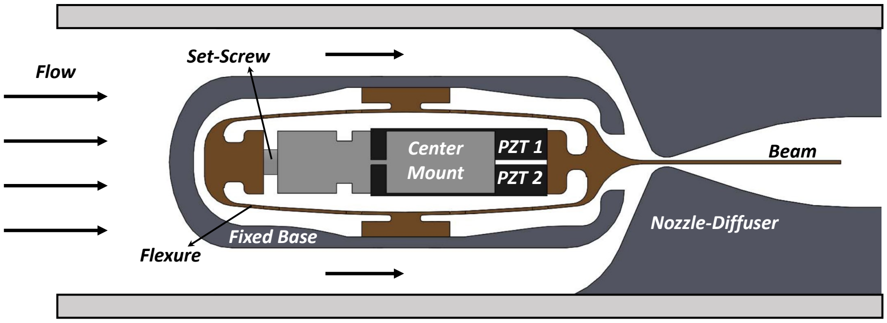

(b) Current version of flextensional flow-energy harvester with custom designed flexure.

Figure 1.3: Evolution of flextensional flow-energy harvester design, contrasting original version in [26] (1.3a ) to current version tested (1.3b).

A number of changes occurred, including beam interface with actuators, mount details, and the flow path, though to a smaller degree. These have amounted to a change in overall power output by a factor of two [26, 27]. The flexure mechanics of energy conversion in figure 1.3 works in the same way as the flextensional illustrated in figure 1.2: the up and down motion of the cantilever translates into release and compression of the pre-stressed PZT elements inside of it. The elements are always in compression and out of the flow path, as noted before. However, the mechanism by which flow incites the translating motion of the cantilever is no longer discernible between the many instabilities discussed in section 1.2: the diffuser geometry may be operating at transitory stall, a flag-type instability may be driving the pressure differences through trailing edge vortex shedding, and the small throat size may be driving a leakage-flow instability. Of course, a combination of these mechanisms may be at play, driving the system to instability as an aggregate to incite fluid-induced vibration.

## 1.4 Stability of Elastic-Member in Confined Flows

The stability of an elastic member within a constant channel, or as part of the channel has been studied for many decades [29–33]. A number of physical applications fall under this canonical problem, including wind instruments [34, 35], human snoring [36, 37] or vocalization [38], enhanced heat transfer systems [39, 40], and, as it concerns the topic of this thesis, flow-energy harvesting [25–28]. The flutter instability boundary is often the essential result sought, as the functional requirements of engineering designs (i.e. flow-energy harvester, heat management systems) or the manifestation of sound in natural systems (i.e instruments, snoring, voice) are dependent on it.

Direct solution of the fluid-structure interaction by solving the coupled Navier-Stokes and structural equations are, on the other hand, recent. Two dimensional FSI algorithms were used to study channel flow [37, 39], and most recently, to assess the effect of Reynolds number on the flutter boundary [41].

Yet, a challenge with fluid-structure systems is the large number of parameters necessary to describe the subset of possible system regimes; fully coupled computational approaches often require considerable computing time to span a segment of this parameter space. A more tractable but less accurate (or versatile) approach involves reduced-order modeling for the structure displacement and velocities, with fluid forces approximated via simplified equations of motion. The early work of

Miller [30], extended in [29] soon after, appear to be the first to address the divergence instability in channels within nuclear reactor cooling systems in this light. More recent work by Guo and Paidoussis [42] takes an inviscid approach to understanding the onset of flutter in a symmetric channel. Alben [43] solves for the inviscid flutter boundary using a vortex sheet model, and Shoele and Mittal [39] extend a plane wake vortex sheet method by Alben [44] in unconfined flows to constant, asymmetric channel flow.

However, as evident from the recent results of Cisonni et al. [41], the inviscid treatment of the flow for small throat-to-length ratios, $\hat{h}$, poses difficulties to predicting instability boundaries which generally depend on the Reynolds number, particularly when it is small.

More in line with Païdoussis [24] definition of leakage flow is the work Nagakura and Kaneko [33] and Wu and Kaneko [45]. They employ a viscous formulation of fluid forces for elastic beams in channel flow originally proposed by Inada and Hayama [31] for rigid plates in converging or diverging channels. Fujita and Shintani expanded it to cylindrical constant channels [46–48]. Yet, it remains unclear what the parameter bounds are for which the dynamics transition from mostly viscous to mostly inviscid. This thesis address this challenge in particular detail for the two-dimensional case in chapter 4.

## 1.5 Leakage Flow Instability Hypothesis

Previous work noted in sections 1.2 and 1.4, along with our initial experiments can inform the plausibility of different instability mechanisms driving in the current flextensional flow-energy harvester. In particular, by comparing experimental results of the original bimorph based energy harvesters in [25, 28], which maintain a similar flow path as in figure 1.3b, to known flutter boundaries for different mechanisms can help formulate a hypothesis for further exploration.

Starting with the unconfined, two-dimensional flag flutter boundary [49], predicted flow speeds for flutter onset are $\sim 4$ times faster than what is experimentally observed in [28]. Conversely, by considering the flutter boundary for the inviscid channel flow model by Shoele and Mittal [39], the flutter onset is predicted at lower flow speeds than those seen experimentally [28].

Work by Doaré, Sauzade, and Eloy [50] and Doaré et al. [51] suggest that effects of the flow along the spanwise direction cannot be ignored in our system, as the spanwise gap in both the original bimorph and the current flextensional harvester is $O(10^{-2})$ relative to the beam length. Furthermore, it suggest that a mechanism like the one in [39] may be stabilized when such effects are considered. Finally, the work of Inada and Hayama [31] and Nagakura and Kaneko [33] suggest that quantifying viscous effects and channel shape may also be important when quantifying the flutter boundary.

Hence, we take the approach of formulating and quantifying the stability effects of a leakage-flow instability type, where channel shape, viscous effects, and spanwise flow can be considered, and systematically discerned as significant to the onset of flutter in the flextensional flow-energy harvester system.

## 1.6 Thesis Scope and Overview

The overarching goal of this thesis is to elucidate the fluid-structure instability that drives the flextensional based flow-energy harvester. The hypothesis is that the leakage-flow type instability is the primary cause, and that parameters associated with it determine the stability boundary and structural oscillations (and power generation) that ensue.

We first develop a model for the leakage-flow instability under a quasi-1D approximation derived in chapter 2. Continuum equations of motion are simplified through assumptions and parameter limits that represent the narrow passage and flow rate modulation that are the intrinsic definition of leakage-flow. Two distinct models are derived: the first considers leakage flow in the axial direction only, while the second expands the same principles to include leakage flow in both the axial and beam spanwise directions. The former model is compatible with the two-dimensional direct numerical simulations, where details on its validity bounds are explored in detail in chapter 4. The latter is compatible with the experimental set up, and is used to successfully predict aspects of the flutter boundary for the flextensional flow-energy harvester in chapter 5.

Chapter 3 documents the numerical implementation and verification of the axial leakage flow model. It also contains the details of the immersed boundary projection algorithm for solving the two-dimensional direct numerical simulation (DNS) and its corresponding internal flow verification case. Lastly, a set of data analysis algorithms including dynamic mode decomposition (DMD), spectral proper-orthogonal decomposition (SPOD), and the Hilbert transform, are detailed as precursors to producing later results.

Chapter 4 presents a comparison between the axial leakage quasi-1D model and the two-dimensional fluid-structure interaction (FSI) DNS results for a broad set of parameters. In particular, the results address the parametric validity bounds of the quasi-1D model when predicting flutter boundary critical properties. We first consider the comparison between channel flow geometries, then expand results to the elastic-translating boundary condition at the beam leading edge and a diffusing channel. The quasi-1D model is able to capture the stability boundary and critical properties remarkably well through a wide range of parameters.

Experiments that detail the flextensional flow-energy harvester response are in chapter 5, with its last section as a comparison between experimental results and the quasi-1D model that considers spanwise leakage flow. We show that the model prediction agrees well with experimental values, when considering an analogous geometry to the real system.

We compile conclusions and future outlook in chapter 6.

### 1.7 Summary of Contributions

This section summarizes contributions within this thesis:

- Together with NASA JPL, partial conception, design, and development of flextensional flow-energy harvester.
- Developed a reduced-order model for leakage -flow instability through simplification of coupled fluid- structure equations of motion via a closure relation consistent with lubrication theory (chapter 2).
    - Expanded model to include elastic-translating boundary conditions that emulate the dynamics of the flexure mode of the flextensional flow-energy harvester.
    - Further expanded the model to account for leakage flow in the beam spanwise direction. Developed its numerical implementation and solution algorithm.
- Derived and implemented elastic-translating boundary conditions, and internal flow capabilities to the fluid-structure immersed boundary algorithm by Goza and Colonius [52] (chapter 3).
- Demonstrated the dominance of the leakage-flow type instability mechanism for fluid-induced vibration of an elastic member in constant channel and diffusing flows. This is done through a direct numerical simulation campaign

and the successful replication of flutter stability critical properties by the quasi-one-dimensional model (chapter 4) for a subset of parameters.

- Characterization and quantification of the dynamics of the flextensional based flow-energy harvester (chapter 5).
    - Developed method and apparatus for measuring flextensional properties relevant to dynamical responses, including flexure stiffness and damping.
    - Developed, built, and performed experimental campaign for quantification of critical properties of flextensional flow-energy harvester under flowing conditions.
    - Demonstrated leakage flow as a feasible alternative for the main mechanism that drives the flextensional flow-energy harvester into flutter.

*Chapter 2*

# LEAKAGE FLOW MODEL

## 2.1 Introduction

In this chapter we develop a model that combines the fluid equations with those from the solid in a relevant but simplified form, to provide insights into the physical mechanisms that drive the coupled fluid-structure system dynamics. The combined fluid-structure equations are simplified by making assumptions and taking parameter limits that will be verified with numerical simulations in chapter 4, and compared with experimental results in chapter 5. Assumptions and limits focus around the leakage-flow definition discussed in chapter 1, which often refers to flow around large center bodies through small passages, but also applies to general flows through narrow passages [24, p. 1221].

The geometry of the flow-energy harvester is illustrated in figure 2.1 and dimensional parameters in table 2.1. The elastic cantilever is placed in a symmetric converging diverging channel. The flextensional transducer is modeled by connecting the fixed end of the beam to a simple harmonic oscillator. We consider the voltage output of the flow rate (characteristic velocity), geometrical parameters, and material properties. This gives 23 dimensional quantities spanning four fundamental dimensions: length $l$, mass $m$, time $t$, and current $A$. Through the Buckingham-Pie theorem, these yield a total of 19 non-dimensional groups to determine the system dynamics. This large number of a parameters makes a thorough numerical or experimental investigation intractable. Hence, the purpose of the theory in this chapter is to provide a simple model that allows us to analytically identify the most important parameters affecting the stability of the system.

One of the simplest models of leakage flow instability was explored by Inada and Hayama [31]. The passage was first constrained to rigid body translation in the streamwise-normal direction and later included rigid body rotation [32]. In both cases the flow rate and pressure profiles only depended on the streamwise direction. A similar analysis extended for a beam in a constant channel by Nagakura and Kaneko [33], maintained the same leakage-flow forcing model but applied a damped Euler-Bernoulli beam equation rather than the rigid-body motion coupling to the elastic body. This analysis was further extended to include geometrical non-

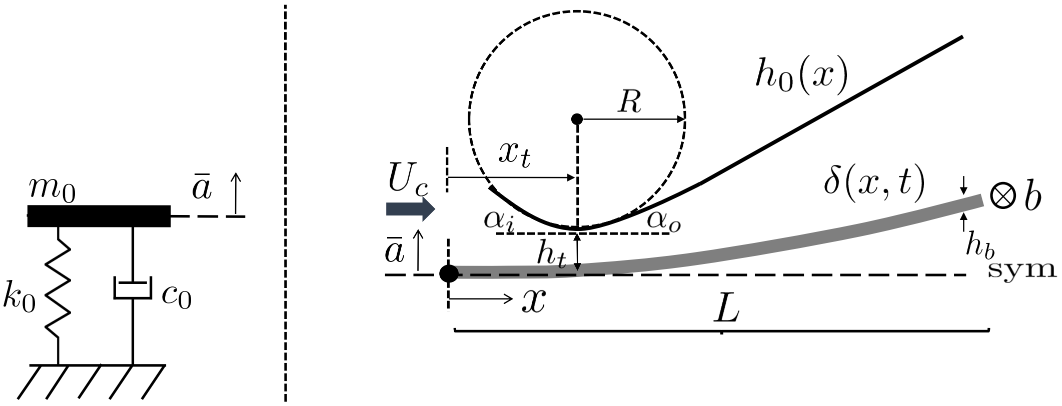

Figure 2.1: Illustration cantilever beam in a converging-diverging channel geometry (right) with simple harmonic boundary condition (left).

Table 2.1: Table of fluid-structure-electrical dimensional parameters.

| **Variable** | **Description** | **Dimension** |
|---|---|---|
| $\delta$ | beam displacement | $l$ |
| $x$ | beam length coordinate | $l$ |
| $t$ | time | $t$ |
| $V$ | voltage | $m * l^2 * t^{-3} * A^{-1}$ |
| $p$ | pressure | $m * l^{-1} * t^{-2}$ |
| $U_c$ | characteristic velocity | $l * t^{-1}$ |
| $k_0$ | flexure stiffness | $m * t^{-2}$ |
| $c_0$ | flexure damping | $m * t^{-1}$ |
| $m_0$ | flexure mass | $m$ |
| $R_e$ | electric resistance | $m * l^2 * t^{-3} * A^{-2}$ |
| $L$ | beam length | $l$ |
| $h_b$ | beam thickness | $l$ |
| $b$ | beam width | $l$ |
| $h_t$ | throat height | $l$ |
| $x_t$ | throat location | $l$ |
| $R$ | radius of curvature | $l$ |
| $\alpha_i$ | nozzle contraction angle | rad |
| $\alpha_o$ | diffuser expansion angle | rad |
| $\rho_f$ | fluid density | $m * l^3$ |
| $\mu_f$ | fluid viscosity | $m * l^{-1} * t^{-1}$ |
| $\rho_s$ | beam density | $m * l^{-3}$ |
| $E$ | Young's modulus | $m * l^{-1} * t^{-2}$ |
| $\nu$ | Poisson's ratio | ND |

linearities associated with large displacement of the beam [45]. Fujita and Shintani [48] also explored a similar form of leakage-flow forcing for flexible cylinders, using the Euler-Bernoulli equation for the structure, in a constant cylindrical narrow passage, while adding a flow and pressure component in the azimuthal direction [46, 47]. Comparison to experiments were also made in [48].

Fundamentally, power extraction from the flow is contingent on the energy conversion from fluid kinetic into structural kinetic and potential energy, later to be transduced into electricity through piezoelectric crystals. The characterization of structural energy can be ascertained by the amplitude $\delta$ and velocity $\dot{\delta}$ of the elastic member. We would like to characterize, through the physics, when these quantities will grow or decay as a function of parameters in table 2.1. The purpose is to develop a set of linear equations in $\delta$ and $\dot{\delta}$ and to assess their stability relative to some equilibrium point $\delta_0$ and $\dot{\delta}_0$. We frame our analysis in part inspired by these authors, and apply our framework to the flow-energy harvester.

The analysis within this chapter derives equations of motion from control volume and applies closures consistent with infinitesimal equations through limiting parameter cases. This is done in order to formulate a physical description that elucidates the appropriate ranges of those parameters in table 2.1 where solutions are applicable, which remains an open question through much of the aforementioned literature.

The derivation will consist of the following steps:

1. Develop an expression for pressure of the exerted by the fluid, as a function of $\delta$ and its derivatives on the elastic member through the Navier-Stokes equations and conservation of mass;
2. Linearize the result in $\delta$ and its derivatives;
3. Close the system with the linear elastic description of $\delta$ using conservation and constituent relations.

We begin by considering the case $b \gg L$ such that the flow is approximately two-dimensional. This is further simplified to a quasi-one-dimensional system of equations in the axial direction. We first consider a clamped cantilever, and then add a moving leading-edge boundary condition to model the flextensional device as a simple harmonic oscillator.

Finally, we extend the model to consider the three-dimensional leakage flow for the finite span case. The effect of confinement in the spanwise direction was detailed by Doaré et al. [50, 51] theoretically and with numerical simulations for the unconfined (in the normal direction) flag configuration [50], and in experiments [51]. Their results showed that only at small spanwise gap to length ratios, $\frac{C}{L}$, would the two-dimensional instability boundaries be observed. Furthermore, they showed that even at $\frac{C}{L} = O(10^{-4})$, a large discrepancy between stability boundaries was still seen relative to the two-dimensional model. Though this work is done for standard flag case outside of a channel, the spanwise confinement effect is likely significant in the flow-energy harvester problem, and as discussed in chapter 5, is crucial when comparing model predictions to experiments.

Our work in this chapter is motivated in part by the previous work of Inada and Hayama [31] and Nagakura and Kaneko [33]. We seek, however, tangible parametric bounds on the validity of the model. This required a different approach to the derivation of equations of motion from previous literature: we start with a control volume analysis and look for relations to close openly defined terms. The form of the closure provides the validity bounds we seek. The final equations are only similar to previous work when constrained to specific cases, such as a rigid beam or constant channel. Even in those cases, however, they differ in coefficients derived through our closure relations. Hence, model derivation steps presented are believed to be novel in the context of leakage-flow. In addition, the generalization of equations to arbitrary channel shapes with an flexible member and a moving boundary condition is also believed to be novel, along with its expansion to include flow in the beam spanwise direction.

## 2.2 Fluid Equations of Motion in Two Dimensions

To develop a relation between pressure, beam displacement and its derivatives, we consider the control volume $V$ defined in $\hat{\mathbf{x}}$ and $\hat{\mathbf{y}}$ illustrated in figure 2.2, which corresponds to a small section of one of the channels in figure 2.1 with $h_0$ representing that shape of the channel and the lower boundary $\delta$ as the "top" of the beam. The channel gap is defined by the top surface of the channel $h_0$, which is a function of axial position $x$ but fixed in time, and the shape of the beam $\delta$, which varies both in time and as a function of $x$.

The vectors that describe the unit normal direction to each boundary, $\mathbf{n}_i$ for $i \in \mathbb{Z} : [1, 4]$ are

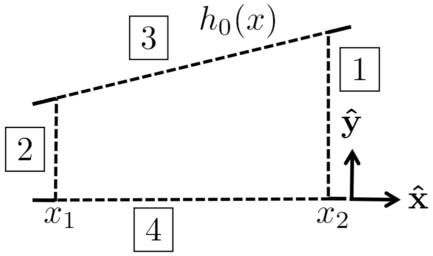

Figure 2.2: Two dimensional channel control volume.

$$[\mathbf{n}_1 \cdots \mathbf{n}_4] = \begin{bmatrix} 1 & -1 & -h_0'(x) & \delta'(x,t) \\ 0 & 0 & 1 & -1 \end{bmatrix}. \tag{2.1}$$

where the prime denotes $\frac{\partial}{\partial x}(\cdot)$.

Note that $||\mathbf{n}_3|| = \sqrt{1 + h_0'^2}$ and $||\mathbf{n}_4|| = \sqrt{1 + \delta'^2}$, while $||\mathbf{n}_1||$ and $||\mathbf{n}_2||$ have magnitude 1. The $\hat{(\cdot)}$ notation represents unit vectors (i.e. $\hat{\mathbf{n}}_3 = \frac{\mathbf{n}_3}{||\mathbf{n}_3||}$). Because $\delta$ varies with time, the control volume in figure 2.2 is moving, with $\hat{\mathbf{n}}_1$, $\hat{\mathbf{n}}_2$, and $\hat{\mathbf{n}}_3$ stationary, and $\hat{\mathbf{n}}_4$ having a speed of $\dot{\delta}$.

We begin with the integral form of mass conservation ([53, p. 98]),

$$\frac{\partial}{\partial t}\left(\int_V \rho_f dV\right) + \int_{\partial V} \rho_f \mathbf{u}_r \cdot \hat{\mathbf{n}} dA = 0 \tag{2.2}$$

where $\rho_f$ is the density of the fluid, and $\mathbf{u}_r$ is the velocity relative to the control volume. Since the lower boundary moves with the fluid, the relative normal velocity is zero there.

By applying equation 2.1, $\mathbf{u}_r$, incompressibility, and taking the limit as $x_2 \longrightarrow x_1$ of equation 2.2,

$$\frac{\partial}{\partial t}\left(\int_\delta^{h_0} dy\right) + \frac{\partial}{\partial x}\left(\int_\delta^{h_0} u dy\right) = 0. \tag{2.3}$$

Next, we consider the integral form of the Navier-Stokes equations in two dimensions on $V$ ([53, p. 102]),

$$\frac{\partial}{\partial t}\left(\int_V \rho_f \mathbf{u} dV\right) - \int_{\partial V} \left(\rho_f \mathbf{u}\right) \mathbf{u}_r \hat{\mathbf{n}} dA = \int_{\partial V} \sigma \hat{\mathbf{n}} dA = -\int_{\partial V} P \hat{\mathbf{n}} dA + \mathcal{F}_{\text{visc}} \tag{2.4}$$

where $\sigma$ is the stress tensor that is separated into a normal pressure component $P$ (positive $P$ is in the negative $\hat{\mathbf{n}}$ direction when $\hat{\mathbf{n}}$ points outside the control volume $V$, per fluid mechanics convention) and a viscous term $\mathcal{F}_{\text{visc}}$. No body forces are considered in 2.4. Once again, applying equations 2.1 and $\mathbf{u}_r$ to equation 2.4, assuming incompressibility, taking the limit as $x_2 \rightarrow x_1$, we obtain

$$\frac{\partial}{\partial t}\left(\int_{\delta}^{h_0}\begin{bmatrix}u\\v\end{bmatrix}dy\right)+\frac{\partial}{\partial x}\left(\int_{\delta}^{h_0}\begin{bmatrix}u^2\\uv\end{bmatrix}dy\right)=$$
$$\frac{-1}{\rho_f}\left\{\frac{\partial}{\partial x}\left(\int_{\delta}^{h_0}\begin{bmatrix}P\\0\end{bmatrix}dy\right)-\begin{bmatrix}h_0'\\-1\end{bmatrix}P|_{y=h_0}+\begin{bmatrix}\delta'\\-1\end{bmatrix}P|_{y=\delta}-\mathbf{F}_{\text{visc}}\right\}. \quad (2.5)$$

In arriving at equation 2.5, we used the no-slip boundary condition and that the channel is gradually varying in the streamwise direction, $h_0'^2 \ll 1$ and $\delta'^2 \ll 1$, such that $\sqrt{1+h_0'^2} \approx 1$ and $\sqrt{1+\delta'^2} \approx 1$ for $x \in [0, L]$.

Our goal is to relate $P$ to $\delta$ and derivatives through conservation laws. The current form of equations 2.3 and 2.5 have $\delta$ as factors and as integration limits; however, mass conservation allows a change of variable to relate $\delta$ to the system flow rate. By defining the flow rate in the $\hat{\mathbf{x}}$ as

$$Q_x = \int_{\delta}^{h_0} u dy, \quad (2.6)$$

equation 2.3 simplifies to

$$-\frac{\partial \delta}{\partial t}+\frac{\partial Q_x}{\partial x}=0, \quad (2.7)$$

since the $h_0$ is not a function of time. Similarly, the $\hat{\mathbf{x}}$ component of equation 2.5 becomes

$$\frac{\partial Q_x}{\partial t}+\frac{\partial \mathcal{N}_x}{\partial x}=-\frac{1}{\rho_f}\left\{\frac{\partial}{\partial x}\left(\int_{\delta}^{h_0} P dy\right)-h_0' P|_{y=h_0}+\frac{\partial \delta}{\partial x}P|_{y=\delta}-F_{\text{visc},x}\right\}. \quad (2.8)$$

where $\mathcal{N}_x$ is

$$\mathcal{N}_x = \int_{\delta}^{h_0} u^2 dy. \quad (2.9)$$

Next we quantify the viscous term $\mathbf{F}_{\text{visc}}$ for an incompressible Newtonian fluid. Considering its integral form in equation 2.4,

$$\mathcal{F}_{\text{visc}} = \mu_f \int_{\partial V} \left(\nabla \mathbf{u} + \nabla \mathbf{u}^\top\right) \hat{\mathbf{n}} dA, \tag{2.10}$$

where $\mu_f$ is the fluid dynamic viscosity, and only the divergence-free part of the strain tensor remains. Applying $\hat{\mathbf{n}}$ from equation 2.1 and geometrical constraints to the channel gap, along with dividing by $x_2 - x_1$, we obtain the $\hat{\mathbf{x}}$ component of the viscous term,

$$F_{\text{visc,x}} = \lim_{x_2 \to x_1} \left[ \frac{\mu_f}{x_2 - x_1} \int_{x_1}^{x_2} \left( -2 \frac{\partial u}{\partial x} \frac{\partial y}{\partial x} + \frac{\partial u}{\partial y} + \frac{\partial v}{\partial x} \right) \Bigg|_{y=\delta}^{y=h_0} dx \right], \tag{2.11}$$

from equation 2.8. To make further progress, we need a closure relation for $\mathcal{N}_x$ and $F_{\text{visc,x}}$ in term of $Q_x$ and $\delta$, whereupon 2.7 and 2.8 specify a relationship between $P$ (or $Q_x$) and $\delta$ and its derivatives. Equation 2.7 can then be used to relate $Q_x$ to $\delta$, and $P$ becomes only a function of $\delta$ and its derivatives in equation 2.8.

### 2.2.1 Lubrication Like Closure for $\mathcal{N}_x$ and $F_{\text{visc,x}}$

Thus far, equations 2.3 and 2.5 only have restrictions on compressibility and derivatives of the channel geometry, which encompass a fairly broad range of problems. Here, we consider further restrictions to the channel geometry associated with the flow-energy harvester designs discussed in chapter 1. Assuming incompressibility, we begin with continuity and the infinitesimal Navier-Stokes equations in two dimensions for a Newtonian fluid, where $\nabla \cdot \sigma = -\nabla P + \mu_f \nabla^2 \mathbf{u}$,

$$\frac{\partial u}{\partial x} + \frac{\partial v}{\partial y} = 0 \tag{2.12}$$

$$\begin{aligned} \rho_f \frac{Du}{Dt} &= -\frac{\partial P}{\partial x} + \mu_f \left( \frac{\partial^2 u}{\partial x^2} + \frac{\partial^2 u}{\partial y^2} \right) \\ \rho_f \frac{Dv}{Dt} &= -\frac{\partial P}{\partial y} + \mu_f \left( \frac{\partial^2 v}{\partial x^2} + \frac{\partial^2 v}{\partial y^2} \right) \end{aligned}. \tag{2.13}$$

Considering the relevant dimensional scales from figure 2.1 and those listed on table 2.1, we would like to non-dimensionalize equations 2.12 and 2.13 in a way to take limits over relevant parameters to yield a useful expression for the velocity profile $u$. We choose the length scale associated with $x$ as $L$, and velocity associated with $u$ as $U_c$. Those are rather clear choices. A less obvious choice is the length scale associated with $y$, hence we define $\bar{h} \sim h_0 - \delta$ as a representative channel gap length scale that will not necessary increase significantly over $L$, given the restrictions from 2.8 on $h_0'^2$ and $\delta'^2$. The value of $\bar{h}$ will depend on the $h_0$ function and initial value for the beam shape $\delta|_{t=0}$, if other than 0. The relation between dimensional and non-dimensional values, the latter with $(\cdot)^*$ notation, are

$$x^* = \frac{x}{L}, \; y^* = \frac{y}{\bar{h}}, \; u^* = \frac{u}{U_c}, \; t^* = \frac{U_c}{L}t. \tag{2.14}$$

The scaling for $v$ is also not obvious. In the absence of an initial beam velocity $\dot{\delta}|_{t=0}$, we consider continuity from equation 2.12; substituting the non-dimensional quantities in 2.14 and normalizing,

$$\frac{\partial u^*}{\partial x^*} + \left(\frac{L}{\bar{h}U_c}\right)\frac{\partial v}{\partial y^*} = 0. \tag{2.15}$$

In order to satisfy continuity, either the two terms are identically 0 or they are equal. Taking the latter hypothesis, the appropriate scaling of $v$ is the factor in front of the $\frac{\partial}{\partial y^*}(\cdot)$. Lastly, $P$ is of the order of the stagnation pressure $P_{\text{in}}$ driving $U_c$. The relevant non-dimensional parameters are

$$x^* = \frac{x}{L}, \; y^* = \frac{y}{\bar{h}}, \; u^* = \frac{u}{U_c}, \; v^* = \frac{L}{\bar{h}U_c}v, \; t^* = \frac{U_c}{L}t, \; P^* = \frac{P}{P_{\text{in}}}. \tag{2.16}$$

Substituting 2.16 into 2.13,

$$\begin{aligned} \varepsilon_h^2 Re_L \frac{Du^*}{Dt^*} &= -\frac{1}{\Lambda}\frac{\partial P^*}{\partial x^*} + \varepsilon_h^2 \frac{\partial^2 u^*}{\partial x^{*2}} + \frac{\partial^2 u^*}{\partial y^{*2}} \\ \varepsilon_h^4 Re_L \frac{Dv^*}{Dt^*} &= -\frac{1}{\Lambda}\frac{\partial P^*}{\partial y^*} + \varepsilon_h^4 \frac{\partial^2 v^*}{\partial x^{*2}} + \varepsilon_h^2 \frac{\partial^2 v^*}{\partial y^{*2}}, \end{aligned} \tag{2.17}$$

where we have defined

$$\varepsilon_h = \frac{\bar{h}}{L}, \; Re_L = \frac{\rho_f U_c L}{\mu_f}, \; \Lambda = \frac{\mu_f L U_c}{P_{\text{in}}\bar{h}^2}, \tag{2.18}$$

as the gap ratio, Reynolds number, and Bearing number, respectively. These parameters are those expected from lubrication theory ([53, p. 319]). We now take the limit as $\varepsilon_h \to 0$, where the channel gap becomes narrow relative to the beam length, and equation 2.17 becomes

$$\begin{aligned} 0 &= -\frac{1}{\Lambda}\frac{\partial P^*}{\partial x^*} + \frac{\partial^2 u^*}{\partial y^{*2}} \\ 0 &= -\frac{1}{\Lambda}\frac{\partial P^*}{\partial y^*}. \end{aligned} \tag{2.19}$$

In this limit we can easily solve for $u^*$. From the $\hat{\mathbf{y}}$ momentum, $P^* = P^*(x,t)$, independent of $y^*$, yields $v^* \approx 0$. The $\hat{\mathbf{x}}$ momentum gives, after applying the no-slip boundary condition at $y^* = \frac{\delta}{\bar{h}}$ and $y^* = \frac{h_0}{\bar{h}}$, a parabolic $u^*$ profile in $y^*$,

$$u^* = \frac{1}{2\Lambda}\frac{\partial P^*}{\partial x^*}\left(\frac{\delta}{\bar{h}} - y^*\right)\left(\frac{h_0}{\bar{h}} - y^*\right). \tag{2.20}$$

The first task is to define $\mathcal{N}_x$ in terms of $Q_x$. We begin by evaluating $\mathcal{N}_x$ from equation 2.9,

$$\mathcal{N}_x = \frac{\bar{h}}{4}\left(\frac{U_c}{\Lambda}\frac{\partial P^*}{\partial x^*}\right)^2 \int_{\delta/\bar{h}}^{h_0/\bar{h}} \left[\left(\frac{\delta}{\bar{h}} - y^*\right)\left(\frac{h_0}{\bar{h}} - y^*\right)\right]^2 dy^* = -\frac{1}{120}\left(\frac{U_c}{\Lambda}\frac{\partial P^*}{\partial x^*}\right)^2 \frac{(\delta - h_0)^5}{\bar{h}^4}. \tag{2.21}$$

Using the definition in equation 2.6 and integrating $u^*$ in equation 2.20,

$$Q_x = \frac{\bar{h}U_c}{12\Lambda}\frac{\partial P^*}{\partial x^*}\int_{\delta/\bar{h}}^{h_0/\bar{h}} \left(\frac{\delta}{\bar{h}} - y^*\right)\left(\frac{h_0}{\bar{h}} - y^*\right) dy^* = \frac{1}{12}\left(\frac{U_c}{\Lambda}\frac{\partial P^*}{\partial x^*}\right)\frac{(\delta - h_0)^3}{\bar{h}^2}. \tag{2.22}$$

Looking closely at equations 2.21 and 2.22, we can define $\mathcal{N}_x$ as

$$\mathcal{N}_x = \int_{\delta}^{h_0} u^2 dy = \xi_x \frac{Q_x^2}{h_0 - \delta}, \tag{2.23}$$

where $\xi_x$ can be considered a "profile factor" that characterizes the velocity profile dependence on $y$. For the parabolic profile of $u^*$ in equation 2.20, $\xi_x = 6/5$ considering equations 2.21 and 2.22, while for an uniform $u^*$ in $y^*$, $\xi_x = 1$.

Next we quantify the viscous term $\mathbf{F}_{\text{visc}}$ based on $u^*$. Taking the limit as $x_2 \to x_1$ of 2.11 and substituting the non-dimensional parameters in equation 2.16 ($F_{\text{visc,xf}}$ remains dimensional),

$$F_{\text{visc,x}} = \left[ -2\varepsilon_h \frac{\mu_f U_c}{L} \frac{\partial u^*}{\partial x^*} \frac{\partial y^*}{\partial x^*} + \frac{\mu_f U_c}{\bar{h}} \frac{\partial u^*}{\partial y^*} + \varepsilon_h \frac{\mu_f U_c}{L} \frac{\partial v}{\partial x} \right]_{y^*=\delta/\bar{h}}^{y^*=h_0/\bar{h}}, \tag{2.24}$$

and by taking the limit as $\varepsilon_h \to 0$ and substituting $u^*$ from equation 2.20

$$F_{\text{visc,x}} \approx \frac{\mu_f U_c}{\bar{h}} \frac{\partial u^*}{\partial y^*} \bigg|_{y^*=\delta/\bar{h}}^{y^*=h_0/\bar{h}} = \mu_f \left( \frac{U_c}{\Lambda} \frac{\partial P^*}{\partial x^*} \right) \frac{\delta - h_0}{\bar{h}^2}. \tag{2.25}$$

We can solve equation 2.22 for the quantity in the parenthesis above, and rewrite 2.25 in terms of $Q_x$,

$$F_{\text{visc,x}} \approx -12\mu_f \frac{Q_x}{(h_0 - \delta)^2}. \tag{2.26}$$

Equations 2.21 (with $\xi_x = 6/5$) and 2.26, along with the conclusion that $P = P(x,t)$ allow us to close equation 2.8,

$$\frac{\partial Q_x}{\partial t} + \frac{\partial}{\partial x} \left( \xi_x \frac{Q_x^2}{h_0 - \delta} \right) = -\frac{1}{\rho_f} \frac{\partial P}{\partial x} (h_0 - \delta) - \frac{12\mu_f}{\rho_f} \frac{Q_x}{(h_0 - \delta)^2}, \tag{2.27}$$

without much regard to the $\hat{\mathbf{y}}$ component of equation 2.5, since $v^* \approx 0$.

In addition to the two-dimensionality of the flow, equation 2.27 is valid under the following conditions:

1. Axial variations in channel gap are not large: $h_0'^2 \ll 1$ and $\delta'^2 \ll 1$;
2. The characteristic length of the channel gap is small: $\varepsilon_h \ll 1$;
3. Inertial effects associated with velocity profile are small: $\varepsilon_h^2 Re_L \ll 1$.

Condition 3 enforces the inertial term in the infinitesimal equation (left-hand-side of equation 2.17) to be small relative to pressure and viscous stresses. The inertia associated with the motion of the channel walls, in particular $\delta$, is captured by $Q_x$ and $\dot{Q}_x$ in equation 2.27. The normalized profile $u^*$ is a function of $\delta$ and $h_0$, and that $\varepsilon_h^2 Re_L \ll 1$ implies that the $u^*$ profile behaves quasi-statically, and that its shape adapts almost instantaneously when compared with $\dot{\delta}$. This may pose a problem if the beam has a large initial velocity $\dot{\delta}|_{t=0} \sim U_c$, so that the scaling of equations 2.16 is no longer appropriate. We will, however, focus on understanding the dynamics around $\dot{\delta}|_{t=0} = 0$ for the analysis at hand (although $\delta|_{t=0} \neq 0$ is allowed). In essence, equation 2.27 allows us to capture the inertial effects of the moving channel walls, while the lubrication theory closure allows us to ignore the inertial effects associated with changing the shape of $u^*$.

Condition 3 also indicates that for a fixed channel geometry, there is an upper limit on the Reynolds number for which the model is valid. That upper bound, however, may be quite large for very narrow channels. Thus, possibility of turbulent flow at high Reynolds number can be accounted for, however crudely, by adjusting the profile shape factor and the equation for $F_{\text{visc,x}}$. It is reasonable to supposed that turbulence "flattens" profile such that $\xi_x \approx 1$ and that $F_{\text{visc,x}}$ can take the form of a turbulent correlation. Following [31, 33], we write

$$F_{\text{visc,x}} = -\frac{f(Q_x)}{4}\frac{Q_x^2}{(h_0 - \delta)^2} \tag{2.28}$$

where $f$ is the Fanning friction factor and takes the form [54],

$$f = \begin{cases} 48Re_h^{-1} & \text{if } Re_h < 1000 \\ 0.26Re_h^{-0.24} & \text{if } Re_h \geq 1000 \end{cases}. \tag{2.29}$$

$Re_h$ is the local Reynolds number based on the channel gap $h_0 - \delta$ and is simply

$$Re_h = \frac{\rho_f Q_x}{\mu_f}, \tag{2.30}$$

with the onset of turbulence at $Re_h = 1000$. We note here that $F_{\text{visc,x}}$ term for $f < 1000$ in equations 2.28 and 2.29 is identical to equation 2.26. We can include in the model the profile factors that we derived

$$\xi_x = \begin{cases} 6/5 & \text{if } Re_h < 1000 \\ 1 & \text{if } Re_h \geq 1000 \end{cases}. \tag{2.31}$$

Substituting equation 2.28 into equation 2.27,

$$\frac{\partial Q_x}{\partial t} + \xi_x \frac{\partial}{\partial x}\left(\frac{Q_x^2}{h_0 - \delta}\right) = -\frac{1}{\rho_f}\frac{\partial P}{\partial x}(h_0 - \delta) - \frac{f}{4}\frac{Q_x^2}{(h_0 - \delta)^2}. \tag{2.32}$$

### 2.2.2 Channel Entrance Length

Another interesting scenario that must be discussed in one where the inlet velocity profile is uniform in $y$ ($\xi_x = 1$), but the channel flow is laminar, such that the profile evolves along $x$ from uniform into parabolic in $y$ and uniform in $x$. The channel section between uniform and fully developed parabolic profiles is the entrance region. The profile evolution is described well both as an analytical exercise and through numerical modeling in [55] and [56]. A good approximation for the entry region $L_e$ in laminar, two-dimensional channel flow is,

$$\frac{L_e}{L} \approx 0.063\varepsilon_h^2 Re_L, \tag{2.33}$$

scaling with the same viscous parameter that determines the importance of the inertial term in lubrication equation 2.17. To appropriately consider non-parabolic inlet conditions, we must hold $\frac{L_e}{L}$ small or, if possible, consider the evolution of the velocity profile in $x$, and bring it into the closure relation, such as defined in equations 2.29 and 2.31. We opt for the former in subsequent chapters, especially since this is consistent with condition 3 for the validity of the lubrication closure.

### 2.2.3 Pressure Boundary Conditions

In order to solve equations 2.27 and 2.7 uniquely, two pressure boundary conditions are required. This is due to the extra order of $\frac{\partial}{\partial x}(\cdot)$ gained by satisfying conservation of mass, making the highest derivative of pressure second order in $x$. The form of the pressure boundary conditions presented here will allow for the consideration of lossy inlet and outlet conditions, where stagnation pressure is lost. One of the simplest and common empirical treatments is to let the stagnation pressure loss $\Delta P_o$

$$\Delta P_o = \frac{\zeta}{2}\rho_f U^2, \tag{2.34}$$

where $\zeta$ is the "loss coefficient" associated with a specific device and flow, and $U$ is an appropriate velocity scaling, typically the average velocity along a duct's axial or primary flow direction. Dimensional analysis indicates that $\zeta$ is often a function of $Re$ and geometrical parameters, depending on the specific process. Examples include abrupt expansions or contractions, orifice plates to restrict the flow, frictional channel flow, separated flow in diffusers, to name a few [57] . Figure 2.3 illustrates the input pressure $P_{\text{in}}$ at the system inlet, the pre-inlet pressure drop $\Delta P_1$, the channel inlet boundary pressure $P|_{x=0}$, the channel outlet pressure $P|_{x=L}$, a post-outlet pressure drop $\Delta P_2$, and the pressure at the system outlet $P_{\text{out}}$.

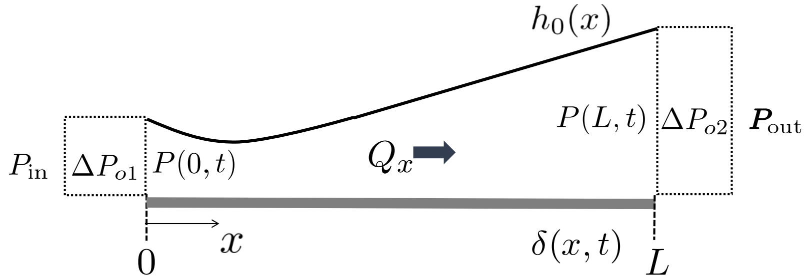

Figure 2.3: Channel geometry illustration with pressure boundary conditions.

We define $P_{\text{in}}$ and $P_{\text{out}}$ as constants and will relate $P|_{x=0}$ and $P|_{x=L}$ to flow parameters next. In the spirit of simplicity, we begin with the steady Bernoulli equation with the added pressure drop looking upstream of the channel inlet,

$$P_{\text{in}} + \frac{1}{2}\rho_f \bar{u}_{\text{in}}^2 = P(t)|_{x=0} + \frac{1}{2}\rho_f \bar{u}^2(t)|_{x=0} + \Delta P_{o1} \tag{2.35}$$

where $\bar{u}_{\text{in}}$ and $\bar{u}|_{x=0}$ are the $y$ averaged velocities at the system inlet and the channel inlet respectively,

$$\bar{u} = \frac{1}{h_0 - \delta}\int_{\delta}^{h_0} u dy = \frac{Q_x}{h_0 - \delta}. \tag{2.36}$$

When $\Delta P_1$ takes the form in equation 2.34 assuming a dependency on the channel inlet velocity $\bar{u}|_{x=0}$, using the definition of $\bar{u}$ in equation 2.36, we can solve equation 2.35 for $P(t)|_{x=0}$,

$$P(t)|_{x=0} = P_{\text{in}} + \frac{1}{2}\rho_f \bar{u}_{\text{in}}^2 - \frac{(\zeta_1 + 1)}{2}\rho_f \left[\left(\frac{Q_x}{h_0 - \delta}\right)^2\right]_{x=0}. \tag{2.37}$$

Similar to equation 2.35, the outlet relation is

$$P(t)|_{x=L} + \frac{1}{2}\rho_f \bar{u}^2(t)|_{x=L} = P_{\text{out}} + \frac{1}{2}\rho_f \bar{u}_{\text{out}}^2 + \Delta P_{o2}. \tag{2.38}$$

Substituting equation 2.34 for $\Delta P_2$, with a dependence on the channel outlet velocity $\bar{u}|_{x=L}$, again using the definition of $\bar{u}$, and solving for $P|_{x=L}$,

$$P(t)|_{x=L} = P_{\text{out}} + \frac{1}{2}\rho_f \bar{u}_{\text{out}}^2 + \frac{(\zeta_2 - 1)}{2}\rho_f \left[\left(\frac{Q_x}{h_0 - \delta}\right)^2\right]_{x=L} . \tag{2.39}$$

Appropriate values for $\zeta_1$ and $\zeta_2$ depend on the flow regime and geometry. If no stagnation pressure is lost at either the inlet or the exit, $\zeta_{1,2} \equiv 0$. A typical inlet loss correlation for a sudden contraction (SC) is given in [57, p. 388] valid for $d/D \leq 0.76$,

$$\zeta_{\text{SC}} \approx 0.42 \left[1 - \left(\frac{d}{D}\right)^2\right]; \tag{2.40}$$

while an expression for the loss coefficient for a sudden expansion (SE) is also given as,

$$\zeta_{\text{SE}} = \left[1 - \left(\frac{d}{D}\right)^2\right]^2 , \tag{2.41}$$

and obtained via a control volume analysis neglecting shear stresses in the corner separated flow. The variable $d$ is the hydraulic diameter of the contraction/expansion small dimension, while $D$ is hydraulic diameter of the contraction/expansion large dimension. The hydraulic diameter is defined as

$$D_{\text{H}} = 4\frac{A}{\mathcal{P}}, \tag{2.42}$$

where $A$ is the area and $\mathcal{P}$ is the perimeter of a relevant flow cross-section.

If we further define the system inlet as a reservoir, where $P_{\text{in}}$ is the upstream stagnation pressure ($\bar{u}_{\text{in}} = 0$), and the system outlet velocity to equal that of the channel outlet ($\bar{u}_{\text{out}} = \bar{u}|_{x=L}$), equation 2.37 becomes

$$P(t)|_{x=0} = P_{\text{in}} - \frac{\zeta_{\text{in}}}{2}\rho_f \left[\left(\frac{Q_x}{h_0 - \delta}\right)^2\right]_{x=0} \tag{2.43}$$

and equation 2.39 is simplified to

$$P(t)|_{x=L} = P_{\text{out}} + \frac{\zeta_{\text{out}}}{2}\rho_f \left[\left(\frac{Q_x}{h_0 - \delta}\right)^2\right]_{x=L} . \tag{2.44}$$

Equations 2.43 and 2.44 are those found often within the leakage-flow literature ([31–33]), which are restricted versions of equations 2.37 and 2.39. The loss coefficients are redefined as

$$\begin{aligned} \zeta_{\text{in}} &= \zeta_1 + 1, \\ \zeta_{\text{out}} &= \zeta_2, \end{aligned} \tag{2.45}$$

where $\zeta_{\text{in}} \geq 1$ and $\zeta_{\text{out}} \geq 0$ for anisentropic phenomena at the channel inlet and outlet, with the equality holding when no stagnation pressure drop occurs.

### 2.2.4 Linearization of Pressure

Choosing the generalized lubrication closure, the coupled partial differential equations for the hydrodynamic pressure with the aforementioned conditions are (below for reference),

$$-\frac{\partial \delta}{\partial t} + \frac{\partial Q_x}{\partial x} = 0, \tag{2.7}$$

and

$$\frac{\partial Q_x}{\partial t} + \xi_x \frac{\partial}{\partial x}\left(\frac{Q_x^2}{h_0 - \delta}\right) = \frac{-1}{\rho_f}\frac{\partial P}{\partial x}(h_0 - \delta) - \frac{f}{4}\frac{Q_x^2}{(h_0 - \delta)^2}. \tag{2.32}$$

for $f$ and $\xi_x$ values in equations 2.29 and 2.31, respectively. The pressure boundary conditions are shown in equations 2.43 and 2.44. Nonlinearities appear in both $\delta$ and $Q_x$ in equation 2.27. Since the goal is to understand the stability of the equilibrium beam shape $\delta_0$ as a function of parameters on table 2.1, linear stability analysis of the coupled fluid-structure system is appropriate.

Thus far, we have two coupled partial differential equations with $\delta$, $Q$, $P$ variables. We begin the linearization by expanding all of them at order $\varepsilon$ about their respective equilibrium (0 subscript) value,

$$P(x, t, \varepsilon) = p_0(x) + \varepsilon p_1(x, t) \tag{2.46}$$

and

$$Q_x(x, t, \varepsilon) = q_{x0}(x) + \varepsilon q_{x1}(x, t) \tag{2.47}$$

for the hydrodynamic variables. We will show shortly that $q_{x0}$ is in fact not a function of $x$, but rather the constant steady flow rate due the steady pressure profile $p_0(x)$. Considering the channel geometry $h_0$, we can define the beam shape $\delta$ as a perturbation of order $\varepsilon$ to the channel gap and expand the perturbation term as a sum of basis functions $g_i(x)$ with amplitudes $a_i(t)$, for $i \in \mathbb{Z} : [0, \infty]$,

$$\begin{aligned} h_0(x) - \delta(x,t) &= h_0(x) - (\delta_0(x) + \varepsilon\delta_1) \\ &= h_e(x) + \varepsilon\delta_1 \\ &= h_e(x) - \varepsilon \sum_{i=0}^{\infty} a_i(t) g_i(x), \end{aligned} \tag{2.48}$$

where we define $h_e = h_0 - \delta_0$ as the equilibrium channel gap. Lastly, we must linearize $f(Q_x)$ around $q_{x0}$,

$$f(Q_x) \approx f(q_{x0}) + (Q_x - q_{x0}) \left[\frac{\mathrm{d}f}{\mathrm{d}Q_x}\right]_{Q_x = q_{x0}} = f_0 + \varepsilon\eta q_{x1}(x,t), \tag{2.49}$$

where $\eta = \mathrm{d}f/\mathrm{d}Q_x$ and obtained by taking a derivative of equation 2.29 in $Q_x$.

We begin integrating both sides of mass conservation conservation equation 2.7 by $x$,

$$Q_x(x,t) = \bar{Q}_x(t) + \int_0^x \left(\frac{\partial}{\partial t}\delta(x,t)\right) dx_1, \tag{2.50}$$

where $\bar{Q}_x(t)$ is the flow rate at $x = 0$. Since we have expanded the left-hand-side $Q_x$ in powers of $\varepsilon$, we must also expand $\bar{Q}(t)$ as

$$\bar{Q}_x(t) = \bar{Q}_{x0} + \varepsilon\bar{Q}_{x1}(t). \tag{2.51}$$

Substituting equations 2.47, 2.48, and 2.51 into 2.50,

$$Q_x(x,t,\varepsilon) = q_{x0}(x) + \varepsilon q_{x1}(x,t) = \bar{Q}_{x0} + \varepsilon\left[\bar{Q}_{x1}(t) + \int_0^x \left(\frac{\partial}{\partial t}\delta_1(x,t)\right) dx_1\right], \tag{2.52}$$

where we note that the integration variable $\bar{Q}_{x0}$ is the constant steady flow rate at $x = 0$. Combining this with the left-hand-side equilibrium flow rate $q_{x0}(x)$, it stands that

$$q_{x0} = \bar{Q}_{x0} = \text{constant}, \tag{2.53}$$

where both describe the steady, uniform flow rate at $x = 0$ due to $p_0(x)$. Substituting equations 2.46, 2.47, and 2.48 into $x$ momentum equation 2.32, collecting powers of $\varepsilon$ and equating its coefficients, we obtain differential equations for each order $\varepsilon$. For $\varepsilon^0$, we have

$$\frac{\mathrm{d}}{\mathrm{d}x} p_0(x) = \rho_f\, q_{x0}^2 \left( \xi_x \frac{\frac{\mathrm{d}}{\mathrm{d}x} h_e(x)}{h_e(x)^3} - \frac{f_0}{4\, h_e(x)^3} \right), \tag{2.54}$$

which is separable and can readily be integrated from 0 to $x$ to obtain

$$p_0(x) = p_0(0) + \rho_f\, q_{x0}^2 \left( \xi_x \int_0^x \frac{\frac{\mathrm{d}}{\mathrm{d}x_2} h_0(x_2)}{h_e(x_2)^3} dx_2 - \int_0^x \frac{f_0}{4\, h_e(x_2)^3} dx_2 \right), \tag{2.55}$$

where $p_0(0)$ is the constant pressure at $x = 0$. The two integration constants, $q_{x0}$ and $\bar{P}_0$ can be solved using the linearized boundary conditions, obtained by substituting linear $\delta$ and $Q_x$ into equations 2.43 and equating $\varepsilon^0$ coefficients,

$$p_0(0) = P_{\text{in}} - \zeta_{in} \frac{\rho_f\, {q_{x0}}^2}{2\, h_e(0)^2}; \tag{2.56}$$

and similarly for equation 2.44,

$$p_0(L) = P_{\text{out}} + \zeta_{\text{out}} \frac{\rho_f\, q_{x0}^2}{2\, h_e(L)^2}. \tag{2.57}$$

Substituting $p_0(0)$ from equation 2.56 into 2.55,

$$p_0(x) = P_{\text{in}} - \rho_f\, q_{x0}^2 \left( \frac{f_0}{4} \int_0^x \frac{dx_2}{h_e(x_2)^3} - \xi_x \int_{h_e(0)}^{h_e(x)} \frac{dh_e}{h_e^3} + \frac{\zeta_{in}}{2\, h_e(0)^2} \right), \tag{2.58}$$

and the constant $q_{x0}$ by equating 2.57 to 2.58 evaluated at $x = L$,

$$q_{x0} = \sqrt{\frac{P_{\text{in}} - P_{\text{out}}}{\rho_f \left[ \frac{\zeta_{\text{out}}}{2h_e(L)^2} + \frac{\zeta_{\text{in}}}{2h_e(0)^2} - \xi_x \left( \int_{h_e(0)}^{h_e(L)} \frac{dh_e}{h_e^3} \right) + \frac{f_0}{4} \left( \int_0^L \frac{dx_2}{h_e(x_2)^3} \right) \right]}}. \tag{2.59}$$

The steady equations here at similar to those obtained by Inada [31], assuming $\xi_x = 1$, and $\delta_0 = 0$. Equation 2.58 has three distinct terms in the parenthesis, the first with $f_0$ as a factor represents the pressure drop due to viscous effects as a function of the integral equilibrium gap shape over $x$; the second integral, multiplied by $\xi_x$, comes from the inertia term and is only a function of the initial ($x = 0$) and the current (at $x$) gap size, representing the pressure change due to the gap expansion or contraction; and the third is solely due to system inlet conditions. If $\zeta_{\text{in}} = 1$ (minimum allowed value from equation 2.45), then the only pressure drop comes from accelerating the flow to the average inlet velocity. Equation 2.59 shows that, as expected in incompressible flow, the steady flow rate is a function of the difference in system inlet and outlet pressures, $P_{\text{in}}$ and $P_{\text{out}}$, rather than their absolute values. To get the absolute steady pressure at a location $x$, only two out of $P_{\text{in}}$, $P_{\text{out}}$, or $q_{x0}$ need to be specified, and the third can be calculated from equation 2.59.

Next we collect and equate coefficients to $\varepsilon^1$ to obtain the linear perturbation to $p_0$ and $q_{x0}$ as a function of $\delta_1$ and hence as linear function of basis coefficients $a_i$. From the integrated mass conservation equation in 2.52,

$$q_{x1}(x,t) = \bar{Q}_{x1}(t) + \int_0^x \left(\frac{\partial}{\partial t}\delta_1(x,t)\right) dx_1. \tag{2.60}$$

From the $x$ momentum equation,

$$\begin{aligned}\frac{\partial}{\partial x}p_1(x,t) = \left[\xi_x \frac{\rho_f\, q_{x0}^2}{h_e(x)^3}\frac{\partial}{\partial x}(\cdot) - \frac{3}{h_e(x)}\frac{\mathrm{d}}{\mathrm{d}x}p_0(x)\right]\delta_1(x,t) \; - \\ \left[\frac{\rho_f}{h_e(x)}\frac{\partial}{\partial t}(\cdot) + 2\xi_x \frac{\rho_f q_{x0}}{h_e(x)^2}\left(\frac{\partial}{\partial x}(\cdot) - \frac{1}{h_e(x)}\frac{\mathrm{d}}{\mathrm{d}x}h_e(x)\right) + \right. \\ \left. \frac{\rho_f q_{x0}}{2\,h_e(x)^3}\left(f_0 + \eta\,\frac{q_{x0}}{2}\right)\right] q_{x1}(x,t),\end{aligned} \tag{2.61}$$

is a PDE in $x$ and $t$ that depends on $\delta_1$ and $q_{x1}$ and their equilibria. Similar to the $0^{\text{th}}$ order case, continuity is substituted for $q_{x1}$ (equation 2.60), and equation 2.54 for $\frac{\mathrm{d}p_0}{\mathrm{d}x}$, such that $\frac{\partial p_1}{\partial x}$ only depends on $\delta_1$, its derivatives, the components of flow rate at $x = 0$, $q_{x0}$ and $\bar{Q}_{x1}(t)$, and can be integrated in $x$ to obtain $p_1$. This is tractable to the extent that the integrals of the right-hand-side of equation 2.61 can be evaluated in some manner. We use the $1^{\text{st}}$ order of the boundary condition expansion to determine $\bar{Q}_{x1}$: the $\varepsilon^1$ coefficients of the pressure boundary conditions are,

$$p_1(0,t) = \frac{2\left(P_{\text{in}} - p_0(0)\right)}{h_e(0)} \delta_1(0,t) - \zeta_{\text{in}} \frac{\rho_f \, q_0}{h_e(0)^2} q_1(0,t) \tag{2.62}$$

and

$$p_1(L,t) = \frac{2\,\left(P_{\text{out}} - p_0(L)\right)}{h_e(L)} \delta_1(L,t) + \zeta_{\text{out}} \frac{\rho_f \, q_0}{h_e(L)^2} q_1(L,t)\,. \tag{2.63}$$

Equations 2.62 and 2.63 are where the dependence of the beam's boundary conditions enter the pressure operator, both through $\delta_1(0,t)$ and $q_{x1}(0,t)$ in equation 2.60. They must be defined through constraints imposed on the specifics of the elastic member, done so in the next section.

Hence, substituting equations 2.54, 2.58, 2.60 into 2.61, integrating the result from 0 to $x$, closing the relation for $p_1(0,t)$ and $\bar{Q}_{x1}$ with equation 2.62 and 2.63, and substituting the basis expansion of $\delta_1$ as in equation 2.48, we obtain an expression for $p_1$ that is linear in the coefficients $a_i$ and $\bar{Q}_{x1}$, where $\dot{(\cdot)} = \frac{\mathrm{d}}{\mathrm{d}t}(\cdot)$,

$$p_1(x,t) = T_{\text{f}}(x)\bar{Q}_{x1}(t) + \sum_{i=1}^{\infty} \Big( M_{\text{f}i}(x)\ddot{a}_i(t) + C_{\text{f}i}(x)\dot{a}_i(t) + K_{\text{f}i}(x)a_i(t) \Big). \tag{2.64}$$

The coefficients $M_{\text{f}i}(x)$, $C_{\text{f}i}(x)$, and $K_{\text{f}i}(x)$, represent the mass, damping, and stiffness parts of the fluid pressure operator, and $T_{\text{f}}(x)$ is a boundary forcing term proportional to $\bar{Q}_{x1}$ that arises from the (originally nonlinear) boundary conditions. Similar to solving for $q_{x0}$, the boundary condition equations 2.62 and 2.63 give an ordinary differential equation to describe the evolution of $\bar{Q}_{x1}$ in time,

$$\dot{\bar{Q}}_{x1}(t) = G_{\text{q}}\bar{Q}_{x1}(t) + \sum_{i=0}^{\infty} \Big( B_{\text{q}i}\ddot{a}_i(t) + D_{\text{q}i}\dot{a}_i(t) + E_{\text{q}i}a_i(t) \Big). \tag{2.65}$$

The terms $B_{\text{q}i}$, $D_{\text{q}i}$, and $E_{\text{q}i}$ do not depend on $x$, but rather the integral from 0 to $L$ in $x$ that includes each basis function $g_i$. $G_{\text{q}}$ is a scalar and also does not depend on $x$, but rather on the integral of $h_e$ in $x$ from 0 to $L$. Furthermore, $p_1$ is formulated so that it depends on $q_{x0}$, and not on $P_{\text{in}}$ and $P_{\text{out}}$, meaning that the operator, and its stability, only depend on $q_{x0}$ rather than any absolute pressure measure of the system. All coefficients in equations 2.64 and 2.65 were obtained using the MATLAB symbolic engine and can be seen in their full form in appendix A.

## 2.3 Fluid-Structure Coupling

The fluid pressure described in the previous sections acts on the elastic member. We now must develop equations that describe the beam displacement as a function of applied hydrodynamics forces.

### 2.3.1 Structure Equations of Motion

Considering a material control volume in figure 2.4 illustrating a section of the elastic member shown as boundary 4 (lower boundary) in figure 2.1 in transverse vibration, we apply Newton's second law to derive the Euler-Bernoulli beam equation [58, p. 494] ,

$$\rho_s b h_b \frac{\partial^2}{\partial t^2}\delta(x,t) + \frac{\partial^2}{\partial x^2}\left(EI\frac{\partial^2}{\partial x^2}\delta(x,t)\right) = F_{\text{net}}(x,t), \tag{2.66}$$

where $b$ is the cross-section span, $h_b$ is the beam thickness, $E$ is Young's modulus, $I$ is the cross-section area moment of inertia, and $F_{\text{net}}$ is the net external force acting on the beam. The labels in figure 2.4 are $F$ for shear stresses, $M_{\text{o}}$ for moments, and pressures are labeled according to figure 2.5.

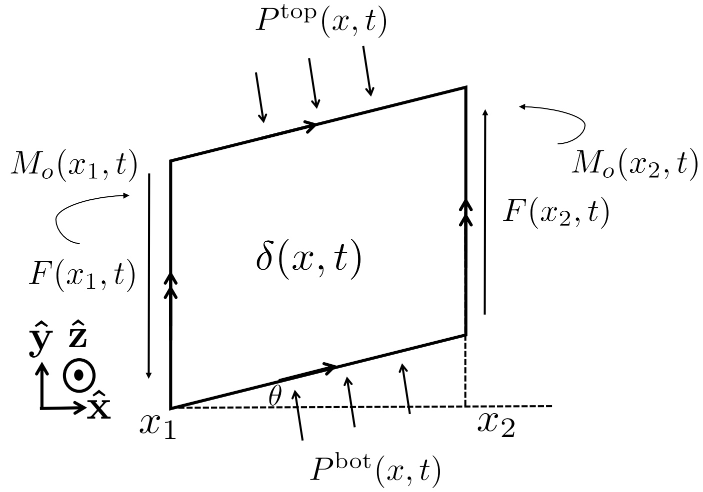

Figure 2.4: Illustration of control volume free-body diagram of beam cross-section.

The Euler-Bernoulli model assumes the following:

1. The bending wavelength is much larger than the cross sectional dimensions of the beam, and hence only valid for the lower wavenumber solutions (restricting solution to lower eigenvalues in equation 2.76);

2. Rotational inertia is negligible. Specifically, the translational inertia in $\hat{\mathbf{y}}$ is much greater than that from the rotation of the element in the control volume;
3. Beam extension, or displacement in $\hat{\mathbf{x}}$ direction, is negligible compared with the transverse displacement $\delta(x,t)$ in $\hat{\mathbf{y}}$ direction;
4. Shear displacement is negligible as compared to $\delta(x,t)$.

Assumptions 3 and 4 forces the parallel constraints illustrated in figure 2.4 between top and bottom, left and right faces of the control volume. It also follows from assumption 3 that since there is no beam extension, flow shear stresses do not impact the motion of the elastic member. Lastly, assumption 1 restricts $L >> h_b$, and is consistent with condition 1 from the pressure operator derivation in section 2.2.1, such that

$$F_{\text{net}}(x,t) \approx P_{\text{bot}}(x,t) - P_{\text{top}}(x,t).$$

### 2.3.2 Structural and Viscous Damping Models

We note that equation 2.66 does not include solid/structural energy dissipation terms. Banks and Inman [59] discuss the mechanisms for energy dissipation relevant to Euler-Bernoulli beam model, and provide experiments and methods to obtain empirical coefficients. Damping mechanisms are attributed to internal and external (to the solid) forms of energy dissipation. Internal mechanisms include those modeled as proportional to the strain-rate, for example, such as Kelvin-Voigt damping, which takes the form,

$$F_d \sim \frac{\partial^5 \delta}{\partial^4 x \partial t}, \tag{2.67}$$

or time- or spatial- hysteretic, where the damping term includes the history of the previous strains in the system (in time and space) added to the current strain-rate. In addition to the partial-differential equation, these forms modify the standard beam boundary conditions that include the strain terms, such as the standard “free-end”, discussed later in this section. External damping on the other hand may take the form of viscous damping from the surrounding fluid, for example. It is considered the simplest damping model and often referred to as Rayleigh damping,

$$F_{\text{d}} = c\frac{\partial \delta}{\partial t}, \tag{2.68}$$

where $c \geq 0$ is the damping constant that defines the damping force $F_\text{d}$ proportional to the beam velocity. Hence, it is evident that the "external" damping should be included in $P_\text{top}$ and $P_\text{bot}$ as part of the $F_\text{net}$ on the structure, most notably in the absence of flow. However, as we take the limit of $q_{x0} \to 0$ in equations 2.64 and 2.29, $f_0 \to \infty$. A number of issues arise with the current formulation of the pressure operator in this limit, primarily that the lubrication closure no longer holds, and that the model 2.7 and 2.32 no longer represent the dominant form of the fluid forces on the elastic member. Sader and Eysden in [60–62] explore the fluid force in an unconfined, stagnant fluid for long, narrow, thin beams, where they show that the appropriate hydrodynamic viscous force scaling is $Re_{\omega_1} = \frac{\rho_f \omega_{\text{vac},1} b^2}{4\mu_f}$, where $\omega_{\text{vac},1}$ is the fundamental resonant angular frequency of their respective beam in a vacuum. Their hydrodynamic force formulation follows an adaptation of Rosenhead, using boundary layer theory around an oscillating cylinder [63] corrected for a flat plate. Although the confinement in a channel may ultimately prove dominant in the stagnant limit, the appropriate viscous time scale still remains only defined by properties of the structure. However, as $q_{x0}$ increases and the channel flow-through-time, $\frac{\bar{h}L}{q_{x0}}$, becomes the appropriate time scale for the viscous forces, we recover the current hydrodynamic pressure model.

Hence we believe that Rayleigh damping is therefore not appropriate for the $q_{x0} > 0$ formulation of the hydrodynamic pressure and not included in the structural equations of motion. In the spirit of simplicity, we choose to also not include internal structural damping in the structural system, although this can be done by including a term such as 2.67 in equation 2.66, and adapting the expansions to satisfy the appropriate boundary conditions applied to the free end.

### 2.3.3 Structure Boundary Conditions

To uniquely solve the structural model 2.66, four boundary conditions are necessary. In this section we consider two types of boundary conditions that are relevant for the flow-energy harvester problem. First is the typical cantilever boundary, where the leading edge is clamped and trailing is free. Second is the elastic-translating boundary used to emulate the dynamics of the flextensional transducer.

#### Clamped-Free Boundary Condition

The clamped-free boundary, where the leading edge is clamped and the trailing edge is free, is defined as

$$\delta(0,t) = 0,\ \frac{\partial}{\partial x}\delta(0,t) = 0,\ \frac{\partial^2}{\partial x^2}\delta(L,t) = 0,\ \frac{\partial^3}{\partial x^3}\delta(L,t) = 0. \tag{2.69}$$

Clamped means no allowed displacement or rotation. Conversely, the free end allows translating and angular motion, but has zero transverse load and zero moment.

### Elastic-Translating Boundary Condition

The second boundary condition of interest it one where the $\hat{\mathbf{y}}$ displacement, $\bar{a}$, is determined by the dynamics of a second system, while the remaining three boundary conditions are those of the clamped-free beam,

$$\delta(0,t) = \bar{a},\ \frac{\partial}{\partial x}\delta(0,t) = 0,\ \frac{\partial^2}{\partial x^2}\delta(L,t) = 0,\ \frac{\partial^3}{\partial x^3}\delta(L,t) = 0. \tag{2.70}$$

As illustrated in figure 2.1, we characterize the dynamics of the leading edge translation as the response to a simple harmonic oscillator to the reacting force $f_r$,

$$\frac{m_0}{b}\ddot{\bar{a}} + \frac{c_0}{b}\dot{\bar{a}} + \frac{k_0}{b}\bar{a} = f_r, \tag{2.71}$$

where $\frac{m_0}{b}$, $\frac{c_0}{b}$, and $\frac{k_0}{b}$ are the boundary mass, damping, and stiffness constants *per unit span*. The reacting force $f_r$ is equivalent to the integral of the force acting on the structure, which is simply the integral over the beam length of the pressure difference between the channels,

$$\begin{aligned} f_r = \int_{\partial V} f_f dA &= \int_0^L \left(P^{\text{bot}} - P^{\text{top}}\right) dx \\ &= \int_0^L \left[p_0^{\text{bot}} - p_0^{\text{top}} + \varepsilon\left(p_1^{\text{bot}} - p_1^{\text{top}}\right]\right) dx, \end{aligned} \tag{2.72}$$

where the right-hand-side is the linearized net force on the structure. Expanding $\bar{a}$ in orders of $\varepsilon$, substituting equation 2.72 into equation 2.71, and once again collecting and equating coefficients, we have the equilibrium equation for the boundary as

$$\frac{m_0}{b}\ddot{\bar{a}}_0 + \frac{c_0}{b}\dot{\bar{a}}_0 + \frac{k_0}{b}\bar{a}_0 = \int_0^L \left(p_0^{\text{bot}} - p_0^{\text{top}}\right) dx, \tag{2.73}$$

and $\varepsilon^1$ terms as

$$\frac{m_0}{b}\ddot{\bar{a}}_1 + \frac{c_0}{b}\dot{\bar{a}}_1 + \frac{k_0}{b}\bar{a}_1 = \int_0^L \left(p_1^{\text{bot}} - p_1^{\text{top}}\right) dx. \tag{2.74}$$

To account for the boundary movement within the beam shape, we augment the expansion of $\delta(x,t)$

$$\delta(x,t) = \bar{a}_0 + \delta_0(x) + \varepsilon\left(\bar{a}_1(t) + \delta_1(x,t)\right). \tag{2.75}$$

We must also redefine the system equilibrium as $h_e(x) = h_0(x) - (\delta_0(x) + \bar{a}_0)$. To solve for $h_e$, equation 2.73 must be solved in conjunction with equation 2.90. As before, symmetric channels ($h_0^{\text{top}} = -h_0^{\text{bot}}$) is a sufficient condition for $\delta_0(x) = 0$ and $\bar{a}_0 = 0$ as an equilibrium, which is where we will focus our analysis.

### 2.3.4 Discretization Basis Functions

The solutions to the homogeneous version of partial differential equation 2.85 can provide insight to the solution of equation 2.93. In conjunction with the boundary conditions, they provide a set of basis functions we use to discretize the equations of motion in order to solve the fluid-structure system numerically. In solving equation 2.93 through separation of variables, we recover the eigenvalue problem to the one-dimensional biharmonic operator,

$$\frac{\mathrm{d}^4\phi}{\mathrm{d}x^4} + \beta^4\phi = 0. \tag{2.76}$$

When considered in the domain $x \in [0, L]$ with appropriate boundary conditions, the solutions $\phi_k$, $k \in \mathbb{Z} : [1, \infty]$, may provide a complete basis by which any square integrable function can be expanded [58, 59]. Physically, $\phi_k$ represent the orthogonal modes of a linear-elastic beam, represented by equation 2.85. The addition of damping and forcing terms by the hydrodynamic pressure in equation 2.93 will change the modes, such that they are no longer orthogonal, but coupled (non-normal). Sader [60] discusses this briefly when deriving a model for the dynamics of a three-dimensional cantilever in stagnant fluid. If modes are not changed considerably, the undamped modes may remain a good representation of modified mode shapes. Here we consider “a good representation” as one where the series expansion may need fewer terms to obtain a desired error level when compared to other basis functions such as cubic-splines and Chebyshev polynomials. The solution to the biharmonic operator eigenvalue problem is given by

$$\phi(x) = A\cos(\beta x) + B\sin(\beta x) + C\sinh(\beta x) + D\cosh(\beta x), \tag{2.77}$$

where the boundary conditions can be used to determine $\beta$ and coefficients $A$, $B$, $C$, and $D$. We will consider two structure boundary conditions in our analysis.

### Basis Functions for Clamped-Free Boundary Condition

The first is the clamped-free boundary, where the leading edge is clamped and the trailing edge is free. From equation 2.69, we have

$$\phi_i(0) = 0,\ \frac{\partial}{\partial x}\phi_i(0) = 0,\ \frac{\partial^2}{\partial x^2}\phi_i(L) = 0,\ \frac{\partial^3}{\partial x^3}\phi_i(L) = 0. \tag{2.78}$$

Equation 2.77 with boundary conditions 2.78 gives the complete solution with eigenfunctions

$$\phi_k(x) = \cosh(\beta_k\, x) - \cos(\beta_k\, x) + \left[\frac{\cos(\beta_k\, L) + \cosh(\beta_k\, L)}{\sin(\beta_k\, L) + \sinh(\beta_k\, L)}\right]\Big(\sin(\beta_k\, x) - \sinh(\beta_k\, x)\Big), \tag{2.79}$$

and characteristic equation

$$\cosh(\beta_k L)\cos(\beta_k L) + 1 = 0 \tag{2.80}$$

for $k \in \mathbb{Z} : [1, \infty]$. The first six values are listed in table 2.2.

Table 2.2: Table of solutions to the characteristic equation 2.80.

| $\beta_1 L$ | $\beta_2 L$ | $\beta_3 L$ | $\beta_4 L$ | $\beta_5 L$ | $\beta_6 L$ |
|---|---|---|---|---|---|
| 1.8751 | 4.6941 | 7.8548 | 10.9955 | 14.1372 | 17.2788 |

Hence, for boundary conditions 2.69, the equations 2.96 can be approximated with a finite expansion using eigenfunctions 2.79, so that $k \in \mathbb{Z} : [1, n]$, such that

$$g_i(x) = \begin{cases} 0 & \text{for } i = 0 \\ \phi_i(x) & \text{for } i = [1, n] \end{cases}. \tag{2.81}$$

**Basis Functions for Elastic-Translating Boundary Condition**

The elastically translating boundary condition stems from equation 2.70, where we apply the basis $\phi_i(x)$

$$\delta(0,t) = \bar{a},\ \frac{\partial}{\partial x}\phi_i(0) = 0,\ \frac{\partial^2}{\partial x^2}\phi_i(L) = 0,\ \frac{\partial^3}{\partial x^3}\phi_i(L) = 0. \tag{2.82}$$

Making use of linear superposition to obtain a solution to equation 2.91 with data 2.70 that satisfies equation 2.74, we use the basis expansion 2.79, from 1 to $n$ terms, such that $a_i$ satisfy data 2.78 and $\bar{a}_1$ satisfies equation 2.74. We can further define,

$$\delta_1(x,t) = \bar{a}_1(t) + \sum_{i=1}^{m} a_i(t)\phi_i(x) = \sum_{i=0}^{n} a_i(t)g_i(x), \tag{2.83}$$

where $a_0(t) = \bar{a}_1(t)$ and the basis functions are augmented such that

$$g_i(x) = \begin{cases} 1 & \text{for } i = 0 \\ \phi_i(x) & \text{for } i = [1,n] \end{cases}. \tag{2.84}$$

### 2.3.5 Fluid-Structure Coupled Operator

In the current formulation, we disregard the spanwise direction in the Euler-Bernoulli beam equation,

$$\rho_s h_b \frac{\partial^2}{\partial t^2}\delta(x,t) + \frac{\partial^2}{\partial x^2}\left(EI_{2\mathrm{D}}\frac{\partial^2}{\partial x^2}\delta(x,t)\right) = P^{\mathrm{bot}}(x,t) - P^{\mathrm{top}}(x,t), \tag{2.85}$$

where

$$I_{2\mathrm{D}} = \frac{h_b^3}{12(1-\nu^2)} \tag{2.86}$$

is the cross-section area moment of inertia (in two Dimensions), and $P^{\mathrm{bot}}(x,t)$ and $P^{\mathrm{top}}(x,t)$ are the pressure operators for the bottom and top channels respectively. Figure 2.5 illustrates the force balance as a function of beam shape. To connect the pressures in the top and bottom channels, we write the geometrical constraint,

$$h_0^{\mathrm{top}}(x) - \delta^{\mathrm{top}}(x,t) + \left(\delta^{\mathrm{bot}}(x,t) - h_0^{\mathrm{bot}}(x)\right) = h_0^{\mathrm{top}}(x) - h_0^{\mathrm{bot}}(x), \tag{2.87}$$

where we recover the simple relationship

$$\delta(x,t) = \delta^{\text{top}}(x,t) = -\delta^{\text{bot}}(x,t). \tag{2.88}$$

The geometrical constraint for the total gap size of the two channels means that we only have one shape of the beam, $\delta$, that relates the two pressures.

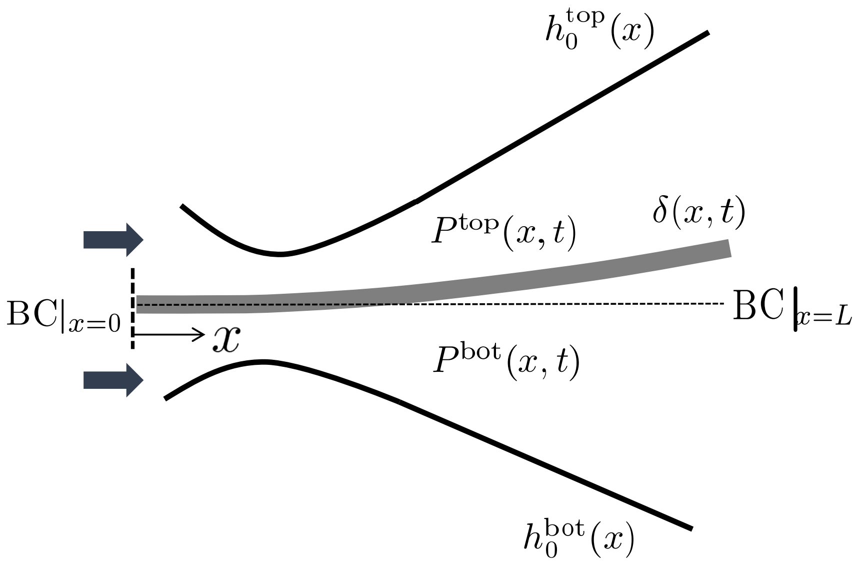

Figure 2.5: Illustration hydrodynamic force balance as a function of beam shape.

Substituting the linear expansion for $\delta$ and $P$ into equation 2.85, and assuming that $E$ and $I$ are spatially uniform in $x$,

$$EI_{2\text{D}}\frac{\mathrm{d}^4}{\mathrm{d}x^4}\delta_0(x) + \varepsilon\left(\rho_s h_b \frac{\partial^2}{\partial t^2}\delta_1(x,t) + EI_{2\text{D}}\frac{\partial^4}{\partial x^4}\delta_1(x,t)\right) = p_0^{\text{bot}} - p_0^{\text{top}} + \varepsilon\left(p_1^{\text{bot}} - p_1^{\text{top}}\right). \tag{2.89}$$

Here we note that the left-had-side of equation 2.89 depends only on $\delta$, as it represents the internal stresses and acceleration of the beam. The right-hand-side, however, depends on the channel gap size, which includes $h_0$ and $\delta$ ($h_e$). Equating $\varepsilon$ coefficients, we can solve for the equilibrium beam shape $\delta_0$ by solving the nonlinear ODE at 0th order,

$$EI_{2\text{D}}\frac{\mathrm{d}^4}{\mathrm{d}x^4}\delta_0(x) = p_0^{\text{bot}} - p_0^{\text{top}}, \tag{2.90}$$

where $p_0^{\text{bot}}$ and $p_0^{\text{top}}$ are the equilibrium pressures in equation 2.58 evaluated at $h_0^{\text{bot}}$ and $h_0^{\text{top}}$, respectively. Here we note that if $h_0^{\text{top}} = -h_0^{\text{bot}}$, making the system symmetric, the right-hand-side of equation 2.90 is zero, and hence a sufficient condition for the equilibrium beam shape $\delta_0$ to also equal zero. Due to the nonlinear nature of $p_0$, and the broad definition of $h_0(x)$, other equilibria may exist. Although we will focus our analysis on the stability of $\delta_0 = 0$ case, equation 2.90 gives the means to tune $h_e$ to yield different equilibria and perhaps different system behaviors. The linear term at $\varepsilon^1$ follows,

$$\rho_s h_b \frac{\partial^2}{\partial t^2}\delta_1(x,t) + EI_{\text{2D}}\frac{\partial^4}{\partial x^4}\delta_1(x,t) = p_1^{\text{bot}} - p_1^{\text{top}}, \tag{2.91}$$

where

$$\begin{aligned} p_1^{\text{bot}} - p_1^{\text{top}} = T_{\text{f}}^{\text{bot}}(x)\bar{Q}_{x1}^{\text{bot}}(t) - \sum_{i=0}^{\infty}\left(M_{\text{f}i}^{\text{bot}}(x)\ddot{a}_i(t) + C_{\text{f}i}^{\text{bot}}(x)\dot{a}_i(t) + K_{\text{f}i}^{\text{bot}}(x)a_i(t)\right) - \\ \left[T_{\text{f}}^{\text{top}}(x)\bar{Q}_{x1}^{\text{top}}(t) + \sum_{i=0}^{\infty}\left(M_{\text{f}i}^{\text{top}}(x)\ddot{a}_i(t) + C_{\text{f}i}^{\text{top}}(x)\dot{a}_i(t) + K_{\text{f}i}^{\text{top}}(x)a_i(t)\right)\right], \end{aligned} \tag{2.92}$$

are the first order pressure perturbations from equation 2.64 evaluated at the the top and bottom channels, and includes the substitution of equation 2.88 and the basis function expansion for $\delta_1$. By expanding $\delta_1$ on left-hand-side of equation 2.91 using the same basis functions, we obtain a coupled, linear ODE for $a_i$,

$$\begin{aligned} \sum_{i=0}^{\infty}\Big(M_{\text{s}i}(x)\ddot{a}_i(t) + C_{\text{s}i}(x)\dot{a}_i(t) + K_{\text{s}i}(x)a_i(t)\Big) = T_{\text{f}}^{\text{bot}}(x)\bar{Q}_{x1}^{\text{bot}}(t) - T_{\text{f}}^{\text{top}}(x)\bar{Q}_{x1}^{\text{top}}(t) - \\ \sum_{i=0}^{\infty}\Big[\left(M_{\text{f}i}^{\text{bot}}(x) + M_{\text{f}i}^{\text{top}}(x)\right)\ddot{a}_i(t) + \left(C_{\text{f}i}^{\text{bot}}(x) + C_{\text{f}i}^{\text{top}}(x)\right)\dot{a}_i(t) + \\ \left(K_{\text{f}i}^{\text{bot}}(x) + K_{\text{f}i}^{\text{top}}(x)\right)a_i(t)\Big], \end{aligned} \tag{2.93}$$

where

$$M_{\text{s}i} = \rho_s h_b g_i(x),\ K_{\text{s}i} = EI_{\text{2D}}\frac{\mathrm{d}^4}{\mathrm{d}x^4}g_i(x), \tag{2.94}$$

and $C_{\mathrm{s}i}$ is the damping term associated with the moving boundary condition, to be defined in the next sub-section, in our current formulation. We note that $C_{\mathrm{s}i}$ can also be associated with internal damping models of the beam if any are included in equation 2.85, although none currently are. Equation 2.93 represents the fully-coupled linear fluid-structure operator, and can account for two independent channels. Looking at the fundamental structure of equations 2.90 and 2.93, in order, allows us to understand the dynamics of the system. To construct a discrete operator that can be evaluated, we carry out the Galerkin projection of equation 2.93 on a subset of basis functions $g_j$ for $j \in \mathbb{Z} : [0, n]$ to formulate its weak form,

$$\begin{aligned}
&\int_0^L \sum_{i=0}^{n} \Big( M_{\mathrm{s}i}(x)\ddot{a}_i(t) + C_{\mathrm{s}i}(x)\dot{a}_i(t) + K_{\mathrm{s}i}(x)a_i(t) \Big) g_j(x)dx = \\
&\quad \int_0^L \left( T_{\mathrm{f}}^{\mathrm{bot}}(x)\bar{Q}_{x1}^{\mathrm{bot}}(t) - T_{\mathrm{f}}^{\mathrm{top}}(x)\bar{Q}_{x1}^{\mathrm{top}}(t) \right) g_j(x)dx - \\
&\quad \int_0^L \sum_{i=0}^{n} \Big[ \left( M_{\mathrm{f}i}^{\mathrm{bot}}(x) + M_{\mathrm{f}i}^{\mathrm{top}}(x) \right) \ddot{a}_i(t) + \left( C_{\mathrm{f}i}^{\mathrm{bot}}(x) + C_{\mathrm{f}i}^{\mathrm{top}}(x) \right) \dot{a}_i(t) + \\
&\quad \left( K_{\mathrm{f}i}^{\mathrm{bot}}(x) + K_{\mathrm{f}i}^{\mathrm{top}}(x) \right) a_i(t) \Big] g_j(x)dx.
\end{aligned} \tag{2.95}$$

Coupled with equation 2.65, we can rewrite the system of equations in matrix form as the evolution of states $a_i$, $\dot{a}_i$, and $\bar{Q}_{x1}$, by solving for $\ddot{a}_i$,

$$\begin{bmatrix} \dot{a}_0 \\ \vdots \\ \dot{a}_n \\ \ddot{a}_0 \\ \vdots \\ \ddot{a}_n \\ \dot{\bar{Q}}_{x1}^{\mathrm{bot}} \\ \dot{\bar{Q}}_{x1}^{\mathrm{top}} \end{bmatrix} = \begin{bmatrix} 0 & \mathbf{1} & 0 & 0 \\ M^{-1}K & M^{-1}C & M^{-1}T^{\mathrm{bot}} & M^{-1}T^{\mathrm{top}} \\ -[E_q^{\mathrm{bot}} + B_q^{\mathrm{bot}}(M^{-1}K)] & -[D_q^{\mathrm{bot}} + B_q^{\mathrm{bot}}(M^{-1}C)] & -B_q^{\mathrm{bot}}(M^{-1}T^{\mathrm{bot}}) & [G_q^{\mathrm{bot}} - B_q^{\mathrm{bot}}(M^{-1}T^{\mathrm{top}})] \\ E_q^{\mathrm{top}} + B_q^{\mathrm{top}}(M^{-1}K) & D_q^{\mathrm{top}} + B_q^{\mathrm{top}}(M^{-1}C) & G_q^{\mathrm{top}} + B_q^{\mathrm{top}}(M^{-1}T^{\mathrm{bot}}) & B_q^{\mathrm{top}}(M^{-1}T^{\mathrm{top}}) \end{bmatrix} \begin{bmatrix} a_0 \\ \vdots \\ a_n \\ \dot{a}_0 \\ \vdots \\ \dot{a}_n \\ \bar{Q}_{x1}^{\mathrm{bot}} \\ \bar{Q}_{x1}^{\mathrm{top}} \end{bmatrix}, \tag{2.96}$$

where the following exist in $\mathbb{R}^{n+1\,\times\,n+1}$,

$$\begin{aligned}
M_{ij} &= \frac{1}{N_{ij}} \int_0^L \left( M_{\mathrm{s}i}(x) + M_{\mathrm{f}i}^{\mathrm{bot}}(x) + M_{\mathrm{f}i}^{\mathrm{top}}(x) \right) g_j(x) dx, \\
C_{ij} &= -\frac{1}{N_{ij}} \int_0^L \left( C_{\mathrm{s}i}(x) + C_{\mathrm{f}i}^{\mathrm{bot}}(x) + C_{\mathrm{f}i}^{\mathrm{top}}(x) \right) g_j(x) dx, \\
K_{ij} &= -\frac{1}{N_{ij}} \int_0^L \left( K_{\mathrm{s}i}(x) + K_{\mathrm{f}i}^{\mathrm{bot}}(x) + K_{\mathrm{f}i}^{\mathrm{top}}(x) \right) g_j(x) dx,
\end{aligned} \tag{2.97}$$

where the norm is defined as,

$$N_{ij} = \int_0^L g_i(x) g_j(x) dx. \tag{2.98}$$

The following exist in $\mathbb{R}^{n+1 \times 1}$,

$$\begin{aligned}
T_j^{\mathrm{bot}} &= \frac{1}{N_{ij}} \int_0^L T_{\mathrm{f}}^{\mathrm{bot}}(x) g_j(x) dx \\
T_j^{\mathrm{top}} &= -\frac{1}{N_{ij}} \int_0^L T_{\mathrm{f}}^{\mathrm{top}}(x) g_j(x) dx.
\end{aligned} \tag{2.99}$$

The vectors $B_q$, $D_q$, and $E_q$ exist in $\mathbb{R}^{1 \times n+1}$, and are the evaluated coefficients in equation 2.65 for their respective channels. The state vector is comprised of the coefficients of the expansion $a_i$, their time derivatives $\dot{a}_i$ and the forcing flow rate from the top and bottom channels, $\bar{Q}_{x1}^{\mathrm{top}}$ and $\bar{Q}_{x1}^{\mathrm{bot}}$. Equation 2.96 is the linear time evolution of the state vector, and by evaluating it at an equilibrium point, calculated by solving the nonlinear equation 2.90, its eigenvalues and eigenvectors dictate what rate and shape a small disturbance will grow or decay. The part that remains is defining the structural boundary conditions and an expansion basis $g_i$ that satisfy them.

### Structural Constants for Elastic-Translating Boundary Condition

When applying the elastic translating boundary conditions with basis functions in equation 2.84, we augment the structural constants to include those in the boundary equation 2.74,

$$M_{\mathrm{s}i} = \begin{cases} \frac{m_0}{b} & \text{for } i = 0 \\ \rho_s h_b g_i(x) & \text{for } i = [1, n] \end{cases}, \tag{2.100}$$

$$C_{\mathrm{s}i} = \begin{cases} \frac{c_0}{b} & \text{for } i = 0 \\ 0 & \text{for } i = [1, n] \end{cases}, \tag{2.101}$$

$$K_{\mathrm{s}i} = \begin{cases} \frac{k_0}{b} & \text{for } i = 0 \\ EI_{2\mathrm{D}} \frac{\mathrm{d}^4}{\mathrm{d}x^4} g_i(x) & \text{for } i = [1, n] \end{cases}. \tag{2.102}$$

When definitions in equations 2.100 - 2.102 are considered in equations 2.95, 2.97, and 2.99, then equation 2.96 becomes the linear map including a translating boundary condition in data 2.70 defined by 2.71 as $a_0(t)$ and $\dot{a}_0(t)$ states. We will refer to these equations are the quasi-1D model with either clamped-free or elastic-translating/moving boundary conditions in the subsequent text.

### 2.3.6 Non-Dimensional Fluid-Structure Equations

To non-dimensionalize the coupled fluid-structure equations, we begin by assuming that the top and bottom channels are symmetric to simplify the hydrodynamic operator to a single length scale. Hence, similar to the lubrication closure, we define $\bar{h} \sim h_e$ as a constant that is characteristic of the channel gap. With the characteristic velocity is $U_c = \frac{q_{x0}}{\bar{h}}$, and motivated by equation 2.61, we see the relevant pressure parameter $p_1 \sim \rho_f U_c^2$. We define the relevant time scale as the flow through time over $L$, as the primary flow is along the beam length, and write all parameters as:

$$\begin{gathered} x^* = \frac{x}{L},\ t^* = \frac{q_{x0}}{\bar{h}L}t,\ h_e^*(x^*) = \frac{h_e(x)}{\bar{h}}, \\ g_i{}^*(x^*) = \frac{g_i(x)}{\bar{h}},\ P^* = \frac{2}{\rho_f}\left(\frac{\bar{h}}{q_{x0}}\right)^2,\ \bar{Q}^*_{x1}(t^*) = \frac{\bar{Q}_{x1}(t)}{q_{x0}}. \end{gathered} \tag{2.103}$$

Normalizing $P$, equation 2.93 simplifies to,

$$\sum_{i=0}^{\infty} M_i^* \frac{\mathrm{d}^2 a_i}{\mathrm{d}t^{*2}} = -\sum_{i=0}^{\infty} \left[ C_i^* \frac{\mathrm{d}a_i}{\mathrm{d}t^*} + K_i^* a_i \right] - T_{\mathrm{f}}^* \bar{Q}^*_{x1}. \tag{2.104}$$

where the coefficients are,

$$
\begin{aligned}
M_i^* &= \frac{2}{\rho_f L^2}\Big(M_{\mathrm{s}i} + 2M_{\mathrm{f}i}\Big) = M_{\mathrm{s}i}^* + M_{\mathrm{f}i}^*,\\
C_i^* &= \frac{2}{\rho_f q_{x0}}\frac{\bar{h}}{L}\Big(2C_{\mathrm{f}i} + C_{\mathrm{s}i}\Big) = C_{\mathrm{f}i}^* + C_{\mathrm{s}i}^*,\\
K_i^* &= \frac{2}{\rho_f}\frac{\bar{h}^2}{q_{x0}^2}\Big(2K_{\mathrm{f}i} + K_{\mathrm{s}i}\Big) = K_{\mathrm{f}i}^* + K_{\mathrm{s}i}^*,\\
T_{\mathrm{f}}^* &= \frac{2}{\rho_f}\frac{\bar{h}^2}{q_{x0}}\Big(2T_{\mathrm{f}}\Big).
\end{aligned}
\tag{2.105}
$$

We examine the definition of the fluid coefficients in more detail by aggregating parts of equations in appendix A, where we can separate viscous, geometrical, and boundary terms from one another. Looking closely at equations A.1 - A.8, they consist of integral and differential operators of the channel geometry, $h_e$ and $g_i$, often multiplied by either $\xi_x$, $f_0$, $\eta$, $\zeta_{\mathrm{in}}$, or $\zeta_{\mathrm{out}}$. We will define viscous terms as those integral and differential operators with a factor of either $f_0$ or $\eta$ (subscript v), geometrical or nonlinear as those with a factor of $\xi_x$ or only a function of the geometry (subscript g), and boundary terms those with factors of either $\zeta_{\mathrm{in}}$ or $\zeta_{\mathrm{out}}$ (subscript b). For disambiguation, we will list the parameter dependence, before the semi-colon, as each term is defined. Non-dimentionalizing the mass term from equation A.1, as defined in equation 2.105,

$$
M_{\mathrm{f}i}^* = \frac{4}{\rho_f L^2} M_{\mathrm{f}i} = 4M_{\mathrm{g}i}^*(x^*).
\tag{2.106}
$$

Similarly, the damping term from equation A.2,

$$
\begin{aligned}
C_{\mathrm{f}i}^* &= \frac{4}{\rho_f q_{x0}}\frac{\bar{h}}{L} C_{\mathrm{f}i}\\
&= 4\left(C_{\mathrm{g}i}^*(\xi_x; x^*) + C_{\mathrm{b}i}^*(\zeta_{\mathrm{out}}; x^*)\right) + 4\left(\frac{L}{\bar{h}}\right)\left(\frac{f_0}{2} + \frac{q_{x0}\eta}{4}\right) C_{\mathrm{v}i}^*(x^*),
\end{aligned}
\tag{2.107}
$$

the stiffness term from equation A.3,

$$
\begin{aligned}
K_{\mathrm{f}i}^* &= \frac{4}{\rho_f}\frac{\bar{h}^2}{q_{x0}^2} K_{\mathrm{f}i}\\
&= 4\left(K_{\mathrm{g}i}^*(\xi_x; x^*) + K_{\mathrm{b}i}^*(\zeta_{\mathrm{in}}, \zeta_{\mathrm{out}}; x^*)\right) + 4\left(\frac{L}{\bar{h}}\right)\left(\frac{3f_0}{4}\right) K_{\mathrm{v}i}^*(x^*),
\end{aligned}
\tag{2.108}
$$

and the flow rate forcing term in equation A.4,

$$\begin{aligned} T_{\mathrm{f}}^{*} &= \frac{4}{\rho_f}\frac{\bar{h}^2}{q_{x0}}T_{\mathrm{f}} \\ &= 4\left(T_{\mathrm{g}}^{*}(\xi_x; x^*) + T_{\mathrm{b}}^{*}(\zeta_{\mathrm{in}}, \zeta_{\mathrm{out}}; x^*)\right) + 4\left(\frac{L}{\bar{h}}\right)\left(\frac{f_0}{2} + \frac{q_{x0}\eta}{4}\right)T_{\mathrm{v}}^{*}(x^*). \end{aligned} \tag{2.109}$$

We must also non-dimentionalize the ODE 2.65 for $\bar{Q}_{x1}$,

$$\frac{\mathrm{d}\bar{Q}_{x1}^{*}}{\mathrm{d}t^{*}} = \sum_{i=0}^{\infty}\left[B_{\mathrm{q}i}^{*}\frac{\mathrm{d}^2 a_i}{\mathrm{d}t^{*2}} + D_{\mathrm{q}i}^{*}\frac{\mathrm{d}a_i}{\mathrm{d}t^{*}} + E_{\mathrm{q}i}^{*}a_i\right] + G_{\mathrm{q}}^{*}\bar{Q}_{x1}^{*}. \tag{2.110}$$

where the coefficients are, for acceleration in equation A.5

$$B_{\mathrm{q}i}^{*} = \frac{1}{\bar{h}L}B_{\mathrm{q}i} = B_{\mathrm{qg}i}^{*}(x^*), \tag{2.111}$$

for velocity in equation A.6,

$$\begin{aligned} D_{\mathrm{q}i}^{*} &= \frac{1}{q_{x0}}D_{\mathrm{q}i} \\ &= \left(D_{\mathrm{qg}i}^{*}(\xi_x; x^*) + D_{\mathrm{qb}i}^{*}(\zeta_{\mathrm{out}}; x^*)\right) - \left(\frac{L}{\bar{h}}\right)\left(\frac{f_0}{2} + \frac{q_{x0}\eta}{4}\right)D_{\mathrm{qv}i}^{*}(x^*), \end{aligned} \tag{2.112}$$

for displacement in equation A.7,

$$\begin{aligned} E_{\mathrm{q}i}^{*} &= \frac{\bar{h}L}{q_{x0}^2}E_{\mathrm{q}i} \\ &= \left(E_{\mathrm{qg}i}^{*}(\xi_x; x^*) + E_{\mathrm{qb}i}^{*}(\zeta_{\mathrm{in}}, \zeta_{\mathrm{out}}; x^*)\right) - \left(\frac{L}{\bar{h}}\right)\left(\frac{3f_0}{4}\right)E_{\mathrm{qv}i}^{*}(x^*), \end{aligned} \tag{2.113}$$

for the forcing flow rate in equation A.8,

$$\begin{aligned} G_{\mathrm{q}}^{*} &= \frac{\bar{h}L}{q_{x0}}G_{\mathrm{q}} \\ &= \left(G_{\mathrm{qg}}^{*}(\xi_x; x^*) + G_{\mathrm{qb}}^{*}(\zeta_{\mathrm{in}}, \zeta_{\mathrm{out}}; x^*)\right) - \left(\frac{L}{\bar{h}}\right)\left(\frac{f_0}{2} + \frac{q_{x0}\eta}{4}\right)G_{\mathrm{qv}}^{*}(x^*). \end{aligned} \tag{2.114}$$

Equations 2.106 - 2.109 and 2.111 - 2.114 show that the hydrodynamic boundary and geometrical terms are not impacted by the length scale of the gap $\bar{h}$, but rather the “shape” of the channel gap along the axial direction. However, by changing the relative scaling of the channel, $\frac{\bar{h}}{L}$, we affect the viscous term. Looking specifically at the laminar flow case as defined in equation 2.29, and the definition in equation 2.49,

$$\eta = \left.\frac{\mathrm{d}f}{\mathrm{d}Q_x}\right|_{Q_x=q_{x0}} = -\frac{48}{Re_{\bar{h}}}\frac{1}{q_{x0}} = -\frac{f_0}{q_{x0}}, \tag{2.115}$$

the coefficients of all viscous terms simplify to

$$\frac{3}{4}f_0\frac{L}{\bar{h}} = \frac{36}{Re_{\bar{h}}}\frac{L}{\bar{h}} \sim \left(\varepsilon_h^2 Re_L\right)^{-1}, \tag{2.116}$$

as defined in the lubrication closure in equation 2.18. Once again, the parameter $\varepsilon_h^2 Re_L$ appears an the dominant viscous ratio, rather than $Re_L$ or $\varepsilon_h Re_L = Re_h$. As $\varepsilon_h^2 Re_L$ increases, two important things occur:

1. Viscous effects diminish, as all the viscous coefficients for equations 2.106 - 2.109 and 2.111 - 2.114 become small;
2. The hydrodynamic model with the lubrication closure becomes less representative of the flow physics since inertial terms in equation 2.17 become important, as noted in condition 3 in section 2.2.1.

We now examine the relevance of structural non-dimensional parameters. First considering the elastic-translating boundary conditions from equation 2.70 using the non-dimensional structural terms in equation 2.105,

$$M_{\mathrm{s}i}^* = \frac{2}{\rho_f L^2}M_{\mathrm{s}i} = \begin{cases} 2\left(\frac{1}{\rho_f L^2}\frac{m_0}{b}\right)\left(\frac{\bar{h}}{L}\right) & \text{for } i = 0 \\ 2\left(\frac{\rho_s h_b}{\rho_f L}\right)\left(\frac{\bar{h}}{L}\right)g_i^*(x^*) & \text{for } i = [1, n] \end{cases}, \tag{2.117}$$

$$C_{\mathrm{s}i}^* = \frac{2}{\rho_f q_{x0}}\frac{\bar{h}}{L}C_{\mathrm{s}i} = \begin{cases} 2\left(\frac{\bar{h}}{\rho_f q_{x0}}\frac{c_0}{bL}\right)\left(\frac{\bar{h}}{L}\right) & \text{for } i = 0 \\ 0 & \text{for } i = [1, n] \end{cases}, \tag{2.118}$$

$$K_{\mathrm{s}i}^* = \frac{2}{\rho_f}\frac{\bar{h}^2}{q_{x0}^2}K_{\mathrm{s}i} = \begin{cases} 2\left(\frac{\bar{h}^2}{\rho_f q_{x0}^2}\frac{k_0}{b}\right)\left(\frac{\bar{h}}{L}\right) & \text{for } i = 0 \\ 2\left(\frac{\bar{h}^2 E}{\rho_f q_{x0}^2}\frac{I_{\mathrm{2D}}}{L^3}\right)\left(\frac{\bar{h}}{L}\right)\frac{\mathrm{d}^4}{\mathrm{d}x^{*4}}g_i^*(x^*) & \text{for } i = [1, n] \end{cases}. \tag{2.119}$$

The parameters for the clamped-free boundary condition in equations 2.70 are the elements of equations 2.117, 2.118, and 2.119 applicable for $i = [1, n]$. Writing the coupled system as proportional to the non-dimensional order of magnitude for each term for the beam, where we aggregate with like terms parameters in $F^*$ [1], we have

$$\left(\frac{\bar{h}}{L}\right)\left[\left(\frac{\rho_s h_b}{\rho_f L}\right)F^*_{\text{sM}} + \left(\frac{\bar{h}^2 E}{\rho_f q_{x0}^2}\frac{I_{\text{2D}}}{L^3}\right)F^*_{\text{sK}}\right] \sim F^*_{\text{fg}} + F^*_{\text{fb}} + \left[\left(\frac{\bar{h}}{L}\right)^2 Re_L\right]^{-1} F^*_{\text{fv}}, \tag{2.120}$$

and similarly for the elastic boundary condition,

$$\begin{aligned}\left(\frac{\bar{h}}{L}\right)\Bigg[&\left(\frac{1}{\rho_f L^2}\frac{m_0}{b}\right)F^*_{\text{sbM}} + \left(\frac{\bar{h}}{\rho_f q_{x0}}\frac{c_0}{bL}\right)F^*_{\text{sbC}} + \left(\frac{\bar{h}^2}{\rho_f q_{x0}^2}\frac{k_0}{b}\right)F^*_{\text{sbK}} + \\ &\left(\frac{\rho_s h_b}{\rho_f L}\right)F^*_{\text{sM}} + \left(\frac{\bar{h}^2 E}{\rho_f q_{x0}^2}\frac{I_{\text{2D}}}{L^3}\right)F^*_{\text{sK}}\Bigg] \sim F^*_{\text{fg}} + F^*_{\text{fb}} + \left[\left(\frac{\bar{h}}{L}\right)^2 Re_L\right]^{-1} F^*_{\text{fv}}.\end{aligned} \tag{2.121}$$

The four non-dimensional parameter that appear in the clamped-free system are shown in table 2.3. An additional three pertain only to the moving elastic boundary condition, shown in table 2.4. Equations 2.120 and 2.121 illustrate the general effect of each non-dimensional parameter on individual terms in the equations of motion. Clearly $\hat{h}$ scales the influence of structure as compared with the fluid right-hand-side, indicating that as it diminishes, the fluid terms will dominate the dynamics. As mentioned, $\hat{h}Re_h$ dictates the fluid viscous effects. Once the elastic boundary condition is included, its structural parameters then play a role on the overall system dynamics are well.

The total number of non-dimensional parameters with the elastic-translating boundary conditions is 7. Not all parameters in table 2.1 have been used in the fluid-structure portion of the analysis, namely those relating to electrical quantities. We also note that $h_t$, $x_t$, $R$, $\alpha_i$, and $\alpha_o$ are parameters used to describe the shape of the channel, all either with units of $l$ or non-dimensional. Once the gap is normalized by $\bar{h}$, then the remaining $l$ dimensional parameters will also be normalized by $\bar{h}$, and their contribution embedded into the $F$ terms in equations Equations 2.120 and

---

[1] Subscripts s for structure, f for fluid, b for boundary, M for mass, C for damping, K for stiffness, and as previously defined, g for geometrical, v for viscous. The point of this exercise is not to define the non-dimensional expressions for $F^*$, but to show the coefficients that scale as a function of dimensional parameters forming non-dimensional groups.

Table 2.3: Table of clamped-free fluid structure non-dimensional parameters.

| **Variable** | **Expression** | **Description** |
|---|---|---|
| $\hat{m}$ | $\frac{\rho_s h_b}{\rho_f L}$ | mass ratio |
| $\hat{k}$ | $\frac{\bar{h}^2 E}{\rho_f q_{x0}^2} \frac{I_{2D}}{L^3}$ | stiffness ratio |
| $\hat{h}$ | $\frac{\bar{h}}{L} = \varepsilon_h$ | gap or throat ratio |
| $\hat{h}Re_h$ | $\varepsilon_h^2 Re_L = \left(\frac{\bar{h}}{L}\right)^2 Re_L$ | viscous parameter |

Table 2.4: Table of elastic-translating fluid structure non-dimensional parameters.

| **Variable** | **Expression** | **Description** |
|---|---|---|
| $\hat{m}_{\mathrm{bc}}$ | $\frac{1}{\rho_f L^2} \frac{m_0}{b}$ | boundary mass ratio |
| $\hat{k}_{\mathrm{bc}}$ | $\frac{\bar{h}^2}{\rho_f q_{x0}^2} \frac{k_0}{b}$ | boundary stiffness ratio |
| $\hat{c}_{\mathrm{bc}}$ | $\frac{\bar{h}}{\rho_f q_{x0} L} \frac{c_0}{b}$ | boundary damping ratio |

2.121. The span $b$ will be discussed further in the next section, as we derive the quasi-1D model that includes spanwise leakage flow.

## 2.4 Fluid Equations of Motion including Spanwise Leakage Flow

In this section we consider the quasi-1D leakage model with the additional influence spanwise flow. The goal of this analysis is to introduce leakage flow rates into the system as additional states that augment the two-dimensional equations. In similar fashion to section 2.2, we consider a three-dimensional control volume analysis of the half-span section of the channel in order to obtain an expression that contains the $\hat{\mathbf{z}}$ momentum terms [2]. Figure 2.6 illustrates the control volume boundaries, with only half of the channel demarcating the control surfaces in $\hat{\mathbf{z}}$. The surface normal vector are

$$[\mathbf{n}_1 \cdots \mathbf{n}_6] = \begin{bmatrix} 1 & -1 & -h_0'(x) & \delta'(x,t) & 0 & 0 \\ 0 & 0 & 1 & -1 & 0 & 0 \\ 0 & 0 & 0 & 0 & 1 & -1 \end{bmatrix}, \tag{2.122}$$

similar to equation 2.1. The beam span $b$ defines the characteristic length in $\hat{\mathbf{z}}$, and we assume the beam is rigid in $z$, such that $\delta = \delta(x,t)$. Solid walls are in $\mathbf{n}_3$ and $\mathbf{n}_4$.

---

[2] If the total span is considered, the spanwise flow rates are canceled in momentum conservation because of the symmetry of the flow in the problem.

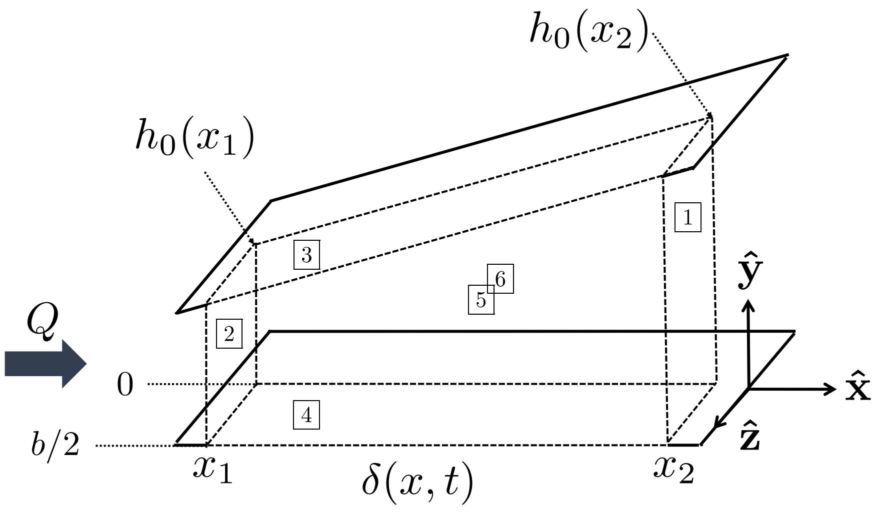

(a) Three-dimensional channel control volume.

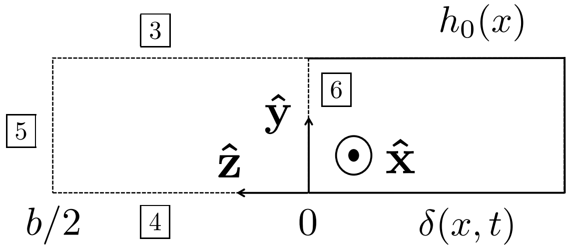

(b) Front view of three dimensional channel control volume.

Figure 2.6: Three-dimensional control volume illustration for the spanwise quasi-1D leakage flow model.

Starting with mass conservation in equation 2.2 and the three-dimensional velocity vector, we have

$$\frac{\partial}{\partial t}\left(\int_0^{b/2}\int_\delta^{h_0} dydz\right) + \frac{\partial}{\partial x}\left(\int_0^{b/2}\int_\delta^{h_0} udydz\right) + \int_\delta^{h_0} wdy\bigg|_{z=b/2} = 0, \quad (2.123)$$

where the same limits and assumptions were applied to obtain equation 2.123 and in equation 2.3. Next we consider the integral momentum conservation in 2.4. Following the same steps as in equation 2.5, we have

$$
\begin{aligned}
&\frac{\partial}{\partial t}\left(\int_0^{b/2}\int_\delta^{h_0}\begin{bmatrix}u\\ v\\ w\end{bmatrix}dydz\right)+\frac{\partial}{\partial x}\left(\int_0^{b/2}\int_\delta^{h_0}\begin{bmatrix}u^2\\ uv\\ uw\end{bmatrix}dydz\right)+\int_\delta^{h_0}\begin{bmatrix}uw\\ vw\\ w^2\end{bmatrix}dy\Bigg|_{z=b/2}=\\
&-\frac{1}{\rho_f}\left\{\frac{\partial}{\partial x}\left(\int_0^{b/2}\int_\delta^{h_0}\begin{bmatrix}P\\ 0\\ 0\end{bmatrix}dydz\right)-\int_0^{b/2}\begin{bmatrix}h_0'\\ -1\\ 0\end{bmatrix}P|_{y=h_0}dz+\int_0^{b/2}\begin{bmatrix}\delta'\\ -1\\ 0\end{bmatrix}P|_{y=\delta}dz+\right.\\
&\left.\int_\delta^{h_0}\begin{bmatrix}0\\ 0\\ P|_{z=b/2}-P|_{z=0}\end{bmatrix}dy-\mathbf{F}_{\text{visc}}\right\}. \qquad (2.124)
\end{aligned}
$$

From the definition of $Q_x$ in equation 2.6, we define now define an equivalent variable in $\hat{\mathbf{z}}$,

$$Q_z(x,z,t)=\int_\delta^{h_0}wdy. \qquad (2.125)$$

Applying equations 2.6 and 2.125 to 2.123, mass conservation simplifies to

$$\frac{\partial Q_x}{\partial x}+\frac{2}{b}\,Q_z|_{z=b/2}=-\frac{\partial\delta}{\partial t}. \qquad (2.126)$$

The two-dimensional axial momentum in equation 2.8 is integrated in $z$ and augmented by a nonlinear cross-term

$$\mathcal{N}_{xz}=\int_\delta^{h_0}uwdy, \qquad (2.127)$$

so that

$$
\begin{aligned}
&\frac{\partial}{\partial t}\left(\int_0^{b/2}Q_xdz\right)+\int_0^{b/2}\frac{\partial\mathcal{N}_x}{\partial x}dz+\mathcal{N}_{xz}|_{z=b/2}=\\
&\quad-\frac{1}{\rho_f}\left\{\int_0^{b/2}\left[\frac{\partial}{\partial x}\left(\int_\delta^{h_0}Pdy\right)-h_0'P|_{y=h_0}+\frac{\partial\delta}{\partial x}P|_{y=\delta}\right]dz-F_{\text{visc},x}\right\}, \qquad (2.128)
\end{aligned}
$$

The system has an additional spanwise momentum equation,

$$\frac{\partial}{\partial t}\left(\int_0^{b/2} Q_z dz\right) + \frac{\partial}{\partial x}\left(\int_0^{b/2} \mathcal{N}_{xz} dz\right) + \mathcal{N}_z|_{z=b/2} = \int_\delta^{h_0} \left(P|_{z=b/2} - P|_{z=0}\right) dy - F_{\text{visc,z}} \quad (2.129)$$

with the nonlinear advection term in $z$,

$$\mathcal{N}_z = \int_\delta^{h_0} w^2 dy. \quad (2.130)$$

The goal of this analysis it to obtain an expression for the pressure as a function of $\delta$ and $Q_z$. Once again, we must find a closure for the advection terms $\mathcal{N}_x$, $\mathcal{N}_z$, and $\mathcal{N}_{xz}$, along with $F_{\text{visc,x}}$ and $F_{\text{visc,z}}$. We must also relate the local pressure values in $y$ and $z$ to the integrated pressure over $y$ and $z$.

### 2.4.1 Closure Relations for $\mathcal{N}$, $F_{\text{visc}}$, and Evaluated Quantities

Similar to section 2.2.1, we consider the infinitessimal Navier-Stokes equations in three dimensions with the lubrication theory non-dimensionalization as before in equations 2.16 and 2.18

$$\begin{aligned}
\varepsilon_h^2 Re_L \frac{Du^*}{Dt^*} &= -\frac{1}{\Lambda}\frac{\partial P^*}{\partial x^*} + \varepsilon_h^2 \frac{\partial^2 u^*}{\partial x^{*2}} + \frac{\partial^2 u^*}{\partial y^{*2}} + \varepsilon_h^2 \varepsilon_b^{-2} \frac{\partial^2 u^*}{\partial z^{*2}} \\
\varepsilon_h^4 Re_L \frac{Dv^*}{Dt^*} &= -\frac{1}{\Lambda}\frac{\partial P^*}{\partial y^*} + \varepsilon_h^4 \frac{\partial^2 v^*}{\partial x^{*2}} + \varepsilon_h^2 \frac{\partial^2 v^*}{\partial y^{*2}} + \varepsilon_b^{-2} \varepsilon_h^4 \frac{\partial^2 v^*}{\partial z^{*2}}, \\
\varepsilon_b^2 \varepsilon_h^2 Re_L \frac{Dw^*}{Dt^*} &= -\frac{1}{\Lambda}\frac{\partial P^*}{\partial z^*} + \varepsilon_h^2 \varepsilon_b^2 \frac{\partial^2 w^*}{\partial x^{*2}} + \varepsilon_b^2 \frac{\partial^2 w^*}{\partial y^{*2}} + \varepsilon_h^2 \frac{\partial^2 w^*}{\partial z^{*2}}
\end{aligned} \quad (2.131)$$

with the additional nondimensional spanwise parameters $\varepsilon_b = \frac{b}{L}$ and $w^* = \frac{w}{U}\varepsilon_b$. In taking the limit $\varepsilon_h \longrightarrow 0$, we simplify equation 2.131 to

$$\begin{aligned}
0 &= -\frac{1}{\Lambda}\frac{\partial P^*}{\partial x^*} + \frac{\partial^2 u^*}{\partial y^{*2}} \\
0 &= -\frac{1}{\Lambda}\frac{\partial P^*}{\partial y^*} \\
0 &= -\frac{1}{\Lambda}\frac{\partial P^*}{\partial z^*} + \varepsilon_b^2 \frac{\partial^2 w^*}{\partial y^{*2}}
\end{aligned} \quad . \quad (2.132)$$

We would like to use equation 2.132 to inform a choice of $u$ and $w$ that are consistent with the problem at hand. In particular, we would like a simple choice that captures the essence of the profiles given the symmetry of the problem in $\hat{\mathbf{z}}$. Arguments in this section are heuristic, with the goal of providing a simple starting point for assessing the effect of spanwise leakage.

The first assumption is that the flow remains largely one-dimensional in $x$ for $u$ and $v$, so that we recover the parabolic profile of $u^* = u^*(x^*, y^*, t^*)$ in equation 2.20 from section 2.2.1, with $v \approx 0$. Next, we assume that no net pressure is externally applied in $z$, and that any $\frac{\partial P^*}{\partial z^*}$ is due to the motion of the channel walls. In that, $w^*$ must be odd in $z = \left[-\frac{b}{2}, \frac{b}{2}\right]$ and $w^*|_{z=0} = 0$ and $P^*$ symmetric in $z = \left[-\frac{b}{2}, \frac{b}{2}\right]$ due to the symmetry of the geometry shown in figure 2.6. If $\frac{\partial P^*}{\partial z^*} \neq 0$ and $P^* = P^*(x, z, t)$, the spanwise component in equation 2.132 can be integrated twice to also recover a parabolic profile of $w^*$ in $y^*$, with the no-slip conditions, as done for $u^*$. Combined with a linear function in $z$, the simplest that satisfies the specified symmetries, we assume a functional form for the spanwise velocity profile as

$$w^*(x^*, y^*, z^*, t) \sim z^* \left(\frac{\delta(x^*, t^*)}{\bar{h}} - y^*\right)\left(\frac{h_0(x^*)}{\bar{h}} - y^*\right). \tag{2.133}$$

Substituting the form in 2.133 into the spanwise component of 2.132, we acertain that

$$P^* \propto z^{*2}. \tag{2.134}$$

With the profile relation specified in the form 2.133, we can define the advection terms as in equation 2.23,

$$\mathcal{N}_z = \int_\delta^{h_0} w^2 dy = \xi_z \frac{Q_z^2}{h_0 - \delta}, \tag{2.135}$$

and

$$\mathcal{N}_{xz} = \int_\delta^{h_0} uw dy = \xi_{xz} \frac{Q_x Q_z}{h_0 - \delta} \tag{2.136}$$

where $\xi_z$ and $\xi_{xz}$ are the constant profile shape factors for spanwise velocity and the cross-coupling between spanwise and axial velocities, respectively. The $F_{\text{visc,x}}$ takes the form in equation 2.26, with $F_{\text{visc,z}}$ similarly defined as

$$F_{\text{visc,z}} \approx -12\mu_f \frac{Q_z}{(h_0 - \delta)^2}. \tag{2.137}$$

The remaining terms are the definition of relations between evaluated and integrated quantities of $P$ and $Q_z$ in $y$ and $z$. We define the integrated quantities in $z$ as our new set of model variables, normalizing them such that they represent the spatial average of $P$ and $Q_z$ over $z = \left[0, \frac{b}{2}\right]$,

$$\bar{P} = \frac{2}{b} \int_0^{b/2} P dz, \tag{2.138}$$

and

$$\bar{Q}_z = \frac{2}{b} \int_0^{b/2} Q_z dz. \tag{2.139}$$

Using the relation in the form 2.133 for the $w^*$, we have the evaluated flow rate at $z = b/2$

$$Q_z|_{z=b/2} = 2\bar{Q}_z. \tag{2.140}$$

Similarly for the center-line channel pressure using the form 2.134

$$P|_{z=0} = \frac{3}{2}\bar{P}. \tag{2.141}$$

Applying equations 2.23, 2.135, 2.136 - 2.141 into mass conservation in 2.126,

$$\frac{\partial Q_x}{\partial x} + \frac{4}{b}\bar{Q}_z = -\frac{\partial \delta}{\partial t} \tag{2.142}$$

Similarly, substituting the equations into axial momentum equation 2.128, we have

$$\frac{\partial Q_x}{\partial t} + \frac{\partial}{\partial x}\left(\xi_x \frac{Q_x^2}{h_0 - \delta}\right) + 4\xi_{xz}\frac{Q_x \bar{Q}_z}{b\,(h_0 - \delta)} \;=\; -\frac{1}{\rho_f}\frac{\partial \bar{P}}{\partial x}\,(h_0 - \delta) + F_{\text{visc,x}}. \tag{2.143}$$

The viscous term in equation 2.143 is defined as in equations 2.28 and 2.29. Lastly, substitution into spanwise momentum equation 2.129 yields,

$$\begin{aligned}\frac{\partial \bar{Q}_z}{\partial t} + \frac{\partial}{\partial x}\left(\xi_{xz}\frac{Q_x \bar{Q}_z}{h_0 - \delta}\right) + 8\xi_z \frac{\bar{Q}_z^2}{b\,(h_0 - \delta)} &= \\ -\frac{2\,(h_0 - \delta)}{b\rho_f}\left(P|_{z=b/2} - \frac{3}{2}\bar{P}\right) - \frac{12\mu_f}{\rho_f}&\frac{\bar{Q}_z}{(h_0 - \delta)^2},\end{aligned} \tag{2.144}$$

The last undefined quantity is the boundary value $P|_{z=b/2}$. The shape factor $\zeta_z = \frac{6}{5}$ and $\zeta_{xz} = \zeta_x$, depending on system $Re_h$

### 2.4.2 Pressure Boundary Condition in $z$

The boundary value for $P|_{z=b/2}$ is an additional boundary condition that needs to be defined according to the problem in figure 2.6. Boundary conditions from section 2.2.3 hold with the averaged spanwise pressure $\bar{P}$ at the end points $x = 0$ and $x = L$. We maintain the same form to define the pressure at the edge surface $z = b/2$, such that

$$P(x,t)|_{z=b/2} = p_0(x) + \frac{\zeta_{\text{out,z}}}{2}\rho_f \left(\frac{2\bar{Q}_z(x,t)}{h_0 - \delta}\right)^2 . \tag{2.145}$$

Equation 2.145 states that when $\bar{Q}_z = 0$, the pressure at the boundary is the steady pressure of the two-dimensional channel $p_0$. This is consistent with assumptions in section 2.4.1 used to obtain the velocity profiles. The pressure loss coefficient is $\zeta_{\text{out,z}}$. The effect of this boundary condition framework is equivalent to accounting for any pressure losses in the movement of the flow through the side $z$ segments of the geometry that connect the top and bottom channels, for example. The pressure loss coefficients may be a function of the gap size in $z$, between the end of the span of the cantilever at $\frac{b}{2}$ and a rigid channel wall. With the assumption that the flow remains largely in the axial direction, the system effectively reduces to one where the $z$ boundaries are thought to be unconfined. This means that flow in $x$ on surface 5 in figure 2.6 is the same as that of surface 6.

### 2.4.3 Linearization

Since we are interested in the stability of the system, we linearize equations 2.142, 2.143 and 2.144 as we did the two-dimensional system in section 2.2.4, with the redefinition of $P$ as $\bar{P}$. We substitute variable expansions in equations 2.47, 2.48, 2.49, and the addition of the average spanwise flow rate,

$$\bar{Q}_z = q_{z0}(x) + \varepsilon q_{z1}(x,t), \tag{2.146}$$

into equations 2.142, 2.143 and 2.144. The last assumption we will make is that the spanwise steady flow rate $q_{z0}(x) = 0$. As stated through the closures in section 2.4.1 in order to obtain the $w^*$ profile, we associate the leakage flow $\bar{Q}_z$ with the movement of the channel walls. The symmetries that ensue are the basis for the linear $z$ profile applied. In specifying the boundary condition in equation 2.145, we ensure that indeed when $q_{z0}(x) = 0$ the boundary pressure does not pose a pressure gradient in equation 2.144, such that $\bar{P} = P|_{z=b/2} = p_0$. Moreover, by specifying the equilibrium $q_{z0}(x) = 0$ directly, the $\varepsilon^0$ order system of equations becomes the original two-dimensional system, such that $p_0$ in equation 2.58, and $q_{x0}$ in equation 2.59 are the $\varepsilon^0$ order solution for the spanwise system of equations as well.

The $\varepsilon^1$ equations are: the integrated conservation of mass (as in equation 2.50),

$$q_{x1} = \int_0^x \dot{\delta}_1 dx_1 - \frac{4}{b}\int_0^x q_{z1} dx_1 + \bar{Q}_{x1}(t), \tag{2.147}$$

axial momentum,

$$\begin{aligned} \dot{q}_{x1} + 2\xi_x \bar{Q}_0 \frac{\partial}{\partial x}\left(\frac{q_{x1}}{h_0}\right) + \frac{\bar{Q}_0}{2h_0^2}\left(\lambda_0 + \frac{\eta}{2}\bar{Q}_0\right) q_{x1} = \\ \xi_x \frac{\bar{Q}_0^2}{h_0^2}\frac{\partial \delta_1}{\partial x} - \frac{3}{\rho_f}\frac{\partial p_0}{\partial x}\delta_1 - 4\xi_{xz}\frac{\bar{Q}_0}{b h_0} q_{z1} - \frac{h_0}{\rho_f}\frac{\partial \bar{p}_1}{\partial x} \end{aligned} \tag{2.148}$$

and spanwise momentum,

$$\dot{q}_{z1} + \xi_{xz}\bar{Q}_0 \frac{\partial}{\partial x}\left(\frac{q_{z1}}{h_0}\right) + \frac{12\mu}{\rho_f h_0^2} q_{z1} = \frac{h_0}{3\rho_f}\bar{p}_1. \tag{2.149}$$

Manipulation is required to obtain an expression for $\bar{p}_1$ as a function of $\delta_1$, $q_{z1}$, and their derivatives. It is not useful to show the full form of the expression because of its length and complexity. However, the following steps are carried out in MATLAB symbolic toolbox that can be followed: first we differentiate in $x$ equation 2.148, then substitute equation 2.147 into the result of the previous step. Next, we solve equation 2.149 for $\dot{q}_{z1}$ and substitute the resulting expression into the previous result for the combined set of equations. We can then separate the pressure dependent terms as,

$$\bar{p}_1'' + \left(\frac{h_0'}{h_0}\right)\bar{p}_1' - \frac{12}{b^2}\bar{p}_1 = r(x,t), \tag{2.150}$$

where we have an inhomogeneous ODE for $\bar{p}_1$ with the right-hand-side $r(x,t)$ as a forcing term containing $\delta_1$ and its derivative, along with $q_{z1}$ and its derivatives.

Equation 2.150 cannot be solved analytically for arbitrary forms of $h_0$. Two solvable forms of $h_0$, however, are for constant and linear channels. For each of those cases, 2.150 is solved with variation of parameters, such that

$$\bar{p}_1 = \bar{p}_{1,h} + \bar{p}_{1,p}, \tag{2.151}$$

where the fundamental solutions are found by solving the homogeneous problem ($r(x,t) = 0$), then used through the convolution in the variation of parameters integral to obtain the particular solution $\bar{p}_{1,p}$. Finally, the full unique solution is calculated by solving for the coefficients of the homogeneous form through the pressure boundary conditions $x = 0$ and $x = L$ from equations 2.62 and 2.63, which, as noted, are the same between the two- and three- dimensional models. The fundamental solutions for the constant channel case are two real exponential functions, while those for the linear system are a set of modified Bessel functions. These steps are carried out symbolically to ensure mistakes are minimized, and an implementable form of $\bar{p}_1$ is readily obtained.

Once $\bar{p}_1$ is defined, two other relations are needed to complete the hydrodynamic system of equations. Just like in section 2.2.4, we must solve for the ODE that describes the boundary forcing flow rate $\bar{Q}_{x1}$ in equation 2.147. This is done by substituting $\bar{p}_1$ into equation 2.150 and solving for $\dot{\bar{Q}}_{x1}$ in terms of $\delta_1$, $q_{z1}$, and their derivatives. The last equation of the system is the time evolution of $q_{z1}$, which is obtained by substituting $\bar{p}_1$ into equation 2.148 and solving for $\dot{q}_{z1}$ in terms of $\delta_1$, $q_{z1}$, and their derivatives once again.

### 2.4.4 Fluid Structure Coupling and $q_{z1}$ Discretization

Similar to steps in 2.3.5, the coupled fluid-structure system is closed with the structural equations through the net force applied on the beam as the pressure difference of the bottom and top channels. We constrain the model to a symmetric set of linear channel shapes, and apply $\bar{p}_1$ from equation 2.151 to the fully coupled system in equation 2.91. Eigenfunctions from equations 2.81 or 2.84 are used to expand $\delta_1$ depending on the beam boundary conditions; however, the beam eigenfunctions do not enforce the boundary values for $q_{z1}$ at $x = 0$ and $x = L$. Specifically, $q_{z1}|_{x=0}$ is determined by the ODE in time attained when equation 2.149 is evaluated at $x = 0$ and the pressure boundary condition at $x = 0$ in equation 2.62 applied,

$$\dot{q}_{z1}|_{x=0} = \frac{h_0}{3\rho_f}\bar{p}_1\bigg|_{x=0} - \xi_{xz}\,\bar{Q}_0\frac{\partial}{\partial x}\left(\frac{q_{z1}}{h_0}\right)\bigg|_{x=0} - \frac{12\mu}{\rho_f h_0^2}q_{z1}\bigg|_{x=0}. \tag{2.152}$$

Terms that depend on the $x$ derivative are obtained prior to being evaluated as discussed in section 2.4.3. The same is done for the boundary value $q_{z1}|_{x=L}$, with the pressure boundary condition at $x = L$ applied from equation 2.63,

$$\dot{q}_{z1}|_{x=L} = \frac{h_0}{3\rho_f}\bar{p}_1\bigg|_{x=L} - \xi_{xz}\,\bar{Q}_0\frac{\partial}{\partial x}\left(\frac{q_{z1}}{h_0}\right)\bigg|_{x=L} - \frac{12\mu}{\rho_f h_0^2}q_{z1}\bigg|_{x=L}. \tag{2.153}$$

The spanwise flow rate is expanded as

$$q_{z0}(x,t) = \tilde{q}_{z0}(t)\left(1 - \frac{x}{L}\right) + \sum_{i=1}^{n}\tilde{q}_{zi}(t)\psi_i(x) + \tilde{q}_{zL}(t)\left(\frac{x}{L}\right), \tag{2.154}$$

where $i \in \mathbb{Z} : [1, n]$. We use the principle of linear superposition to obtain the solution of the inhomogeneous boundary problem as the sum of solutions that satisfy the inhomogeneous boundary conditions, but homogenous equation, and those that satisfy the homogeneous boundary condition, but inhomogeneous problem. A sine series expansion, truncated at $n$ terms, is used since homogeneous Dirichlet boundaries are necessary,

$$\psi_i(x) = \sin\left(\frac{i\pi x}{L}\right). \tag{2.155}$$

Applying the expansion of $\delta_1$ in $g_i(x)$ and $q_{z1}$ in $\psi_i(x)$, $\left(1 - \frac{x}{L}\right)$, and $\left(\frac{x}{L}\right)$, we simplify the coupled equations of motion (for a symmetric channel) obtained through steps discussed in section 2.4.3 and closed with the structural equations. First, the fluid coupled equations are

$$\begin{aligned}\sum_{i=0}^{n}\Big(M_{\mathrm{s}i}(x)\ddot{a}_i(t) + C_{\mathrm{s}i}(x)\dot{a}_i(t) + K_{\mathrm{s}i}(x)a_i(t)\Big) &= -2T_{\mathrm{z}}(x)\bar{Q}_{x1}(t) - \\ 2\sum_{i=0}^{n}\Big(M_{\mathrm{z}i}(x)\ddot{a}_i(t) + C_{\mathrm{z}i}(x)\dot{a}_i(t) + K_{\mathrm{z}i}(x)a_i(t)\Big) &- 2\sum_{j=0}^{m}H_{zj}(x)\tilde{q}_{zi}(t),\end{aligned} \tag{2.156}$$

with $M_{\mathrm{s}i}$, $C_{\mathrm{s}i}$, $K_{\mathrm{s}i}$ defined in equations 2.100, 2.101, and 2.102 respectively. Coefficients $T_{\mathrm{z}}$, $M_{\mathrm{z}i}$, $C_{\mathrm{z}i}$, $K_{\mathrm{z}i}$, and $H_{zi}$ are defined through solving the hydrodynamic system described in section 2.4.3. Similarly, the dynamics of $\bar{Q}_{x1}$ are given by

$$\dot{\bar{Q}}_{x1}(t) = G_{\mathrm{Q}}\bar{Q}_{x1}(t) + \sum_{i=0}^{n}\Big(B_{\mathrm{Q}i}\ddot{a}_i(t) + D_{\mathrm{Q}i}\dot{a}_i(t) + E_{\mathrm{Q}i}a_i(t)\Big) + \sum_{j=0}^{m} H_{\mathrm{Q}j}\tilde{q}_{zi}(t), \quad (2.157)$$

and the spanwise leakage dynamics as

$$\dot{\tilde{q}}_{z1}(t) = G_{\mathrm{q_z}}\bar{Q}_{x1}(t) + \sum_{i=0}^{n}\Big(B_{\mathrm{q_z}i}\ddot{a}_i(t) + D_{\mathrm{q_z}i}\dot{a}_i(t) + E_{\mathrm{q_z}i}a_i(t)\Big) + \sum_{j=0}^{m} H_{\mathrm{q_z}j}\tilde{q}_{zi}(t). \quad (2.158)$$

Coefficients for $a_i$, $\dot{a}_i$, and $\tilde{q}_{zi}$ are also determined through the hydrodynamics forces and discussed in section 2.4.3. They include the boundary values in equations 2.152 and 2.153 at $i = 0$ and $i = m$, respectively. We obtain the semi-continuous system in time through a Garlerkin projection of equation 2.156 onto test functions $g_k(x)$, and of equation 2.158 onto test functions $\psi_k(x)$ as in section 2.3.5. Finally, writing the fully coupled operator as

$$\begin{bmatrix} \dot{a}_0 \\ \vdots \\ \dot{a}_n \\ \ddot{a}_0 \\ \vdots \\ \ddot{a}_n \\ \dot{\bar{Q}}_{x1} \\ \dot{\tilde{q}}_{z0} \\ \vdots \\ \dot{\tilde{q}}_{zn+1} \end{bmatrix} = \begin{bmatrix} 0 & \mathbf{1} & 0 & 0 \\ M_z^{-1}K_z & M_z^{-1}C_z & M_z^{-1}T_z & M_z^{-1}H_z \\ E_Q & D_Q & G_Q & H_Q \\ E_{q_z} & D_{q_z} & G_{q_z} & H_{q_z} \end{bmatrix} \begin{bmatrix} a_0 \\ \vdots \\ a_n \\ \dot{a}_0 \\ \vdots \\ \dot{a}_n \\ \bar{Q}_{x1} \\ \tilde{q}_{z0} \\ \vdots \\ \tilde{q}_{zn+1} \end{bmatrix}. \quad (2.159)$$

We restrict $m = n + 1$, where $i = m$ is the boundary value for $q_{z1}$ at $x = L$. The system of equations in 2.159 emulates the form of the two-dimensional model in 2.96, however it has been simplified for a symmetric channel and includes the spanwise leakage flow rates as states of the system.

## 2.5 Linear Stability Analysis

The premise of linear stability analysis is to understand the dynamics of a linear operator through its eigendecomposition. In particular, we are interested in solving the problem,

$$\mathbf{A}\mathbf{v}_i = \lambda \mathbf{v}_i, \tag{2.160}$$

where $\mathbf{A}$ is either the operator in equation 2.96 or 2.159, and $[\lambda_i, \mathbf{v}_i]$ is an eigenvalue-eigenvector pair of $\mathbf{A}$. An unstable system requires $\mathrm{Re}[\lambda] > 0$, such that a degree of freedom within the system will exponentially grow unbounded. The flutter instability is characterized as $\mathrm{Re}[\lambda] > 0$ with $\mathrm{Im}[\lambda] \neq 0$. By tracking the evolution of $\lambda$ as a function of parameters in the system, in particular those in tables 2.3 and 2.4, we can track when, if ever, the system reaches the marginally stable (also called neutrally stable) point $\mathrm{Re}[\lambda] = 0$ with $\mathrm{Im}[\lambda] \neq 0$ [64]. This is defined as the flutter boundary and assessed in detail in chapters 3, 4, and 5 for the flow-energy harvester fluid-structure system. The varied parameter is called the bifurcation parameter if indeed a bifurcation is encountered. By definition, the flutter instability is reached through a Hopf bifurcation, defined as when a system equilibrium point looses stability with $\mathrm{Im}[\lambda] \neq 0$. Another bifurcation of interest is the steady type, where $\mathrm{Re}[\lambda] > 0$ with $\mathrm{Im}[\lambda] = 0$. The ensuing instability is called divergence in the fluid-structure literature [24]. The eigenvector $\mathbf{v}_i$ gives the mode shapes in terms of displacement, velocity, and the driving flow rate $\bar{Q}_{x1}$. For operator in equation 2.159, this list also includes the spanwise flow rates $q_{z1}$. When plotting mode shapes, we restrict the state-space to those of the transverse amplitude coefficients, $a_i$.

The equations from this chapter are used to solve the eigenvalue problem in equation 2.160, where the flutter boundary is sought as different parameters are varied. Flutter indicates the onset of a parameter combination that is likely to give rise to high power extraction regimes. This is discussed as experimental results are explored in chapter 5.

*Chapter 3*

# NUMERICAL METHODS FOR SIMULATIONS AND DATA ANALYSIS

## 3.1 Introduction

In this chapter we describe the numerical implementation and validation of the quasi-1D model and the fluid-structure direct numerical simulation algorithm. We will also describe the signal processing methods used to obtain relevant quantities from the computed and measured data sets.

## 3.2 Quasi-1D Model Numerical Implementation

We discretize the continuous operators in equations 2.90, 2.96, and 2.159 using the eigenfunctions described in either equation 2.81 or 2.84, for clamped-free or elastic translating boundary condition, respectively; and equation 2.154 for the spanwise flow rate expansion. All cases analyzed in this thesis are symmetric about the center-line, as shown in figure 2.1, such that $\delta_0 = 0$, $\dot{\delta}_0 = 0$, and for the cases that include the translating boundary condition, $\bar{a}_0 = 0$ and $\dot{\bar{a}}_0 = 0$, are the equilibria the system is linearized about. The linear equations are developed using the MATLAB symbolic toolbox, the spatial derivative operators are calculated analytically with respect to each basis expansion, $g_i(x)$, or equilibrium channel shape, $h_e(x)$, and the integral operators in coefficients A.1 - A.8 are calculated with MATLAB's adaptive step quadrature `integral` function, with an absolute tolerance of $10^{-10}$ and relative tolerance of $10^{-6}$. The Galerkin projection operator step in equations 2.97 and 2.99 is calculated using Simpson's quadrature rule [65]. The number of basis functions kept in the expansion is 6 for all cases, was found, through trial and error, to converge the first two beam eigenvalues (lowest frequency modes) to within a tolerance of $10^{-2}$ in convective time units.

### 3.2.1 Leakage Flow in Constant Channel Verification

We verify the algorithm's implementation by comparing our results to those of Nagakura and Kaneko [33], who carried out a similar analysis for a cantilever in a constant, symmetric channel. They employed nonlinear operators 2.7 and 2.32 with $h_e = \bar{h} =$ constant, and $\xi_x = 1$ for all Reynolds numbers, with the same definition for $f$ as in equation 2.29. The work of Wu and Kaneko [45] also provides another reference, where the authors compared numerical simulations to the original linear stability work [33], and use the same data set for their comparison. The Euler-Bernoulli beam equation is employed with viscous damping,

$$\rho_s h_b \frac{\partial^2}{\partial t^2}\delta(x,t) + \xi_i \omega_i \rho_s h_b \frac{\partial}{\partial t}\delta(x,t) + EI\frac{\partial^4}{\partial x^4}\delta(x,t) = p_1^{\text{bot}}(x,t) - p_1^{\text{top}}(x,t), \quad (3.1)$$

where $\xi_i$ is the modal damping coefficient and $\omega_i$ are the angular frequencies of each mode of the undamped beam (solution to the homogeneous PDE 2.85). This is different from the model proposed in section 2.3.2, and is only used in this section to compare with existing results. Nagakura and Kaneko [33] parameters are shown in table 3.1. Although they report that the cantilever was made from bronze, they provide no reference for their chosen value of modal damping coefficient $\xi_i = 0.01$, for all $i$. There also is no discussion around other forms of material damping that may dominate the behavior of the system (especially at low flow rates), as discussed by Banks and Inman [59].

Table 3.1: Nagakura and Kaneko [33] constant channel dimensional parameters.

| **Parameter** | **Value** | **Units** |
|---|---|---|
| $\rho_f$ | 1.20 | kg/m$^3$ |
| $\mu_f$ | 1.80e-05 | Pa*s |
| $\rho_s$ | 8.78e+03 | kg/m$^3$ |
| $E$ | 1.10e+11 | Pa |
| $\xi_i$ | 1.0e-02 | ND |
| $h_b$ | 2.0e-04 | m |
| $b$ | 1.0e-01 | m |
| $L$ | 2.0e-01 | m |
| $\bar{h}$ | 2.5e-03 | m |
| $q_{x0}$ | 0 - 5e-2 | m$^2$/s |
| $\zeta_{in}$ | 1 | ND |
| $\zeta_{out}$ | 0 | ND |

The flow rate per unit span is varied from 0 to 5.0e-2 [m$^2$/s] in the simulations. We compare two data sets extracted and replotted from [33] and [45]: the spectrum evolution of the system as $q_{x0}$ is increased for the parameters in table 3.1, and the neutral stability line, or flutter boundary, characterized by critical dimensional velocity $\bar{U}_{\text{cr}} = \frac{q_{x0\text{cr}}}{\bar{h}}$ as a function of dimensional throat size $\bar{h}$. Figure 3.1 shows

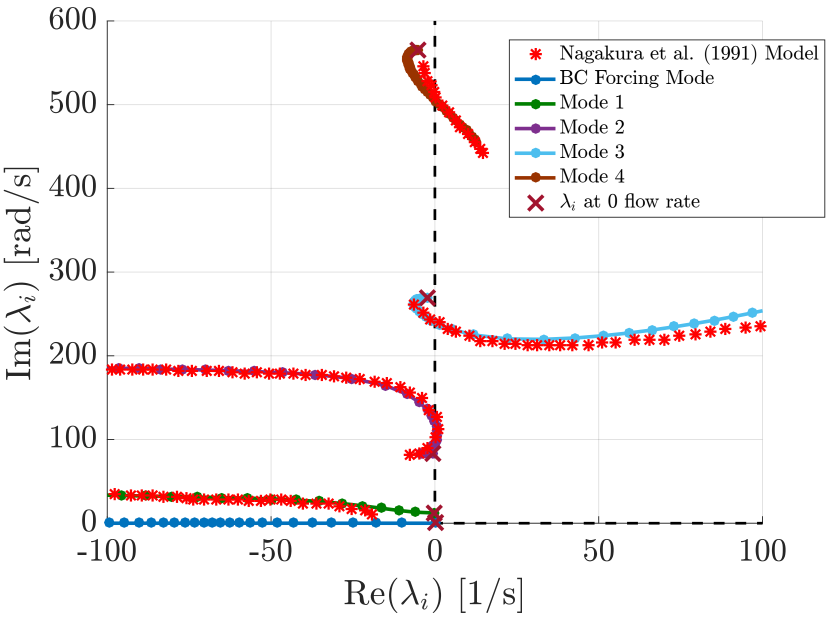

Figure 3.1: Comparison of eigenvalues $\lambda_i$ as a function of flow rate per unit span $q_{x0}$ to simulation results in [33]. The plot shows the path as $q_{x0}$ is increased.

good agreement between the eigenvalues of the four beam modes for the range of flow rates. The current work is plotted from $q_{x0} = 0$, while [33] from a small finite value not disclosed in the article.

In our results, the flutter boundary is computed as the interpolated $\bar{U}_{\text{cr}}$ where the first eigenvalue $\lambda$ becomes marginally stable ($\text{Re}\,[\lambda] = 0$). The corresponding critical angular frequency $\omega_{\text{cr}} = \text{Im}\,[\lambda]\,|_{\bar{U}_{\text{cr}}}$. A detailed description of the method is in section 4.2.4. This is in contrast with the energy formulation in [33] used to characterize the marginally stable point, where $\bar{U}_{\text{cr}}$ corresponds to its value when no energy is added or removed from to the beam. Figures 3.2 and 3.3 show good agreement between the critical quantities of the model and our implementation. The flutter boundary in $\bar{U}_{\text{cr}}$ is not an injective function of $\bar{h}$ because the boundary represents a crossing from stable to unstable dynamics, but also from unstable to stable for a subset of parameters. That is seen specifically $\bar{h} \approx 0.0025$ m values in figures 3.2 and 3.3.

The agreement shown in figures 3.1, 3.2, and 3.3 gives us confidence that the coupled equations have been implemented correctly, and that the numerical algorithm produces results similar to others in the literature. Our model predicts the experiments as well as previous models [33, 45] do, most notably capturing the mode

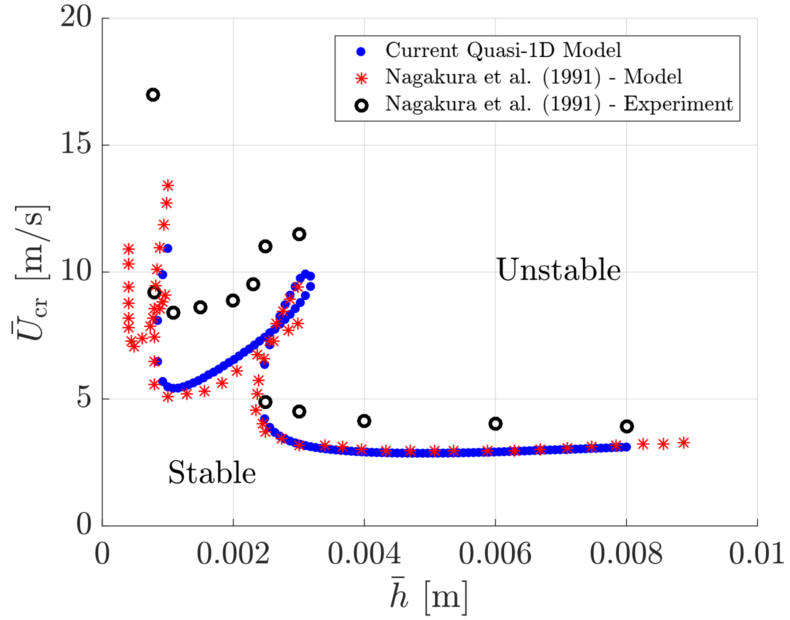

Figure 3.2: Comparison of critical velocity $\bar{U}_{\mathrm{cr}}$ as a function of throat size $\bar{h}$ to experimental and simulation results in [33] and [45].

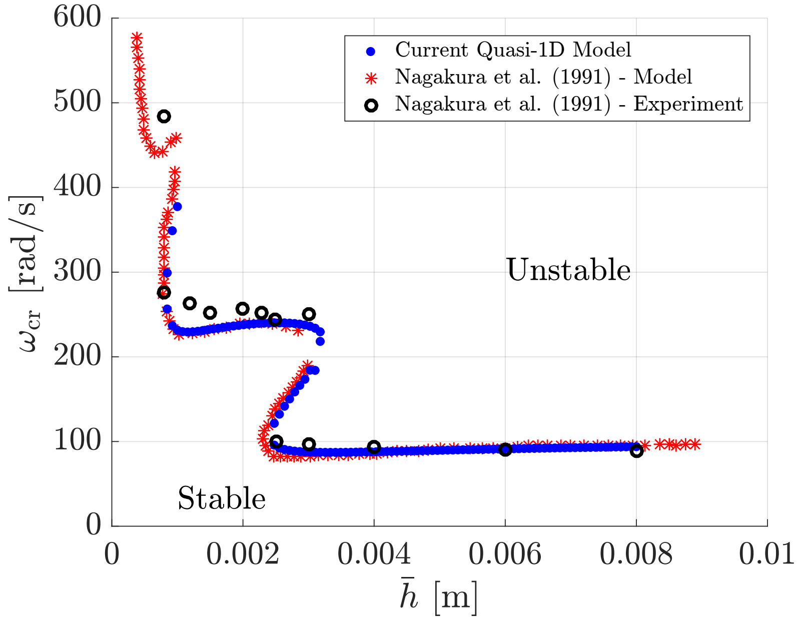

Figure 3.3: Comparison of critical velocity $\bar{U}_{\mathrm{cr}}$ as a function of throat size $\bar{h}$ to experimental and simulation results in [33] and [45].

switching seen in the transition from lower to higher $\omega_{\mathrm{cr}}$ in figure 3.3: as $\bar{h}$ decreases, progressively higher frequency modes bifurcate through a Hopf type into instability. A detailed study on these dynamics follows in section 4.2.

## 3.3 Fluid-Structure Immersed-Boundary Direct Numerical Simulation

In order to validate aspects of the quasi-1D model developed in chapter 2, we employ a two-dimensional fluid-structure algorithm developed by Goza and Colonius [52] that uses the immersed boundary (IB) projection method along with Newton-Raphson approach to solve the strongly-coupled fluid-structure system. Strong-coupling ensures that the nonlinear constraint between the fluid and the structure is enforced at each time step, and is necessary for accurate computation of large structural deformations.

Details of the flow solver can be found in [66, 67], the IB force solution in [68, 69], and the strongly-coupled algorithm in [52, 70, 71]. The current implementation uses a corotational formulation of the structural equations for the beam, where strains are assumed small within constituent material equations in the beam-local frame [72]. The beam-fluid non-dimensional parameters that govern the dynamics are defined as

$$Re_L = \frac{\rho_f U_c L}{\mu_f}, \ \hat{m} = \frac{\rho_s h_b}{\rho_f L}, \ \hat{k} = \frac{EI}{\rho_f U^2 L^3}, \tag{3.2}$$

and similar to those in table 2.3. The characteristic velocity $U_c$ is one appropriate for the flow, and $EI$ is the (dimensional) bending stiffness of the beam per unit span. $I$ for two dimensions is defined in equation 2.86.

The stationary multi-body implementation did not require changes to the algorithm in [67], and the inlet boundary condition to the channel is implemented by prescribing a finite velocity profile at a set of Lagrangian mesh points distributed across the inlet plane.

The initial discrete delta function used in the IB method is constructed as follows. We specify an initial kernel over 3 support points,

$$\psi_h^{(3)}(r) = \begin{cases} \frac{1}{3h}\left[1 + \sqrt{1 - 3\left(\frac{|r|}{h}\right)^2}\right] & |r| \leq \frac{h}{2} \\ \frac{1}{6h}\left[5 - \frac{3|r|}{h} - \sqrt{1 - 3\left(1 - \frac{|r|}{h}\right)^2}\right] & \frac{h}{2} \geq |r| \leq \frac{3h}{2} \\ 0 & \text{otherwise} \end{cases}, \tag{3.3}$$

where $h$ is the support grid spacing, $r$ is the relative position of the smearing point to the center of the delta function, with $|r|$ as its magnitude. This kernel is then smoothed three times using the recursive formula developed by Yang et al. [73] and studied in detail in [68],

$$\mathcal{S}\left[g(r)\right] = \int_{r-1/2}^{r+1/2} g(\tilde{r})d\tilde{r}, \tag{3.4}$$

such that its support is a total of 6 points. The full expression for $\psi_h^{(3),***}$ can be found in the appendix B, where each $*$ represents the consecutive application of equation 3.4 to the resulting smoother discrete delta function kernel. This kernel was chosen in contrast to others because it presented good computational time and accuracy of local stresses. We find, just as Goza et al. [68], that smoother discrete delta functions yield better local force predictions, which translates into more accurate system responses for a given discretization.

### 3.3.1 Internal Flow Fluid-Structure-Interaction Verification

The algorithm has been verified extensively in [71] for external flows, where regimes of the standard and inverted flags [1] were explored and compared to results from other strongly-coupled fluid-structure solvers. In this section, we verify the algorithm for internal flows using the suggested benchmark of an elastic member in an internal, incompressible, laminar flow [38, 74–76].

The IB projection method as developed by Colonius and Taira [66, 67] uses a multi-domain approach to treat its far-field zero vorticity boundary condition. This means that the geometry solved as internal flow lives as part of a larger, quiescent fluid cell. This verification exercise is in part to ensure that the inlet and equivalent outflow boundary conditions behave as other algorithms do when solving a similar problem.

The geometry consists of a cylindrical bluff body within a slightly asymmetric channel and a flexible cantilever (standard clamped flag) immediately downstream in its wake, as illustrated in figure 3.4. The cantilever is infinitesimally thin, but has a structural thickness according to its bending stiffness and mass ratio. Its equivalent numerical thickness will be discussed in further detail in section 4.2, but is inconsequential for cases in this section. The parabolic profile has an average velocity $\bar{U} = U_c$, which is the characteristic velocity for the Reynolds number $Re_D$ based on the cylinder diameter $D$. We consider the same two cases as in Shoele

---

[1] Standard refers to a flag with clamped or pinned leading edge, where as inverted the pinned or clamped boundary condition is at the trailing edge.

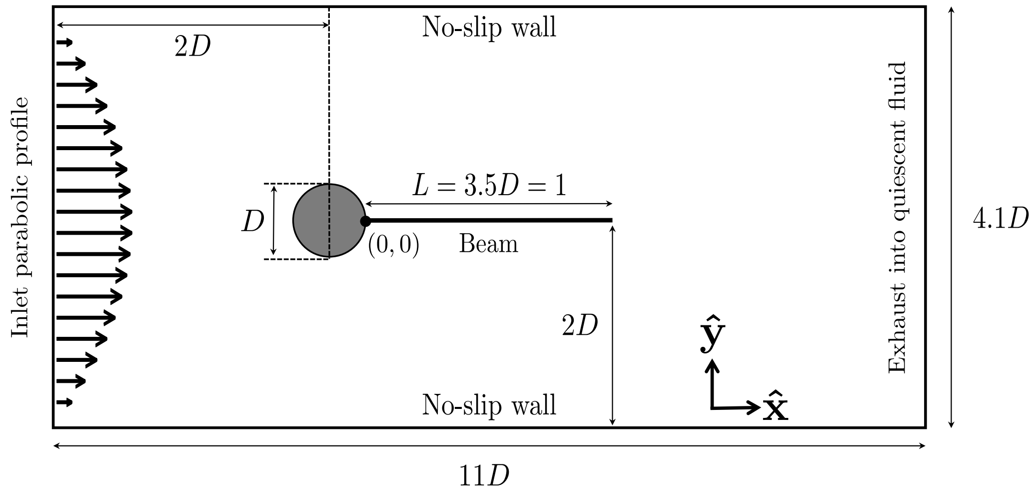

Figure 3.4: Illustration of FSI DNS validation geometry by [74].

and Mittal [76]: $Re_L = 350$ ($Re_D = 100$) and $\frac{\rho_s}{\rho_f} = 10$ as case 1, and $Re_L = 700$ ($Re_D = 200$) and $\frac{\rho_s}{\rho_f} = 1$ as case 2, both with the same $\hat{k}$.

Table 3.2: Non-dimensional and mesh parameters for DNS FSI verification cases in terms of beam length $L$.

| **Parameter** | **Case 1** | **Case 2** |
|---|---|---|
| $Re_L$ | 350 | 700 |
| $\hat{m}$ | 0.5710 | 0.05710 |
| $\hat{k}$ | 0.0218 | 0.0218 |
| $\Delta x^* = \Delta x/L$ | 0.00571 | 0.0028 |
| $\Delta t^* = \Delta t U_c/L$ | 5.714E-4 | 2.86E-4 |
| $Re_{\Delta x} = Re_L \Delta x^*$ | 2 | 2 |
| $CFL = \Delta t^*/\Delta x^*$ | 0.3 | 0.3 |

Table 3.2 denotes the relevant meshing and non-dimensional parameters for each case in terms of the beam length $L$, per equations 3.2. The two-dimensional fluid grid has uniform spacing $\Delta x$ in $\hat{\mathbf{x}}$ and $\hat{\mathbf{y}}$, and defined as $\Delta x^*$ when normalized by $L$. The Lagrangian grids used as immersed boundaries on all bodies have a spacing $\Delta s^* = 2\Delta x^*$, including the cylinder, walls, inlet, and beam. There are a total of 88 Lagrangian points on the beam for cases 1 and 176 for case 2. The target grid Reynolds number $Re_{\Delta x}$ for all cases is 2, and the target $CFL = 0.3$, with $\approx 2600$ time steps per beam tip oscillation cycle for case 1 and $\approx 3500$ time steps per cycle

for case 2. This ensures that the fluid-structure algorithm is stable and resolved. The total simulation time horizon is over 70 $L$ convective time units for cases 1 and and 20 for case 2. The beam tip has reached a steady amplitude and frequency for at least 8 cycles before results were measured in both cases.

### FSI DNS Verification Results

Figures 3.5 and 3.6 show an instantaneous snapshot of the flow velocities when the cantilever is at its peak amplitude for cases 1 and 2, respectively. The wake of the cylinder is clearly visible in both cases, with $\hat{\mathbf{x}}$ velocities fastest at the cylinder top and bottom, and at the channel restriction point by cantilever tip. Stagnation points can be seen at the cylinder surface closest to the inlet, and the tip displacement is visibly higher for case 1 than case 2.

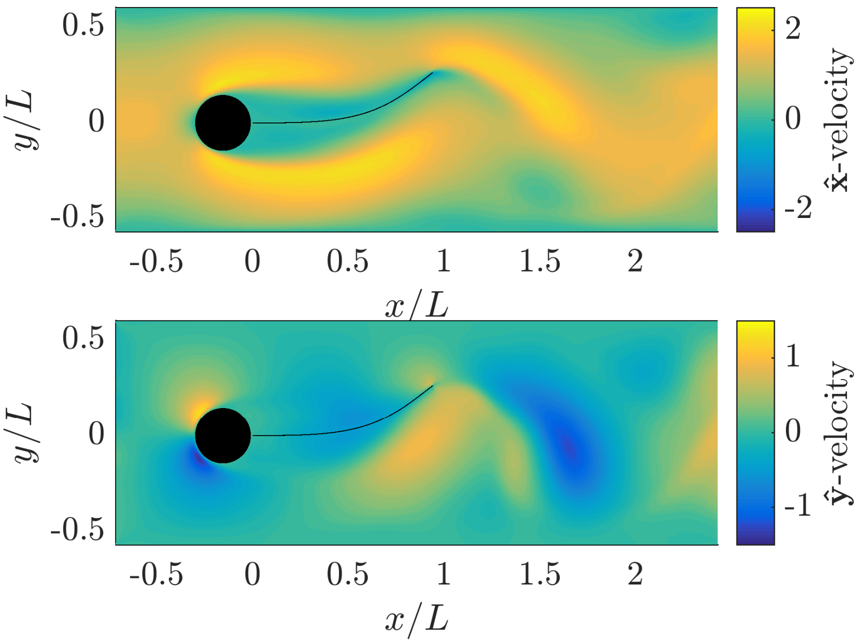

Figure 3.5: Case 1 (table 3.2) velocity contour plot when beam tip (i.e. trailing edge) is at its maximum amplitude.

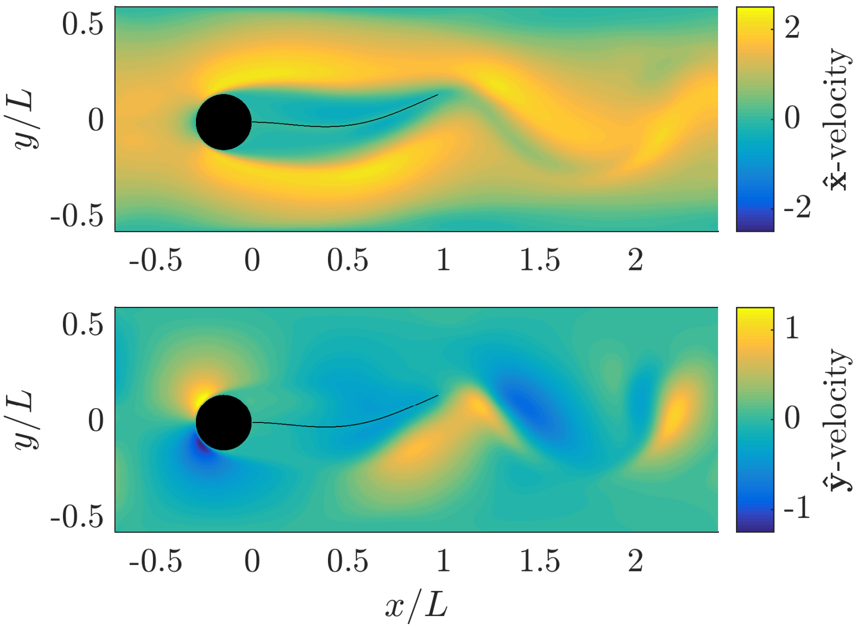

Figure 3.6: Case 2 (table 3.2) velocity component contour plot when beam tip (i.e. trailing edge) is at its maximum amplitude.

Figure 3.7 shows the length normalized $y_{\text{tip}}$ and $x_{\text{tip}}$ displacements of the beam (i.e. trailing edge) for the last two tip oscillation cycles in our simulations. $T$ is the $L$ convective time immediately before the last two oscillations. Our results are compared to those in the appendix of [76]. The length scale in all plots is $L$ (as opposed to $D$) and the origin is at the leading edge of the beam, as illustrated in figure 3.4. The data acquired from [76] was scaled accordingly to reflect the correct length and time scale. The time history of tip displacements appear to be in fair agreement, both in $\hat{\mathbf{x}}$ and $\hat{\mathbf{y}}$.

Table 3.3 with our appended values is reproduced from [76], notably with a rescaling of $L$ as the reference length scale. The definition of measured values are

$$\frac{A_m}{L} = \frac{\max\left[y_{\text{tip}}\right] - \min\left[y_{\text{tip}}\right]}{2L}, \; St = \frac{fL}{U_c}, \; C_D = \frac{2F_x}{\rho_f U_c^2 L}, \tag{3.5}$$

where $f$ is the dimensional frequency of oscillation. Fair agreement between all values is seen both case 1 and case 2. The general spread among measured quantities for case 1 is smaller than that of case 2, but our results appear to fall within the variance of previous algorithms. These results give us confidence that our discretization

Table 3.3: Quantitative comparison of measured values for FSI DNS verification, with cases defined in table 3.2.

| **#** | **Sources** | $A/L$ | $St$ | $C_D$ |
|---|---|---|---|---|
| **Case 1** | Current FSI DNS | 0.260 | 0.663 | 1.285 |
| | Shoele and Mittal [76] | 0.254 | 0.665 | 1.197 |
| | Turek and Hron [74] | 0.237 | 0.665 | 1.180 |
| | Bhardwaj and Mittal [75] | 0.263 | 0.665 | 1.017 |
| | Tian et al. [38] | 0.223 | 0.665 | 1.174 |
| **Case 2** | Current FSI DNS | 0.142 | 1.000 | 0.774 |
| | Shoele and Mittal [76] | 0.125 | 0.945 | 0.709 |
| | Turek and Hron [74] | 0.103 | 0.910 | 0.657 |
| | Bhardwaj and Mittal [75] | 0.117 | 0.980 | 0.629 |
| | Tian et al. [38] | 0.091 | 1.015 | 0.617 |

parameters and the boundary conditions replicate results that are consistent with the literature.

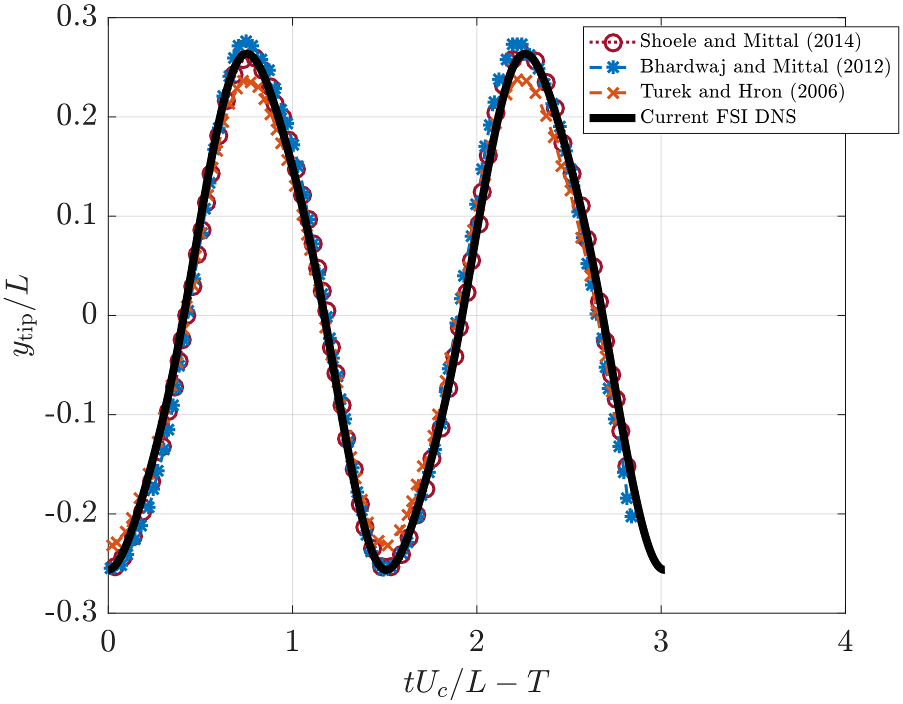

(a) Comparison of case 1 $y_{\text{tip}}$ displacement for last 2 cycles.

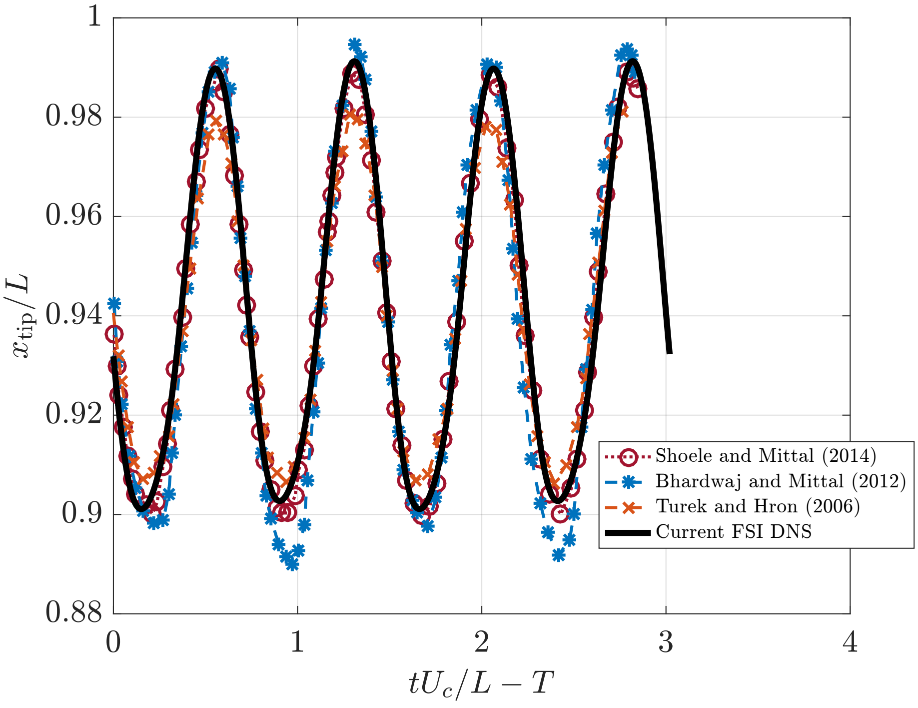

(b) Comparison of case 1 $x_{\text{tip}}$ displacement for last 2 cycles.

Figure 3.7: Comparison of beam tip displacement for case 1 with data set in appendix of [76]. The data includes Shoele and Mittal (2014) [76], Bhardwaj and Mittal (2012) [75], and Turek and Hron (2006) [74].

### 3.3.2 Immersed-Boundary Elastic-Translating Boundary Condition

In section 2.3.3, structural equations and their discretization were augmented to include the elastic-translating boundary condition. We describe here an implementation of this boundary condition in the IB framework.

we can discretize it in time using an implicit Newmark scheme consistent with [52],

$$\left(\frac{4}{\Delta t^2}\frac{m_0}{b}+\frac{k_0}{b}\right)\bar{a}_{k+1}+\frac{c_0}{b}\dot{\bar{a}}_{k+1}-f_{\mathrm{r}k+1}=\frac{m_0}{b}\left(\frac{4}{\Delta t^2}\bar{a}_k+\frac{4}{\Delta t}\dot{\bar{a}}_k+\ddot{\bar{a}}_k\right), \tag{3.6}$$

$$\frac{2}{\Delta t}\bar{a}_{k+1}-\dot{\bar{a}}_{k+1}=\frac{2}{\Delta t}\bar{a}_k+\dot{\bar{a}}_k, \tag{3.7}$$

where we have split the terms that depend on the current time step $k$ from those that depend on the future time step $k+1$ of size $\Delta t$. We have added two states, $\dot{\bar{a}}_{k+1}$ and $\bar{a}_{k+1}$ and two equations, 3.6 and 3.7, to the fluid-structure system. The force $f_{\mathrm{r}k+1}$ is naturally part of the existing system through the fully discretized Navier-Stokes equations. Equations 3.6 and 3.7 can be directly implemented into [52]. The only modification is to include the damping term, but solely at the boundary node; the remainder of the equations are formulated such that all states can be readily included into the discrete system of equations.

## 3.4 Signal Analysis Methods

Three techniques are used to provide insight into the fluid-structure system dynamics in both simulations and experiments. First, the dynamic mode decomposition, or DMD, allows for a clear distinction between the growth and decay rates of multiple beam modes. We apply DMD to FSI DNS results to extract comparable dynamical quantities to the quasi-1D model eigenvalues and eigenmodes. In a noisy experimental environment, we employ the spectral proper orthogonal decomposition, or SPOD, to understand the limit cycle behavior of the system where noise and multi-mode dynamics exist in the data set. Lastly, we use the Hilbert transform to measure single mode decay and frequency in structure impulse-response experiments of the flow-energy harvester flexure. This section comprises a discussion of each method's mathematical formulation and implementation.

### 3.4.1 Dynamic Mode Decomposition

Dynamic mode decomposition (DMD) is a data decomposition technique that approximates the eigenmodes of the linear operator that best describes the dynamics of the system, i.e. from one time instance to the next. Developed over the last decade [77] as an alternative or complement to POD, it provides a means of assessing the time coherent, large scale structures as a linear map that does not require modes to be orthogonal. The linear map is also fully described by a single eigenvalue per degree-of-freedom, which encompasses one growth- or decay- rate and one frequency per mode. This highlights that time, not space, is orthogonalized in the method [77, 78]. Another notable result by Chen, Tu, and Rowley [79] establishes the equality of DMD to the discrete Fourier transform (DFT) in zero-mean periodic data, when snapshots are linearly consistent [2].

We employ DMD in chapter 4 to calculate growth/decay rates and frequencies of the beam in FSI DNS simulations, which are compared to the quasi-1D model eigenvalues. Similarly, DMD modes are analogous to quasi-1D eigenmodes, and their shapes qualitatively compared.

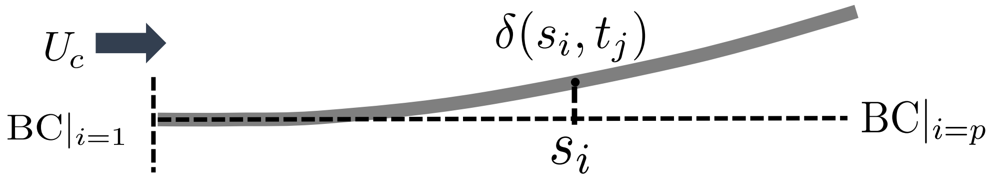

Figure 3.8: Illustration of elastic member displacement and discrete formulation of data matrix elements.

We choose the transverse displacement $\delta$, illustrated in Figure 3.8, as the primary quantity to characterize the fluid-structure system dynamics. The Lagrangian coordinate $s$ follows the arc length of the beam, with $\hat{y}$ displacement at discrete $s_i$ ($i \in \mathbb{Z} : [1, p]$) and time $t_j$ ($j \in \mathbb{Z} : [1, n]$ ) as $\delta(s_i, t_j) = \delta_i^{(j)}$. We define the data matrix $\mathbf{X}$,

$$\mathbf{X} = \begin{bmatrix} \delta_1^{(1)} & \delta_1^{(j)} & \dots & \delta_1^{(n)} \\ \delta_i^{(1)} & \delta_i^{(j)} & \dots & \delta_i^{(n)} \\ \vdots & \vdots & \ddots & \vdots \\ \delta_p^{(1)} & \delta_p^{(j)} & \dots & \delta_p^{(n)} \end{bmatrix} \in \mathbb{R}^{p \times n}. \tag{3.8}$$

The rows of $\mathbf{X}$ are measurements of points along the beam, and the columns are the time series for each point with size $\Delta t$. For typical fluid applications, $p \gg n$,

---

[2] This is when snapshots, or the columns of the data matrix, share the same nullspace.

as the discretization of the fluid-domain requires a large number of points as compared to the number of time steps analyzed. However, $p \ll n$ for our system as $i$ only spans the one-dimensional beam discretization. Specifically, $p \sim 10^2$ while $n \sim \left[10^4 - 10^5\right]$ for our $\mathbf{X}$ matrices processed. This poses issues due to rank limitations of $\mathbf{X}$ when calculating DMD eigenvalues, as they become very susceptible to variations in the time segment length (as seen in [80, pg. 12]). To overcome this, we implement an augmented data matrix as typically done in the eigensystem realization algorithm (ERA). ERA was developed in the controls community to identify the lowest order linear operator that describes an output data set from specified inputs. Tu et al. in [80, pg. 20–23] describe the connection between DMD and ERA modes, and the benefits of augmenting the data matrix as,

$$\mathbf{H}' = \begin{bmatrix} \delta_1^{(1)} & \delta_1^{(l)} & \dots & \delta_1^{(N)} \\ \delta_k^{(1)} & \delta_k^{(l)} & \dots & \delta_k^{(N)} \\ \vdots & \vdots & \ddots & \vdots \\ \delta_p^{(1)} & \delta_p^{(l)} & \dots & \delta_p^{(N)} \\ \delta_{p+1}^{(1)} & \delta_{p+1}^{(l)} & \dots & \delta_{p+1}^{(N)} \\ \vdots & \vdots & \ddots & \vdots \\ \delta_{2p}^{(1)} & \delta_{2p}^{(l)} & \dots & \delta_{2p}^{(N)} \\ \vdots & \vdots & \ddots & \vdots \\ \delta_{(\frac{n}{N})p}^{(1)} & \delta_{(\frac{n}{N})p}^{(l)} & \dots & \delta_{(\frac{n}{N})p}^{(N)} \end{bmatrix} \in \mathbb{R}^{(\frac{n}{N})p \times N}, \tag{3.9}$$

where $l \in \mathbb{Z} : [1, N]$, $p < N \leq n \in \mathbb{Z}$ is the total number of snapshots in each time series block, $k \in \mathbb{Z} : [1, \left(\frac{n}{N}\right) p]$ is the index for the augmented states. Matrix $\mathbf{H}$ is the input matrix, and a segmented version of the time series of $\mathbf{X}$: we have defined a new time series length $N < n$, divided the original into blocks and appended each block to the columns of $\mathbf{H}$. We choose $N > \frac{n}{N}p$ such that $k$ is still the small dimension, with typical values of $\frac{n}{N}$ used range from 1 to 4 at most. The output matrix is

$$\mathbf{H} = \begin{bmatrix} \delta_1^{(2)} & \delta_1^{(l+1)} & \dots & \delta_1^{(N+1)} \\ \delta_k^{(2)} & \delta_k^{(l+1)} & \dots & \delta_k^{(N+1)} \\ \vdots & \vdots & \ddots & \vdots \\ \delta_p^{(2)} & \delta_p^{(l+1)} & \dots & \delta_p^{(N+1)} \\ \delta_{p+1}^{(2)} & \delta_{p+1}^{(l)} & \dots & \delta_{p+1}^{(N+1)} \\ \vdots & \vdots & \ddots & \vdots \\ \delta_{2p}^{(2)} & \delta_{2p}^{(l+1)} & \dots & \delta_{2p}^{(N+1)} \\ \vdots & \vdots & \ddots & \vdots \\ \delta_{(\frac{n}{N})p}^{(2)} & \delta_{(\frac{n}{N+1})p}^{(l+1)} & \dots & \delta_{(\frac{n}{N})p}^{(N+1)} \end{bmatrix} \in \mathbb{R}^{(\frac{n}{N})p \times N}, \tag{3.10}$$

Following the 'exact DMD' procedure [80], we compute the reduced singular value decomposition (SVD) of **H**,

$$\mathbf{H} = \mathbf{U\Sigma V}^* \tag{3.11}$$

where $\mathbf{U} \in \mathbb{C}^{\frac{n}{N}p \times \frac{n}{N}p}$ is unitary, $\mathbf{\Sigma} \in \mathbb{C}^{\frac{n}{N}p \times \frac{n}{N}p}$ is diagonal containing the singular values, and $\mathrm{V}^* \in \mathbb{C}^{\frac{n}{N}p \times N}$. We define matrix

$$\tilde{\mathbf{A}} \equiv \mathbf{U}^*\mathbf{H}'\mathbf{V\Sigma}^{-1}, \tag{3.12}$$

where $\mathbf{U}^*$ and **V** are the conjugate transposes of **U** and $\mathbf{V}^*$, respectively. Solving for the eigenvalue problem for $\tilde{\mathbf{A}}$ as $\tilde{\mathbf{A}}\mathbf{w}_k = \sigma_k \mathbf{w}_k$ produce DMD eigenvalues $\sigma_k$. Solving for the eigenvectors vectors **w**, the DMD modes are

$$\hat{\mathbf{u}}_k = \frac{1}{\sigma_k}\mathbf{H}'\mathbf{V\Sigma}^{-1}\mathbf{w}_k. \tag{3.13}$$

Since $\tilde{\mathbf{A}}$ represents the discrete linear map between sequential data sets **H** and **H′**, we obtain growth/decay rates and angular frequency (DMD spectrum) at each $\sigma_k$ from inverting the exponential solution,

$$\lambda_k = \ln\left(\frac{\sigma_k}{\Delta t}\right). \tag{3.14}$$

In contrast to POD modes, which are arranged according to each mode's energy content in the data, DMD modes are not arranged in any particular order. POD naturally selects the modes that are dynamically significant, where as we must understand from the data set which DMD eigenvalue eigenmode pair best represents it. Assuming the underlying dynamics come from a linear time-invariant system, the physically meaningful eigenvalues should remain fixed in time. Therefore, by varying the time segment for which we define $\mathbf{X}$ (along with $\mathbf{H}$ and $\mathbf{H}'$), we can discern physical modes as those that are associated with invariant eigenvalues. Let $\mathbf{X}_1$ and $\mathbf{X}_2$ be different data matrices as defined in equation 3.8, both as subsets of a single time series for the beam in figure 3.8. Let $\lambda_l$ be the DMD spectrum of $\mathbf{X}_1$ and $\lambda_q$ that of $\mathbf{X}_2$. A mode $\hat{\mathbf{u}}_l$ is physically meaningful if its corresponding $\lambda_l$ meets the condition

$$\min_q \left[ |\lambda_l - \lambda_q| \right] < D, \tag{3.15}$$

where $D$ is the invariant tolerance and defined as 1E-2 for our cases. Once physically meaningful eigenvalues have been determined, we track the least stable eigenvalue $\lambda_{\max} = \max_{\lambda_m} \{\mathrm{Re}\left[\lambda_m\right]\}$, where $\lambda_m$ is the set of $\lambda_l$ that meets criteria 3.15 ($m \leq l$).

The last step is to check whether $\lambda_{\max}$ captures what is observed as the dynamics of the tip response, $\delta_p^{(j)}$. This is done by fitting a exponential to the peaks of $\delta_p^{(j)}$, and taking a DFT of the demodulated signal, such that the segment is represented by

$$\delta_p^{(j)} \sim \mathrm{e}^{\zeta j \Delta t} \cos\left(\omega_{\max} j \Delta t\right). \tag{3.16}$$

The signal phase and absolute amplitude are not necessarily relevant for our comparison, only the amplitude growth/decay $\zeta$ and the oscillating frequency $\omega_{\max}$. We compare $\zeta$ to $\mathrm{Re}[\lambda_{\max}]$ and $\omega_{\max}$ to $\mathrm{Im}[\lambda_{\max}]$. If the system is dominated by a single frequency response, this gives us confidence that we have obtained the correct DMD eigenvalue and eigenmode pair. If more than one more dominates the response, the check provides a general search area for the decay rate and dominant frequencies. If no $\lambda_l$ meets criteria 3.15, we increase the $\frac{n}{N}$ ratio and iterate. Similarly, we may iterate with a longer time series that captures the linear portion of the dynamics better, for example.

Figures 3.9, 3.10, and 3.11 illustrate this procedure for an example data set from a stable, constant channel flow FSI DNS simulation discussed in detail in section 4.2. Figure 3.9 shows the full time series of two beam locations, the tip at $\delta_p$ and at the beam half-way point, $\delta_{p/2}$. Two subsets of the full time series are also shown for the two beam location, where $T_1 > T_2$ are time shifts to obtain each subsegment.

The data matrices $\mathbf{X}_1$ for segment with a time shift $T_1$ and $\mathbf{X}_2$ for a time shift $T_2$, are built from equation 3.8, and their respective $\mathbf{H}'$ and $\mathbf{H}$ follow from equations 3.9 and 3.10. The exponential fit and power spectral density for the tip displacement in the $\mathbf{X}_1$ are shown in figure 3.10, with $\zeta = -0.011$ and $\omega_{\max} = 3.77$. Figure 3.11 then compares the positive frequency DMD eigenvalues and the fit parameters $\zeta$ and $\omega_{\max}$.

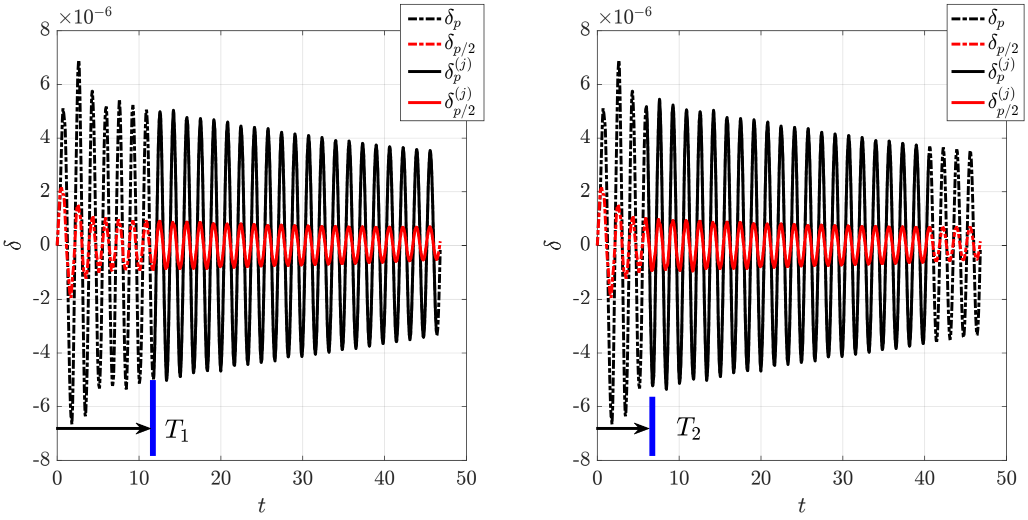

(a) (b)

Figure 3.9: Stable beam time series at the beam tip, $\delta_p$ and at beam midpoint, $\delta_{p/2}$. The figure illustrates a segment data set $X_1$ (3.9a) and $X_2$ (3.9b) with a time shift of $T_1 > T_2$, respectively.

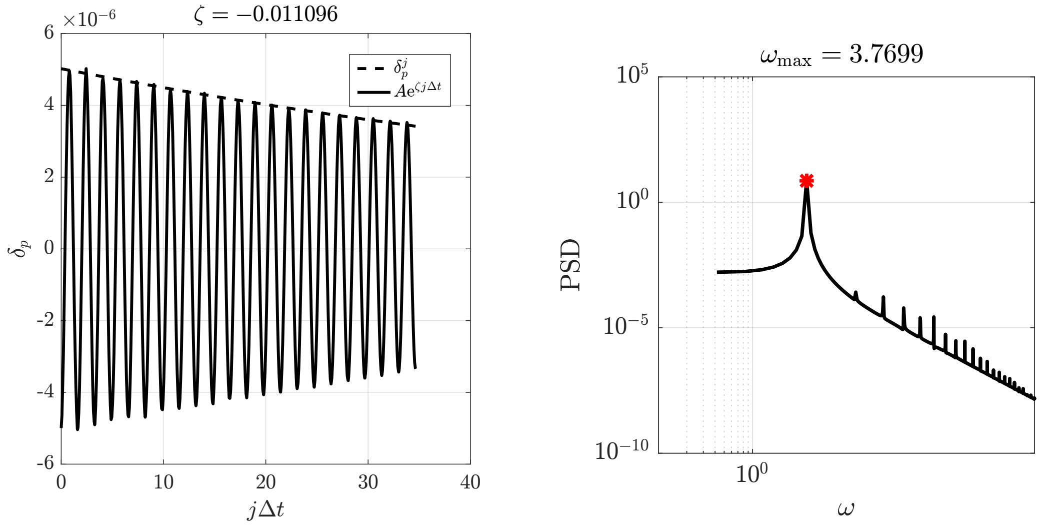

(a)

(b)

Figure 3.10: Beam tip $\delta_p^{(j)}$ for $\mathbf{X}_1$ segment. The figure illustrates the exponential fit (3.10a) with a $\zeta = -0.0111$ and the DFT of the demodulated signal (3.10b) with $\omega_{\text{max}} = 3.77$.

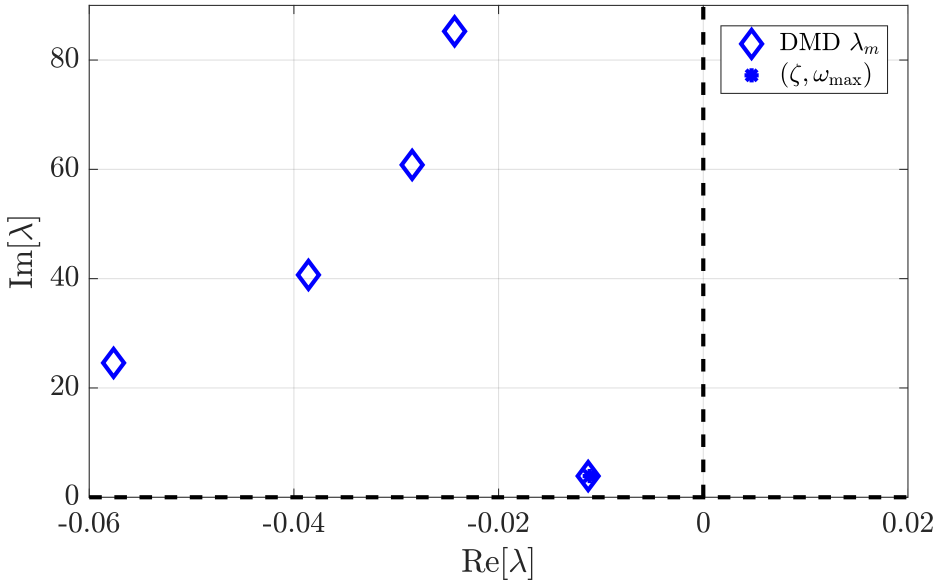

Figure 3.11: Comparison of DMD eigenvalues (shown for $\mathrm{Im}[\lambda] > 0$ ) and fit pair $(\zeta, \omega_{\text{max}})$ from the beam tip time series.

In practice, if the system is dominated by a single eigenmode eigenvalue pair, as in the example, proceeding with the algorithm in reverse order may be desirable: by finding $\zeta$ and $\omega_{\text{max}}$ that describe the tip displacement first, $\lambda_{\text{max}}$ can be informed and narrowed, and the verification step becomes the comparison between $\mathrm{X}_1$ and

$X_2$ DMD spectra.

Lastly, because of the $\mathbf{X}$ augmentation to produce $\mathbf{H}$ and $\mathbf{H}'$, $\hat{\mathbf{u}}_k \in \mathbb{C}^{\frac{n}{N}p\times 1}$. In order to compare mode shapes with the quasi-1D model, we employ a similar procedure to ERA and restrict the observables to the first $p$ elements of $\hat{\mathbf{u}}_k$. This is equivalent to producing a reduced order model from $\mathbf{H}$ with the same dimension as the output of the dynamical system represented by $\mathbf{X}$ [80]. $\lambda_m$ and the restricted $\hat{\mathbf{u}}_m$ provide direct quantitative measures for a comparison between FSI DNS time series and the eigendecomposition of the quasi-1D model equations.

### 3.4.2 Spectral Proper Orthogonal Decomposition

Proper orthogonal decomposition (POD) is a method used widely in fluid mechanics to find flow coherence through modes that optimally capture the energy within a data set [78, 81, 82]. In this context, the data set and energy, or norm, must be defined, and often encompass only the spatial dimension in typical applications [78]. The spectral proper orthogonal decomposition is the frequency domain version of POD, which captures optimal modes with an energy definition in space and time. Though introduced many decades ago [83, 84], a recent analysis [78] elucidates its strength as a tool for extracting coherence in the dynamics that include stochastic white-noise forcing. They also draw a direct relation between the method, DFT, DMD, and the resolvent. SPOD relates the correlation of an ensemble of measurements in time an space by identifying and ordering modes at a particular frequency that have the strongest coherence first. The mode ordering gives a sense of the dimensionality of the problem over the spectrum, but also at each individual frequency. Specifically, SPOD not only answers whether preferential frequencies exist in the system dynamics, which shapes captures what percentage of the energy in that frequency. We employ SPOD on experimental data consisting of video frames of the elastic member in turbulent flow ($Re_L \sim 10^6$, $Re_{\bar{h}} \sim 10^4$). The resulting SPOD modes provide a means to filter the time-domain data, and understand the predominant dynamics of the data set. Specifically, whether the system exhibits limit cycle or amplifier/intermittent state behavior in our case [85].

To begin, we consider the definition of the data matrix from figure 3.8 and in equation 3.8. Assuming that the system is stationary and consistent with the procedure in [78, 86], the DFT of each row of our $\mathbf{X}$ is carried out using Welch's method [87]. In the procedure, each discrete time series is segmented into 50% overlapping blocks of size $n_f \leq n$, Fourier transformed, and assembled into a Fourier domain data matrix $\tilde{\mathbf{X}}_{f_l}$ at each discrete frequency $f_l$,

$$\tilde{\mathbf{X}}_{f_l} = \begin{bmatrix} \tilde{\delta}_1^{(1)} & \tilde{\delta}_1^{(k)} & \dots & \tilde{\delta}_1^{(N)} \\ \tilde{\delta}_i^{(1)} & \tilde{\delta}_i^{(k)} & \dots & \tilde{\delta}_i^{(N)} \\ \vdots & \vdots & \ddots & \vdots \\ \tilde{\delta}_p^{(1)} & \tilde{\delta}_p^{(k)} & \dots & \tilde{\delta}_p^{(N)} \end{bmatrix}_{f_l} \in \mathbb{C}^{p\times N}, \tag{3.17}$$

where $l \in \mathbb{Z} : [1, n_f]$, $N \geq 1 \in \mathbb{Z}$ is the total number of blocks in Welch's method, $k \in \mathbb{Z} : [1, N]$ is a Fourier realization of the data and block number index. Elements in $\tilde{\mathbf{X}}_{f_l}$ are

$$\tilde{\delta}_i^{(k)} = \frac{1}{\sqrt{n_f}} \sum_{j=\frac{n_f}{2}(k-1)+1}^{\frac{n_f}{2}(k+1)} \delta_i^{(j)} \mathrm{e}^{-2\pi\sqrt{-1}(l-1)\frac{j-1}{n_f}}, \tag{3.18}$$

for a rectangular windowing function, and discrete frequencies

$$f_l = \begin{cases} \frac{l-1}{n_f \Delta t} & \text{for } l \leq n_f/2 \\ \frac{l-1-n_f}{n_f \Delta t} & \text{for } l > n_f/2 \end{cases}. \tag{3.19}$$

We build the cross-spectral density matrix at each $f_l$,

$$\tilde{\mathbf{S}}_{f_l} = \frac{\Delta t}{n_f N} \tilde{\mathbf{X}}_{f_l} \tilde{\mathbf{X}}_{f_l}^* \in \mathbb{C}^{p\times p}, \tag{3.20}$$

where $\tilde{\mathbf{X}}_{f_l}^*$ is the conjugate transpose of $\tilde{\mathbf{X}}_{f_l}$ and $\Delta t$ is the time increment for the series. $\tilde{\mathbf{S}}_{f_l}$ is hermitian and represents the cross-correlation of measurement $i$ Fourier coefficients with all other measurements, averaged over all realizations. We can eigendecompose $\tilde{\mathbf{S}}_l$,

$$\tilde{\mathbf{S}}_l = \hat{\mathbf{U}}_l \boldsymbol{\Sigma}_l \hat{\mathbf{U}}_l^* \tag{3.21}$$

where $\hat{\mathbf{U}}_l$ is unitary (along with its conjugate transpose $\hat{\mathbf{U}}_l^*$) and its columns $(\hat{\mathbf{u}}_i)_l$ are orthonormal eigenvectors of $\tilde{\mathbf{S}}_l$. $\boldsymbol{\Sigma}_l \in \mathbb{R}^{p\times p}$ is a diagonal matrix with its entries as the eigenvalues $(\sigma_i)_l$ in descending order. $(\sigma_i)_l$ can be interpreted as the amount of energy its pair $(\hat{\mathbf{u}}_i)_l$ contains at $f_l$. The cross-spectral density at each $f_l$ is tensor invariant $\mathrm{tr}(\hat{\mathbf{S}}_l) = \mathrm{tr}(\mathbf{\Sigma}_l)$, and represents the total energy at each frequency. The fraction of energy each mode contains is

$$(\hat{\sigma}_i)_l = \frac{(\sigma_i)_l}{\mathrm{tr}(\hat{\mathbf{\Sigma}}_l)}. \tag{3.22}$$

The system may be reduced further if a single $(\hat{\sigma}_i)_l$, $(\hat{\mathbf{u}}_i)_l$ pair contains most of the energy at these peak frequencies. In systems where both holds true, it is often useful to understand the dynamics of these predominant modes. Frequencies where $\mathrm{tr}(\hat{\mathbf{\Sigma}}_l)$ peaks indicate periodic behavior, but do not discern between periodic oscillations characteristic of a limit-cycle, or intermittent periodic behavior associated with a stochastically forced under-damped system. However, the SPOD modes provide a means to filter the original time domain data and discern those states exactly. Schmidt, Colonius, and Bres [85] first explored this by projecting time domain pressure data onto the leading SPOD modes to find intermittent behavior of noise in a turbulent jet. Here, we would like to do the same by projecting the time domain beam displacement data onto the leading SPOD beam shapes.

Suppose the system has $m < n_f$ peak frequencies in $\mathrm{tr}(\hat{\mathbf{\Sigma}}_l)$. To explore the time behavior of the most energetic modes at each peak frequency, we build a basis,

$$\hat{\mathbf{\Phi}} = \left[(\hat{\mathbf{u}}_1)_1, \cdots, (\hat{\mathbf{u}}_1)_m\right] \in \mathbb{C}^{p \times m}, \tag{3.23}$$

where subscript 1 in $\hat{\mathbf{u}}_1$ indicates the leading mode. We would like to approximate the time domain data $\mathbf{X}$ as

$$\mathbf{X} \approx \hat{\mathbf{\Phi}}\mathbf{A} \tag{3.24}$$

where $\mathbf{A}$ is the matrix with coefficients of each basis (rows) in $\hat{\mathbf{\Phi}}$ over time (columns). To solve for $\mathbf{A}$,

$$\mathbf{A} = \left(\hat{\mathbf{\Phi}}^*\hat{\mathbf{\Phi}}\right)^{-1}\hat{\mathbf{\Phi}}^*\mathbf{X}. \tag{3.25}$$

where $\hat{\mathbf{\Phi}}^*$ is the conjugate transpose of $\hat{\mathbf{\Phi}}$. The columns of $\hat{\mathbf{\Phi}}$ are not orthogonal, and $\left(\hat{\mathbf{\Phi}}^*\hat{\mathbf{\Phi}}\right)^{-1}$ accounts for the cross-coupling between the modes. By construction, modes are orthonormal within a single frequency, but not across frequencies when only considering the spatial norm[3].

The map between $\mathbf{A}$ and $\mathbf{X}$ is, in essence, a spatial filter that when applied to the time-domain data elucidates how each shape $\hat{\mathbf{u}}_1$ behaves in time. With $\mathbf{X}$ built as transverse displacement $\delta_p^{(j)}$, each basis in $\hat{\mathbf{\Phi}}$ represents a beam mode shape and the columns of $\mathbf{A}$ their amplitudes at a particular instance in time.

Since $\mathbf{A}$ represents beam displacement over time, the velocity of each shape can be defined as $\frac{\mathrm{d}\mathbf{A}}{\mathrm{d}t}$ and estimated through a discrete time derivative for the data set. We can access a two-dimensional phase-portrait of each mode, and discern their individual dynamics: periodic orbits will be closed orbits (donut shape), while amplifier states as points clumped around the origin, as the mode is perturbed stochastically, but decays back to its equilibrium.

### 3.4.3 Hilbert Transform

The Hilbert transform is widely used in signal processing to obtain the "analytic" equivalent from real valued signal [88], and it is particularly helpful in obtaining the instantaneous growth or decay from dynamical systems [89–91]. We will employ the Hilbert transform to estimate flexure parameters in chapter 5 by considering the real valued voltage output from piezoelectric elements.

To begin, we define the Hilbert transform of the real valued signal in time $V(t)$ as

$$\mathcal{H}\left\{V(t)\right\} = \frac{1}{\pi}\int_{-\infty}^{\infty}\frac{V(y)}{t-y}dy, \tag{3.26}$$

which represents the complex part of the analytical signal $z(t)$,

$$z(t) = z_{Re}(t) + iz_{Im}(t) = V(t) + i\mathcal{H}\left\{s(t)\right\}. \tag{3.27}$$

Using Euler's formula, equation 3.27 becomes

$$z(t) = A(t)\mathrm{e}^{i\phi_{\mathrm{ph}}(t)}, \tag{3.28}$$

where we the modulating amplitude is

---

[3] Modes across frequencies are orthogonal in the temporal sense. However, if the spatial modes are considered in the projection framework here, they are not orthogonal in that the norm $(\hat{\mathbf{u}}_1)_i^*(\hat{\mathbf{u}}_1)_j \neq 0$ for $i \neq j$.

$$A(t) = \sqrt{z_{Re}^2(t) + z_{Im}^2(t)}, \tag{3.29}$$

and instantaneous phase

$$\phi_{\mathrm{ph}}(t) = \tan^{-1}\left(\frac{z_{Re}(t)}{z_{Im}(t)}\right). \tag{3.30}$$

The discrete formulation and implementation of the Hilbert transform is performed in MATLAB with the `hilbert` function. Least-square linear fits are used to find the exponential decay of $V$ as the slope of $\ln A(t)$ over $t$ from equation 3.29, and its angular frequency as the slope of $\phi(t)$ in equation 3.30.

## *Chapter 4*

# TWO-DIMENSIONAL MODELING AND SIMULATION RESULTS

### 4.1 Introduction

In this chapter, we present numerical results for both the analytical quasi-1D model derived in chapter 2 and the fluid-structure interaction direct numerical simulations discussed in chapter 3. The comparison between modeling and simulations allows us to assess the validity of the model assumptions and, in doing so, the physical mechanisms that drive the fluid-structure dynamics. We begin with a constant channel flow geometry and test model predictions against those of the DNS over four relevant non-dimensional parameters: mass ratio, stiffness ratio, throat-to-length ratio, and the Reynolds number. Next, the translating leading edge is added as a simple harmonic oscillator and dynamics are compared to include the additional parameter set from the boundary. Finally, we define that channel geometry as a diffuser and appraise model predictions considering also a channel diffuser angle for both cases where the elastic member is an elastically-mounted translating rigid mean and a cantilevered flexible beam.

### 4.2 Cantilever in Constant Channel Flow

A detailed overview of previous work in channel flows was given in section 1.4. The primary thrust of this study is to understand the physical mechanisms that drive the fluid-structure instabilities of an elastic member in channel flow. The quasi-1D model applies assumptions and simplifications to the coupled equations of motion, where as the FSI DNS algorithm solves the full equations numerically, where simplifications are not physical but in the discretization of the equations. Hence, we are fundamentally comparing two imperfect models that approach reality in their respective limits. In contrasting them, we must connect their input parameters and boundary conditions such that the overall physics are evaluated rather than their numerical or implementation differences. When a reduced-order model is derived on parameter assumptions based on a particular mechanism, verifying its results lends credibility to the mechanisms themselves. In this vein, we use the FSI DNS results to verify the flutter boundary for a range of parameters for the quasi-1D model. By asserting the robustness of the quasi-1D model prediction to these parameter ranges (in tables 2.3 and 2.4), we assess the extent to which a leakage flow type instability drives the system dynamics.

This section is organized as follows: first we formulate the channel flow problem, with its geometry and boundary conditions in 4.2.1. The specifics of the FSI DNS numerical discretization follows in section 4.2.2, which defines mesh parameters for the FSI DNS. Then a grid study follows in section 4.2.3, setting an $\hat{h}_{\text{corr}}$ for comparison between FSI DNS and quasi-1D results in section 4.2.4. An extensive computational effort was carried out with more than 4000 FSI DNS simulations and 100,000 cpu/hrs to map the flutter instability boundary over the range of non-dimensional parameters. The parameter ranges chosen were loosely based on flow-energy harvester dimensions and proportions (shown in figure 5.2), but are primarily devised to test conditions derived in section 2.2.1 for the validity of the quasi-1D model. We follow the DNS study with a comparison between the quasi-1D model results with those of existing inviscid model in section 4.2.5, and a set of detailed stability boundary predictions in the parameter ranges validated. Finally, we include the elastic-translating boundary condition and, once again, compare DNS results with those of our model.

### 4.2.1 Problem Formulation

The FSI DNS computational domain is illustrated in figure 4.1. The coordinate system has its origin at the beam leading edge, and the channel is defined at a constant halfwidth, $\bar{h}$. The initial beam position $\delta(s, 0) = 0$, and its velocity is $\frac{\partial}{\partial t}\delta(s, 0) = 0$, where $s$ is the Lagrangian coordinate that describes the beam parametrized by its arc length. The boundary conditions are clamped and free for leading and trailing edges of the beam, respectively. A uniform velocity profile is specified at the inlet as $U_{\text{in}}$ and used as the reference parameter for non-dimensionalization of other quantities. The channel boundaries are no-slip immersed boundaries. The flow is impulsively started and the beam is perturbed by a small body force at the initial time step in order to break symmetry.

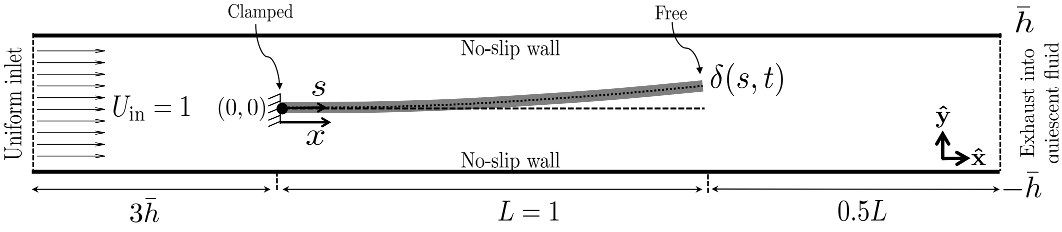

Figure 4.1: Illustration for fluid-structure constant channel domain and boundary conditions.

Figure 4.1 is contrasted with the domain in figure 2.3, where quasi-1D model parameters are illustrated. First, the steady flow rate, $q_{x0}$ (the steady part of $Q_x$ in figure 2.3), specified for the quasi-1D model constitutes half the integrated $\hat{\mathbf{x}}$ flow velocity (in the channel) over $\hat{\mathbf{y}}$ from $-\bar{h}$ to $\bar{h}$ immediately downstream of the inlet. The beam boundary conditions for the quasi-1D model are the same as the DNS. As discussed in section 2.2.1, the quasi-1D model results are independent of the inlet velocity profile. Results also do not depend on inlet and outlet distances except through loss coefficients $\zeta_{o1}$ and $\zeta_{o2}$ defined in equations 2.35, 2.37. We assume that stagnation pressure loss at either end is negligible and take the no loss coefficients values, $\zeta_{o1} = 0$ and $\zeta_{o2} = 0$ for the remainder of this section.

Lastly, we are interested in the dynamics near the DNS initial conditions, which, apart from the small body force to deflect the beam, represents a (potentially unstable) equilibrium for both the DNS and the quasi-1D model. In this limit the coordinate $x$, shown in both figures 2.3 and 4.1, coincides with the Lagrangian coordinate $s$ in figure 4.1. For small perturbations, the Lagrangian beam shape then becomes the beam $\hat{\mathbf{y}}$ displacement, $\delta(x,t)$.

We will use DMD to find the least-stable mode of the DNS results using the procedure discussed in section 3.4.1. These results are directly comparable with the eigenvalues and eigenmodes of the quasi-1D linear operator in equation 2.96, and describe the linear dynamics of the system. In order to compare to DMD growth rate, only the most dynamically significant eigenvalue of the quasi-1D will be shown as well. If this eigenvalue has an imaginary part (and complex conjugate pair since the data matrix is real), we will track the positive frequency counterpart. Given the non-dimensionalization in 2.104 and 3.2, the model eigenvalues and DMD spectrum, represented as $\lambda$, are scaled with the inverse of non-dimensional convective time units. The Strouhal number is

$$St = \frac{\mathrm{Im}\,[\lambda]}{2\pi} = \frac{f_s L}{U}, \tag{4.1}$$

where $f_s$ is the dimensional frequency response of the beam.

### 4.2.2 FSI DNS Discretization and Data Analysis

The FSI DNS Eulerian mesh is uniform in $\hat{\mathbf{x}}$ and $\hat{\mathbf{y}}$ with grid spacing $\Delta x^* = \frac{\Delta x}{L}$ similar to the verification cases in section 3.3.1. Because the parametric study spans a wide range of $Re_L$ and $\hat{h}$ values, with over 4000 simulations are carried out, the $\Delta x^*$ is automatically determined by the most restrictive of three conditions: the grid Reynolds number $Re_{\Delta x} \leq 2$; the minimum number of grid elements in $\hat{h}$ is 20; the minimum number of elements on the beam surface is 160,

$$\Delta x^* = \min\left\{\frac{2}{Re_L}, \frac{\hat{h}}{20}, \frac{1}{160}\right\}. \tag{4.2}$$

The Lagrangian grid spacing is always $\Delta s^* = 2\Delta x^*$, as suggested in [68]. The time step size $\Delta t^*$ is determined by holding the $CFL = \frac{\Delta t^*}{\Delta x^*} = 0.2$ for the $\Delta x^*$ that satisfies the criteria 4.2. These conditions were determined by trial and error to capture least 200 time steps per beam oscillating cycle for all results. The grid Reynolds number chosen captures fluid advection and diffusion terms well. The resulting $\Delta x^*$, $\Delta t^*$ combination produces results within acceptable wall-time for the number of simulations ran in this study. We explore the effect of grid refinement from criteria 4.2 in our results in section 4.2.3.

#### Data Analysis

To help clarify results in subsequent sections, we step through a representative example of the FSI DNS data to obtain critical flutter values. The relevant dimensionless parameters for the clamped-free boundary conditions are derived in section 2.3.6, and defined in table 2.3 (reproduced here for reference).

The beam displacement response is analyzed for each simulation in the series. We show in figure 4.2 a segment of the beam tip displacement over time for the two $\hat{k}$ values in the series immediately adjacent to the stability boundary: $\hat{k} = 4.17$ as stable and $\hat{k} = 4.11$ as unstable. The figure also shows the least-squares fit to the exponential function coefficient $\zeta$ that captures the envelope of the amplitude decay and growth of each segment, respectively. Their power spectra are shown in figure 4.3, with respective peak angular frequencies labeled $\omega_{\max}$.

Table 4.1: Table of fluid structure non-dimensional parameters in FSI DNS grid convergence study.

| **Parameter** | **Value** |
|---|---|
| $\hat{m}$ | 100 |
| $\hat{k}$ | [3 - 4.5] |
| $\hat{h}$ | 0.05 |
| $Re_L$ | 200 |
| $\hat{h}^2 Re_L$ | 0.5 |
| $\Delta x^*$ | 0.0025 |

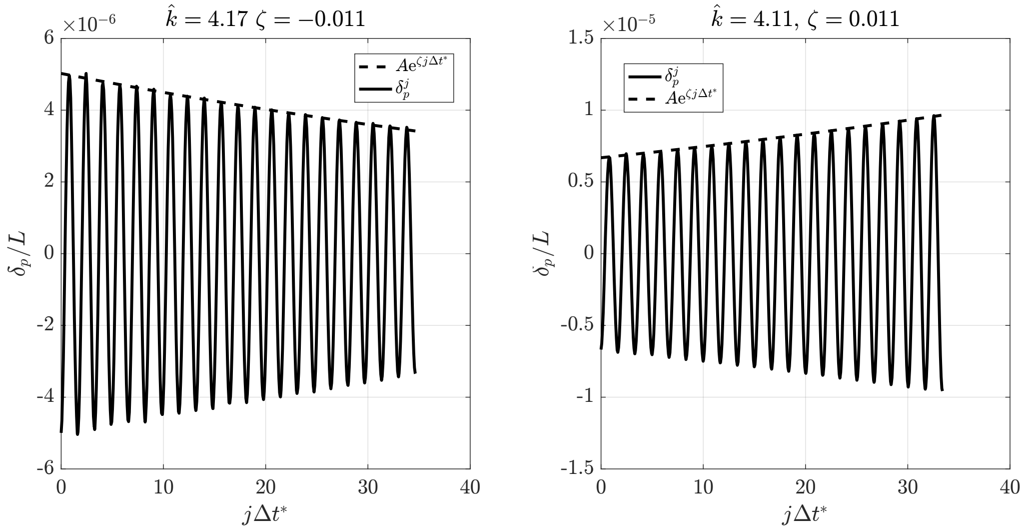

(a) Stable $\hat{k}$ = 4.17.

(b) Unstable $\hat{k}$ = 4.11.

Figure 4.2: Beam tip amplitude time segment for FSI DNS results in table 4.1 for stable and unstable $\hat{k}$ values.

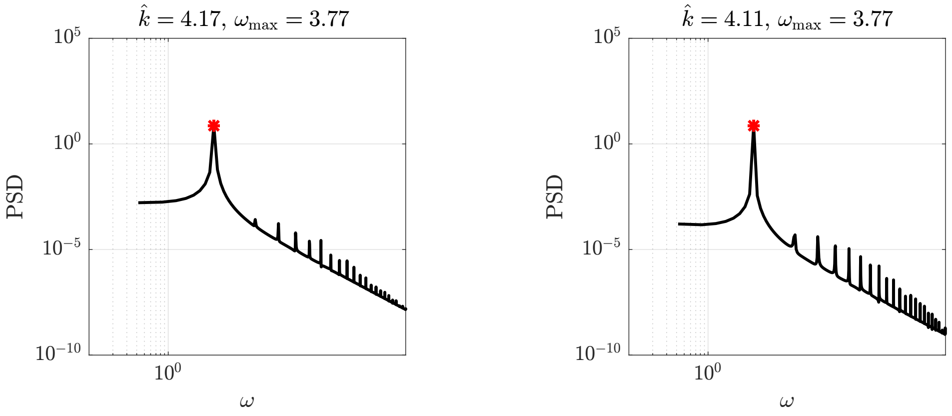

(a) Stable $\hat{k}$ = 4.17.

(b) Unstable $\hat{k}$ = 4.11.

Figure 4.3: Beam tip amplitude power spectrum for FSI DNS results in table 4.1 for stable and unstable $\hat{k}$ values.

Each DNS result is processed according to the procedure in section 3.4.1. We now plot the result of the DMD procedure as the physically meaningful spectra of $\hat{k} = 4.11$ and $\hat{k} = 4.17$, once again, along with their tip displacement fit parameter $\zeta$, $\omega_{\max}$ pairs in figure 4.4. The $\lambda$ tracked corresponds to $\lambda = \max_{\lambda_i} \mathrm{Re}\,[\lambda_i]$ and can be seen as the ones closest to $\zeta$ and $\omega_{\max}$ pair at each $\hat{k}$.

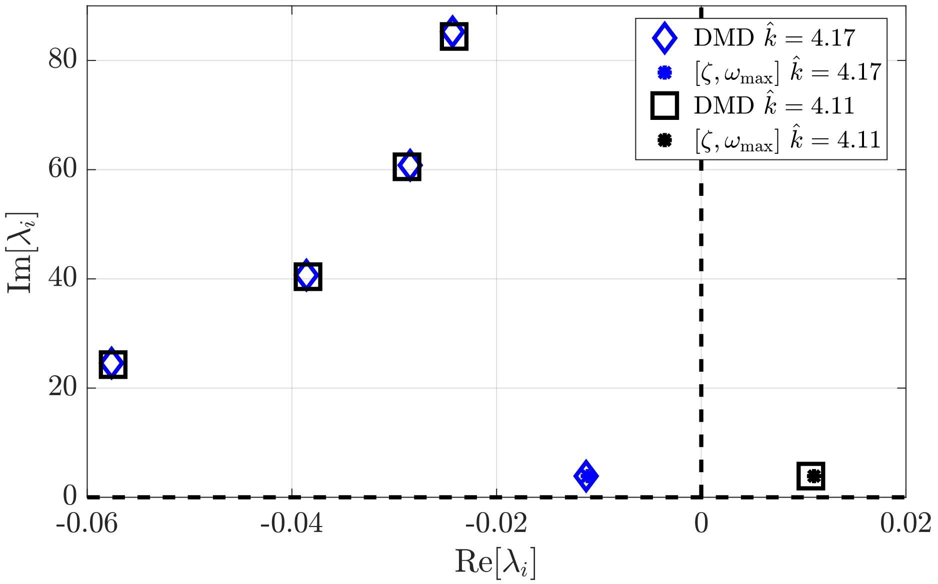

Figure 4.4: Comparison of dynamically significant DMD spectra (shown for $\mathrm{Im}[\lambda] > 0$ ) and fit pair $(\zeta, \omega_{\max})$ for $\hat{k} = 4.11$ and $\hat{k} = 4.17$.

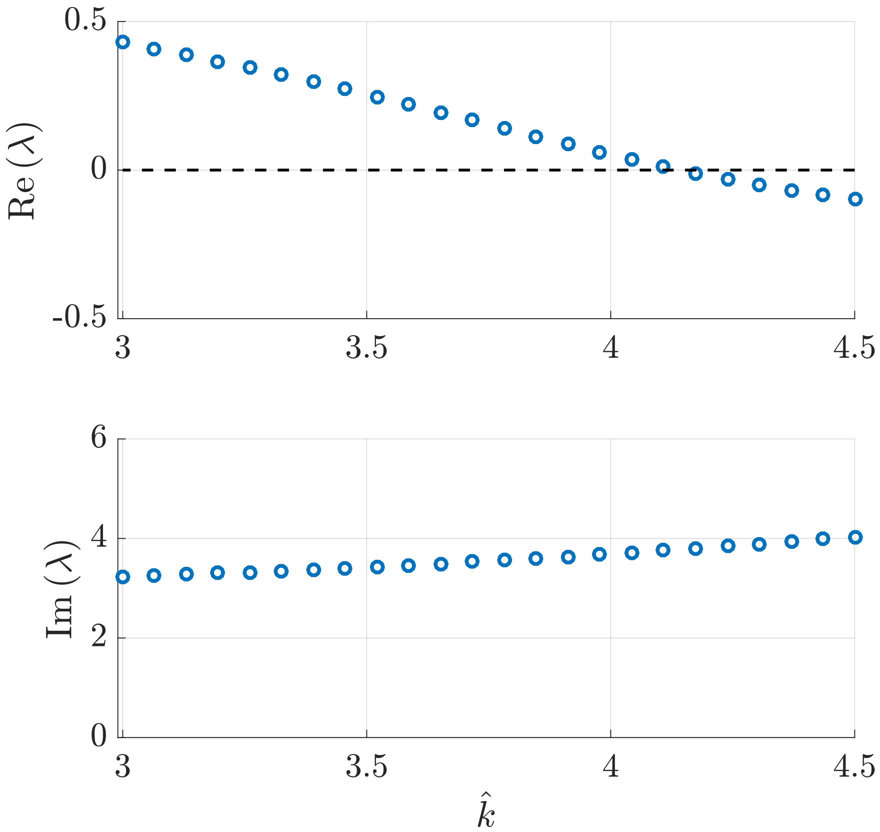

Figure 4.5: DMD $\lambda$ for simulation series in table 4.1.

Figure 4.5 shows $\lambda$ values obtained through this process for all 24 simulations in the series in table 4.1.

The flutter boundary critical values, $\hat{k}_{\text{cr}}$, is calculated as the linearly interpolated result between the stable and unstable (superscripts $j$ and $j+1$, respectively) $\hat{k}$ values corresponding to the stable and unstable values of Re$[\lambda]$ at Re$[\lambda] = 0$,

$$\hat{k}_{\text{cr}} = -\text{Re}\left[\lambda^{(j)}\right]\left(\frac{\Delta\hat{k}}{\Delta\lambda_{\text{Re}}}\right) + \hat{k}^{(j)}. \tag{4.3}$$

where $\Delta\hat{k} = \hat{k}^{(j+1)} - \hat{k}^{(j)}$ and $\Delta\lambda_{\text{Re}} = \text{Re}\left[\lambda^{(j+1)}\right] - \text{Re}\left[\lambda^{(j)}\right]$. Similarly, the critical angular frequency, Im$[\lambda]_{\text{cr}}$, is the interpolated value of Im$[\lambda]$ across the boundary at Re$[\lambda] = 0$,

$$\text{Im}\left[\lambda\right]_{\text{cr}} = -\text{Re}\left[\lambda^{(j)}\right]\left(\frac{\Delta\lambda_{\text{Im}}}{\Delta\lambda_{\text{Re}}}\right) + \text{Im}\left[\lambda^{(j)}\right], \tag{4.4}$$

where $\Delta\lambda_{\text{Im}} = \text{Im}\left[\lambda^{(j+1)}\right] - \text{Im}\left[\lambda^{(j)}\right]$. For the data set in table 4.1, $\hat{k}_{\text{cr}} = 4.14$ and $\text{Im}\left[\lambda\right]_{\text{cr}} = 3.78$.

To illustrate the FSI DNS solution as the beam amplitude increases in time, we select a representative unstable parameter set from table 4.1, where $\hat{k} = 3.07 < 4.14 = \hat{k}_{\text{cr}}$, as seen in figure 4.5. The cantilever tip time evolution is shown in figure 4.6 with $\Delta t^* =$5E-4, with exponential growth rate $\sim 0.4$.

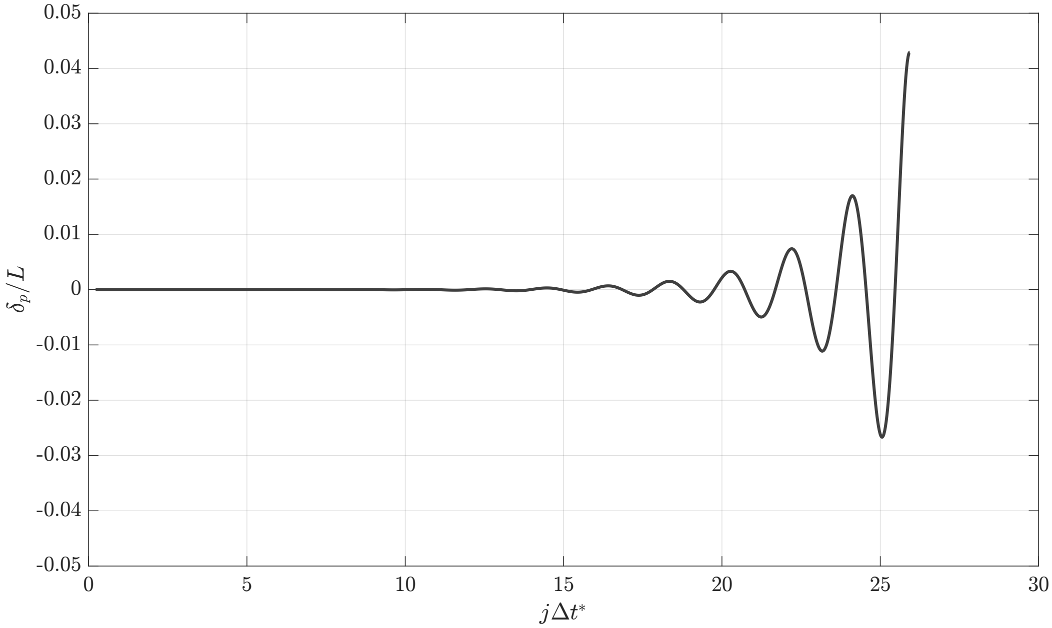

Figure 4.6: FSI DNS cantilever tip amplitude time evolution for case in table 4.1 at $\hat{k} = 3.07$.

The $x$ velocity profile within the channel at different snapshots in $t^* = j\Delta t^*$ are shown in figure 4.7. The cantilever can be seen to still remain close to its equilibrium at $t^* = 7.5$. A slight shape change can be seen at $t^* = 20$, and quickly evolves of the next 5 convective time units to tip displacements close to the channel walls. The snapshot at $t^* = 25$ illustrates how the restriction of the upper channel over most of the length of the cantilever corresponds to higher axial velocities. This can also be seen toward the final 10% of the cantilever length on the lower channel as well. A resemblance to the second orthogonal Euler-Bernoulli beam mode becomes apparent after $t^* = 22.5$. This can be seen in the normalized DMD mode shown in figure 4.8 in both the real and imaginary parts of the model shape.

Hence, the system shown becomes unstable at a single eigenvalue corresponding to a single mode shape. The critical parameters when the stable-to-unstable transition occurs is acquired via simulation over a range of parameters and interpolating between the set that captures negative and positive growth rates.

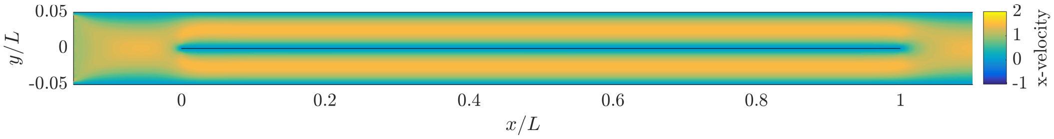

(a) $t^* = 7.5$.

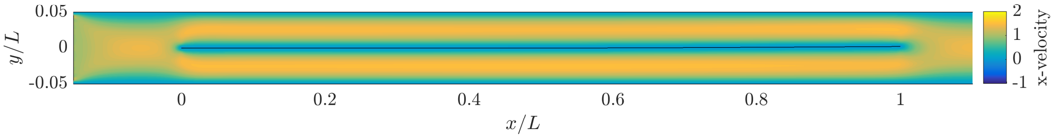

(b) $t^* = 20$.

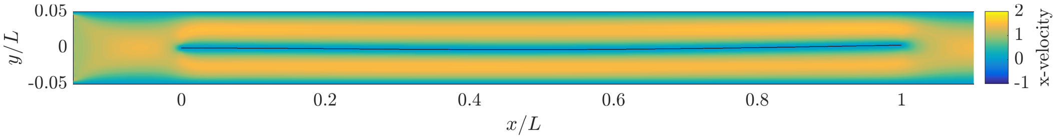

(c) $t^* = 22.5$.

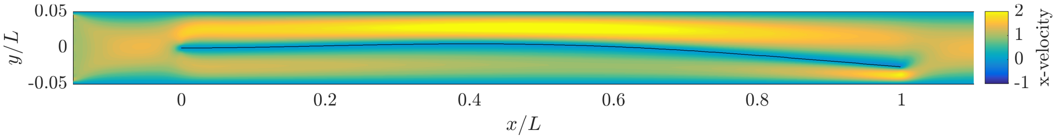

(d) $t^* = 25$.

Figure 4.7: FSI DNS $x$ velocity contour snapshots at different convective time units $t^*$ for case in table 4.1 and $\hat{k} = 3.07$.

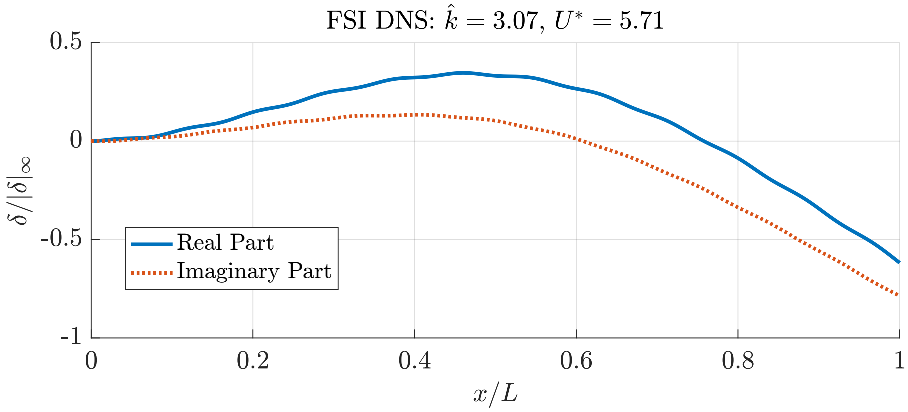

Figure 4.8: Real and imaginary parts of unstable FSI DNS mode for case in table 4.1 at $\hat{k} = 3.07$.

### 4.2.3 Grid Convergence and Effective Beam Thickness

The convergence of the FSI DNS beam dynamics as a function of the spatial discretization is explored through a grid refinement study. Once again, the parameter set in table table 4.1 is chosen for this analysis. This is because they insure that the lubrication-theory approximations introduced in section 2.2.1 are satisfied, and thus the quasi-1D model is expected to accurately represent the fully-coupled system. $\hat{k}$ is varied as the bifurcation parameter, while $\hat{m}$, $\hat{h}$, and $\hat{h}^2 Re_L$ are held constant; DMD eigenvalues are calculated for $\Delta x^*$, $\frac{\Delta x^*}{2}$, and $\frac{\Delta x^*}{3}$, where $\Delta x^*$ satisfies criteria 4.2. The procedure described in section 3.4.1 is applied to the beam displacement results from simulations with the parameter ranges in table 4.1 and for each refined $\Delta x^*$ value.

Figure 4.9 shows the real and imaginary parts of the least-damped eigenvalue for all $\hat{k}$ and $\Delta x^*$ grid values. The leading quasi-1D model eigenvalues are also shown for parameters in table 4.1. As the FSI DNS grid is refined, the DMD spectrum appears to be converging to the model eigenvalues: the real part of the DMD spectrum are monotonically moving toward the real part of the model eigenvalues; yet most notably, the imaginary part of the DMD spectrum is moving down for points where $\hat{k} < 3.6$ and up for $\hat{k} > 3.6$, approximating the quasi-1D curve shape.

To better understand the slow $\lambda$ convergence, we consider the beam thickness in light of the immersed boundary projection method. If the Eulerian mesh does not resolve the physical thickness of the beam, the immersed boundary produces an "effective" beam thickness that is proportional to $\Delta x^*$. This phenomenon is caused by the discrete kernel of the delta function (equation 3.3) being always positive, in additional to the unidirectional flow conditions on both sides of the beam (i.e. moving in the $+\hat{\mathbf{x}}$ direction). The IB projection method ensures that the no-slip condition is *exactly* enforced at each Lagrangian IB point. Once the discrete delta function smears it onto the flow, the Navier-Stokes equations are altered by the wall forcing for Eulerian points within the delta function kernel support. The flow outside its support, however, behaves as if the no-slip condition had been applied at the IB point locations. This effective thickness is not necessarily a physical quantity and cannot be systematically measured, but an upper bound for the effective thickness is the number of Eulerian support points of delta function kernel (6 for equation 3.3) and expected to vary with $\Delta x^*$. By refining $\Delta x^*$, we are also decreasing the beam's effective thickness, and slightly increasing the channel size. This effect would be more pronounced as $\hat{h}$ decreases, when the dynamics become a stronger function

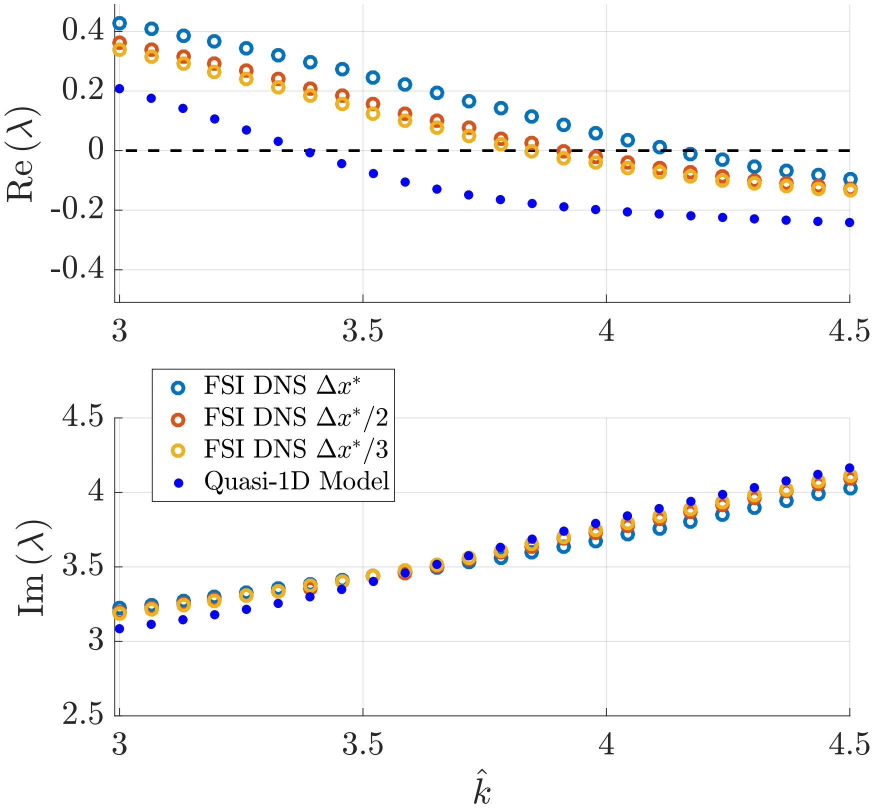

Figure 4.9: DMD spectrum and quasi-1D model eigenvalues in DNS grid refinement study.

of $\hat{h}$ [39, 41, 42, 76].

Running the full parametric study with the finest grid in figure 4.9 presents issues due to computational resource restrictions and time constraints[1]. These problems would be significantly amplified should the actual beam thickness need to be resolved by the Eulerian mesh.

---

[1] $\Delta x^*$ grid results require approximately 32 hours of wall-time computation, while $\frac{\Delta x^*}{3}$ grid requires approximately 13 days.

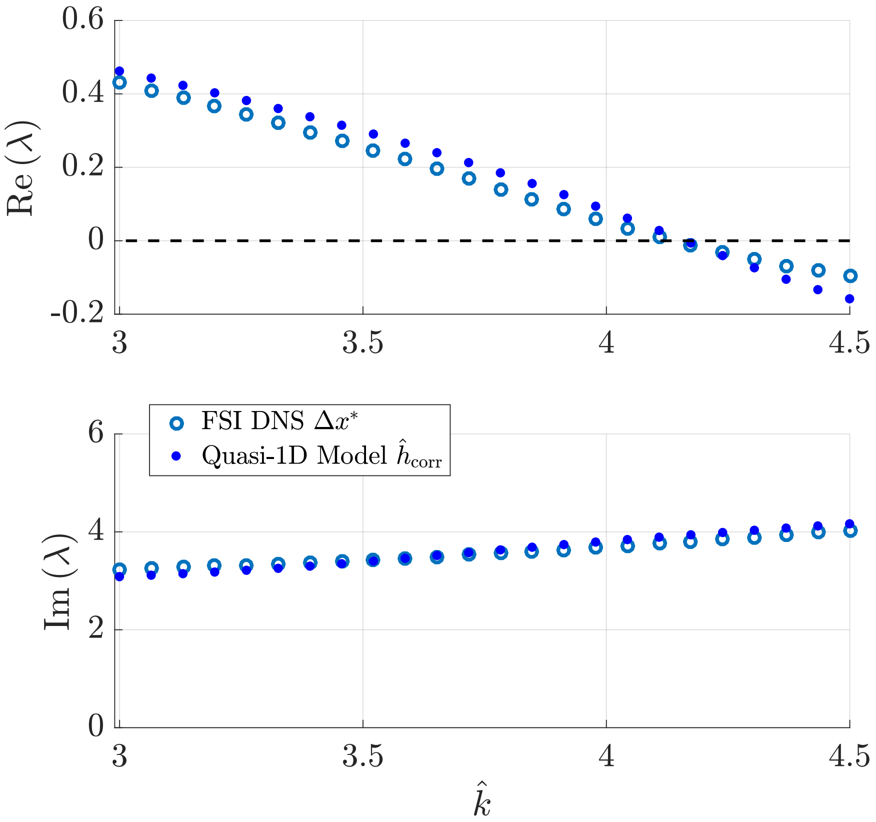

Figure 4.10: DMD spectrum and quasi-1D model eigenvalues for corrected channel width $\hat{h}$.

Hence, we explore instead altering the channel thickness within the quasi-1D model to understand whether the slight change in channel width could explain the slow convergence. Figure 4.10 shows the comparison of the DMD spectrum for $\Delta x^*$ and the quasi-1D model with a corrected channel width,

$$\hat{h}_{\text{corr}} = \hat{h} - 1.7\Delta x^*, \tag{4.5}$$

which gives an effective beam thickness slightly smaller than 3.5 Eulerian cells (or slightly larger than 1.5 Lagrangian cells). This result replicates the DMD spectrum extremely well, both in shape and in the instability boundary at $\hat{k}_{\text{cr}} = 4.17$; it also confirm the sensitivity of the dynamics to $\hat{h}$, and lends creditability to the plausibility of the convergence hypothesis. Hence, we apply the grid criteria 4.2 in subsequent results presented in section 4.2.4. We assume that the effective beam thickness is captured by equation 4.5 when comparing between FSI DNS DMD spetra and quasi-1D eigenvalues for all grids in this study.

### 4.2.4 Comparison of FSI DNS and Quasi-1D Model Results

The aim of this section is to understand non-dimensional parametric values where the quasi-1D model is a good approximation of the fluid-structure physics. Specifically, we choose our parameter set to assess the boundary of conditions described in section 2.2.1:

1. *Axial variations in channel gap are not large:* $h_0'^2 \ll 1$ *and* $\delta'^2 \ll 1$. This implies higher wave-numbers beam modes are not well captured. At a constant $\hat{h}$, higher modes are excited as $\hat{m}$ decreases. Here, we will restrict our analysis to $\hat{m} > 1$ and to the first two unstable modes of the beam.

2. *The characteristic length of the channel gap is small:* $\hat{h} \ll 1$. The analysis is restricted to $\hat{h} \leq 0.125$.

3. *Inertial effects associated with velocity profile are small:* $\hat{h}^2 Re_L \ll 1$. We will explore a wider margin of the viscous parameter and present detailed results up to $\hat{h}^2 Re_L < 10$, but focus on those around $\hat{h}^2 Re_L \sim 1$.

Similar to section 4.2.2, FSI DNS simulations are run for a set of parameters, with $\hat{k}$ as the bifurcation parameter in all simulations. For each parameter trio $\left[\hat{h},\ \hat{m},\ Re_L\right]$, we find the pair $\hat{k}_{\text{cr}}$ and $\text{Im}[\lambda]_{\text{cr}}$ as the critical values for the flutter boundary per equations 4.3 and 4.4.

We first explore the flutter boundary (i.e. $\hat{k}_{\text{cr}}$) at a constant $\hat{h}$ and $Re_L$ as $\hat{m}$. $Re_L$ values are chosen such that $\hat{h}^2 Re_L$ remains constant across the different $\hat{h}$ values tested. Table C.1 in appendix C shows the non-dimensional input parameter ranges and grid information for this first combination of FSI DNS simulations, along with $\Delta x^*$ and corresponding $\hat{h}_{\text{corr}}$ values used. Since the $\hat{k}$ values were adapted in order to find the flutter boundary for each parameter triplet, the table also shows the maximum $\Delta\hat{k}$, $\Delta\lambda_{\text{Re}}$, and $\Delta\lambda_{\text{Im}}$ across the instability boundary for all $\hat{m}$ values within the range specified. Table 4.2 is a summary of table C.1.

Convention in the literature [39, 41, 76] is to have solid-centric non-dimensional groups as opposed to the fluid-centric ones shown in table 2.3. A good reason for this representation is the clear observation of the mode switching behavior, as the non-dimensional frequency when scaled with structural parameters remain constant for each mode. We will follow this convention with our results, and introduce two new dimensionless groups as combinations of $\hat{m}$ and $\hat{k}$,

Table 4.2: Table of cases for constant channel flow simulations with varying $\hat{m}$ and $\hat{k}$.

| Case # | $\hat{h}$ | $\hat{h}^2 Re_L$ | $Re_L$ | $\hat{m}$ | $\hat{k}$ |
|---|---|---|---|---|---|
| 1 | 0.0250 | 0.5000 | 800 | [100 – 2] | [0.01 – 50] |
| 2 | 0.0500 | 0.5000 | 200 | [100 – 1] | [0.04 – 50] |
| 3 | 0.0500 | 1.2500 | 500 | [100 – 1] | [0.01 – 2.5] |
| 4 | 0.0500 | 2.5000 | 1000 | [100 – 1] | [0.01 – 2.5] |
| 5 | 0.1250 | 0.5000 | 32 | [100 – 1] | [0.0008 – 40] |
| 6 | 0.1250 | 1.2500 | 80 | [100 – 1] | [0.008 – 40] |

$$U^* = \sqrt{\frac{\hat{m}}{\hat{k}}} = \frac{t_s}{t_f}, \; M^* = \frac{1}{\hat{m}}. \tag{4.6}$$

$U^*$ represents the ratio of the solid time scale $t_s$ to that of the fluid $t_f$. In this space, $U^*$ is a proxy for $\hat{k}$ and $M^*$ for $\hat{m}$. The solid-centric frequency response can be calculated from the Strouhal number as

$$f_s^* = U^* St = f_s t_s, \tag{4.7}$$

where $St$ is defined in equation 4.1.

### Flutter Boundary as a Function of Mass and Confinement

Results in this section are given in the order of table 4.2. We present the (the stable-to-unstable) flutter boundary transversed by increasing $U^*_{\text{cr}}$, as well as the solid-centric frequency response $f^*_{s\text{cr}}$, as functions of $\hat{h}$ and $M^*$. Relevant representative mode shapes are also shown.

Figure 4.11 shows the narrowest channel at $\hat{h} = 0.025$. The quasi-1D model predicts the flutter boundary exceptionally well for the range of $M^*$ simulated. The corresponding beam mode shapes are given in figure 4.12, and these are qualitatively similar in both the DMD and quasi-1D results. We attribute small oscillations superimposed onto the primary mode shape to the DMD data matrix having components from the impulsive start and body force perturbation at $t = 0$. Mode switching is evident as $M^*$ increases from 0.01 to 0.3: not only is there an abrupt jump in $f^*_{s\text{cr}}$, but an additional effective node appears in both the real and imaginary parts of the modes shown. Specifically, figure 4.12 shows unstable mode shapes at two $M^*$ values: 0.01 and 0.3. The corresponding $U^*$ is shown at the top of each mode shape, and chosen as the second unstable discrete $U^*$ point from $U^*_{\text{cr}}$ for the FSI DNS DMD modes. The companion quasi-1D mode is shown for the closest quasi-1D discrete $U^*$ result available. Mode shapes are normalized by the magnitude of the largest component within each respective vector, so that the amplitudes plotted are independent of the underlying $x$ grid, and a qualitative comparison can be made more easily between shapes. This format is followed for subsequent mode shape figures in the cases that follow.

Modes at $M^* = 0.01$ in figure 4.12 resemble mostly a combination of the fundamental and second orthogonal beam modes in equations 2.79 and 2.80 (index $k = \{1, 2\}$), while modes at $M^* = 0.3$ bear a resemblance to the third orthogonal beam mode (index $k = \{1, 2, 3\}$).

Similar results for $U^*_{\text{cr}}$, $f^*_{s\text{cr}}$, and mode shapes are seen in figures 4.13 and 4.14, respectively, where the channel has been doubled in width to $\hat{h} = 0.05$ holding $\hat{h}^2 Re_L$ constant. In particular, we confirm that quasi-1D model replicates the flutter boundary well for all $M^*$ values simulated. Quasi-1D results show multiple boundaries at a single value of $M^*$. The second boundary point is at a given $M^*$ is representative of a second eigenvalue crossing the stability boundary in the stable-to unstable direction as $U^*$ increases. This is true for all flutter boundary plots shown that lack the injective mapping between $M^*$ and $U_{\text{cr}}$

Figures 4.15 and 4.16 show similar results for the case where $\hat{h}^2 Re_L$ is raised to 1.5, holding $\hat{h} = 0.05$ . The flutter boundary has moved to higher values of $U^*$, indicating stabilization with increasing $Re_L$. Quasi-1D and FSI DNS modes still mirror each other, but $M^* = 0.01$ and $M^* = 0.3$ are now primarily composed combinations of the fundamental and second orthogonal beam modes. This shift can be seen as the mode switching inflection point has moved higher in $M^*$ relative to cases 1 and 2.

A further increase $\hat{h}^2 Re_L = 2.5$ yields results in figures 4.17 and 4.18. The quasi-1D model marginally under-predicts the FSI DNS boundary in figure 4.17 (i.e quasi-1D model is less stable), with the bias increasing with $M^*$. Consequently, the mode switching $M^*$ point and higher mode boundary are under-predicted, yet $f^*_{s\text{cr}}$ remains in close agreement. The modes at $M^* = 0.01$ in figure 4.18 also show some disagreement, with the DMD results resembling orthogonal beam mode three more than the quasi-1D model.

Further increasing $\hat{h}$ causes an increasing discrepancy between the DNS and quasi-1D model prediction at higher $M^*$ values. Figure 4.19 shows the flutter boundary for $\hat{h}^2 Re_L = 0.5$, but with $\hat{h} = 0.125$. The model accurately predicts flutter properties for $M^* < 0.2$, but underestimates the higher mode boundary and critical frequencies for $M^* > 0.4$. This is also evident in the mode shapes in figure 4.20, as the $M^* = 0.01$ modes are in agreement, but the $M^* = 0.3$ modes are not. Holding constant $\hat{h} = 0.125$, but further increasing $\hat{h}^2 Re_L$ to 1.25 in case 6, figures 4.21 and 4.22, we also begin to see larger differences in the lower $M^*$ range. The quasi-1D model over-estimates the flutter boundary (i.e model is more stable) relative to the FSI DNS simulations for $M^* < 0.2$ but under-estimates it for $M^* > 0.4$, also missing the mode switching $M^*$ point. $f^*_{scr}$ values remain well predicted through all values of $M^*$, however, as long as the system is in the correct branch.

Thus, $\hat{h} \leq 0.05$ and $\hat{h}^2 Re_L \leq 0.5$, the results support the claims associated with the lubrication closure, and show that the quasi-1D model predicts critical flutter values well in this limit. This remains true even as condition 1 is violated as $M^*$ increases past mode switching. Results where $\hat{h}^2 Re_L = 0.5$ is kept constant and $\hat{h}$ increases from 0.025 to 0.125 illustrate that, indeed, as we violate condition 2, the quasi-1D boundary predictions worsen. Their results miss the mode switching $M^*$ along with the critical properties for $M^* \geq 0.4$. Yet even at $\hat{h} = 0.125$, critical values for $M^* < 0.2$ remain well approximated by the model. This indicates that as long as condition 1 holds, and only the lowest mode is considered, the model remains accurate. Cases where we hold $\hat{h} = 0.05$ constant and increase $\hat{h}^2 Re_L$ from 0.5 to 2.5 ($Re_L$ from 200 to 1000), show that condition 3 does not restrict the quasi-1D model to $\hat{h}^2 Re_L \ll 1$ for accurate predictions. This is true as condition 1 is violated with increasing $M^*$ through mode switching. However, considering case 6, we see the $\hat{h}$ effect as we violate 2. In summary, condition 2 appears to be the strongest restriction: as long as $\hat{h}$ remains small (i.e. $\hat{h} \leq 0.05$), the quasi-1D model predicts the flutter boundary for a wide range of $M^*$.

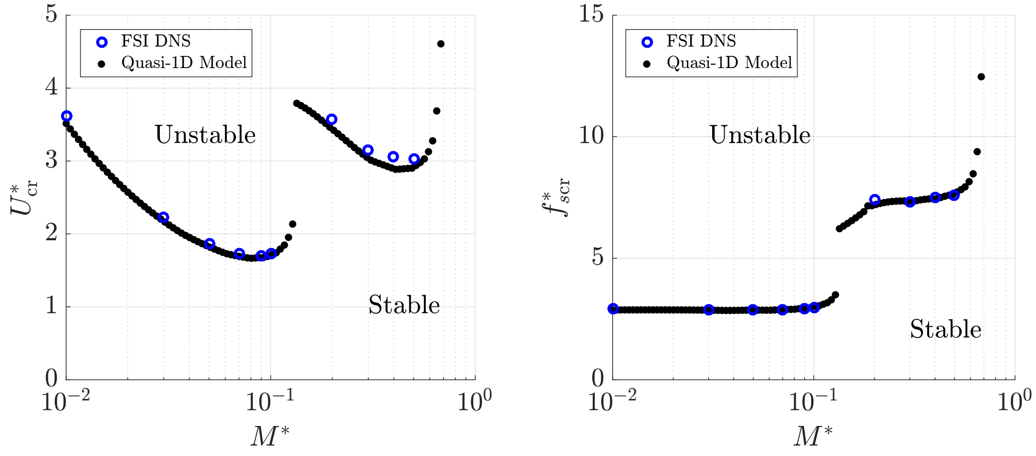

(a) $U^*_{\rm cr}$ as a function of $M^*$.   (b) $f^*_{scr}$ as a function of $M^*$.

Figure 4.11: Comparison of FSI DNS and quasi-1D model flutter boundary critical values at $\hat{h} = 0.025$ and $\hat{h}^2 Re_L = 0.5$, case 1 in table 4.2.

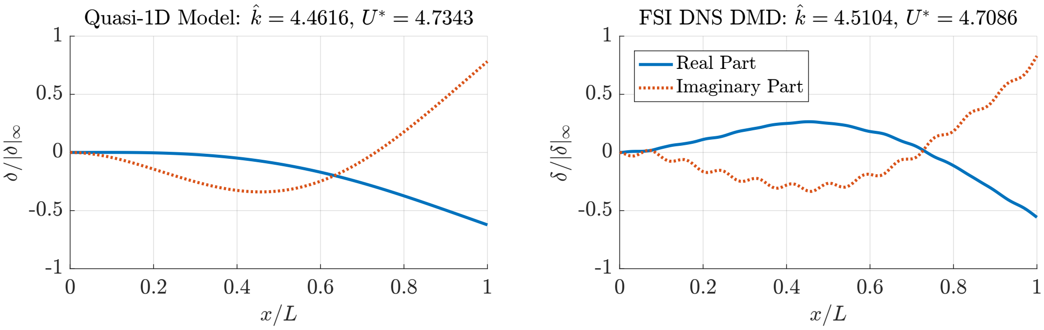

(a) $M^* = 0.01$.

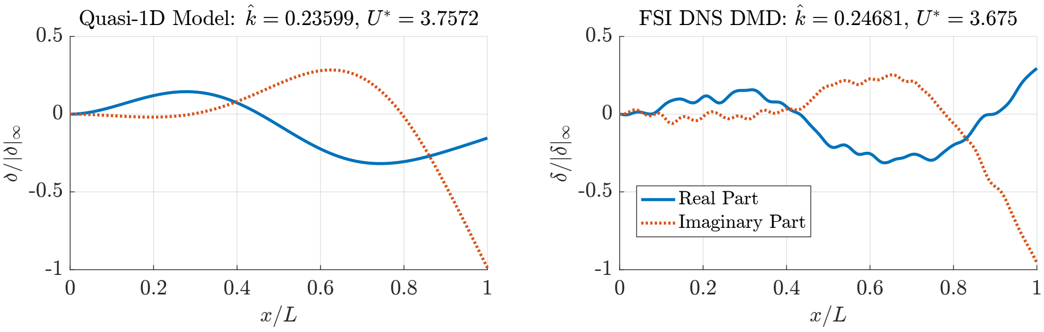

(b) $M^* = 0.3$.

Figure 4.12: Comparison of real and imaginary parts of unstable mode near flutter boundary from quasi-1D model (left) and FSI DNS (right) at $\hat{h} = 0.025$ and $\hat{h}^2 Re_L = 0.5$ (case 1 in table 4.2).

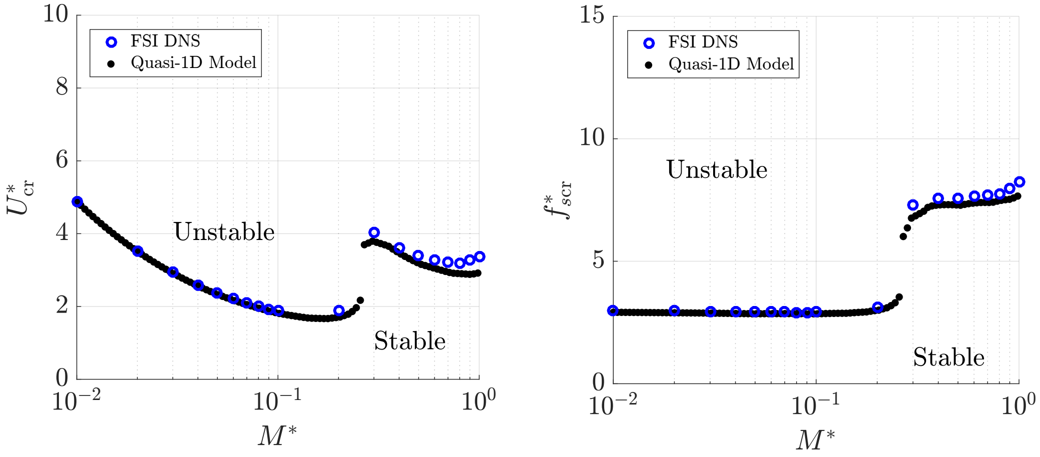

(a) $U^*_{\mathrm{cr}}$ as a function of $M^*$.

(b) $f^*_{scr}$ as a function of $M^*$.

Figure 4.13: Comparison of FSI DNS and quasi-1D model flutter boundary critical values at $\hat{h} = 0.05$ and $\hat{h}^2 Re_L = 0.5$, case 2 in table 4.2.

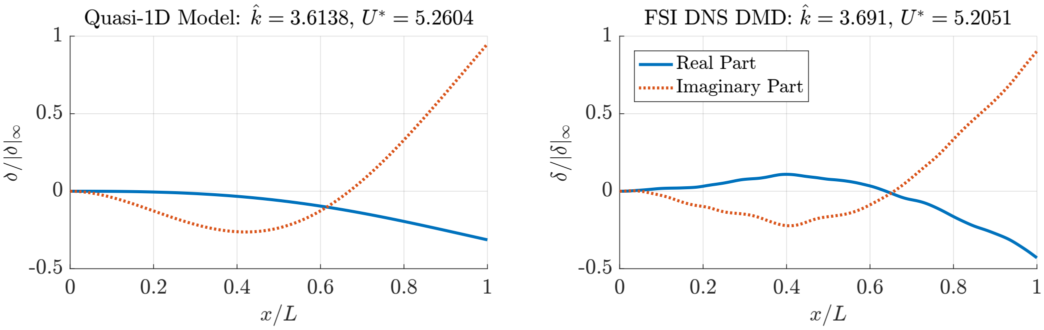

(a) $M^* = 0.01$.

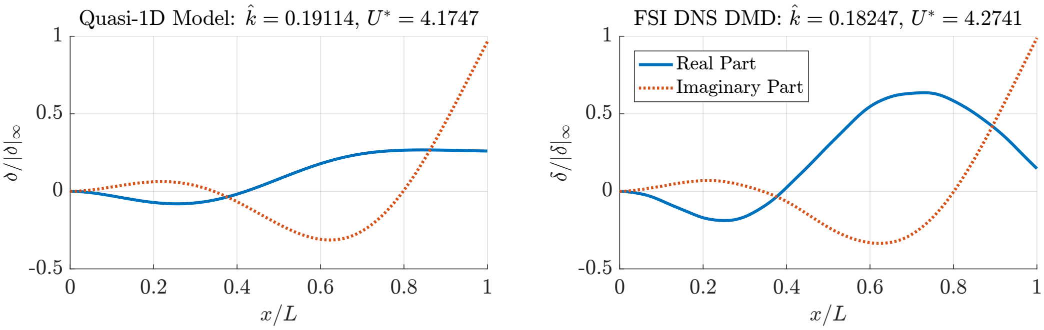

(b) $M^* = 0.3$.

Figure 4.14: Comparison of real and imaginary parts of unstable mode near flutter boundary from quasi-1D model (left) and FSI DNS (right) at $\hat{h} = 0.05$ and $\hat{h}^2 Re_L = 0.5$ (case 2 in table 4.2).

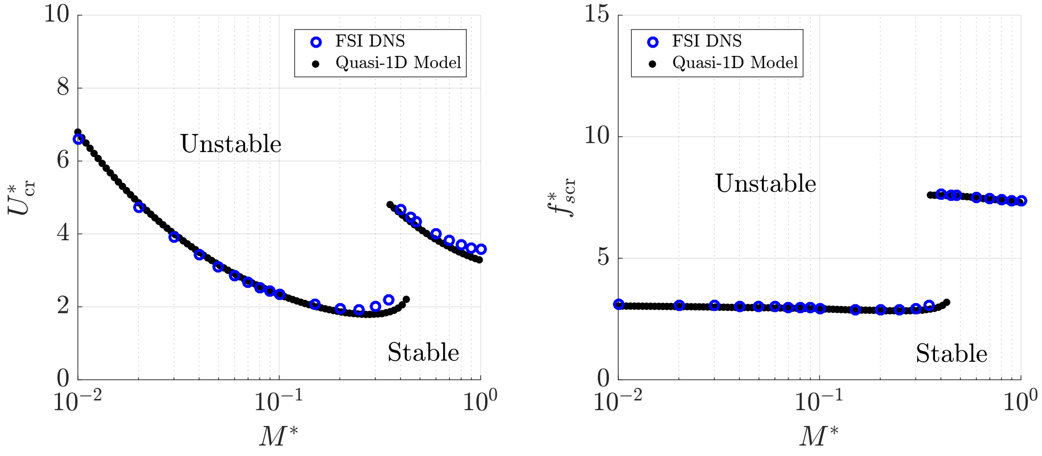

(a) $U^*_{\mathrm{cr}}$ as a function of $M^*$.

(b) $f^*_{scr}$ as a function of $M^*$.

Figure 4.15: Comparison of FSI DNS and quasi-1D model flutter boundary critical values at $\hat{h} = 0.05$ and $\hat{h}^2 Re_L = 1.25$, case 3 in table 4.2.

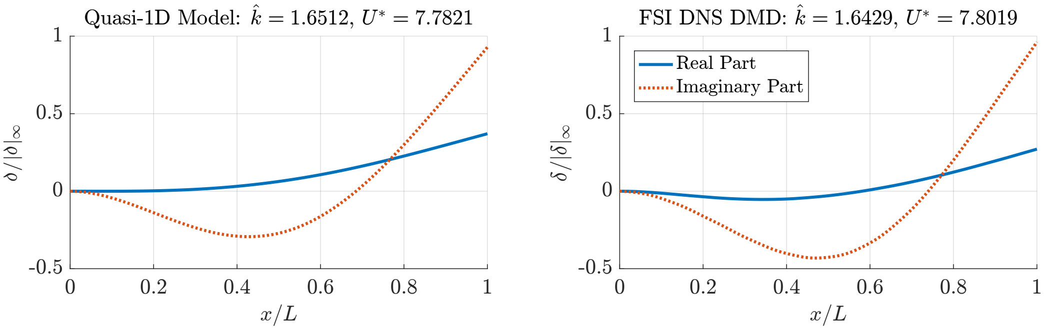

(a) $M^* = 0.01$.

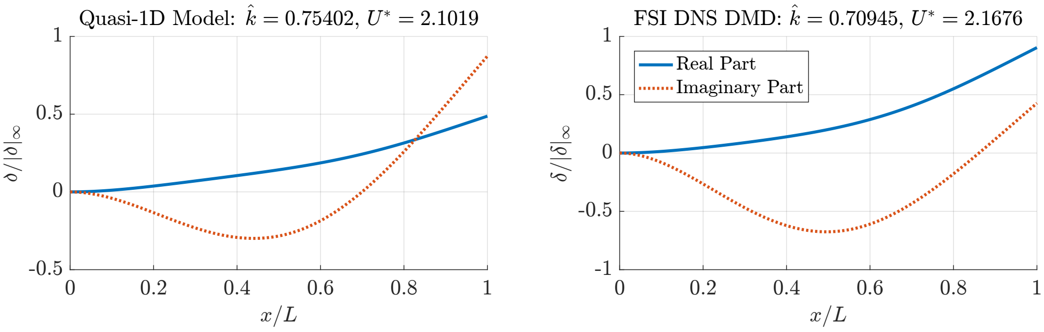

(b) $M^* = 0.3$.

Figure 4.16: Comparison of real and imaginary parts of unstable mode near flutter boundary from quasi-1D model (left) and FSI DNS (right) at $\hat{h} = 0.05$ and $\hat{h}^2 Re_L = 1.25$ (case 3 in table 4.2).

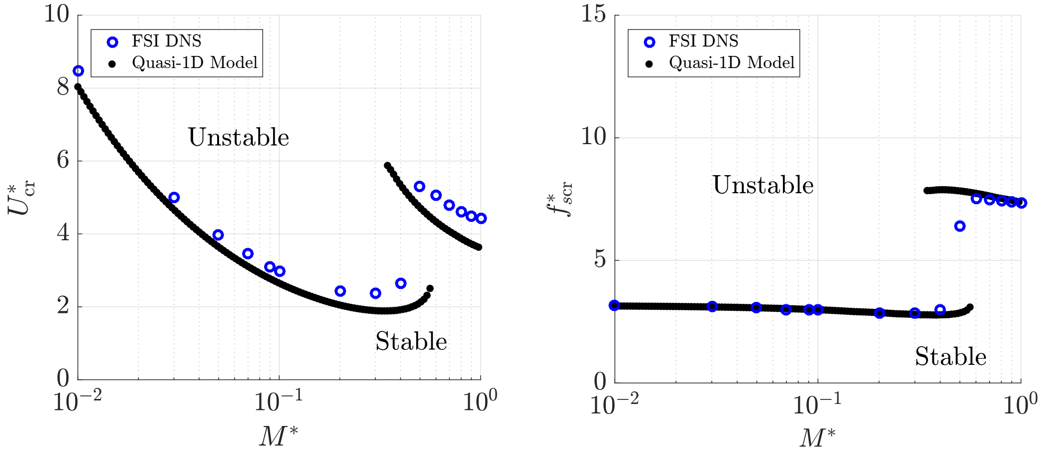

(a) $U^*_{\mathrm{cr}}$ as a function of $M^*$.

(b) $f^*_{scr}$ as a function of $M^*$.

Figure 4.17: Comparison of FSI DNS and quasi-1D model flutter boundary critical values at $\hat{h} = 0.05$ and $\hat{h}^2 Re_L = 2.5$, case 4 in table 4.2.

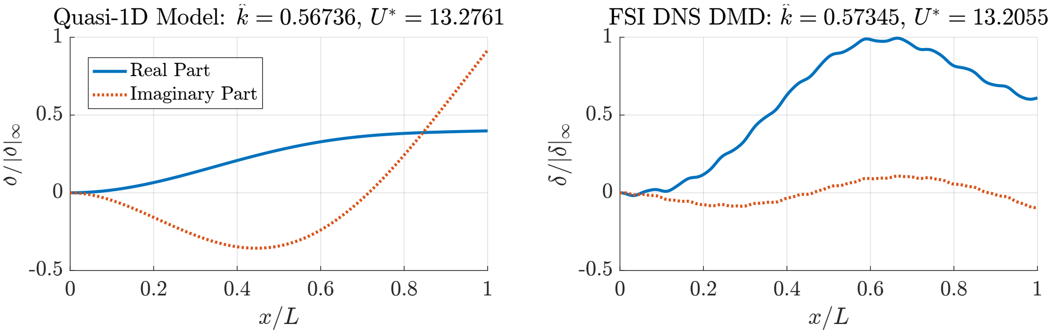

(a) $M^* = 0.01$.

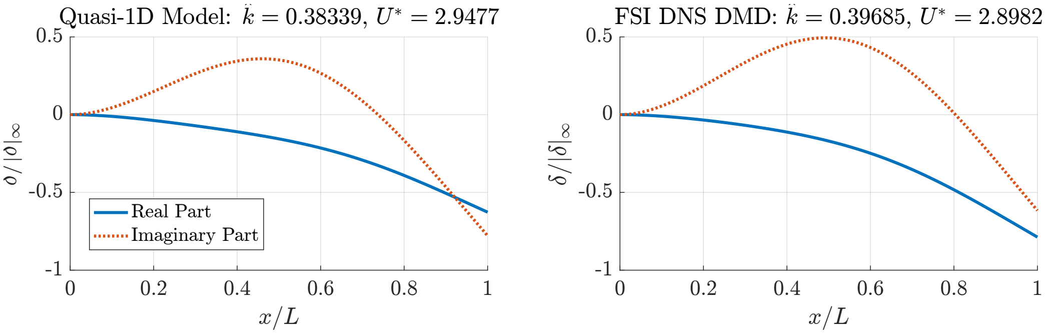

(b) $M^* = 0.3$.

Figure 4.18: Comparison of real and imaginary parts of unstable mode near flutter boundary from quasi-1D model (left) and FSI DNS (right) at $\hat{h} = 0.05$ and $\hat{h}^2 Re_L = 2.5$ (case 4 in table 4.2).

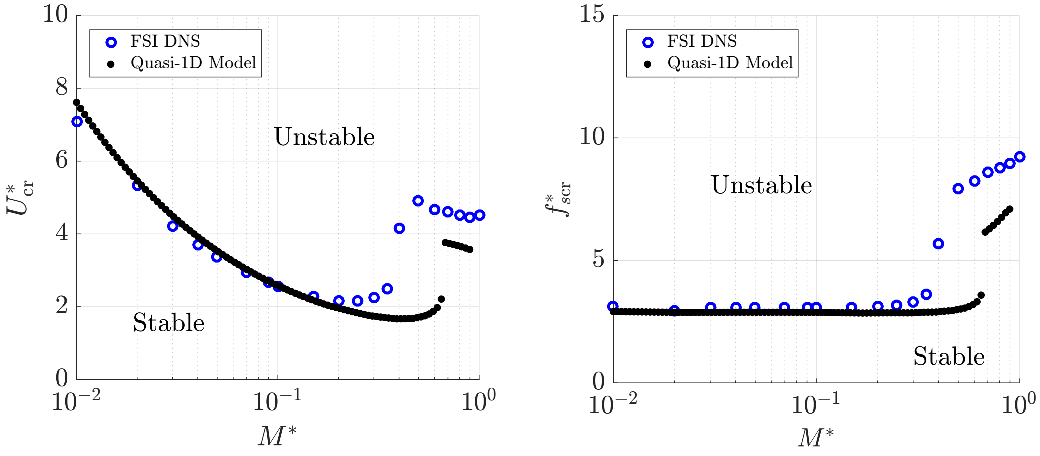

(a) $U^*_{\mathrm{cr}}$ as a function of $M^*$.

(b) $f^*_{scr}$ as a function of $M^*$.

Figure 4.19: Comparison of FSI DNS and quasi-1D model flutter boundary critical values at $\hat{h} = 0.125$ and $\hat{h}^2 Re_L = 0.5$, case 5 in table 4.2.

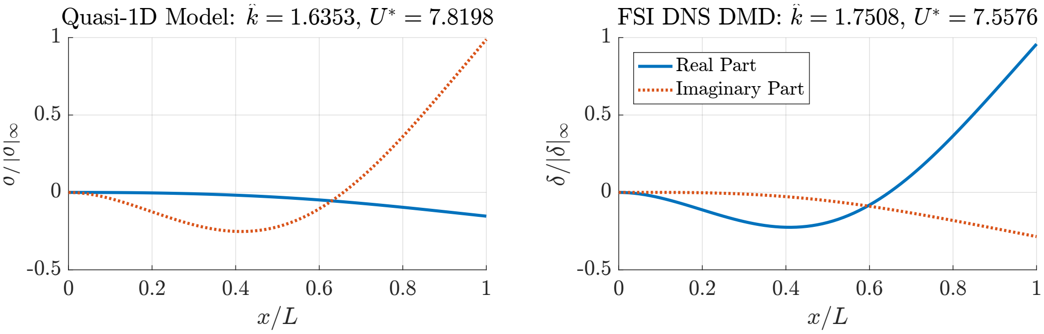

(a) $M^* = 0.01$.

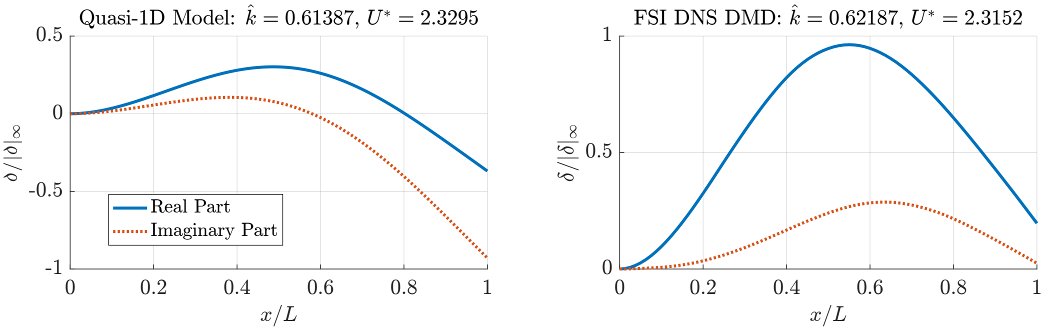

(b) $M^* = 0.3$.

Figure 4.20: Comparison of real and imaginary parts of unstable mode near flutter boundary from quasi-1D model (left) and FSI DNS (right) at $\hat{h} = 0.125$ and $\hat{h}^2 Re_L = 0.5$ (case 5 in table 4.2).

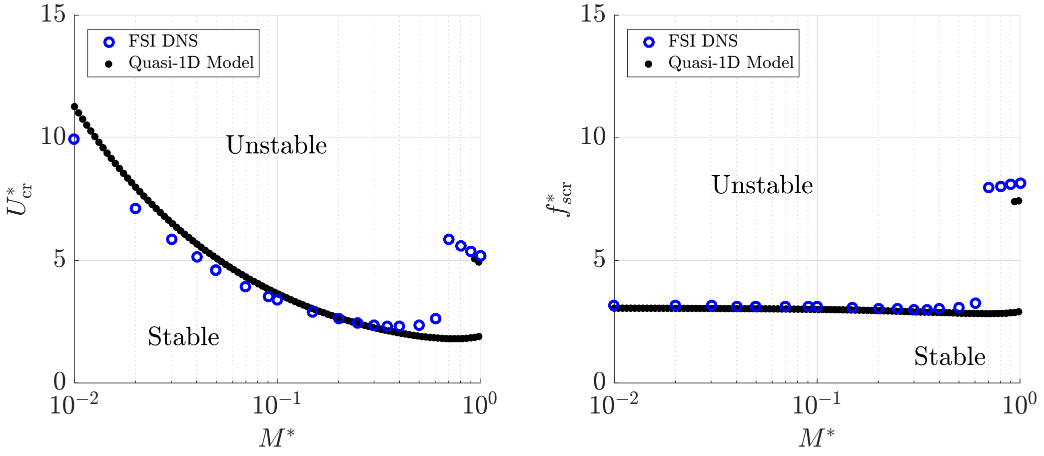

(a) $U^*_{\mathrm{cr}}$ as a function of $M^*$.

(b) $f^*_{scr}$ as a function of $M^*$.

Figure 4.21: Comparison of FSI DNS and quasi-1D model flutter boundary critical values at $\hat{h} = 0.125$ and $\hat{h}^2 Re_L = 1.25$, case 6 in table 4.2.

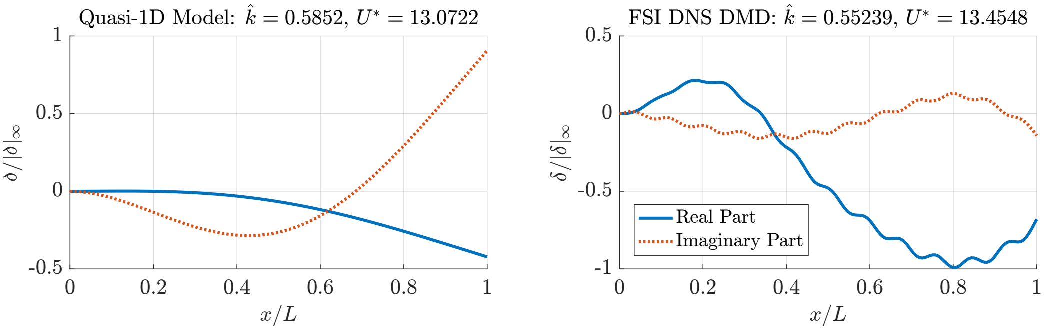

(a) $M^* = 0.01$.

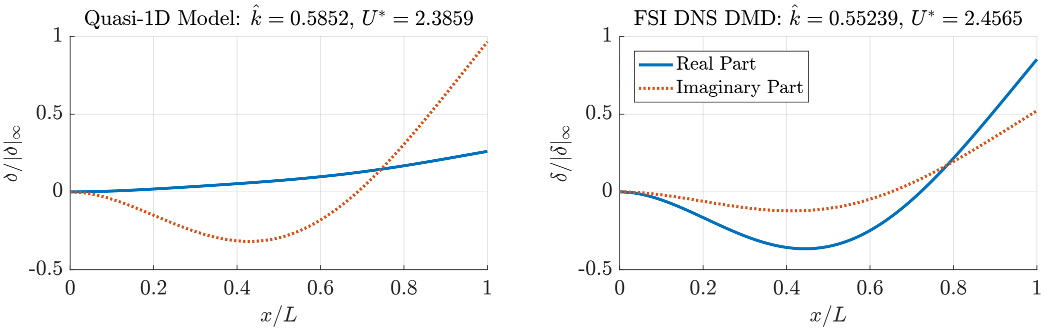

(b) $M^* = 0.3$.

Figure 4.22: Comparison of real and imaginary parts of unstable mode near flutter boundary from quasi-1D model (left) and FSI DNS (right) at $\hat{h} = 0.125$ and $\hat{h}^2 Re_L = 1.25$ (case 6 in table 4.2).

### Flutter Boundary as a Function of Viscosity and Confinement

Here we restrict fluid-to-structure mass ratio $M^* = 0.01$, and explore the robustness of the quasi-1D model predictions when only the lowest mode is considered. Condition 1 is automatically satisfied, and we plot $U^*_{\text{cr}}$ and $f^*_{s\text{cr}}$ with $\hat{h}^2 Re_L$ as the bifurcation parameter for several values of $\hat{h}$ in order to understand the model accuracy when varying conditions 2 and 3, respectively. Table 4.3 summarizes the parameter space, with further details in each entry given in table C.2 in appendix C.

Table 4.3: Table of cases for constant channel flow simulations with varying $\hat{h}^2 Re_L$ and $\hat{k}$.

| Case # | $\hat{h}$ | $\hat{h}^2 Re_L$ | $\hat{k}$ |
|---|---|---|---|
| 1 | 0.05 | [0.1-4.5] | [0.01 – 80] |
| 2 | 0.125 | [0.1-9.5] | [0.01 – 50] |

In case 1, $\hat{h} = 0.05$ and $\hat{h}^2 Re_L$ ranges from 0.1 to 4.5, with an equivalent $Re_L = 1800$ at the upper limit. The flutter boundary is shown in figure 4.23 with $U^*_{\text{cr}}$ and the frequency response in $f^*_{s\text{cr}}$ of the quasi-1D model closely replicating results from FSI DNS. A deviation appears in $U^*_{\text{cr}}$ when $\hat{h}^2 Re_L \approx 3$, but $f_{s\text{cr}}$ is steadfast. Representative modes are shown in figure 4.24 at $\hat{h}^2 Re_L = 3$ and agree well with one another. In case 2, $\hat{h} = 0.125$ and $\hat{h}^2 Re_L$ ranges from 0.1 to 9.5, with an equivalent $Re_L = 608$ at the upper limit. Critical values at the flutter boundary are shown in figure 4.25. Similar to case 1, quasi-1D results agree reasonably well over the range of $\hat{h}^2 Re_L$, with a slight deviation near $\hat{h}^2 Re_L = 2$. Most notable, however, is the agreement at $\hat{h}^2 Re_L > 5$, as both results appear to asymptote to a line $U^*_{\text{cr}} \sim \left(\hat{h}^2 Re_L\right)^{1/2}$. Modes are shown in figure 4.26, with FSI DNS mode having more resemblance to the third orthogonal beam mode than the quasi-1D mode.

In summary, results show that the quasi-1D model is able to predict critical values at the flutter boundary reasonably well for $\hat{h} \leq 0.125$ and $\hat{h}^2 Re_L \leq 10$ for $M^* = 0.01$, corresponding to a “heavy” beam. The results at $\hat{h}^2 Re_L \gg 1$ are particularly surprising given the use of condition 3 in the quasi-1D lubrication closure relation. Recall, however, that this bound appears to only hold in the limit where $M^* \ll 1$.

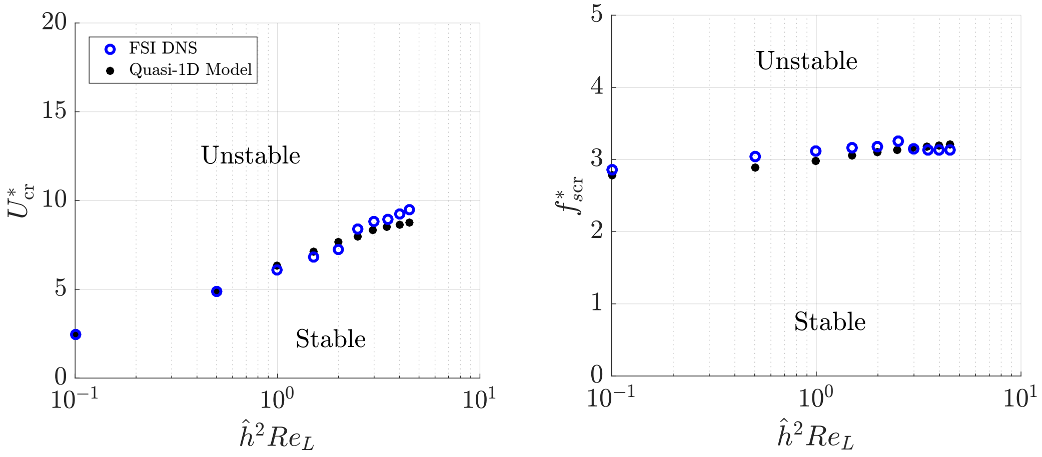

(a) $U^*_{\rm cr}$ as a function of $\hat{h}^2 Re_L$.

(b) $f^*_{scr}$ as a function of $\hat{h}^2 Re_L$.

Figure 4.23: Comparison of FSI DNS and quasi-1D model flutter boundary critical values at $\hat{h} = 0.05$ and $M^* = 0.01$, case 1 in table 4.3.

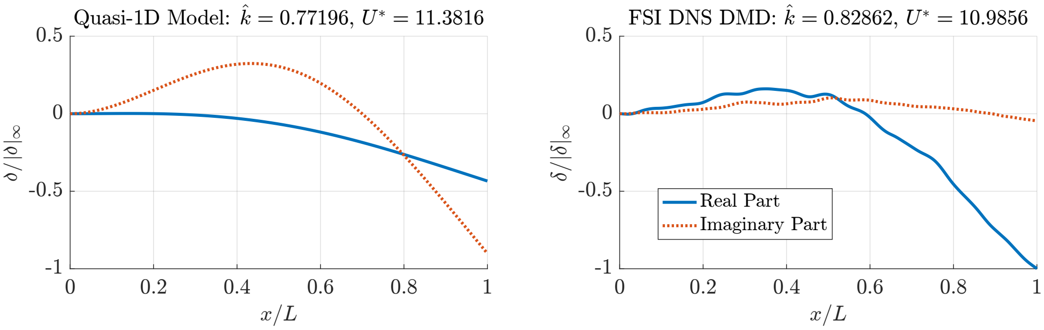

Figure 4.24: Comparison of real and imaginary parts of unstable mode near flutter boundary from quasi-1D model (left) and FSI DNS (right) at $\hat{h} = 0.05$, $M^* = 0.01$, and $\hat{h}^2 Re_L = 3$ (case 1 in table 4.3).

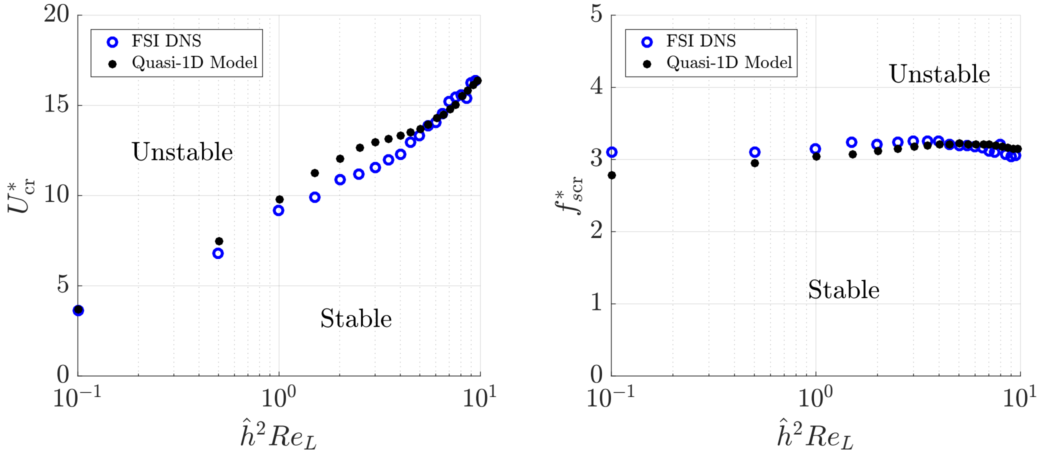

(a) $U^*_{\mathrm{cr}}$ as a function of $\hat{h}^2 Re_L$.

(b) $f^*_{scr}$ as a function of $\hat{h}^2 Re_L$.

Figure 4.25: Comparison of FSI DNS and quasi-1D model flutter boundary critical values at $\hat{h} = 0.125$ and $M^* = 0.01$, case 2 in table 4.3.

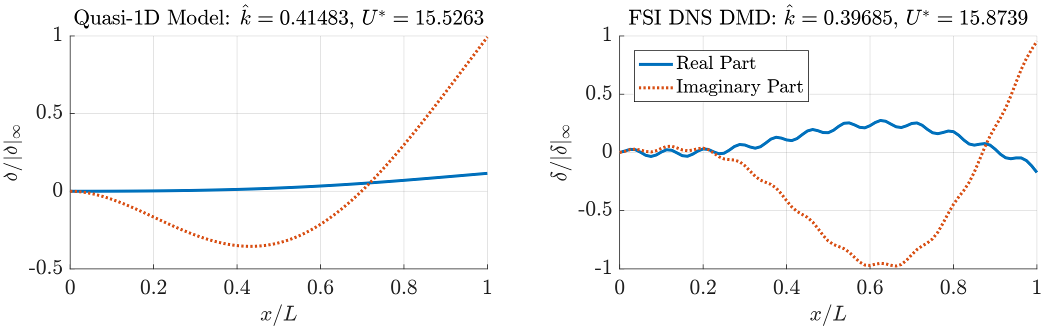

Figure 4.26: Comparison of real and imaginary parts of unstable mode near flutter boundary from quasi-1D model (left) and FSI DNS (right) at $\hat{h} = 0.125$, $M^* = 0.01$, and $\hat{h}^2 Re_L = 3$. (case 2 in table 4.3).

### 4.2.5 Quasi-1D Flutter Boundary Comparison to Inviscid Model

Given results from section 4.2.4, the ability of the quasi-1D model to predict the flutter stability behavior even when $\hat{h}^2 Re_L$ is not small appears promising. We would like to compare quasi-1D predictions in cases where $\hat{h}^2 Re_L \gg 1$ while $\hat{h} \ll 1$ to an inviscid flow solution. Shoele and Mittal [39] derive such an inviscid model for channel flow and explore the flutter stability boundary as a function of $\hat{h}$. $\hat{h} = 0.05$ is the lowest parameter value of $\hat{h}$ they provide. Thus, taking the case for $\hat{h} = 0.05$ and $\hat{h}^2 Re_L = 1.25$ as the starting point, we compare $U^*_{\mathrm{cr}}$ as a function of $M^*$ for $\hat{h}^2 Re_L = [1.25 - 50]$ ($Re_L = [500 - 2 \times 10^4]$) for the lowest frequency mode branch. Results are shown in figure 4.27. Notable trends appear as the viscous term is increased: first, as $\hat{h}^2 Re_L$ increases from 1.25 to 2.50, the system is stabilized as the stability boundary shifts upwards. Yet as $\hat{h}^2 Re_L$ is further increased to 12.50 and thereafter the system is destabilized for $M^* > 0.03$, with the boundary eventually disappearing for $0.03 < M^* < 0.2$ at $\hat{h}^2 Re_L = 50$. This means that no matter the stiffness of the system, the first mode is unstable if the beam is heavy enough. The original stabilization trend for increasing $\hat{h}^2 Re_L$ remains true, however, for $M^* < 0.03$. Furthermore, as $\hat{h}^2 Re_L$ becomes large, the quasi-1D flutter boundary appears to near the inviscid results acquired from [39], with the mode switching inflection nearly matching over all $\hat{h}^2 Re_L$ boundaries shown.

Shoele and Mittal [39] conjectured based on earlier DNS studies [76] that $Re_L \approx 200$ was enough to consider the system inviscid at least over the $\hat{h}$ values in their study. Though this may be true for $\hat{h} > 0.125$, the inviscid behavior boundary for $\hat{h} = 0.05$ appears to be $Re_L \approx 2 \times 10^4$ from figure 4.27. Predictions of the quasi-1D model indicate that the choice of $Re_L$ for inviscid treatment is a strong function of $\hat{h}$.

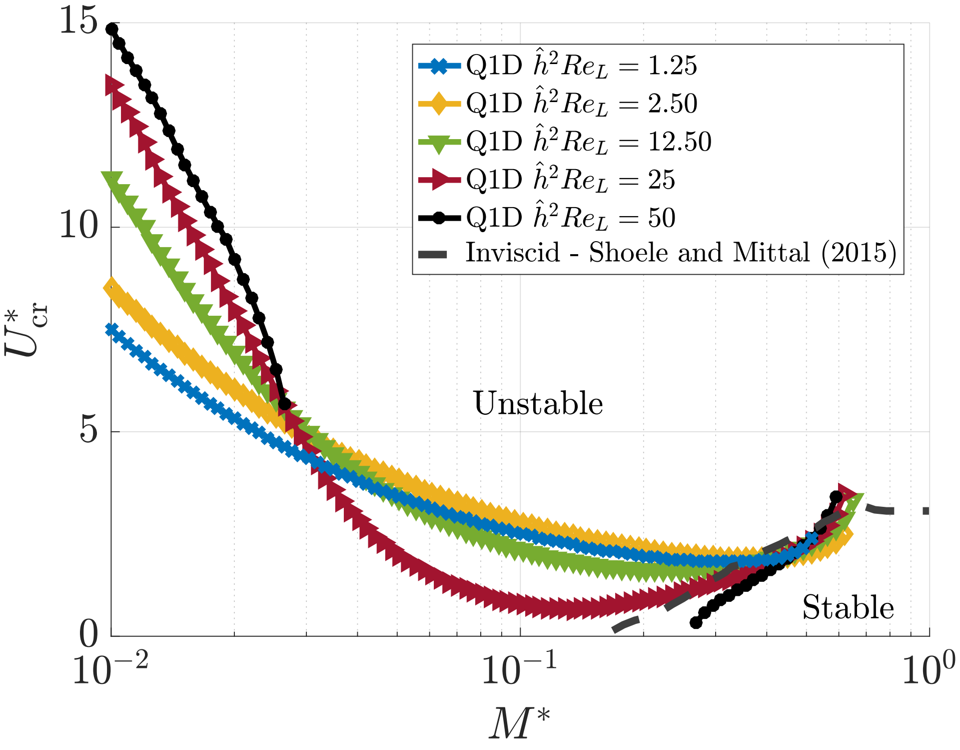

Figure 4.27: Comparison of flutter boundary for lowest frequency mode between different quasi-1D model (Q1D) $\hat{h}^2 Re_L$ values and inviscid model by Shoele and Mittal [39] at $\hat{h} = 0.05$.

In light of these results and those in section 4.2.4, we utilize the quasi-1D model to produce the complete flutter boundary for $M^* = 0.01$ in figure 4.28 and $M^* = 0.1$ in figure 4.29. Both figures only show the flutter boundary for the lowest frequency mode branch. Three trends become apparent from these plots: first, as $M^*$ increases, the lowest frequency mode is destabilized significantly; as $\hat{h}^2 Re_L$ increases, the mode is stabilized. This stabilization is accelerated at higher $\hat{h}$, for values for $\hat{h}^2 Re_L < 10$. Figure 4.27 shows that opposite is true as $\hat{h}^2 Re_L$ is increased further. Lastly, as $\hat{h}$ increases, the lower mode is stabilized.

Though $f^*_{scr}$ remains within a narrow range for the lowest frequency mode, an interesting pattern arises as $\hat{h}^2 Re_L$ and $\hat{h}$ are varied. Bands of lower frequency appear alternating with higher frequency states in both $M^*$ values. This indicates that these parameters have an effect on the frequency response, but it is much less pronounced than their effects on the stability boundary as judged by $U^*_{\text{cr}}$.

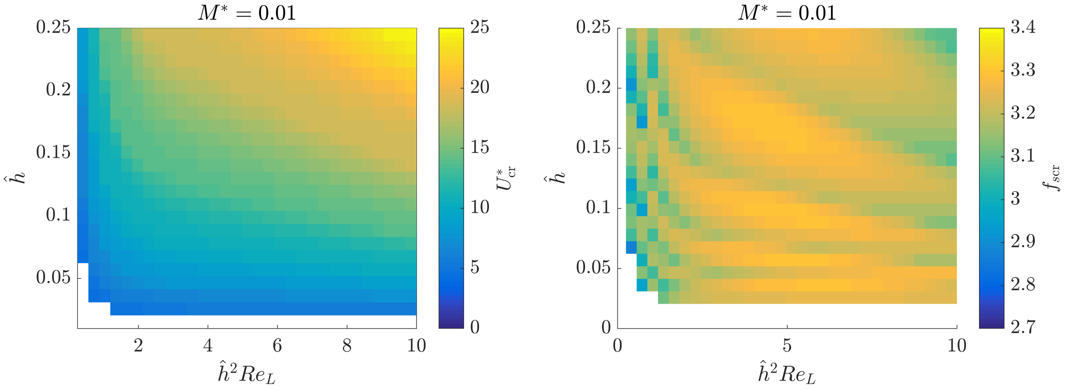

(a) $U^*_{\text{cr}}$ contours vs. $\hat{h}^2 Re_L$ and $\hat{h}$.

(b) $f^*_{scr}$ contours vs. $\hat{h}^2 Re_L$ and $\hat{h}$.

Figure 4.28: Quasi-1D predicted critical flutter values as a function of $\hat{h}^2 Re_L$ and $\hat{h}$ at $M^* = 0.01$.

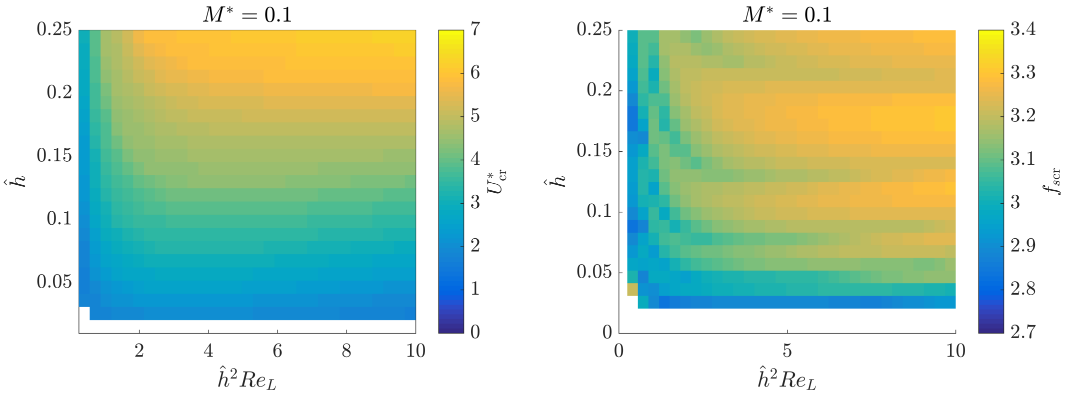

(a) $U^*_{\rm cr}$ contours as a function of $\hat{h}^2 Re_L$ and $\hat{h}$.

(b) $f^*_{\rm scr}$ contours as a function of $\hat{h}^2 Re_L$ and $\hat{h}$.

Figure 4.29: Quasi-1D predicted critical flutter values as a function of $\hat{h}^2 Re_L$ and $\hat{h}$ at $M^* = 0.1$.

### 4.2.6 Elastic-Translating Boundary Condition in a Constant Channel

We now consider the elastic-translating boundary condition defined in section 2.3.3 for the quasi-1D model, and in section 3.3.2 for the FSI DNS. The problem geometry is shown in figure 4.30, with its leading edge boundary condition specified as a simple harmonic oscillator, via non-dimensional parameters $\hat{m}_{\rm bc}$, $\hat{c}_{\rm bc}$, and $\hat{k}_{\rm bc}$ defined in table 2.4.

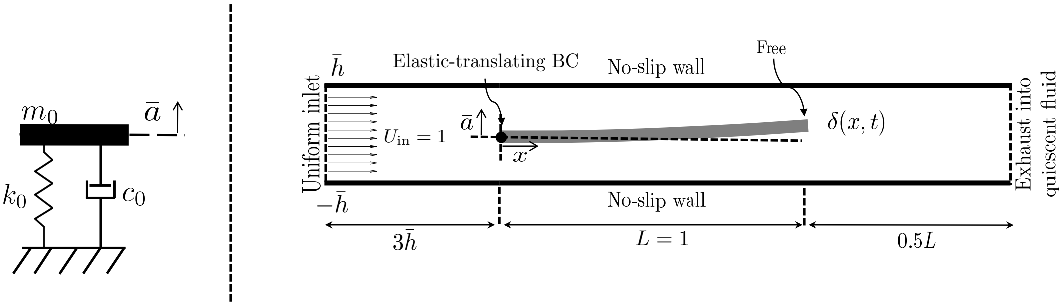

Figure 4.30: Illustration of linear diffuser flow geometry for cantilevered beam (top), and elastically-mounted rigid beam (bottom).

We will, once again, explore agreement between the model and FSI DNS simulations that map the stability boundary in $\hat{k}$ space. Our results are plotted in the convention of $U^*$, as before, defined in equation 4.6. Given results from section 4.2.4, we restrict $M^* = 0.02$, $\hat{h} = 0.125$, $\hat{h}^2 Re_L = 0.5$ as the beam parameters that critical properties are well captured by the clamped-free quasi-1D model, but at the "boundary" of criterion 3, where $\hat{h} \ll 1$ criterion.

Since the clamped-free boundary condition is the limiting case where the boundary stiffness, $\hat{k}_{\text{bc}} \to \infty$, we choose $\hat{k}_{\text{bc}} = 0.01$ to probe the dynamics in the opposite limit of low flexure stiffness. Once again, $\hat{k}$ is the bifurcation parameter, and the $\hat{k}_{\text{cr}}$ (or $U^*_{\text{cr}}$) is mapped as a function of $\hat{m}_{\text{bc}}$ as defined in table 2.4. The structural damping parameter $\hat{c}_{\text{bc}} = 0$ for all cases. Table 4.4 shows the case run in this section, with $\hat{m}_{\text{bc}}$ and $\hat{k}$ parameter ranges shown. Parameter and spatial grid details for can be found in table C.3 in appendix C.

Table 4.4: Table of cases for constant channel flow simulations with elastic-translating boundary conditions. Parameters $\hat{m}_{\text{bc}}$ and $\hat{k}$ are varied.

| Case # | $\hat{h}^2 Re_L$ | $Re_L$ | $\hat{m}$ | $\hat{h}$ | $\hat{k}_{\text{bc}}$ | $\hat{m}_{\text{bc}}$ | $\hat{k}$ |
|---|---|---|---|---|---|---|---|
| 1 | 0.5 | 32 | 50 | 0.125 | 0.1 | [ 7 - 1800] | [ 0.42 - 41.67 ] |

Figure 4.31 shows the critical values for cases in table 4.4. The stability boundary in $U^*$ agrees well between the FSI DNS and quasi-1D model. In particular, the mode branching that occurs as $\hat{m}_{\text{bc}}$ decreases appears to be well captured. Similarly, the critical frequency trend is replicated, though with a slight under prediction by the model. A representative mode is shown in figure 4.32 for $\hat{m}_{\text{bc}} = 100$, also showing good qualitative agreement between model and DNS DMD results.

By spanning 3 orders of magnitude in $\hat{m}_{\text{bc}}$ with a low boundary stiffness value ($\hat{k}_{\text{bc}} = 0.01$), results from figure 4.31 indicate that the model also provides a good approximation of the dynamics when the elastic-translating boundary condition is introduced into the system.

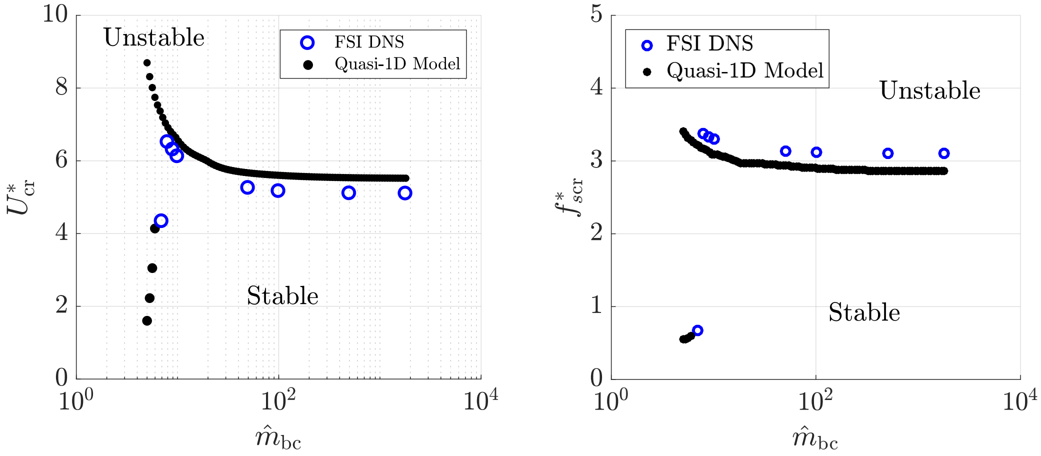

(a) $U^*_{\text{cr}}$ as a function of $\hat{m}_{\text{bc}}$.

(b) $f^*_{scr}$ as a function of $\hat{m}_{\text{bc}}$.

Figure 4.31: Comparison of FSI DNS and quasi-1D model flutter boundary critical values at $\hat{h} = 0.125$, $M^* = 0.02$, and $\hat{h}^2 Re_L = 0.5$ for all cases in table 4.4.

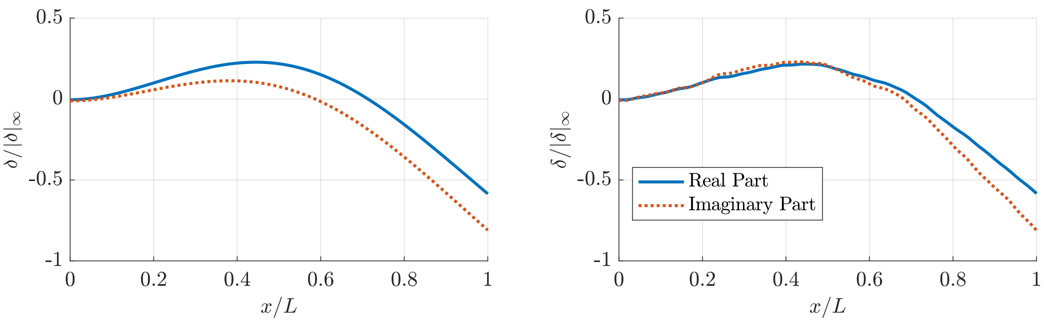

Figure 4.32: Comparison of quasi-1D model (left) and FSI DNS (right) normalized unstable mode shapes at $\hat{h} = 0.125$, $M^* = 0.02$, $\hat{m}_{\text{bc}} = 100$.

## 4.3 Diffusing Channel Flows

Constant channel flow results have shown that the quasi-1D model is able to predict critical properties for the flutter instability over a wide range of parameters. The model was also successful in predicting the stability boundary for the system with a translating leading edge.

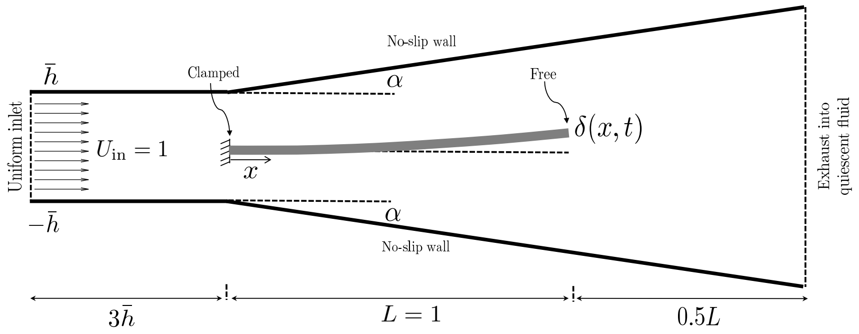

(a) Cantilevered beam.

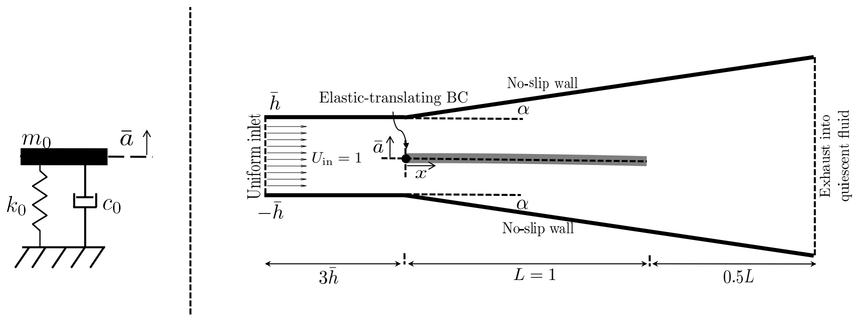

(b) Rigid beam.

Figure 4.33: Illustration of linear diffuser flow geometry for cantilevered beam (bottom), and elastically-mounted rigid beam (top).

We would like to broaden parameter set once again to include diffuser geometries.

In particular, we would like to assess the flutter boundary as angle $\alpha$ is increased from the constant channel cases ($\alpha = 0°$). Figure 4.33 illustrates a symmetric diffuser with both a cantilevered and an elastically mounted rigid beam at its center. As before, the translating boundary condition is constrained to up and down motion as a simple harmonic oscillator. Because of the large parameter space, we consider both geometries separately when comparing FSI DNS results to quasi-1D model predictions. We further restrict the cantilever to $M^* = 0.02$ and the rigid body to a low stiffness case $\hat{k}_{\mathrm{bc}} = 0.1$, as done previously.

### 4.3.1 Cantilever in Diffusing Channel

We begin with the cantilever within a diffusing channel configuration. As mentioned, we restrain cases to heavy beams, with $M^* = 0.02$ ($\hat{m} = 50$), and consider two parameter sets, both of which assess the bifurcation parameter $\hat{k}$ as function of diffuser angle $\alpha$. Table 4.5 shows a summary of cases and parameters, with table C.5 in appendix C containing simulation mesh and flutter boundary interpolation details. The upper bound of $\alpha = 6°$ ($h_0' = \tan 6° \sim 0.1$) is chosen to ensure that both condition $h_0'^2 \ll 1$ is satisfied, along with ensuring that the flow remains attached to the walls of the channels.

Table 4.5: Table of cases for cantilever beam in a diffuser. Parameters $\alpha[°]$ and $\hat{k}$ are varied.

| Case # | $Re_L$ | $\hat{h}^2 Re_L$ | $\hat{m}$ | $\hat{h}$ | $\alpha[°]$ | $\hat{k}$ |
|---|---|---|---|---|---|---|
| 1 | 200 | 0.5 | 50 | 0.05 | [ 1 - 6 ] | [ 50 - 0.1 ] |
| 2 | 400 | 6.25 | 50 | 0.125 | [ 1 - 6 ] | [ 0.83 - 0.042 ] |

Representative FSI DNS flow contour snapshots of $x$ velocity are shown in figure 4.34 for the two cases considered on table 4.5 at $\alpha = 6°$. Plots shown are for stable $U^*$ simulations after at least five $L$ based convective time units. The velocity profiles can be seen as attached to diffuser walls, evident by the non-negative velocity values and, consequently, the lack of a recirculation zone within either top or bottom channels.

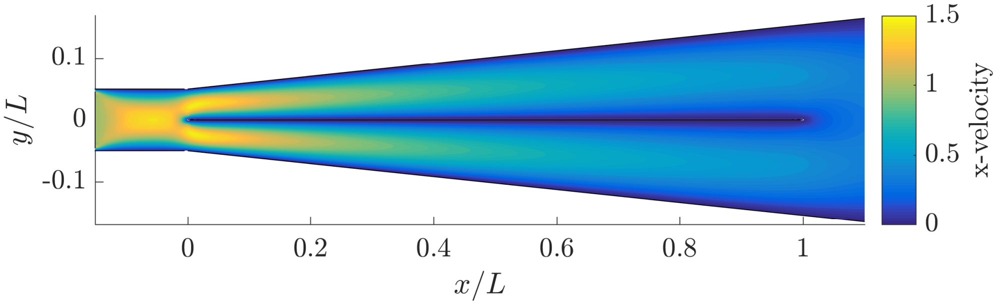

(a) Case 1.

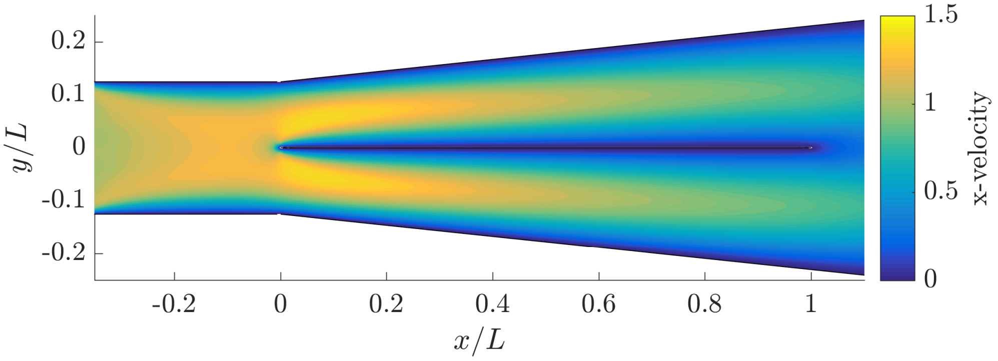

(b) Case 2.

Figure 4.34: Snapshot contours of $x$ velocity for representative stable $U^*$ simulations in table 4.5 cases at $\alpha = 6°$. Snapshots are taken after least five $L$ based convective time units.

The first case is $\hat{h}^2 Re_L = 0.5$ at $\hat{h} = 0.05$, where the quasi-1D model predicted the FSI DNS stability boundary extremely well in a constant channel geometry. The parameters fall within the original criteria for model validity, $\hat{h} \ll 1$, $\hat{h}^2 Re_L \ll 1$, and the gradual $\delta$ and $h_0$ variation is satisfied by the heavy beam constraint ($M^* = 0.02$), ensuring only the lowest system mode bifurcates into flutter. Results of critical values are shown in figure 4.35 and a representative mode shape at $\alpha = 2°$ in figure 4.36. Starting with the latter, mode shapes agree well qualitatively and appear to resemble the second orthogonal beam mode. The critical values also appear to be well captured by the model, especially at the lower diffuser angles, with the model overestimating the stability boundary and underestimating the frequency response especially at $\alpha = 6°$, both by about 10%. The system becomes more stable as $\alpha$ increases. The flow remains attached to channel walls for all tested $\alpha$ values, ascertained by ensuring axial flow profile is unidirectional over the entire channel gap for the length of the elastic member.

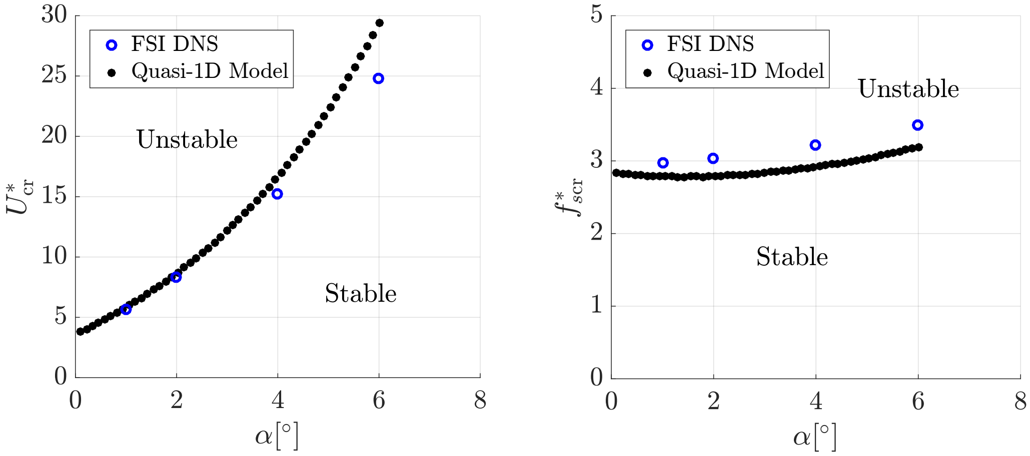

(a) $U^*_{\text{cr}}$ as a function of $\alpha$.

(b) $f^*_{scr}$ as a function of $\alpha$.

Figure 4.35: Comparison of FSI DNS and quasi-1D model flutter boundary critical values at $\hat{h} = 0.05$, $M^* = 0.02$, and $\hat{h}^2 Re_L = 0.5$ for all cases in table 4.5.

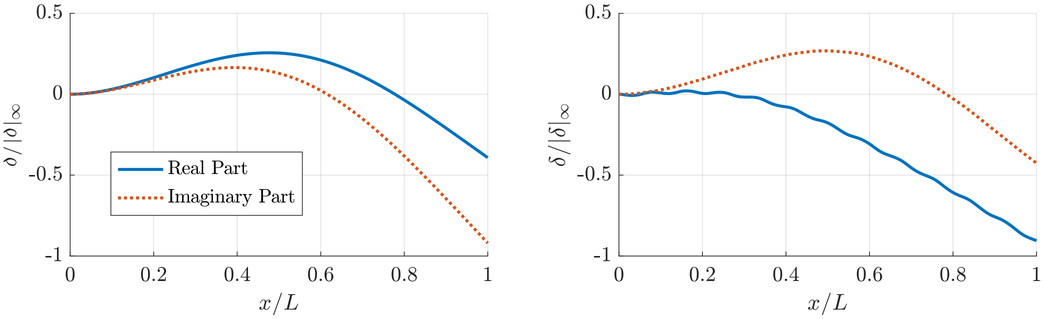

Figure 4.36: Comparison of quasi-1D model (left) and FSI DNS (right) normalized unstable mode shapes at $\hat{h} = 0.05$, $M^* = 0.02$, and $\alpha = 2°$.

The second case is taken at $\hat{h} = 0.125$ and $\hat{h}^2 Re_L = 6.25$, which is at the upper end of applicability of the quasi-1D model based on the results given in section 4.2, where the flutter boundary was only correctly predicted at small $M^*$ values. Critical values shown in figure 4.37, however, show good agreement with the FSI DNS up to about $\alpha \leq 2°$, at which point mode-switching takes place in the model prediction. Both leading and the second eigenvalues, $\lambda_1$ and $\lambda_2$, respectively, are shown and labeled in figure 4.37 to clearly distinguish stability branches as the $U^*_{\text{cr}}$ curves intersect. The mode switching can be seen as $\lambda_2$ becomes the least stable eigenvalue over $\lambda_1$ at $\alpha \sim 2^\circ$ and thereafter. Once again, the model prediction misses the mode switching point and the subsequent dynamics at these higher values of $\hat{h}$ and $\hat{h}^2 Re_L$ for increasing $\alpha$, where condition $h_0^2 \ll 1$ is increasingly violated. The critical frequency response prediction by the model agrees well with the DNS results if $\lambda_1$ had remained the least stable eigenvalue, however the model predicts $f^*_{scr} \sim 10$ for $\alpha \geq 2^\circ$. The mode shapes at $\alpha = 2^\circ$ are plotted in figure 4.38 and show qualitatively good agreement, resembling the second orthogonal beam mode.

When comparing figure 4.35 to figure 4.37, we see that the stabilizing effect when increasing $\alpha$ is stronger in case 1, where $\hat{h} = 0.05$ and $\hat{h}^2 Re_L = 0.5$, than at the higher values associated with case 2. This should be contrasted with the FSI DNS results, which are qualitatively similar to each other in both cases. The monotonically increasing $U^*_{\mathrm{cr}}$ trend in case 1 is also seen in the FSI DNS data in case 2, although the trend is not replicated in case 2 model results, as it misses the mode switching point after $\alpha > 2^\circ$.

In summary, the quasi-1D model captures the effect of the diffuser angle (over the range of angles tested) provided that $\hat{h}$ and $\hat{h}^2 Re_L$ are sufficiently small to ensure the assumptions of the lubrication theory closure.

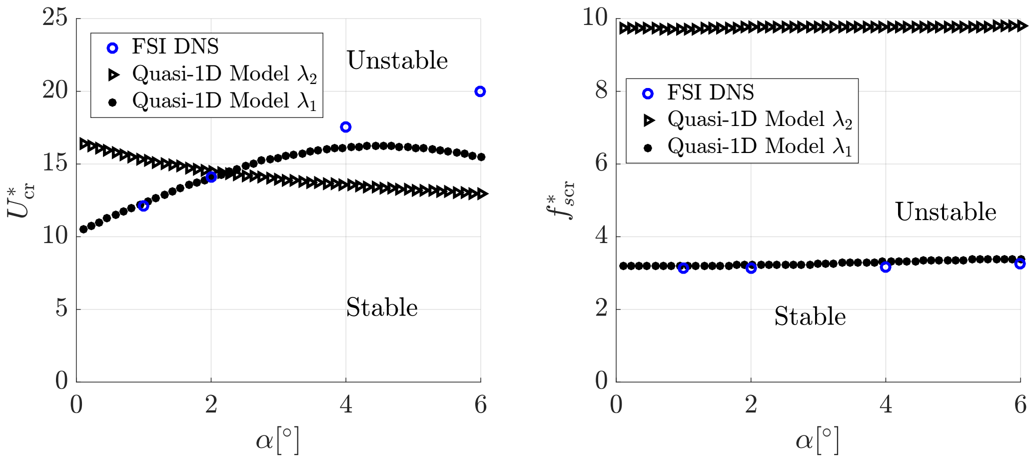

(a) $U^*_{\mathrm{cr}}$ as a function of $\alpha$.

(b) $f^*_{scr}$ as a function of $\alpha$.

Figure 4.37: Comparison of FSI DNS and quasi-1D model flutter boundary critical values at $\hat{h} = 0.125$, $M^* = 0.02$, and $\hat{h}^2 Re_L = 6.25$ for all cases in table 4.5.

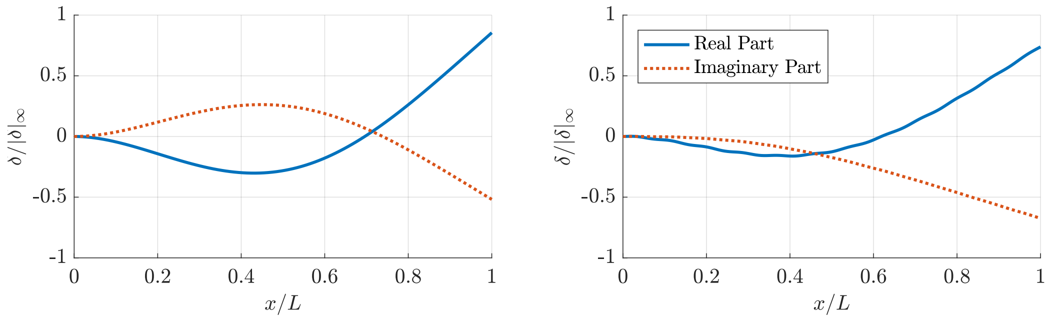

Figure 4.38: Comparison of quasi-1D model (left) and FSI DNS (right) normalized unstable mode shapes at $\hat{h} = 0.125$, $M^* = 0.02$, $\alpha = 2°$.

### 4.3.2 Elastically-Mounted Rigid Beam in Diffusing Channel

Next, we consider an elastically mounted rigid beam set up. As done in the constant channel evaluation of the moving boundary condition, the aim is to consider a case where $\hat{k}_{\text{bc}}$ is low and span the flutter boundary and frequency over wide range of $\hat{m}_{\text{bc}}$. Table 4.6 shows a single case where we consider $\alpha$ the bifurcation parameter as a function of $\hat{m}_{\text{bc}}$, with the complete table for individual simulation sets and mesh parameters in appendix C, table C.4.

Table 4.6: Table of cases for elastically-mounted rigid beam in a diffuser. Parameters $\hat{m}_{\text{bc}}$ and $\alpha[°]$ are varied.

| Case # | $Re_L$ | $\hat{h}^2 Re_L$ | $\hat{k}_{\text{bc}}$ | $\hat{h}$ | $\hat{m}_{\text{bc}}$ | $\alpha[°]$ |
|---|---|---|---|---|---|---|
| 1 | 400 | 6.25 | 0.1 | 0.125 | [ 0.1 - 10 ] | [ 0.1 - 10 ] |

Figure 4.39 shows critical $\alpha_{\text{cr}}$ and $St_{\text{cr}}$ values for FSI DNS and quasi-1D model. The rigid beam is stable at $\alpha \approx 0°$ and becomes unstable at $\alpha_{\text{cr}}$ over the $\alpha$ ranges simulated. The agreement is reasonable in both the boundary and frequency response plots, where a destabilization behavior is evident as $\hat{m}_{\text{bc}}$ increases. Since the beam is rigid, no mode shapes are shown, as only motion in transverse direction can exist in the response.

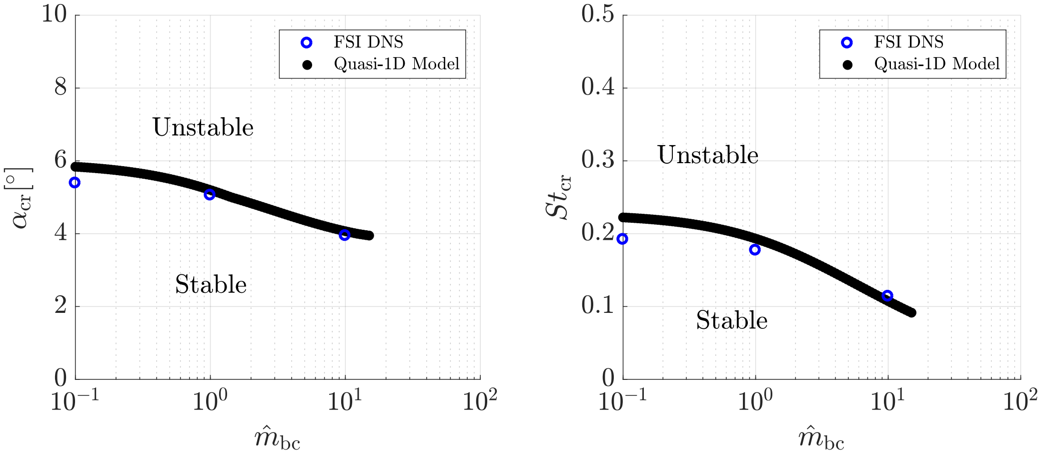

(a) $U^*_{\mathrm{cr}}$ as a function of $\hat{m}_{\mathrm{bc}}$.

(b) $St_{\mathrm{cr}}$ as a function of $\hat{m}_{\mathrm{bc}}$.

Figure 4.39: Comparison of FSI DNS and quasi-1D model elastically mounted rigid beam flutter boundary critical values at $\hat{h} = 0.125$ and $\hat{k}_{\mathrm{bc}} = 0.1$ for all cases in table 4.6.

## 4.4 Summary

The flutter boundary determined from the FSI DNS is well predicted by the quasi-1D model when parameter values are selected so that the assumptions underlying the lubrication-theory closure are met. Moreover, our results show that the validity bounds are flexible: by enforcing $\hat{h} \ll 1$ strictly, the model is able to predict flutter properties at both large $\hat{h}^2 Re_L$ and $M^*$ values. The agreement with FSI DNS values at high $\hat{h}^2 Re_L$ is surprising; yet it is corroborated by the comparison between the inviscid model flutter boundary by Shoele and Mittal [39] as $\hat{h}^2 Re_L \gg 1$. The inclusion of the elastic-translating boundary condition does not alter these findings: the quasi-1D prediction of critical values over a wide range of boundary parameters also agrees well with those predicted by FSI DNS.

The flutter boundary is also well predicted for the range of diffuser angles modeled and simulated. In particular, the bifurcation diffuser angle for the rigid beam can be predicted over a wide range of mass ratios when the elastic-translating leading edge boundary stiffness is low. When considering the cantilever-diffuser geometry at parameter values within lubrication theory bounds, the flutter stability boundary is also well predicted for diffuser angles $< 6°$.

In successfully replicating the stability boundaries from the FSI DNS simulations, the quasi-1D model corroborates the hypothesis that the leakage flow instability is the driving mechanism for the response.

*Chapter 5*

# EXPERIMENTAL STUDY OF FLEXTENSIONAL FLOW-ENERGY HARVESTER

## 5.1 Introduction

In this chapter, we explore the flextensional flow-energy harvester design from an experimental standpoint in the context of fluid-structure interaction. The structure is first characterized with the finite element method in order to understand the fundamental properties of the structure that dictate its dynamics when driven by fluid-flow. Experiments are then carried out to measure structural properties associated with the flexure, including its effective stiffness, mass, and damping. Finally, we measure the device's dynamical response as a function of flow rate. Specifically, we ascertain when the system achieves high amplitude self-sustained oscillations, where the energy conversion from fluid motion to structural vibration is larger than other regimes observed. The last portion of this chapter compares the predicted response from the model proposed in chapter 2 to the experimental results. We use the voltage output from the piezoelectric stacks as a measurement tool, and as a proxy to system dynamics. The primary goal is to characterize the fluid-structure interaction and understand its underlaying physics rather than to optimize the electromechanical design. No energy harvesting circuitry has been implemented in the current set up.

## 5.2 Flextensional Flow-Energy Harvester Design

The flow-energy harvester based on flextensional actuators was first introduced by Lee et al. [26]. Typically, flextensionals are used due to their ability to convert small motion and large forces to small forces and large motions [26]. The idea is to fundamentally invert the use of the actuator as a transducer, and convert the large structural motion into large stresses (and resulting power) onto the piezoelectric elements.

Figure 5.1 illustrates the current flextensional flow-energy harvester. The design has a flexure that supports two piezoelectric stacks (PZT 1 and PZT 2) through a center mount that is attached via set-screw, which allow for multiple flexure structural properties.

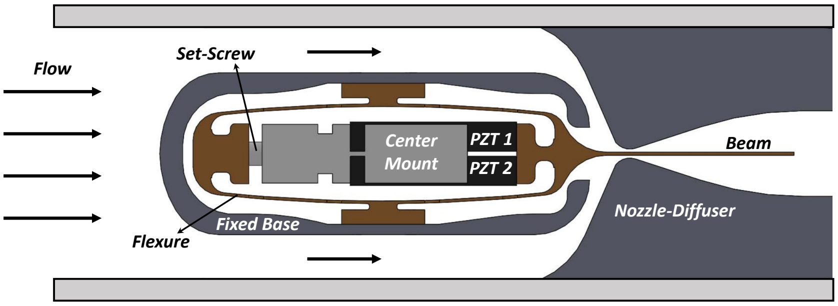

Figure 5.1: Current version of flextensional flow-energy harvester with custom designed flexure.

The amount of torque applied to the set-screw pre-stresses the piezoelectric stacks, and consequently changes the dynamical properties of the flexure. Adding or removing torque to the set-screw is how we will change the stiffness $k_0$, damping $c_0$, and effective mass $m_0$. Measuring those properties will be discussed in more detail in section 5.3.

The flow path begins from a round $\approx$ 15 mm diameter inlet into the test section. The flow impinges on the fixed base and is directed onto the top and bottom paths illustrated in figure 1.3b. The beam is centered along channel, such that the flow path is symmetric. Figure 5.2 illustrates the top channel, with dimensions listed in table 5.1. The flow is converging for $L_2 \approx 0.1L$ along $x$ until it bypasses the constriction at the throat $\bar{h}$, and expands with $\theta = 19°$ diffuser for $\approx 0.7L$. The remaining $0.3L$ the diffuser tapers off into $< 1°$ exit at the end of the beam. The total expansion is $\approx$ 15:1 from $\bar{h}$. The test fluid is air at standard temperature and pressure. This is primarily the case because of initial issues with water and oil experiments: pump-driven flow loops, even with pressure attenuators, would alter the dynamics of the harvester considerably. Using air as the test fluid is a good, low cost iteration at obtaining a data set that could be used to initially characterized the system, in preparation for future, gravity driven liquid tests, if necessary. Air is also representative of a potential subset of applications in carbon dioxide injection wells, for example. However, the ultimate goal is to reproduce results through the theory developed in the previous chapters, which are agnostic to fluid type as long as the foundational assumptions hold. This will be discussed in further detail in section 5.5 of this chapter.

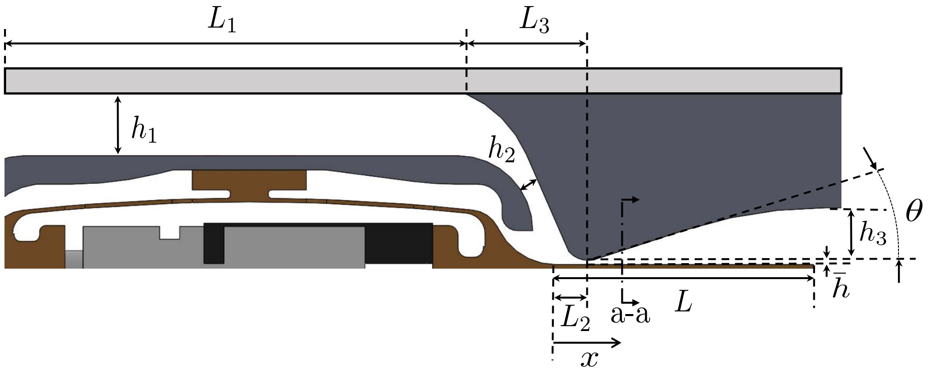

(a) Axial cross-section of flow geometry illustrating flow path.

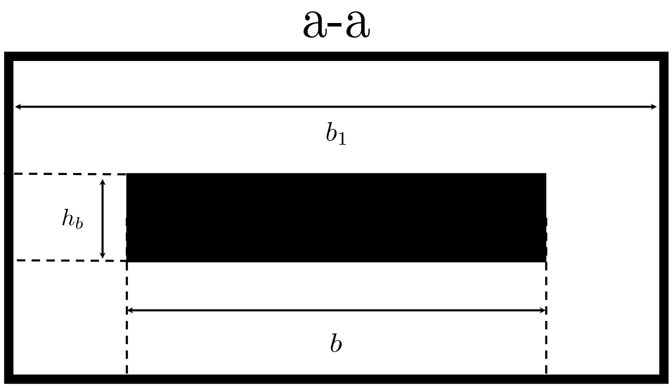

(b) Cut section **a-a** downstream of the throat and illustrated in 5.2a

Figure 5.2: Illustration of flow path and relevant geometry. Values and units are listed on table 5.1.

The detailed exploded view of the flexure assembly is shown in figure 5.3. The flexure and the beam are made of a single aluminum stock, and comprise the moving structure that will be assessed. The fixed base is fastened with screws to both the test section and the flexure, with mounting holes shown in the figure.

The flexure behaves like a translational spring that transfers motion from the beam surface normal direction into compression and expansion of the piezoelectric stacks. The stacks are pre-stressed at the center such that the piezo-elements are always in compression. The set-screw and pre-stressing system is also illustrated in figure 5.3 as part of the assembly. As the flexure moves above the channel centerline, the bottom stack is compressed, and the top stack is released from their pre-stressed conditions. The reverse happens when the beam moves below the channel center-

Table 5.1: Table of flow path parameter dimensions illustrated in figure 5.2.

| **Variable** | **Value** | **Units** |
|---|---|---|
| $L_1$ | 70 | mm |
| $L_2$ | 5 | mm |
| $L_3$ | 19.4 | mm |
| $L$ | 40.7 | mm |
| $h_1$ | 9.8 | mm |
| $h_2$ | 2.3 | mm |
| $h_3$ | 9 | mm |
| $\bar{h}$ | 0.62 | mm |
| $b$ | 14 | mm |
| $b_1$ | 16.5 | mm |
| $h_b$ | 0.7 | mm |
| $\theta$ | 19 | deg |

line, the up and down motion giving rise to two voltage signals that are 180° out of phase.

Finally, figure 5.4 shows a picture of the assembled test section. Vacuum grease and rubber inserts are used to seal and restrain the flow path to that in figure 5.2. An electrical fitting is used to connect the piezoelectric stacks to the data acquisition card on the outside of the test section.

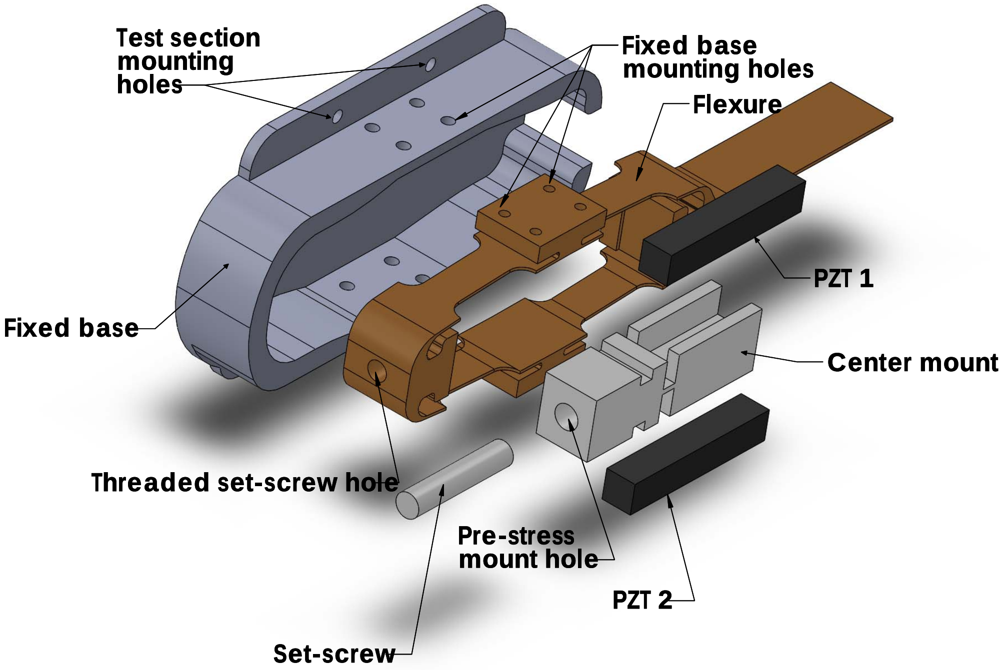

Figure 5.3: Flexure assembly exploded view.

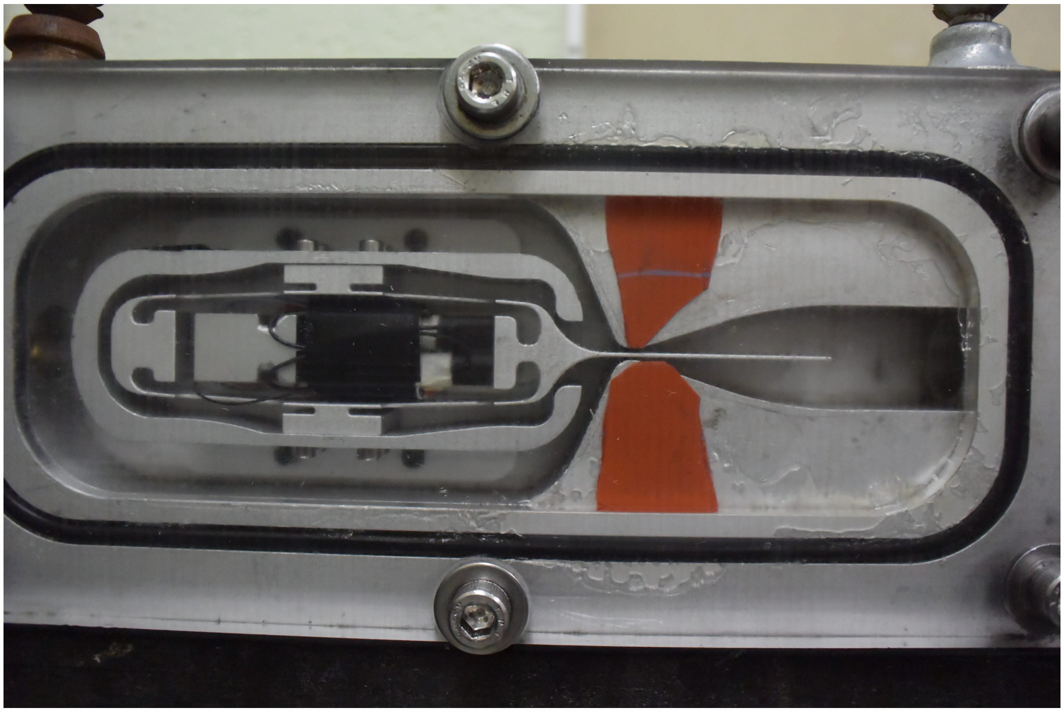

Figure 5.4: Test Section for flowing experiments.

The combination of the flow path, the structure, the piezoelectric elements, and the electronics comprise the flow-energy harvester design. All parameters are interconnected and may affect the system power output. The complexity of the system, and the sheer number of variables make it difficult to exactly predict system behavior, and not the intension of this work. Our thrust is, however, to better understand the underlaying mechanisms that give rise to power generation, and identify relationships between parameters that more strongly affect the power output than others, primarily from the view of fluid-structure interaction.

### 5.2.1 Piezoelectric Stacks

Piezoelectric stacks are composed of multiple thin, alternately poled, piezoelectric layers "stacked", or mechanically connected in series, and electrically in parallel. They operate in what is known as 33 mode, where the applied force is parallel to the poling direction. The effective piezoelectric charge coefficient $d_{33}^*$ and capacitance of stacks $C^*$ are a function of the number of the piezoelectric layers $n$, the charge coefficient $d_{33}$, and capacitance $C$ of each layer,

$$d_{33}^* = d_{33}n, \ C^* = n^2C. \tag{5.1}$$

This layering results in a high capacitance piezoelectric material that is better matched to electrical loads in comparison with a single piece piezoelectric element (monolithic element) of the same dimensions [27]. The ability to have stack piezo-elements, as opposed to bimorphs or unimorphs, allows a more robust and efficient harvester design: the former through the larger electromechanical coupling in the 33 direction, and latter by ensuring that the the piezoelectric ceramic is always in compression. We begin with the constituent equations of piezoelectric materials when strains are small [92],

$$D_i = e_{ij}^{(\sigma)} E_j^{(e)} + d_{im}^{(d)} \sigma_m \tag{5.2}$$

$$\varepsilon_k = d_{jk}^{(c)} E_j^{(e)} + s_{km}^{(E)} \sigma_m \tag{5.3}$$

where $D_i$ is the three dimensional (spatial) electric displacement vector (Coulomb/meter$^2$), $\varepsilon_k$ is the strain in vector representation and dimensionless, $E_j^{(e)}$ is the applied electric field vector in three spatial dimensions (Volt/meter) and $\sigma_m$ is the stress in vector form (Newtons/meter$^2$). The piezoelectric constants are the dielectric permittivity

$e_{ij}^{(\sigma)}$ (Farad/meter), the piezoelectric coefficients $d_{im}^{(d)}$ and $d_{jk}^{(c)}$ (Coulomb/Newton or meter/Volt), and the elastic compliance $s_{km}^{(E)}$ (meter$^2$/Newton), which is the inverse of the material modulus. We restrict equations 5.2 and 5.3 to the stack motion in the 33 mode, and solve for the electric field in equation 5.3 and strains in the poling direction (component 3),

$$\varepsilon_3 = s_{33}^{(D)}\sigma_3 + g_{33}D_3, \tag{5.4}$$

$$E_3^{(e)} = -g_{33}^{(D)}\sigma_3 + \beta_{33}^T D_3, \tag{5.5}$$

where the constants are: $s_{33}^{(D)}$ as the open-circuit elastic compliance, $g_{33}$ the piezoelectric voltage coefficient, and $\beta_{33}^T$ the free dielectric impermeability constant. Applying the dimensions of each layer and we recover the open circuit voltage ($D_3 = 0$), as

$$V_{OC} = -\frac{d_{33}}{C_p}F, \tag{5.6}$$

where $C_p$ is the static capacitance of the material and $F$ is the applied force. Under short-circuit condition ($E^{(e)} = 0$), we have the equivalent charge produced as

$$Q = -d_{33}F. \tag{5.7}$$

When a resistor is placed in parallel with the stack, its response to a step input force is that of an RC circuit with the capacitor having an initial voltage equivalent to the open circuit step-force voltage. Figure 5.5 shows the schematic of this circuit. The voltage $V(t)$ is measured across the resistor $R_e$

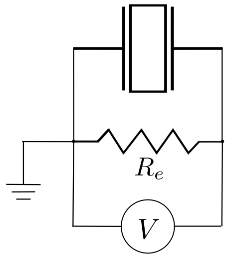

Figure 5.5: Piezoelectric circuit schematic.

Using Kirkoff's law and the capacitance of the piezo as $C_p^*$, we write equation of motion and solve the first-order system for the voltage as a function of time. The solution is the typical exponential decay,

$$V(t) = V_{in} \mathrm{e}^{\frac{-t}{R_e C_p^*}}. \tag{5.8}$$

If the time constant $\tau = R_e C_p^*$ is large enough, the system will act as a low-pass filter: any oscillating voltage upstream of the resistor (opposite to ground) at a frequency $f_{res}$ that satisfies,

$$f_{res} \gg \frac{1}{2\pi\tau} = f_c, \tag{5.9}$$

will not pass through the resistor (to ground). The oscilloscope at $V$ in figure 5.5 will therefore measure it as if the system was an open circuit. We implement the circuit in figure 5.5 and choose an $R_e$ large enough such that the resonances of the structure satisfy condition 5.9. Specifically, we expect the stacks to act as strain gauges for high enough frequencies, where output oscillating voltage is proportional to the flextensional displacement. This can be seen from equation 5.6 and converting $F$ to displacement using the stiffness of the piezo-elements. Table 5.2 lists the properties of the piezoelectric stacks used along with the resistor chosen for our measurements (manufactured by STEMinC - part number # SMPAK155538D40 5x5x36mm). The cut-off frequency from equation 5.9 and properties on table 5.2 is $f_c = 0.65$ [Hz].

Table 5.2: Table of relevant piezoelectric stack properties.

| **Variable** | **Value** | **Units** | **Description** |
|---|---|---|---|
| $C_p^*$ | 3.6 | $\mu$F | stack capacitance |
| $K_s$ | 2.8E7 | N/m | stack stiffness in 33 mode |
| $L_s \times W_s \times H_s$ | 5x5x36 | mm | dimensions |
| $R_e$ | 68 | k$\Omega$ | circuit resistor |
| $\tau$ | 0.245 | s | RC time constant |
| $D_{\mathrm{m}}$ | 40 | $\mu$m | maximum displacement |

The stack piezoelectric elements, along with circuit in figure 5.5, were used for all voltage measurements discussed in this chapter.

### 5.2.2 Flexure Dynamics

One of the principal components of the energy harvester is the flexure. As part of the design initiative, a number of finite-element models were built and tested using in AutoCAD NASTRAN to understand and eventually tune details of the structure. Two sets of finite-element models are discussed. The first is a modal analysis of the structure with boundary conditions, while the second is a static structural displacement that estimates the flexure stiffness. The former analysis is able to discern the primary resonant frequencies and their mode shapes, which are important when contrasting with how piezo-stacks pre-stress and the flow influence structural motion, as they are not encompassed in the simulations. In the latter, we estimate the flexure stiffness, which is shown to correspond to the first, lowest frequency mode for the structure. The same mesh is used for both sets of simulations and is shown in figure 5.6 with respective boundary conditions. There are 170,000 nodes as tetrahedral elements and at least 2 cells across the beam and flexure elements.

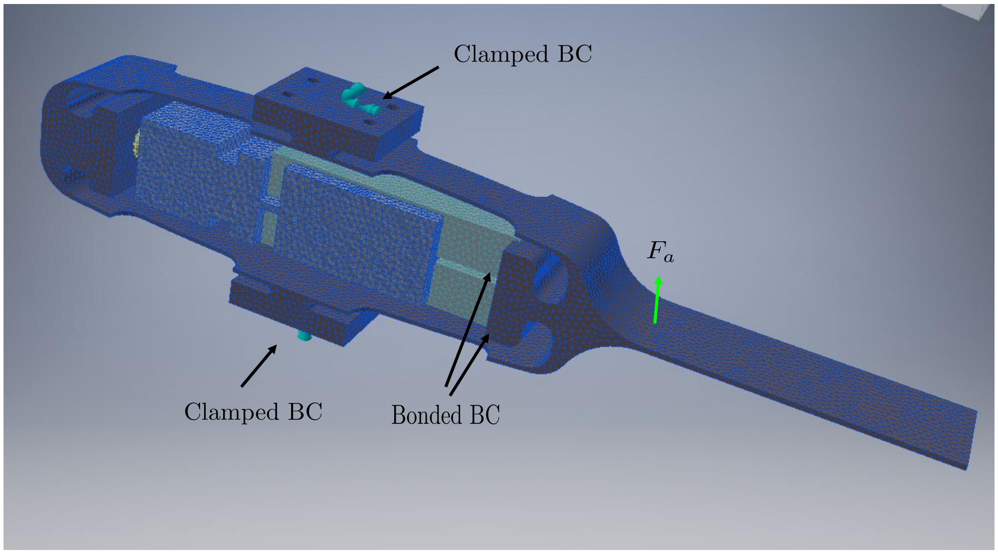

Figure 5.6: Finite element mesh used for static structural and modal analyses.

The boundary conditions are clamped for the interface with the fixed base, and bonded for the piezoelectric elements. The pre-stress in each stack is not accounted in these results. Lastly, the load shown, $F_a$, only applies to the static structural simulation set. The flexure and center mounts are made of aluminum 6061-T6, the set-screw is 304 stainless steel, and the piezoelectric material is lead-zirconate-titanate (PZT-4) Navy-I type. Material properties used are listed in table 5.3.

Table 5.3: Table of structural material properties [93, 94].

| **Variable** | Aluminum | Steel | PZT |
|---|---|---|---|
| Density [kg/m$^3$] | 2700 | 8000 | 7500 |
| Young's modulus [GPa] | 68.9 | 193 | 64.5 |
| Poisson's ratio [ND] | 0.33 | 0.29 | 0.31 |

### Modal Finite-Element Analysis Results

Results from the modal finite element analysis consist of mode shapes and their corresponding eigenvalues, stated as dimensional frequencies here. The fundamental mode of the system is at $f_1 = 169$ [Hz] and its shape is shown in figure 5.7. The amplitude of the modes shapes are arbitrary, and plotted for opposite phases in the figure. This is followed by the second mode at $f_2 = 328$ [Hz], shown in figure 5.8. There is also the first, second, and third flexure bending modes at $f_3 = 1067$ [Hz], $f_4 = 1335$ [Hz], and $f_5 = 1415$ [Hz]. The first beam torsional mode at $f_6 = 1962$ [Hz], and a second transverse mode occurs at at $f_7 = 2053$ [Hz].

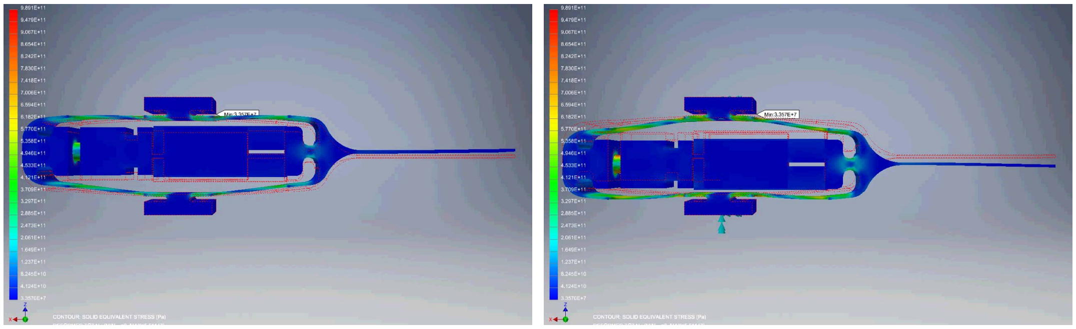

(a)

(b)

Figure 5.7: Results for fundamental mode of flexure at $f_1 = 169$ [Hz]. Figures show snapshots of (a) up- and (b) down- wards movement of the mode shape. The red dashed-lines represent that static shape and contour levels are representative of stress concentration.

As seen in figure 5.7, the fundamental mode consists mostly of transverse movement of the flexure. This is the "flextensional" mode and couples structural motion strongest between the flexure and piezoelectric stacks, as evident by the lighter coloring representative of higher stresses around the flexure support to the piezoelements. The mode also corresponds to a (mostly) rigid-body motion of the beam: though the flexure moves up and down considerably, the cantilever itself remains straight through the cycle of motion. This becomes evident when comparing to the original static shape represented by the red dashed lines.

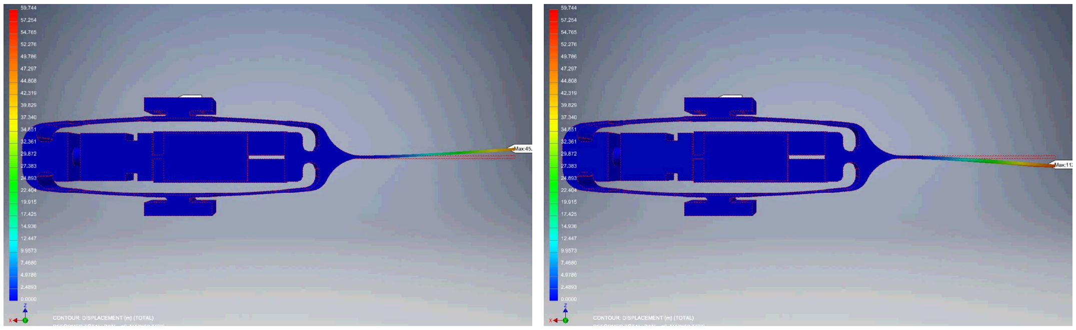

(a) (b)

Figure 5.8: Results for second mode of flexure at $f_2 = 328$ [Hz]. Figures show snapshots of up- and down- wards movement of the mode shape. The red dashed lines represent that static shape and contour levels are representative of total displacement.

The modal analysis shows that the second and 7th modes are transverse bending modes. To understand whether only the beam is excited at those frequencies, we can compared the eigenvalues to those from classical Euler-Bernoulli beam theory. We have defined the theory's eigenfunctions in equation 2.79 and eigenvalues as the solutions to the characteristic equation 2.80, listed on table 2.2. Hence, we can calculate the theoretical clamped-free beam frequencies as

$$f_i = \frac{(\beta_i L)^2}{2\pi L^2}\sqrt{\frac{EI}{\rho_s b h_b}}. \tag{5.10}$$

$I$ is the square cross-section moment of inertia for the beam in three dimensions,

$$I = \frac{h_b^3 b}{12}. \tag{5.11}$$

Table 5.4 lists the FEA modal analysis and Euler-Bernoulli beam results, along with the description of each mode. Property parameters and values used are in tables 5.1 and 5.3. We see that the first two transverse modes frequencies are slightly over-predicted by $\approx 5.5\%$ in classical theory.

Table 5.4: Table of frequency predictions by finite element modal analysis (FEA) and Euler-Bernoulli (E-B) beam theory.

| # | FEA [Hz] | E-B [Hz] | Description |
|---|---|---|---|
| $f_1$ | 169 | - | flextensional transverse mode |
| $f_2$ | 328 | 346 | fundamental cantilever transverse mode |
| $f_3$ | 1067 | - | flexure spanwise bending mode |
| $f_4$ | 1335 | - | flexure transverse bending mode |
| $f_5$ | 1415 | - | 2nd flexure transverse bending mode |
| $f_6$ | 1962 | - | fundamental cantilever torsional mode |
| $f_7$ | 2053 | 2167 | 2nd cantilever transverse mode |

As results in flowing experiments will ascertain in section 5.4, the flow excites primarily the first two modes of the flexure. Hence, it is important that we ensure they can be captured as part of the model. Furthermore, the flow-energy harvester excites the flexure primarily through a transverse force *on the beam*, where the pressure difference between the top and bottom flow paths apply the net force onto the structure. Since classical theory captures $f_2$, and the mode shape in $f_1$ is a rigid body motion of the cantilever, we conclude that it is tractable to represent the $f_1$ mode shape as the elastic-translating leading edge boundary condition. Moreover, the simple harmonic oscillator discussed in section 2.3.3 has a physical analogue: the flexure stiffness, damping, and mass that characterize the dynamics of the flextensional mode at $f_1$.

In summary, the modal analysis provides the fundamental mode shapes and justifies the rigid body motion that characterizes the elastic-translating boundary condition. It also suggests $f_1$ as its representative frequency. Next we estimate the flexure static stiffness and obtain estimates for the simple harmonic oscillator boundary condition model.

### Static Structural Finite Element Analysis

Figure 5.6 shows the static model details, including mesh, boundary conditions, and the position of the load $F_a$. To measure the static stiffness of the flexure, we obtain a relationship between applied force at the beam base versus the resulting displacement. Considering steady verson of equation 2.71, where $\bar{a}$ represents the boundary condition amplitude, we can solve for the boundary condition stiffness as

$$k_0 = \frac{bf_r}{\bar{a}} = \frac{F_a}{\bar{a}}. \tag{5.12}$$

The applied force is then $F_a = bf_r$, where $f_r$ is defined as the force per unit span and $b$ is the span of the beam. Figure 5.9 shows a representative displacement contour for $F_a = 10$ [N].

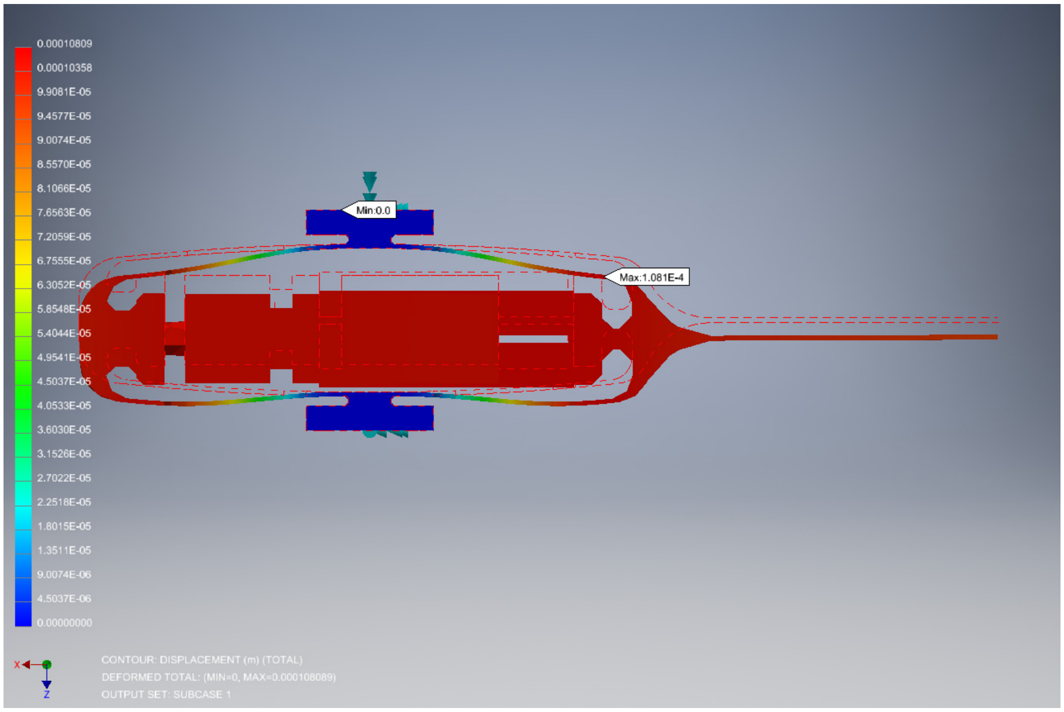

Figure 5.9: Representative displacement at $F_a = 10$ [N] for static structural FEA. Red dashed-lines represent the initial position before $F_a$ is applied.

A series of 7 simulations were carried out with varying $F_a$. Figure 5.10 shows the results as a function of the beam base displacement. The slope of the line is the estimated stiffness $k_{0\text{FEA}} = 58,366$ [N/m]. The modal analysis has no mechanical damping in its solution, therefore $f_1 = 169$ [Hz] is the solution of equation 2.71 for $c_{0\text{FEA}} = 0$. We can now estimate the effective mass component from $f_1$ as

$$m_{0\text{FEA}} = \frac{k_0}{4\pi^2 f_1^2} = 0.052 \text{ [kg]}. \tag{5.13}$$

The values $m_{0\text{FEA}} = 0.052$ [kg] and $k_{0\text{FEA}} = 58,366$ [N/m] are approximations for those we should expect from the experimental measurements in section 5.3. They represent an idealization of the boundary conditions (i.e. no stack pre-stress) and no damping. Though these conditions do not hold for the actual device, they help our understanding of the structure and provide a check on device fabrication and experimental set up.

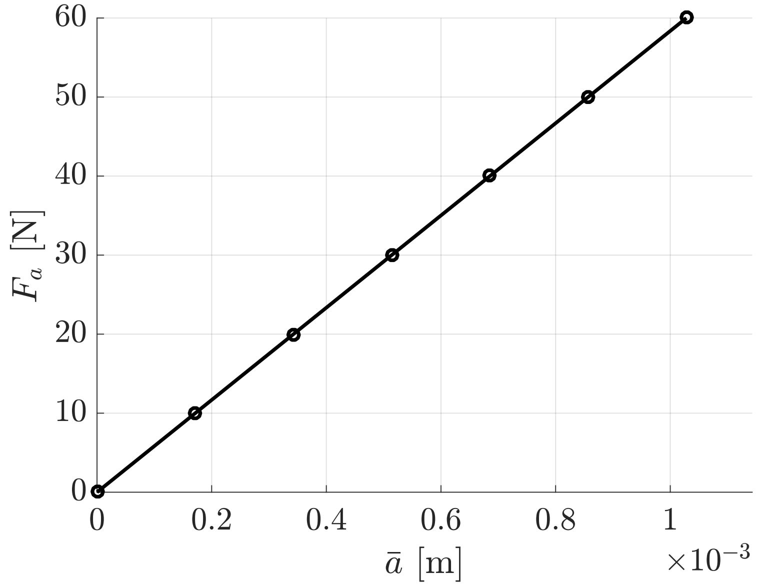

Figure 5.10: $F_a$ as a function of displacement for 7 static structural FEA simulations. The slope represents a stiffness value of $k_{0\text{FEA}} = 58,366$ [N/m].

### 5.3 Flexure Property Measurements

Two experiments are carried out to quantify the no-flow flexure properties, analogous to the two sets of FEA simulations carried out in section 5.2.2. The flexure is immersed in still air at standard pressure and temperature (STP) for all tests in this section, defined here at 101352.9 [Pa] (14.7 [psia]) and 21.1 [° C] (70 [° F]). The stiffness $k_0$ is characterized first through a static stiffness measurement of force $F_a$ and displacement $\bar{a}$, mimicking the static structural FEA. The second experiment measures the piezoelectric voltage output of the stacks when the flextensional fundamental mode is excited. The damped resonant frequency and exponential decay rate are calculated from the voltage outputs. The solution to the homogeneous equation 2.71 ($f_r = 0$) is used to map the voltage response to the flexure damping $c_0$ and flexure mass $m_0$.

Three flexure configurations are measured with values of set-screw torque used to identify each. Since issues exist in solely considering set-screw torque as an injective map to flexure properties, we only use it here to identify each case as we proceed through the flexure property characterization. These issues mostly consist of uncontrollable conditions within the pre-stress mount hole, such as exact alignment of set-screw and presence of oils or other elements that affect set-screw-to-hole friction. Table 5.5 shows the three flexure settings as medium, most, and least set-screw torque, and correspond to flexure settings 1, 2, and 3 respectively. Replication of results need must be based on flexure properties rather than torque values listed.

Table 5.5: Table of experimental flexure settings based on qualitative set-screw torque level, with approximate torque values shown.

| Setting # | Torque Level | Torque Values |
|---|---|---|
| 1 | midlevel | 1.2 [N m] |
| 2 | highest | 2.0 [N m] |
| 3 | lowest | 0.8 [N m] |

### 5.3.1 Flexure Static Stiffness Test

The flexure static stiffness measurement is carried out using the manual force test-stand ES-20 (manufactured by MARK-10 Corporation), with both a displacement dial and a series 2 digital force gauge (±0.5%). A custom mount was designed and built to hold the flextensional fixed base such that the force piston interfaced as close to the cantilever base as possible. Figure 5.11 shows an illustration of the piston and the custom mount with the mounted fixed base and flextensional.

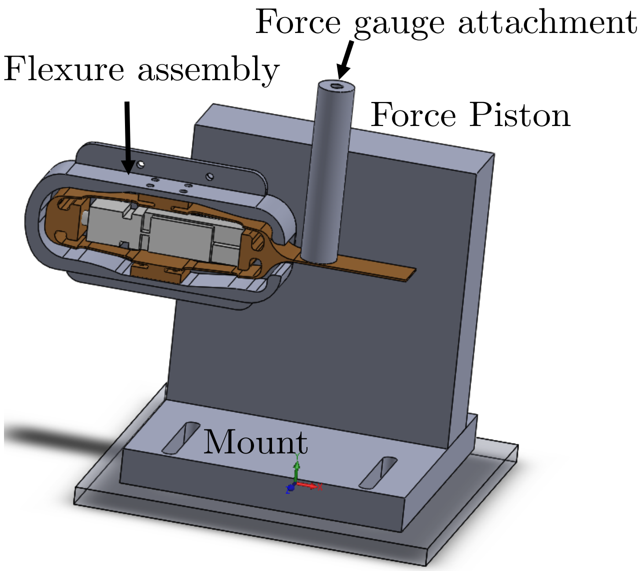

Figure 5.11: Illustration of static stiffness test set up. Mount interface with force piston.

The force required to displace each flexure setting 5, 10, and 20 [mil] was measured, with experiments repeated five times per flexure. Table 5.6 shows the mean results, with variance from the repeated 5 small enough to be neglected here. Figure 5.12 shows the plotted stiffness values $k_0$ [N/m] for each flexure setting, along with the least-squares fit lines through the origin.

Table 5.6: Table of mean displacement and force [N] results for flexure settings in table 5.5, with least-squares best fit stiffness values $k_0$ [N/m].

| **Disp.** [mil] | **Disp.** [m] | **Flex. 1** [N] | **Flex. 2** [N] | **Flex 3** [N] | FEA |
|---|---|---|---|---|---|
| 0 | 0 | 0 | 0 | 0 | - |
| 5 | 0.000127 | 4.86 | 5.4 | 2.8 | - |
| 10 | 0.000254 | 9.12 | 10.04 | 5.44 | - |
| 15 | 0.000381 | 14.44 | 16 | 8.24 | - |
| $k_0$ Least-Squares [N/m] | - | 3.73E4 | 4.12E4 | 2.16E4 | 5.84E4 |

All experimental values fall under the finite element stiffness for the displacements shown, with stiffest flexure setting is at $\approx$ 30 % of its value. This is believed to be acceptable given the discrepancies between the FEA bonded and the experimental pre-stressed boundary conditions. Furthermore, the flexure stiffness appears to correlate with the torque levels applied to the set-screw, from table 5.5. With the information in table 5.6, we can note that flexure setting 2 is the most stiff, flexure setting 3 is the least stiff, and flexure setting 1 falls in the middle, but closer to flexure setting 3 in stiffness.

### 5.3.2 Flexure Dynamic Test

The flexure dynamic test consists of measuring the output voltage from the piezoelectric elements as the flexure responds to an impulsive force. The load location is shown in figure 5.6 as $F_a$, and chosen because it primarily excites the flextensional mode described in section 5.2.2. The stack voltage response $V(t)$ is a direct analogue to the properties of the flexure: its decay rate and oscillating frequency correspond to those of the flextensional plus the RC circuit response. As described in section 5.2.1, a static load to the piezo-elements with a parallel resistor yields an exponential decay with a time constant $\tau = R_e C_p^*$ . Similarly, the response of the flexure to $F_a$ are the results of the static stiffness test in section 5.3.1. If the system is quickly unloaded, the stack dynamic voltage response is the open-circuit voltage in equation 5.6 that follows its load $F(t)$ as long as condition 5.9 is satisfied. $F(t)$ is proportional to the local strains through the stack stiffness $K_e$, which is, by

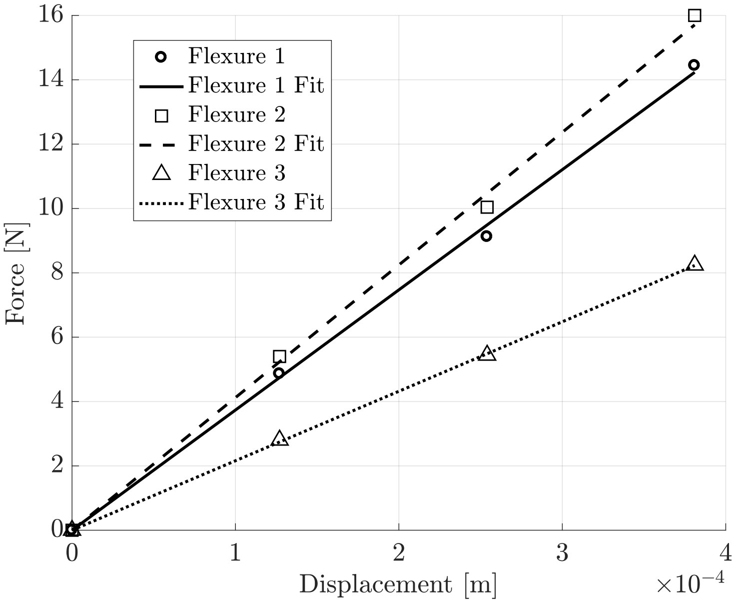

Figure 5.12: Plots of Force over displacement results from table 5.6 and their least-square fit lines representative of stiffness $k_0$.

definition, proportional to displacements of the structure. Hence, with properties listed in table 5.2, we expect the decay rate $\zeta = -4.09$ [1/s] and condition 5.9 is quickly checked and satisfied, as 169[Hz] $\gg$ 0.64[Hz], from table 5.4. Though the flextensional modal frequency here is the one expected through simulation, one of the purposes of the test is to measure $\tau$ and $f_1$ and re-assert condition 5.9.

The three flexure configurations from table 5.5 are considered. Each flexure is tested when it is mounted onto the test section immediately after the flow tests have been carried out in section 5.4. For each flexure setting, the experiment is repeated at least 8 times, with initial forcing as $F_a$ and $-F_a$. The $|F_a| \sim 20$ [N] and only considered in the sense that the system had an observable voltage response. The static flexure displacement from $|F_a|$ is $\approx \bar{h}$, defined in table 5.1.

The figures that follow in the rest of this section are a single representative sample for each flexure experiment. They illustrate the signal processing steps taken to measure the decay rate $\zeta$ and response frequency $\omega$ for the analyzed response. The line noise level $V_n$ was characterized by measuring beginning and end signal and found to be $\mathrm{e}^{-5.75} \approx 0.003$ [V] for flexure settings 1 and 2, and $\mathrm{e}^{-6.25} \approx 0.002$ [V] for flexure setting 3. It is largely attributed to grid power at 60 Hz, but also amplified if the stacks are coupled more strongly to the structure, likely due to ambient vibrational noise (as in the case in flexures 1 and 2). The upper bound for each segment was adapted per flexure setting, as the piezo-element pre-stress condition affects the maximum amplitude voltage response, along with the mechanical flexure properties themselves. The primary consideration for choosing the upper bound was whether nonlinear behavior from the unloading step was observed, and defined as $V_u > \mathrm{e}^{-1} \approx 0.37$ [V] for flexure settings 1 and 2, and $V_u > \mathrm{e}^{-4.25} \approx 0.015$ [V] for flexure setting 3. Data is taken with an NI-DAQ 6212 BNC (National Instruments) at 8 kHz sampling frequency. The reference voltage $V_0 = 1$ [V] in log voltage amplitude plots. In order to obtain the decay rate of the oscillating signal, we implement the Hilbert transform described in section 3.4.3.

### Flexure Setting 1

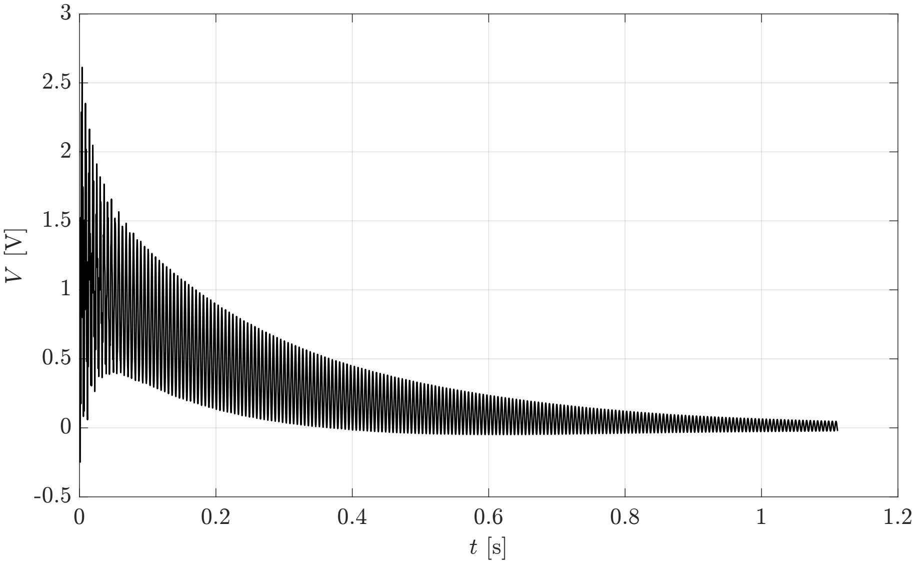

Figure 5.13: Sample voltage output for flexure impulse response from a single piezo-element in experiment .

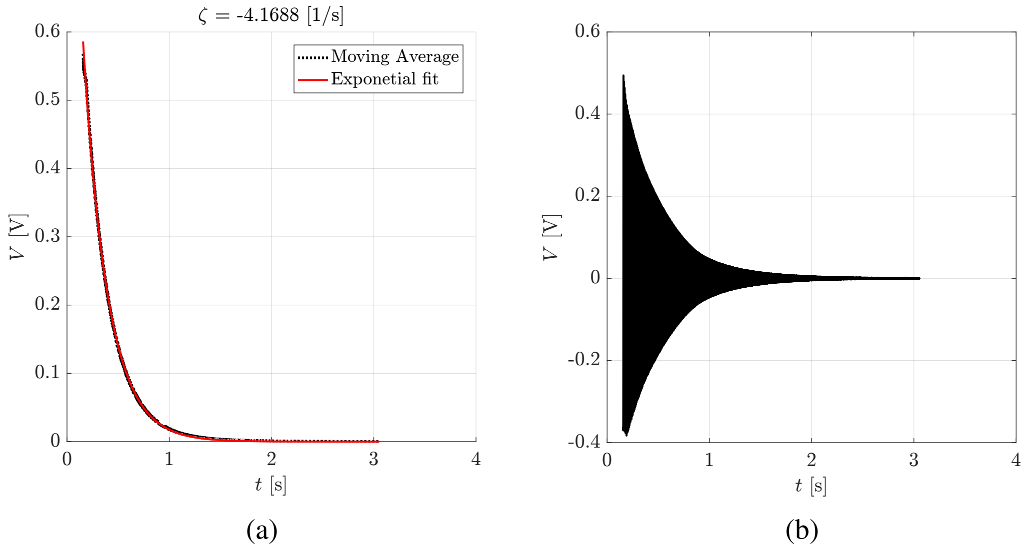

(a) (b)

Figure 5.14: Decomposition of sample signal in figure 5.13 into a moving average from electrical circuit (5.14a) and the oscillating open circuit flexure forcing component (5.14b).

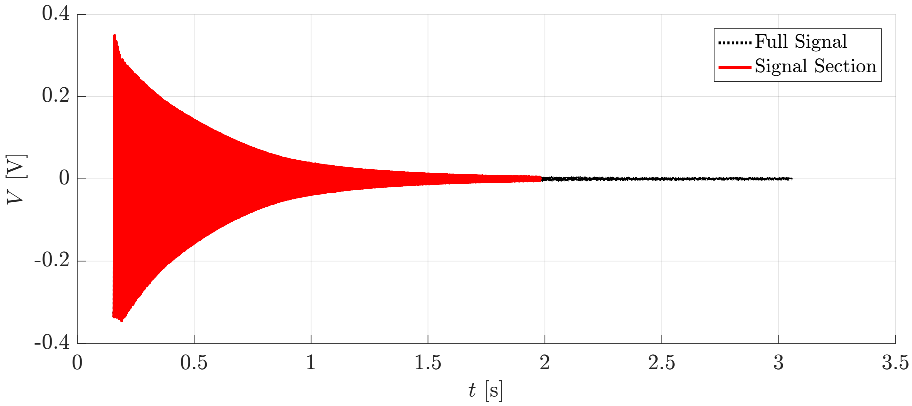

Figure 5.15: Sample voltage output for flexure impulse response illustrating Hilbert transformed section.

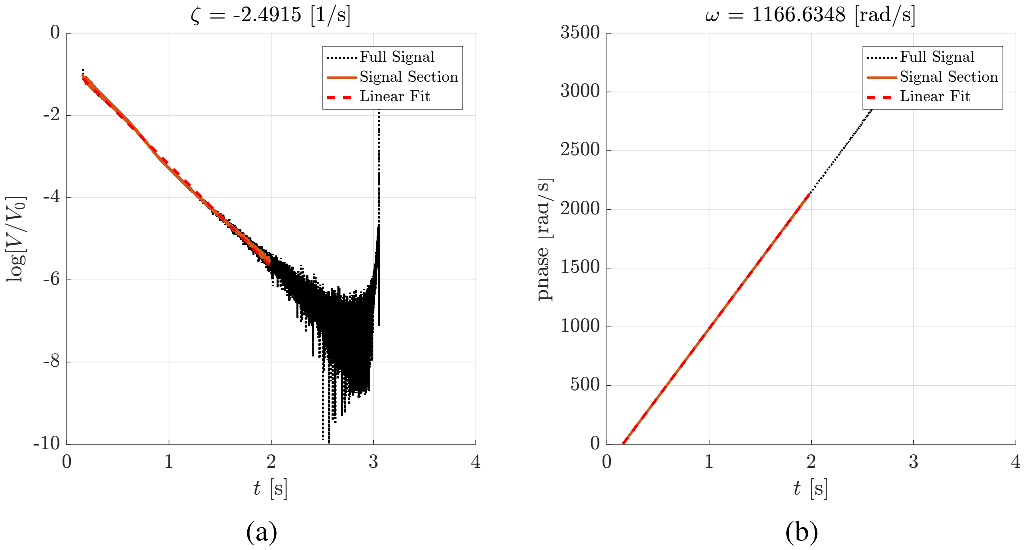

Figure 5.16: Analytic signal amplitude (5.16a) and phase (5.16b).

The flexure 1 representative full signal is shown in figure 5.13. The moving average with 300 samples is shown in figure 5.14a, with the fit $\zeta = -4.17 \approx \frac{1}{R_e C^* p} = -4.09$ [1/s]. The subtracted oscillating part is shown in figure 5.14b, and processed with the Hilbert transform in figure 5.15. Note that the time segment near zero in figures 5.14a and 5.14b are omitted due to the edge effects of the moving-average filtering. This will hold true for all figures of this form. This flexure produced the cleanest signal of all tested, as can be seen for the linear behavior of the analytic signal amplitude in figure 5.16a. Representative $\zeta = -2.49$ [1/s], and $\omega = 1166.6$ [rad/s].

## Flexure Setting 2

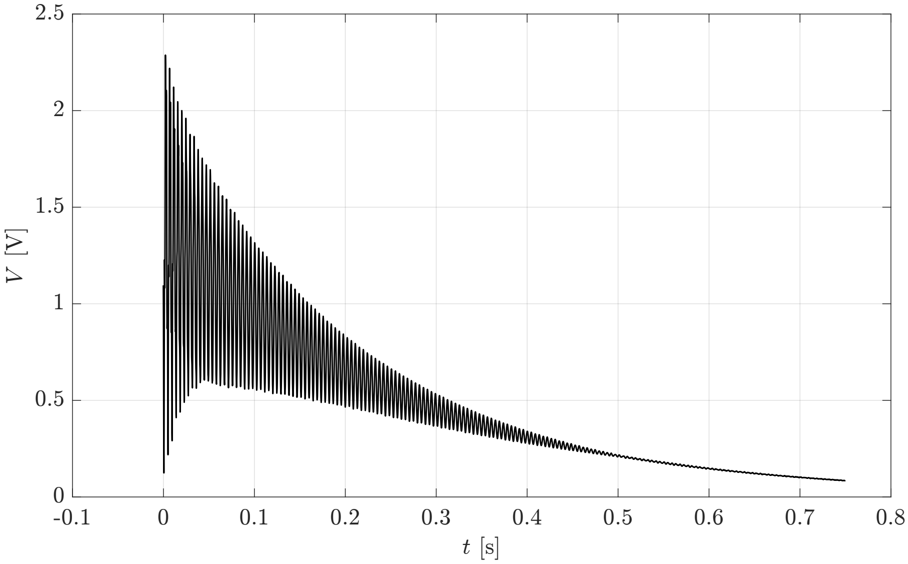

Figure 5.17: Sample voltage output for flexure impulse response from a single piezo-element in experiment .

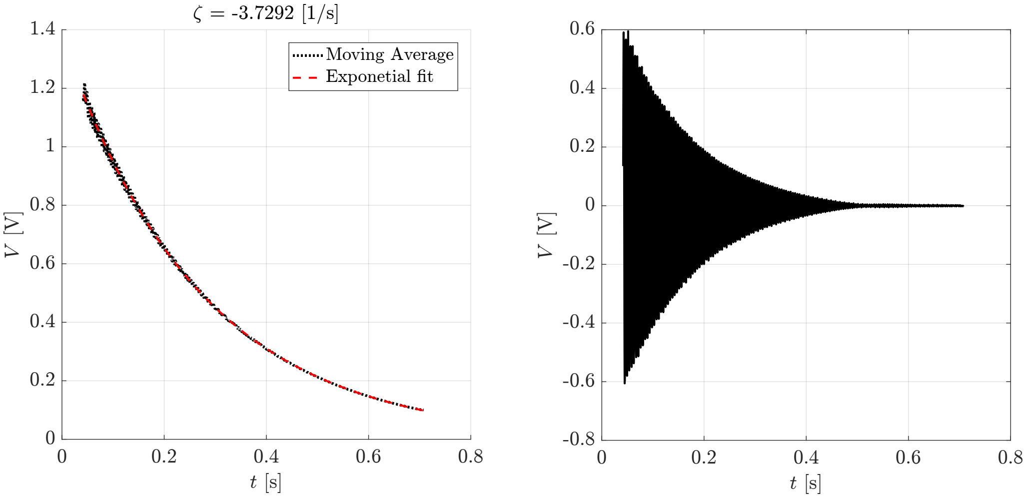

(a) (b)

Figure 5.18: Decomposition of sample signal in figure 5.17 into a moving average from electrical circuit (5.18a) and the oscillating open circuit flexure forcing component (5.18b).

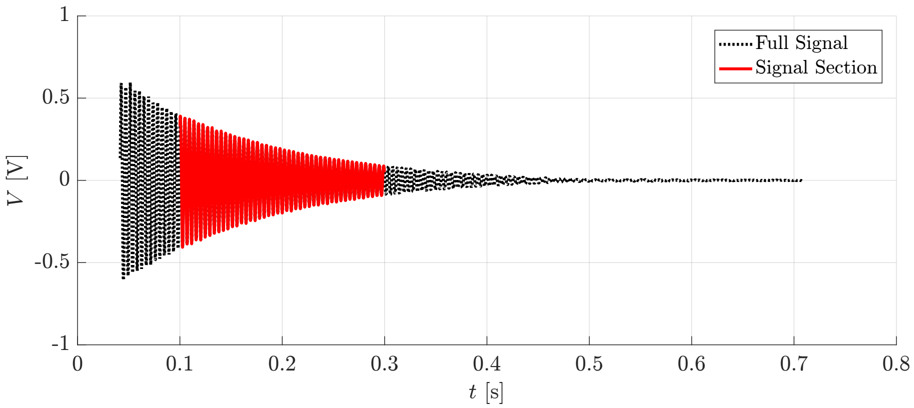

Figure 5.19: Sample voltage output for flexure impulse response illustrating Hilbert transformed section.

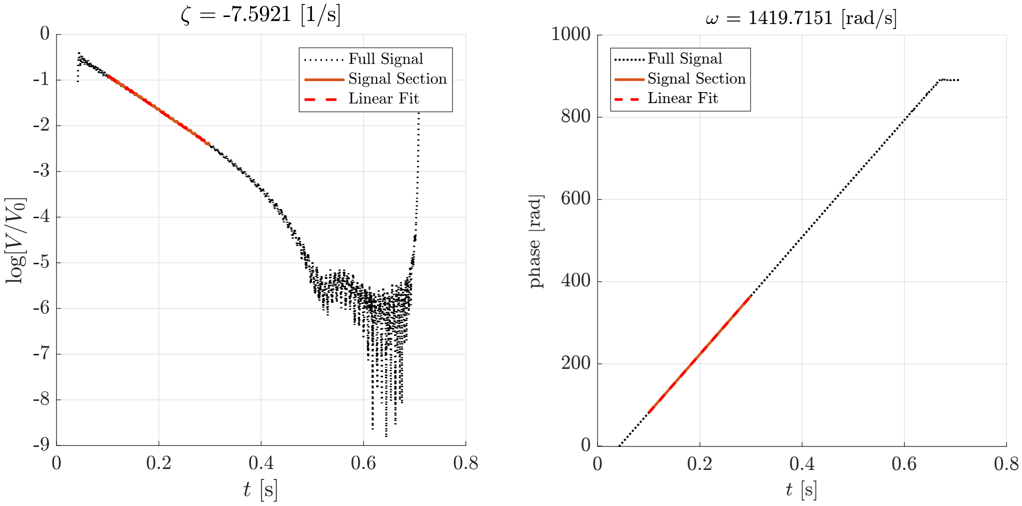

(a) (b)

Figure 5.20: Analytic signal amplitude (5.20a) and phase (5.20b).

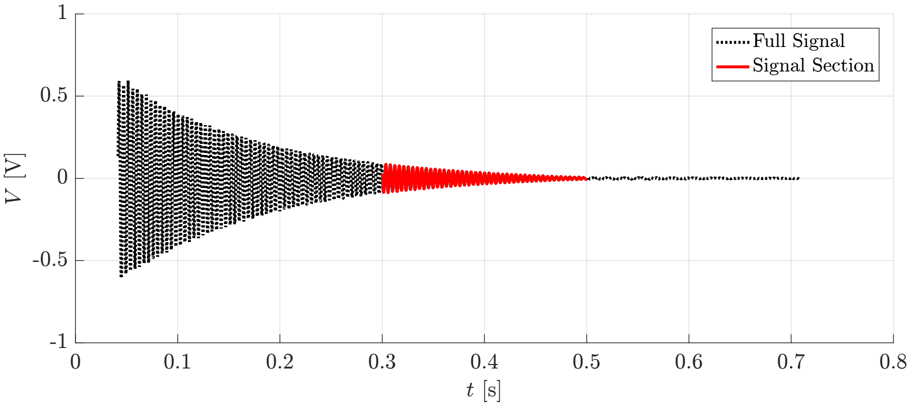

Figure 5.21: Sample voltage output for flexure impulse response illustrating Hilbert transformed section.

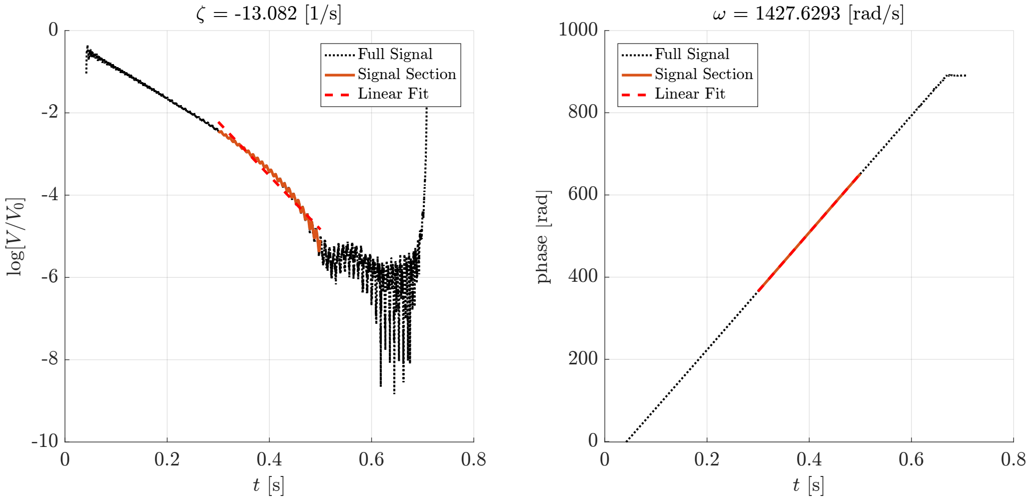

(a)

(b)

Figure 5.22: Analytic signal amplitude (5.22a) and phase (5.22b).

The flexure 2 full signal is shown in figure 5.17. The moving average with 300 samples is shown in figure 5.18a, with the fit $\zeta = -3.73$ [1/s], which is slightly lower than the expect value of -4.09 [1/s]. We believe that it is within a reasonable margin of error when considering the moving average filtering, least squares fitting, and the variation within the capacitance of the piezoelectric elements. Figure 5.20a shows the Hilbert transformed amplitude of the full signal, and an interesting behavior emerges when comparing large and small amplitude voltage decay rates. In particular, the curve, unlike 5.16a, exhibits a nonlinear decay rate after approximately $\log\left[\frac{V}{V_0}\right] < -3$. The angular frequency, however, is relatively fixed for the entire range from $V_n$ to $V_u$. Therefore, we have split the system into a piecewise bilinear fit, with figures 5.20a and 5.20b representing the linear values of $\zeta = -7.59$ [1/s] and $\omega = 1419.7$ [rad/s] (early time segment); while figures 5.22a and 5.22b show the section for small amplitude values that decay ($\zeta = -13.08$ and $\omega = 1427.6$ [rad/s] as late time segment). Flexure 2 has the highest stiffness and pre-stress configuration out of all three settings, and it is plausible that the nonlinearity seen in the analytic signal amplitude may be associated with a high pre-stress regime.

### Flexure 3

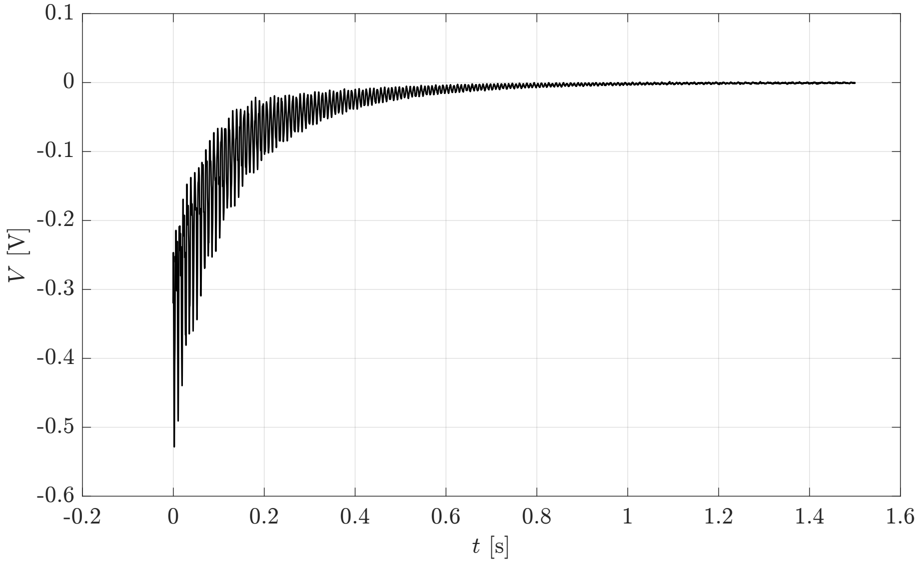

Figure 5.23: Sample voltage output for flexure impulse response from a single piezo-element in experiment .

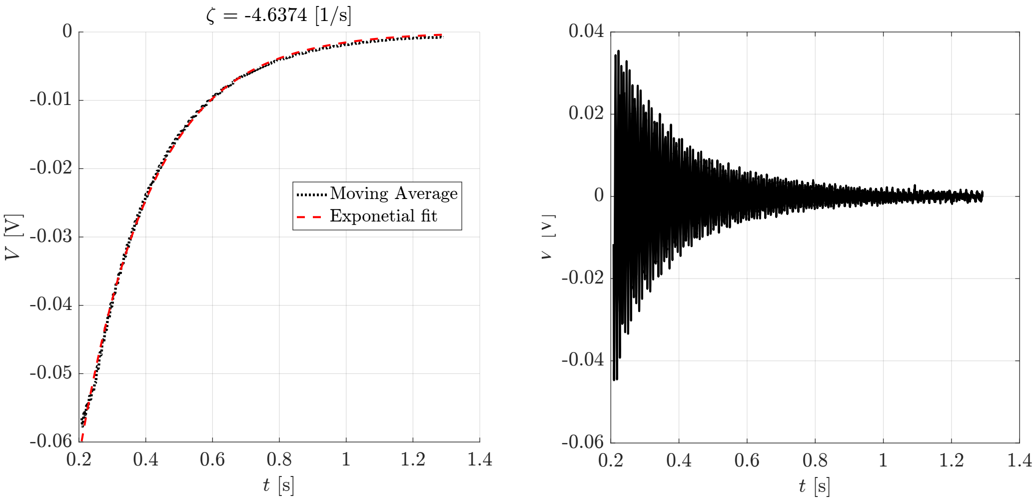

(a) (b)

Figure 5.24: Decomposition of sample signal in figure 5.23 into a moving average from electrical circuit (5.24a) and the oscillating open circuit flexure forcing component (5.24b).

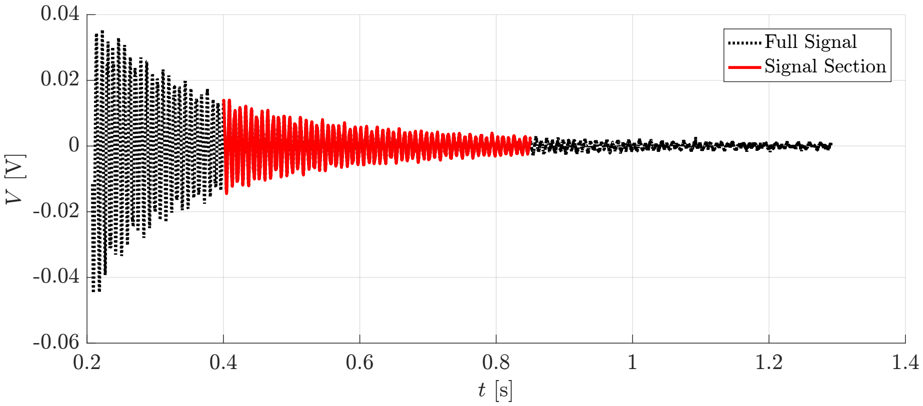

Figure 5.25: Sample voltage output for flexure impulse response illustrating Hilbert transformed section.

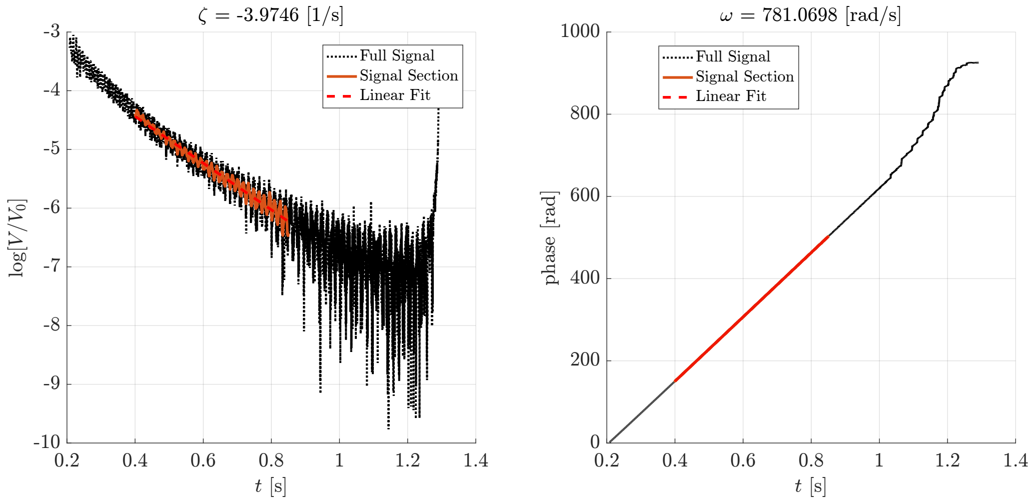

(a) (b)

Figure 5.26: Analytic signal amplitude (5.26a) and phase (5.26b).

The flexure 3 representative full signal is shown in figure 5.23. The moving average with 300 samples is shown in figure 5.24a, with the fit $\zeta = -3.97$ [1/s], slightly lower but within the expected range for the RC time scale variation. This flexure represents the lowest stiffness and stack pre-stress conditions, which can be seen in the phase fit from figure 5.24b, where $\omega = 781.1$ [rad/s]. Another distinction from the other flexure settings is the variation seen in the Hilbert transformed amplitude.

### Summary

Results of the aggregated set of experiments for each flexure is shown on table 5.7. Flexure settings 1 and 2 (early time segment) show little variation among different experiment realizations, while flexure 3 shows the highest. Flexure 2 (late time segment) also shows considerable variation within its own data set, but also when the mean is compared to that of Flexure 2 (early time segment) value. Simple harmonic oscillator model parameters can be directly calculated from values in table 5.7, and discussed next. We quickly re-assert the frequency response through the RC circuit by noting that the frequency responses for flexures 1, 2, and 3 are $\sim$ 185 [Hz], $\sim$ 226 [Hz], and $\sim$ 122 [Hz], respectively, and all $\gg$ 0.64 [Hz]. This confirms that indeed the voltage output from the piezo-stacks behave as the open-circuit voltage measurement. The frequencies for all frexure settings also are within the ballpark of the FEA value of 169 [Hz], serving as a good validation of the structural design.

Table 5.7: Table of experimental flexure values for flexure dynamic test. Setting details are shown in table 5.5.

| Variable | Flexure 1 | Flexure 2 - early time seg. | Flexure 2 - late time seg. | Flexure 3 |
|---|---|---|---|---|
| $\omega$ - mean [rad/s] | 1167.6 | 1423.1 | 1430.7 | 767.7 |
| $\omega$ - STDEV [rad/s] | 0.348 | 4.055 | 3.849 | 18.821 |
| $\zeta$ - mean [1/s] | -2.471 | -7.718 | -13.916 | -3.834 |
| $\zeta$ - STDEV [1/s] | 0.071 | 0.076 | 0.868 | 0.271 |

### 5.3.3 Elastic-Translating Boundary Condition Parameters

The flexure characterization in sections 5.3.1 and 5.3.2 provide the data necessary to estimate the elastic-translating boundary condition coefficients as the analogue to the flextensional mode. We can re-write the simple harmonic oscillator boundary amplitude equation 2.71 into the standard, homogeneous form,

$$\ddot{\bar{a}} + \frac{c_0}{m_0}\dot{\bar{a}} + \frac{k_0}{m_0}\bar{a} = \ddot{\bar{a}} + 2\zeta\dot{\bar{a}} + \omega_n^2\bar{a} = 0. \tag{5.14}$$

Recall that we want to obtain values for the mass $m_0$, damping $c_0$, and stiffness $k_0$ terms ($b$ is the spanwise beam width). Taking the Laplace transform into $s$ from $t$ and solving the characteristic polynomial for $s$

$$s = \frac{c_0}{2m_0} \pm \sqrt{\left(\frac{c_0}{2m_0}\right)^2 - \frac{k_0}{m_0}} = \zeta \pm \sqrt{\zeta^2 - \omega_n^2}. \tag{5.15}$$

Equating the term outside the discriminant, we have

$$c_0 = 2\zeta m_0, \tag{5.16}$$

where $\zeta$ is obtained from the experimental data set of each flexure setting. Next, equating the discriminant term and substituting equation 5.16, we have the damped frequency relation,

$$\omega^2 = \frac{k_0}{m_0} - \zeta^2 \rightarrow m_0 = \frac{k_0}{\omega^2 + \zeta^2}, \tag{5.17}$$

where we can solve for $m_0$ explicitly from $k_0$ values are in table 5.8 and $\omega$ and $\zeta$ values in table 5.7. This allows us to solve for $c_0$ from equation 5.16. Table 5.6 shows the calculated values for each flexure setting in table 5.5. The table also shows the estimated FEA stiffness and mass values for reference. All experimentally measured values fall under, but within the same order as the estimated FEA quantities.

Table 5.8: Table of calculated elastic-translating boundary condition properties for flexure settings in table 5.5.

| **Boundary Constant** | **Flexure 1** | **Flexure 2 (early time seg.)** | **Flexure 2 (late time seg.)** | **Flexure 3** | FEA |
|---|---|---|---|---|---|
| $k_0$ - (N/m) | 3.73E4 | 4.12E4 | 4.12E4 | 2.16E4 | 5.84E4 |
| $m_0$ - mean (kg) | 0.0274 | 0.0204 | 0.0201 | 0.0366 | 0.052 |
| $m_0$ - min (kg) | 0.0274 | 0.0205 | 0.0202 | 0.0385 | - |
| $m_0$ - max(kg) | 0.0274 | 0.0202 | 0.0200 | 0.0349 | - |
| $c_0$ - mean (kg/s) | 0.135 | 0.314 | 0.560 | 0.281 | 0 |
| $c_0$ - min (kg/s) | 0.139 | 0.319 | 0.598 | 0.316 | - |
| $c_0$ - max (kg/s) | 0.131 | 0.309 | 0.522 | 0.248 | - |

Non-dimensional parameters will be defined in the next section at critical $Q_{\text{cr}}$ values for the dimensional quantities in table 5.5 tested in the flowing conditions.

## 5.4 Flextensional Response to Fluid Flow Experiment

This section describes experiments of the flextensional energy harvester design in flowing conditions. The goal of the experiment is to primarily quantify the critical flow rate for different flexure properties, as discussed in previous sections and listed in table 5.5. The dynamics of the flowing system are assessed by measuring the voltage output from each piezoelectric stack, and by processing video images of the beam. The spectral proper orthogonal decomposition (SPOD) discussed in chapter 3 is applied with the video data set to characterize predominant beam modes and their amplitudes over time. As part of the data set, the maximum amplitude of individual modes will be assessed, as well as hysteric effects as the bifurcation is crossed while the system is in its self-sustained oscillating state (by decreasing the flow rate). In the same vein as previous sections, we are interested in critical parameter and the frequency response near the critical point. The following sections will discuss the test set up, the video processing algorithm, and present the stability results.

### 5.4.1 Flow Set up and Test Section

The test set up consists of lab air at standard pressure and temperature, once again defined as 101352.9 [Pa] (14.7 [psia]) and 21.1 [° C] (70 [° F]). The flow path, starting at the outlet of the lab air exhaust, follows onto a manual brass precision seal needle valve used to control the flow rate into the flow meter (Aalborg 1000 L/min air - 3/4" NPT, mass flow rate calibrated relative to STP). The flow then passes an upstream pressure gauge (G1 pressure transducer, 0-300 psi, ±0.5%) before entering the inlet to the test section shown in figure 5.4. A second pressure gauge is downstream of the outlet of the test section, and the exhaust air exits the system through a muffler to decrease audible noise. The pressure gauges are used for safety and rough validation of the flow rate, but the data set is not analyzed as part of the system dynamics. The voltage data acquisition is the same as that for section 5.3.2, where both piezo-stacks voltage responses are recorded accordingly. A LabView VI is used for interfacing with the DAQ, recording stack voltage, pressure, and flow rate data. Lastly, a camera (Z1 J5 Nikon 1200 fps) is set up directly facing the flextensional. The system records high speed video for 3 consecutive seconds for a total of 3600 images per video. Two sequential videos are taken as part of the data acquisition process, for a total of 7200 images per data point processed. The detailed experimental procedure can be found in appendix D.

Figure 5.27 shows a picture of the test set up with the data acquisition and control apparatus.

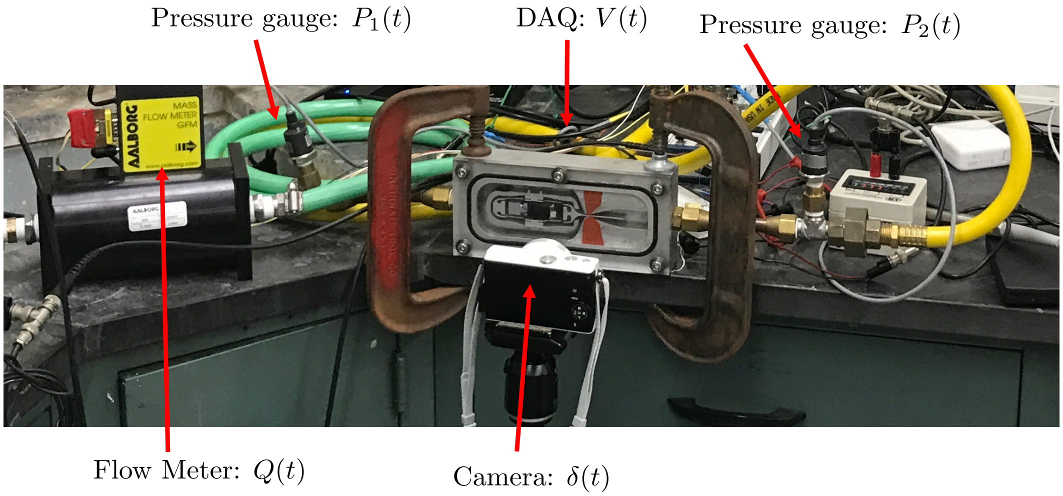

Figure 5.27: Flow test set up.

### 5.4.2 Video Data Processing Algorithm

The video data set is used primarily to characterize the transverse displacement of a section of the elastic beam. The algorithm uses the Canny filter [95] in MATLAB as an edge finding tool.

(a) Flow test raw video image.

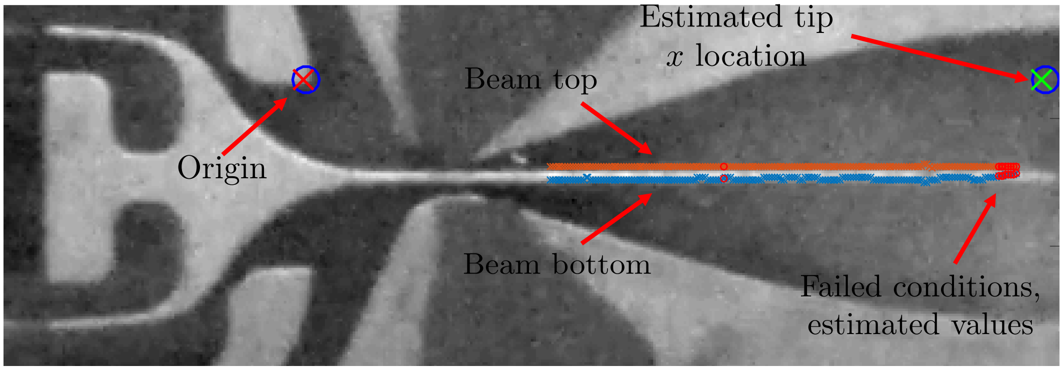

(b) Flow test processed video image.

Figure 5.28: Shows contrast of raw and processed video images for flow test.

Figure 5.28 shows an example of a raw and a processed video frame. The algorithm finds designated points within the image, uses a subset to calibrate and cross-check the scaling in $x$ and $y$ coordinates, and finds the beam $y$ position within a pre-defined search window. Quality assurance (QA) features highlighted in the image are the origin, marked as a red ×, and the predicted $x$ position of the beam tip, marked as a green ×. These are selected and manually verified for the first image of the video. The blue circles near the marked ×'s are the automatically identified features for subsequent images, and are cross-checked with the initial value to ensure accuracy of the edge finding filter properties: all images with more than 1.5 pixel variation are flagged for manual review.

The main features sought after are the beam top and bottom edges, shown as small light red and blue ×, respectively, in near the center of the image. The algorithm searches for beam edge locations within a pre-defined search window specified for every video processed. In reference to the geometry in figure 5.2, the search window begins at least 10 $\bar{h}$ from $L_2$ in the $+x$ coordinate and extends to $0.94L$. It spans past the farthest $y$ point along the diffuser walls, both above and below the channel center. Edges that qualify as part of the beam satisfy two conditions: first is a beam thickness criteria, where the $y$ spacing between two consecutive edges must satisfy,

$$h_w < \bar{h} + \mathrm{tol}_y, \tag{5.18}$$

where $\mathrm{tol}_y$ is a tolerance of 2 pixels converted to spatial dimensions with the image scaling. Second is a continuity criteria between two consecutive edge points in the $x$ coordinate,

$$\Delta y_c < \mathrm{tol}_x, \tag{5.19}$$

where $\mathrm{tol}_x$ is 2 pixels. The search scheme works as follows:

1. Find all image edge points within predefined search window;
2. Loop through all pixels along $x$ coordinate and apply condition 5.18;
3. For the subset of edge points that satisfy 5.18, apply condition 5.19;
4. If a top and bottom beam edge is not found for more than 10 discrete $x$ coordinate, iterate on Canny filver values and repeat all steps;
5. If no combination of edge finding filters are found that satisfy the 10 discrete point limit, flag image for manual review.

For the failed point locations, the algorithm estimates the beam edge by either interpolating between edges, or extrapolating at most 10 points. This is the case shown by red circles near the tip of the beam in figure 5.28. Through these processes, a representative data set for the transverse position of the beam was obtained with an accuracy of ±1.5 pixels. The conditional limits for what constitutes a flagged image where chosen through iteration and are a function of the image resolution and scaling. Values noted here worked well for the data sets presented. Over 500,000 images have been successfully processed with this algorithm in the current study.

### 5.4.3 Flexure Dynamics Results

The video and voltage data sets are processed for the three flexure settings over flow rates ranging from 5 to 500 [L/min]. Modal decomposition using SPOD discussed in section 3.4.2 is carried out for the beam transverse displacements obtained through the image processing algorithm. The voltage data set is processed through peak extraction to obtain average amplitudes over the relevant time signal, and fast Fourier transformed using Welch's method to obtain the signal frequency response. No other processing technique or filtering was applied to the voltage signals, as the system is responding to oscillatory forcing that satisfies condition 5.9[1].

#### Flexure Setting 1

Starting with flexure setting 1, results are aggregated and shown as two sets of plots, and kept consistent in subsequent flexure results subsections. The first, in figure 5.29, shows a single representative sample of the parameter space explored where the system has reached self-sustained oscillations. The sample data set shown in figure 5.29 is for flow rate $Q = 246$ [L/min], 38 [L/min] above the critical flow rate at 208 [L/min]. The spectrum shows a clear peak at $f_1 = 197$ [Hz], and the corresponding mode shown containing more than 99% of the energy in $f_1$. The phase diagram shows a limit cycle behavior and the mode shape resembles the rigid body motion of the cantilever base, denoting excitation of the flexure itself. A second peak occurs at $f_2 = 341$ [Hz], which corresponds to the fundamental mode of the clamped-free cantilever. This can be seen from the predicted value in table 5.4, and also from the mode shape shown. Though the extracted transverse displacement data does not reach the cantilever base, the mode shape monotonically decreases as $x/L$ decreases without any appearance of a node. The illustrated mode shape also contains over 99 % of the energy within $f_2$. The phase diagram shows the under-damped behavior, where the mode amplitude and velocity are perturbed around their equilibria through fluid forcing, but constantly decay down toward it. The under-damped mode is evident where states are gathered around the origin, as a bunched set of points. The periodicity can be verified through the strong spectral response in the power spectrum shown

A distinct third and fourth peak at 394 [Hz] and at 591 [Hz] are also evident on the spectrum, and represent the second and third harmonics of the primary peak.

---

[1] The system is not responding to a constant force, as it did in section 5.3.2, giving rise to the exponential decay from the RC circuit.

The second set of plots, shown in figure 5.30, display the aggregate of amplitude and frequency responses as a function of flow rate. The error bars correspond to the standard deviation of the time series data, which can be seen in the phase diagram as the thickness of the "doughnut" edges at $\dot{a}_1 = 0$. Figure 5.30 shows the amplitude of the displacement of mode 1 over the range of flow rates tested, first increasing then decreasing. Recall that the amplitude is found from the SPOD analysis at the frequency identified as mode 1, and corresponds to the y-axis in the phase diagram shown in figure 5.29. The primary mode amplitude remains small until a critical flow rate $Q_{\mathrm{cr}} = 208$ [L/min]. The critical point clearly demarcates a transition to high-amplitude oscillation. Increasing the flow rate beyond $Q_{\mathrm{cr}}$, however, does not change the amplitude much, there is eventually slightly decrease in amplitude as the beam collides with the throat at the highest flow rate tested (at $\sim$ 400 [L/min]). The frequency response appears constant until $Q_{\mathrm{cr}}$ is reached, at which point it increases slightly with increasing flow rate. A small hysteresis loop is evident as the flow rate is decreased through $Q_{\mathrm{cr}}$. The system does not recover to the original zero equilibrium until $Q_{\mathrm{r}} = 179$ [L/min]. This hysteresis suggests that the system is undergoing a subcritical Hopf bifurcation as $Q$ increases, giving rise to the bi-stable region captured with the hysteresis loop.

The voltage response is shown in figure 5.31 with its amplitude and frequency closely following the behavior of the primary mode in figure 5.30. A one-to-one correspondence between the displacement and the resulting voltage output. This is expected as the piezoelectric coupling is quasi-static in the sense that the stack voltage tracks the strain of the flexure, as discussed in section 5.2.1.

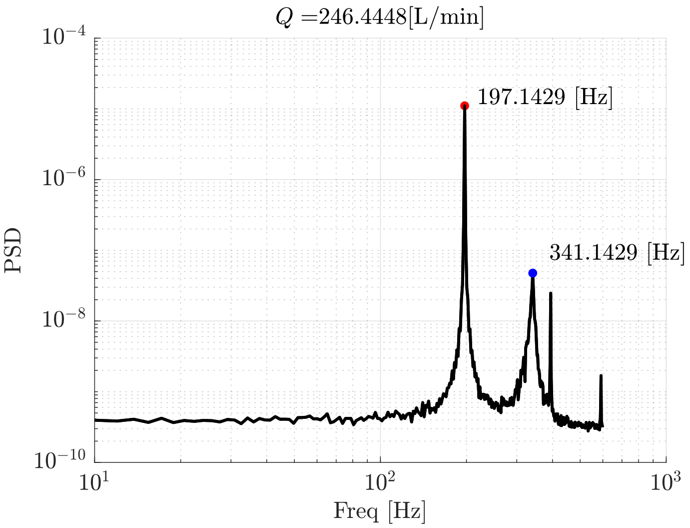

(a) Trace of cross-spectral density matrices at discrete frequencies.

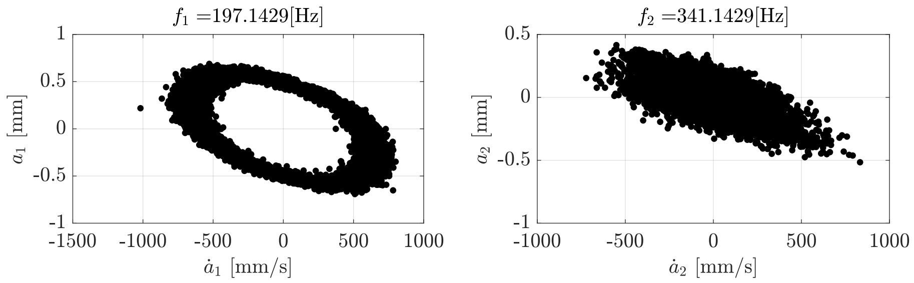

(b) Phase diagrams for mode 1 (left) and mode 2 (right).

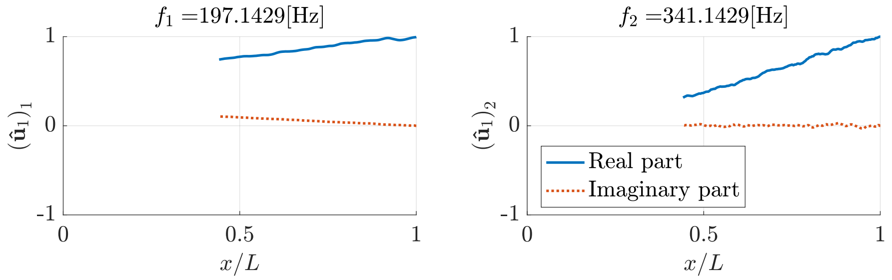

(c) SPOD mode shapes for mode 1 (left) and mode 2 (right).

Figure 5.29: Representative SPOD data processed results for flexure setting 1in table 5.5 showing self-sustained oscillating regime of mode 1 and under-damped regime of mode 2.

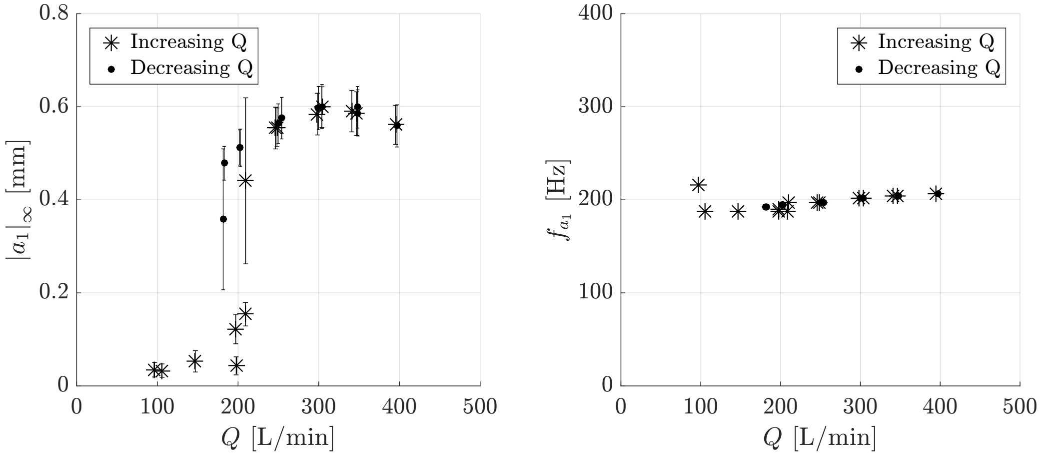

(a) Mode 1 amplitude as a function of flow rate.

(b) Mode 1 frequency response as a function of flow rate.

Figure 5.30: Video data set showing mode 1 amplitude and frequency as a function of flow rate for flexure setting 1.

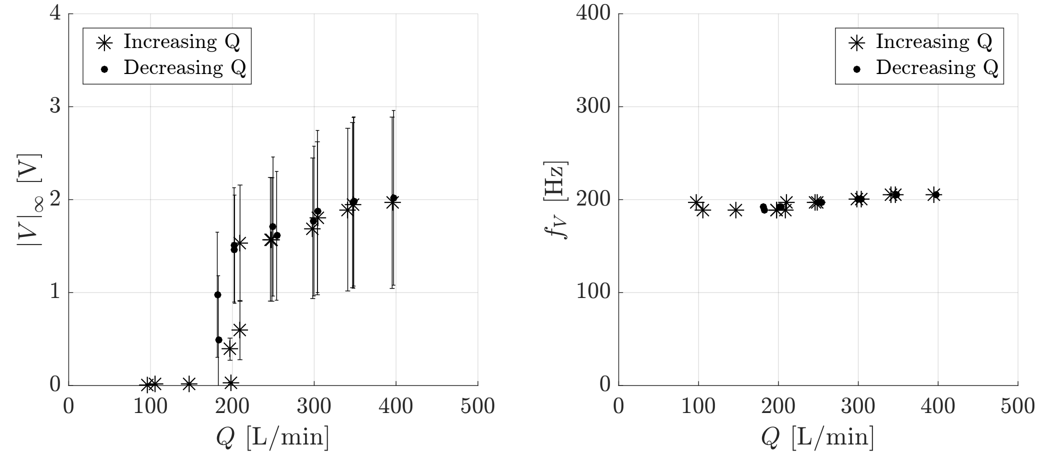

(a) Piezoelectric voltage amplitude response as a function of flow rate.

(b) Piezoelectric frequency response as a function of flow rate.

Figure 5.31: Representative voltage amplitude and frequency response for top piezoelectric stack in flexure setting 1.

### Flexure Setting 2

Flexure setting 2 results are shown in figure 5.32 for $Q$ = 387 [L/min]. Once again, the spectrum has a distinct peak but at a higher frequency of $f_1$ = 226 [Hz] than flexure setting 1. The phase diagram shows the limit cycle behavior and the mode shape appears mostly as the excitation of the flexure, as before. The system dynamics exhibit strong coherence with mode 1 containing over 99 % of the energy within $f_1$. A second mode also occurs at the fundamental clamped-free beam frequency of $f_2 = 342$ [Hz] and displays the under-damped regime in the phase diagram of its amplitude and velocity. Mode 2 shows a similar level of coherence within $f_2$ as mode 1 within $f_1$, where it contains over 99 % of the energy in $f_2$.

Results of leading mode displacement and frequency in $Q$ parameter space are shown in figure 5.33. The onset of flutter happens at $Q_{\mathrm{cr}} = 376$ [L/min], almost twice that of flexure 1. Mode amplitudes are comparable to those in figure 5.30, yet the frequency response does not appear to change as flow rate increases. The voltage amplitude and frequency response can be seen in figure 5.34. Once again, the displacement and voltage data sets are in good agreement. An increase in voltage output magnitude by an additional $0.5V$ is evident relative to flexure 1. The hysteresis loop ends at a flow rate of $Q_{\mathrm{r}} = 334$ [L/min] and is approximately the same size as of flexure 1. This flexure configuration also represents the response with the largest voltage magnitude.

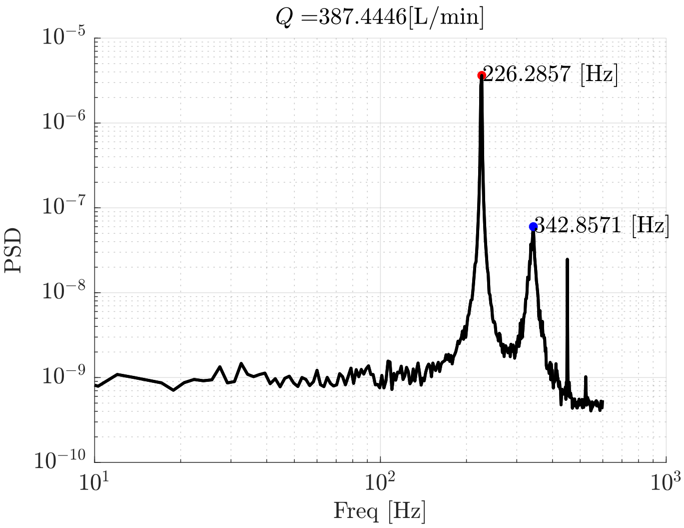

(a) Trace of cross-spectral density matrices at discrete frequencies.

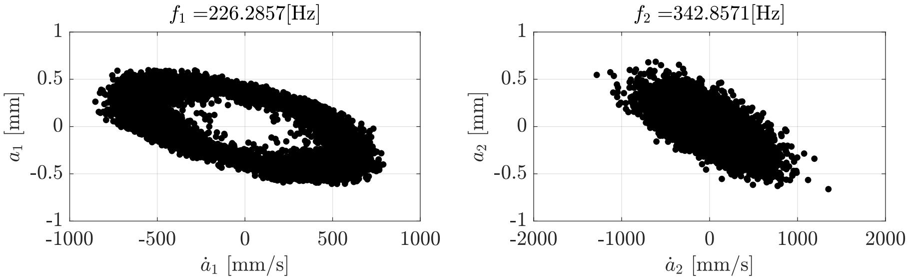

(b) Phase diagrams for mode 1 (left) and mode 2 (right).

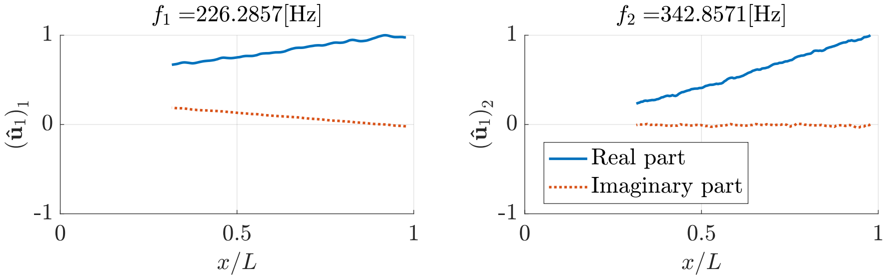

(c) SPOD mode shapes for mode 1 (left) and mode 2 (right).

Figure 5.32: Representative SPOD data processed results for flexure setting 2in table 5.5 showing self-sustained oscillating regime of mode 1 and under-damped regime of mode 2.

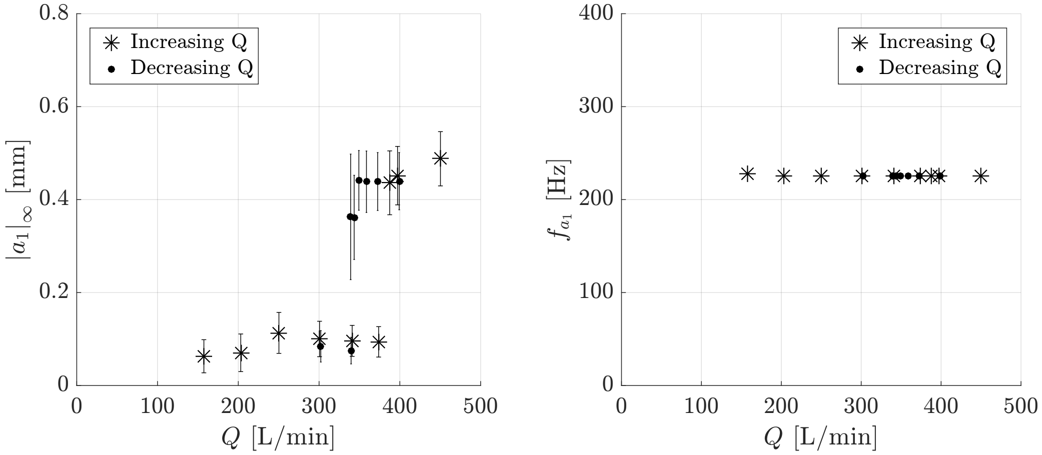

(a) Mode 1 amplitude as a function of flow rate.

(b) Mode 1 frequency response as a function of flow rate.

Figure 5.33: Video data set showing mode 1 amplitude and frequency as a function of flow rate for flexure setting 2.

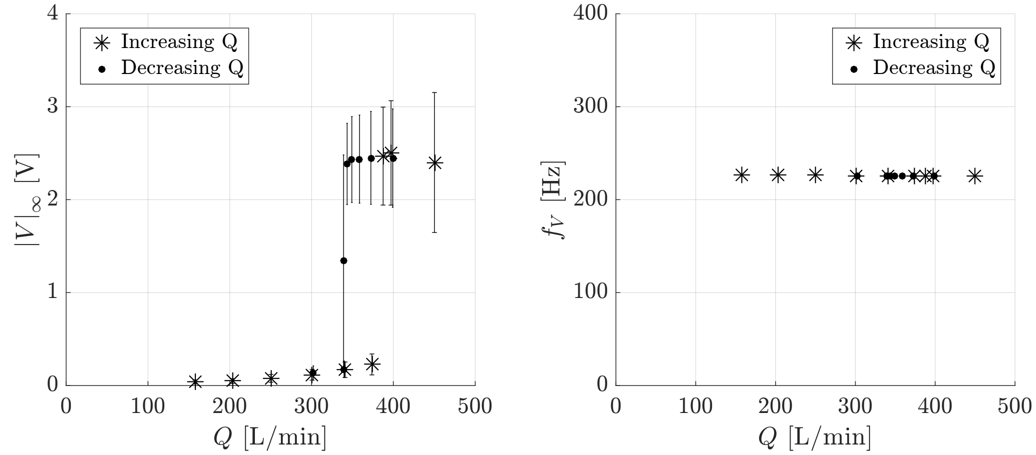

(a) Piezoelectric voltage amplitude response as a function of flow rate.

(b) Piezoelectric frequency response as a function of flow rate.

Figure 5.34: Representative voltage amplitude and frequency response for top piezoelectric stack in flexure setting 2.

### Flexure Setting 3

Figure 5.35 shows a representative data point from flexure setting 3 at a $Q = 449$ [L/min]. The spectrum shows a leading peak at $f_1 = 154$ [Hz], with its leading mode also presenting limit cycle behavior in its phase space. The second peak in the spectrum is the second harmonic of the first peak at 308 [Hz], and the third peak corresponds to the under-damped fundamental beam mode at $f_2$ = 341 [Hz]. Mode 2 is still chosen at $f_2$ = 341 [Hz] for the mode projection step. Mode shapes once again agree with the previous two flexure configurations. Mode 1 amplitude as a function of $Q$ however, presents a considerably larger hysteresis loop than either flexure 1 or 2, with $Q_{\text{cr}}$ = 410 and $Q_{\text{r}}$ = 73 [L/min]. The displacement frequency response also presents a stronger correlation to $Q$, as a shift of over 25 [Hz] occurs at the onset of flutter but monotonically decreases to the initial value as flow rate is also decreased to zero. An new phenomenon can be seen in figure 5.37; though the voltage amplitude tracks the mode 1 displacement well, *the frequency response is a factor of two higher*. This effect is caused by lightly pre-stressed piezoelectric elements, as this flexure configuration represents conditions with the least amount of torque applied on the set-screw. The phenomenology is as follows: once the oscillation reaches the full extension at either the top or bottom of the flextensional stroke, the decompressed stack looses contact with the structure. This in turn causes a strongly nonlinear response that flips the sign of the voltage output, and appears as a frequency doubling through the FFT. The nonlinear loss-of-contact behavior has been observed by Sherrit et al. [96] as flextensional actuators loose their bond between stacks and the flexure. Voltage amplitudes are also notably lower in flexure setting 3 than the other two flexure configurations.

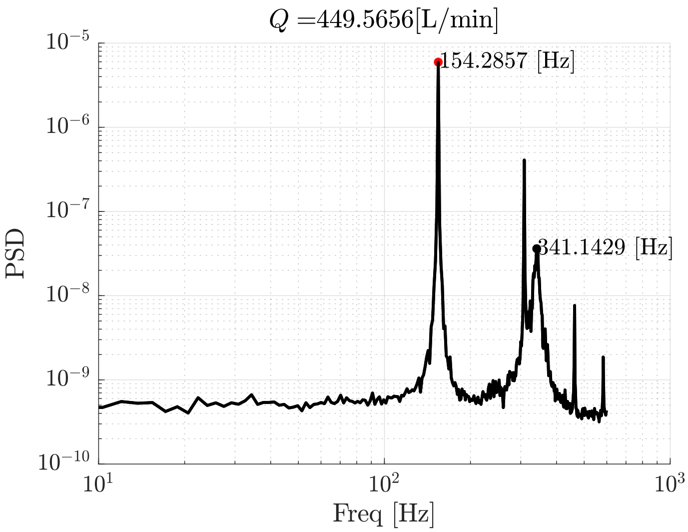

(a) Trace of cross-spectral density matrices at discrete frequencies.

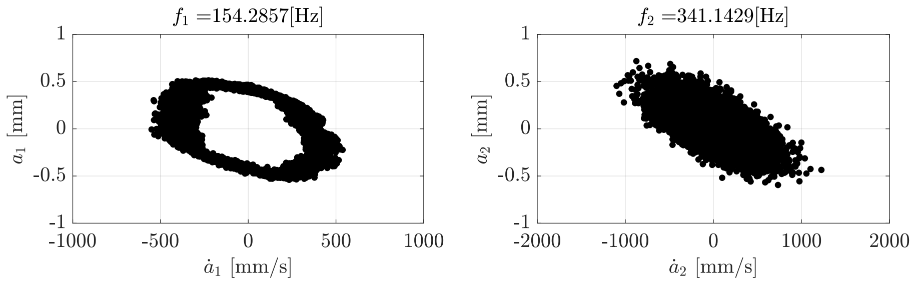

(b) Phase diagrams for mode 1 (left) and mode 2 (right).

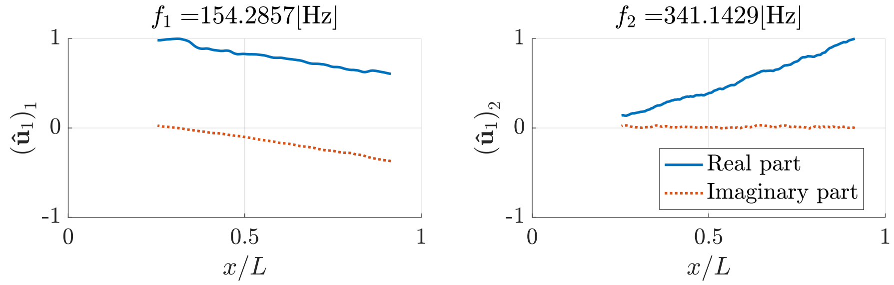

(c) SPOD mode shapes for mode 1 (left) and mode 2 (right).

Figure 5.35: Representative SPOD data processed results for flexure setting 3in table 5.5 showing self-sustained oscillating regime of mode 1 and under-damped regime of mode 2.

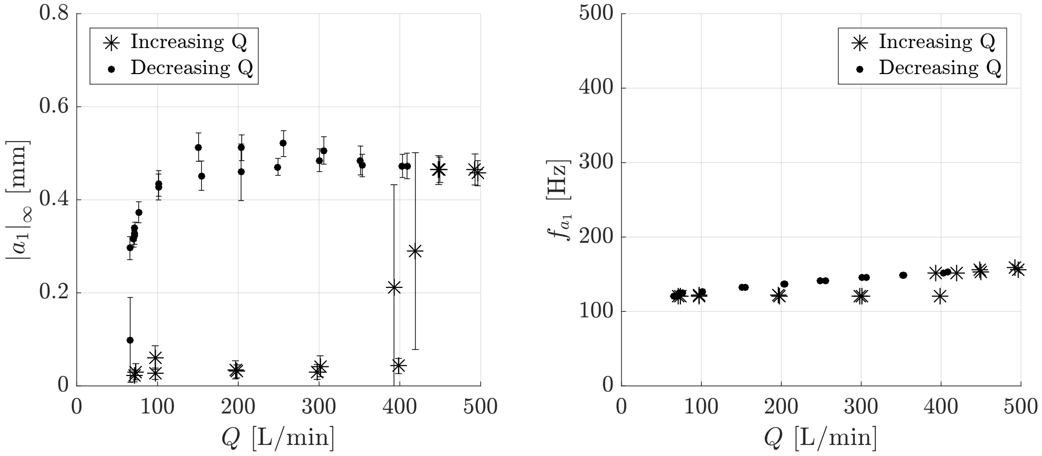

(a) Mode 1 amplitude as a function of flow rate.

(b) Mode 1 frequency response as a function of flow rate.

Figure 5.36: Video data set showing mode 1 amplitude and frequency as a function of flow rate for flexure setting 3.

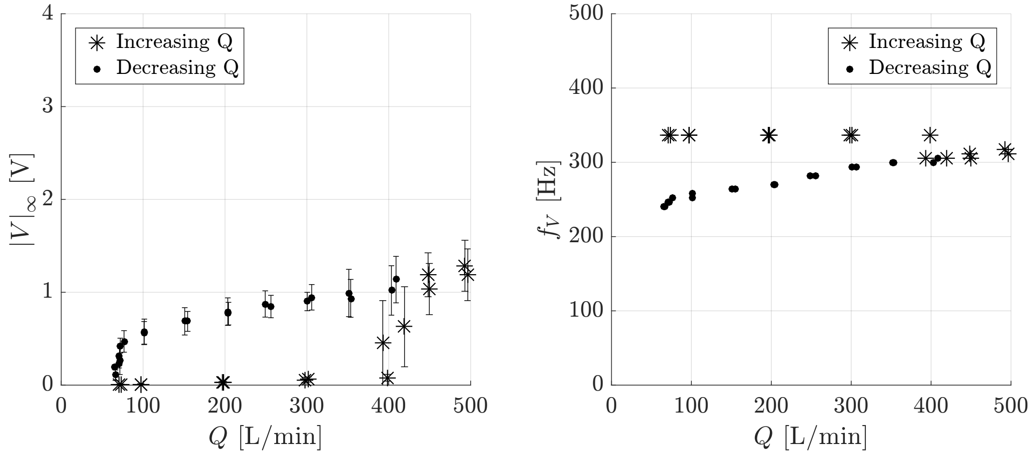

(a) Piezoelectric voltage amplitude response as a function of flow rate.

(b) Piezoelectric frequency response as a function of flow rate.

Figure 5.37: Representative voltage amplitude and frequency response for top piezoelectric stack in flexure setting 3.

## Discussion

We can conclude from the results that flexure properties have a significant effect on the stability properties of the system. Many aspects of the system response remain the same between flexures, including the existence of a bi-stable region and hysteresis loop, and strong self-sustaining oscillations after the critical point.

All other modes remain stable for the parameter space spanned. Lastly, it appears that the larger the structural stiffness, the greater the piezo-element output voltage. This is particularly evident when comparing voltage output from flexures 2 and 3, the most and the least pre-stressed setting. Table 5.9 in the next section presents a compilation of all results for each flexure setting, including the relevant non-dimensional parameters for the flow. Table 5.10 in the next section shows fluid-structure non-dimensional values as defined in tables 2.3 and 2.4 in chapter 2.

### Mach Number Calculation at $Q_{\text{cr}}$

To understand the compressibility effects at the critical flow rate of the different flexure settings presented, we estimate the Mach number at the throat first using the speed of sound at STP, followed by a more detailed analysis using isentropic relations. Assuming initially the that flow is near the incompressible limit,

$$\mathcal{M}_{\text{STP}} = \frac{Q_{\text{cr}}}{A_t}\frac{1}{a_{\text{STP}}} = \frac{U_{\text{cr}}}{a_{\text{STP}}}, \tag{5.20}$$

where $a_{\text{STP}}$ is the speed of sound for air at STP, and $A_t = b_1(2\bar{h} + h_b) - bh_b$ is the area at the throat of the flow path from figure 5.2a and dimensions in table 5.1. The speed of sound can be estimated using the ideal gas law,

$$a = \sqrt{\gamma_{\text{g}} R_{\text{g}} T}, \tag{5.21}$$

where $R_{\text{g}} = 287.0$ [kg/J/K] is the specific gas constant for air, $\gamma_{\text{g}} = 1.40$ is the ratio of specific heats for air [97], and $T$ is the local temperature. At STP, $a_{\text{STP}} = 344.3$ [m/s].

The speed of sound calculation must account for compressibility effects as Mach number approaches 1. The simplest analysis in this vein assumes that the flow acceleration over the converging section of the flow path happens isentropically for an ideal gas. Though pressure data was taken within the each experimental run, the pressure tap locations and dynamic nature of the pressure signal are not reliable enough to estimate the stagnation pressure to acceptable accuracy. Hence, we choose to use the stagnation temperature $T_o = T_{\text{STP}} = 295$ [K], the stagnation density $\rho_o = \rho_{\text{STP}} = 1.20$ [kg/m$^3$], and the mass flow rate measurement at the critical flow rate,

$$\dot{m}_{\text{cr}} = \rho_{\text{STP}} Q_{\text{cr}} = \rho_t A_{\text{t}} U_{\text{cr}}, \tag{5.22}$$

to estimate the throat Mach number [98]. Considering equation 5.21, the definition of mass flow rate 5.22, and stagnation temperature $T_o$ and stagnation density $\rho_o$ isentropic ratios to their respective throat values,

$$\frac{T_o}{T_t} = 1 + \frac{\gamma_g - 1}{2}\mathcal{M}_{\text{t}}^2, \tag{5.23}$$

$$\frac{\rho_o}{\rho_t} = \left(1 + \frac{\gamma_g - 1}{2}\mathcal{M}_{\text{t}}^2\right)^{\frac{1}{\gamma_g - 1}}, \tag{5.24}$$

we have

$$\frac{\dot{m}_{\text{cr}}}{\sqrt{\frac{\gamma_g R_g T_o}{1+\frac{\gamma-1}{2}\mathcal{M}_{\text{t}}^2}}\mathcal{M}_{\text{t}} A_{\text{t}}} = \frac{\rho_o}{\left(1 + \frac{\gamma-1}{2}\mathcal{M}_{\text{t}}^2\right)^{\frac{1}{\gamma-1}}}. \tag{5.25}$$

Equation 5.25 is an implicit relation between the fluid and flow properties and $\mathcal{M}_{\text{t}}$, and is valid for $\mathcal{M}_{\text{t}} \leq 1$ for air values. Table 5.9 shows $\mathcal{M}_{\text{t}}$ values using approaches described.

Table 5.9: Table of critical values for flexure settings listed. The critical velocity, Reynolds and Mach numbers are calculated at the throat.

| **Critical Properties** | **Flexure 1** | **Flexure 2** | **Flexure 3** | **Description** |
|---|---|---|---|---|
| $Q_{\text{cr}}$ [L/min] | 208 | 376 | 410 | critical flow rate |
| $U_{\text{cr}}$ [m/s] | 163 | 286 | 313 | critical velocity |
| $\mathcal{M}_{\text{STP}}$ | 0.47 | 0.83 | 0.91 | incompressible throat Mach number est. |
| $\mathcal{M}_{\text{t}}$ | 0.53 | 1 | 1 | compressible throat Mach number est. |
| $\rho_{\text{t}}$ [kg/m$^3$] | 1.05 | 1.07 | 1.17 | throat density est. |
| $Re_{L\text{cr}}$ | 4.00E+05 | 7.35E+05 | 8.00E+05 | critical length Reynolds number |
| $Re_{h\text{cr}}$ | 6.1E+05 | 1.1E+04 | 1.20E+04 | critical gap Reynolds number |

Equation 5.25 suggests that the flow path with dimensions in table 5.1 chokes at $Q_{\text{ch}} \approx 267$ [L/min], implying that flexure setting 2 and 3 are choked at their critical flow rates $Q_{\text{cr}}$ of 376 and 410 [L/min], respectively. An important note is that both $Q_{\text{cr}}$ values are distinct and *higher* than $Q_{\text{ch}}$, as opposed to equal to it as a choked condition would require. This is possible because the flow meter measurements represent a mass flow rate rather than a purely volumetric one. Since the flow control (needle) valve is upstream of the flow meter and the test section, by further

opening the valve, we are increasing the upstream flowing and stagnation pressures, which, in turn, increase the density at throat and allows for the higher mass flow rate through the system. This happens despite the *volumetric* flow rate remaining constant in the choked condition. To estimate the throat density for the choked settings, we can solve for $\rho_\mathrm{t}$ in equation 5.22 by substituting $U_\mathrm{cr} = a_\mathrm{t}$ using equation 5.23 to solve for $T_\mathrm{t}$, followed by solving equation 5.21 for $a_\mathrm{t}$. The incompressible estimates for $\mathcal{M}$ for those same settings, also note in table 5.9, though not implying choked flow, do suggest that compressibility likely plays a strong role in the flow response with values close to 1.

Compressible and incompressible estimates for flexure setting 1 throat Mach number are with 15% of one another, and suggest the flow may have some compressibility effects ($\mathcal{M} \sim 0.5$), but that it is not choked. The compressible estimates for density at the throat are lower than the STP value, suggesting the compressibility affects the mass ratio parameter between the solid and the structure. These dynamics are relevant in the next section as we attempt to replicate these results using models derived in chapter 2.

### Fluid-Structure Non-Dimensional Parameters

The remaining parameters defined in tables 2.3 and 2.4 are calculated in table 5.10 at the critical velocity values, and include the definition of $M^*$ and $U^*$ in equation 4.6.

Table 5.10: Table of experimental non-dimensional parameters for tested flexure setting.

| **Flex Cond.** | $\hat{m}$ | $\hat{k}_\mathrm{cr}$ | $M^*$ | $U^*_\mathrm{cr}$ | $\hat{m}_\mathrm{bc}$ | $\hat{k}_\mathrm{bc,cr}$ | $M^*_\mathrm{bc}$ | $U^*_\mathrm{bc,cr}$ | $\hat{c}_\mathrm{bc,cr}$ |
|---|---|---|---|---|---|---|---|---|---|
| Flex. 1 | 38.70 | 1.121 | 0.0258 | 5.87 | 970.21 | 91.132 | 0.0010 | 3.263 | 1.260 |
| Flex. 2 - seg. 1 | 38.70 | 0.343 | 0.0258 | 10.62 | 718.67 | 30.804 | 0.0014 | 4.830 | 1.630 |
| Flex. 3 | 38.70 | 0.288 | 0.0258 | 11.58 | 1329.5 | 13.582 | 0.0008 | 9.894 | 1.340 |

## 5.5 Comparison with Quasi-1D Model

We discuss the comparison between model prediction of critical properties and experimental results in this section. We begin by highlighting the shortcomings of modeling the experimental geometry and flowing conditions with the framework derived in chapters 2 and 4. Next, we propose a simplified geometry applied to the quasi-1D model that considers spanwise leakage flow, derived in section 2.4, and compare its predictions to experimental results.

### 5.5.1 Discussion of Modeling Assumptions for Experimental Comparison

A number of potential issues arise when comparing experiments to models in chapters 2 and 4. Though some have been discussed, we will highlight those we believe most relevant in the context of contrasting experimental conditions to model assumptions and restrictions in the subsections to follow. We will begin with flow three-dimensionality and turbulence, followed by flow separation, and compressibility.

#### Flow Three-Dimensionality and Turbulence

The flow path in the experiment has a spanwise gap between the channel wall and the flexure of $C = (b_1 - b)/2 = 1.25$ [mm], with spanwise gap-to-length ratio $\frac{C}{L} = 0.031 \gg 10^{-4}$. This indicates that, at least for the transversely unconfined flag case, the spanwise flow plays a significant role in the stability properties of the system, increasing the critical velocities necessary for the flutter onset in a given flag configuration. As discussed in section 2.1, this is expected to be the case in the experimental flow path as well, which renders both 2D DNS and the "axial only" quasi-1D model, both discussed and compared in chapter 4, inadequate tools to predict the experimental dynamics. The critical gap Reynolds number $Re_h \gg 1000$ for all flexures tested, ensuring that the flow is fully turbulent as well. This further ascertains that the 2D DNS will not capture the appropriate viscous effects due to its low Reynolds number limitations, and that we must consider a turbulent friction factor correlation within the quasi-1D model (as in equation 2.29). The inadequacy of the axial quasi-1D model is validated when experimental conditions and parameters are applied, and no aspect for the experimentally observed regime is evident in its results. Specifically, the model predicts an unstable flextensional mode at a critical flow rates $< 2$ [L/min] and only through a divergence instability rather than flutter. This holds true for all experimental flexure properties and also when parameters are varied through a range of inlet and outlet loss coefficients, diffuser expansion angles, throat sizes, throat positions, denoting that the divergence prediction is robust to a wide range of model parameters. These results were essential in the motivation for the development of the quasi-1D model in section 2.4, which considers flow in the the spanwise direction of the beam.

### Flow Separation and Simplified Modeled Geometry

A linear plane-asymmetric diffuser consists of a diffuser with a flat lower boundary and an upper surface that expands at a constant angle $\theta$. This diffuser configuration captures the essence of the geometry of our experimental flow path, illustrated in figure 5.2, while the beam is near its equilibrium point. High Reynolds number numerical and experimental studies suggest a $\theta_{\mathrm{cr}} \approx 7°$, independent of Reynolds number for turbulent flows, where flow separation is triggered over the upper diffusing wall [99–102]. As $\theta = 19° > \theta_{\mathrm{cr}}$ for our experimental set up, the flow regime realized is one with a separation bubble that extends the entirety of the beam length for all three flexure settings. Flow separation is not explicitly accounted for within the formulation of the quasi-1D models, as the pressure distribution over $x$ is calculated for attached flow: a change in channel geometry would change the force the beam. However, the model allows for anisentropic type phenomena at its inlet and outlet boundary conditions. To account for flow separation within the quasi-1D model, we propose a simplified geometry shown in figure 5.38. The figure shows the model geometry, consisting of a diffuser with angle $\alpha_m$ and an abrupt expansion at its outlet. Three distinct features have been simplified: first the contraction section has been removed under the assumption that losses there are negligible, such that $\zeta_{\mathrm{in}} = 1$ in equation 2.45. This assumes that the net force contribution from the converging section is also negligible. Second, we assume that the outlet boundary pressure variation behaves as an abrupt expansion exists at the outlet, where $\zeta_{\mathrm{out}} = 1$ from equation 2.40.

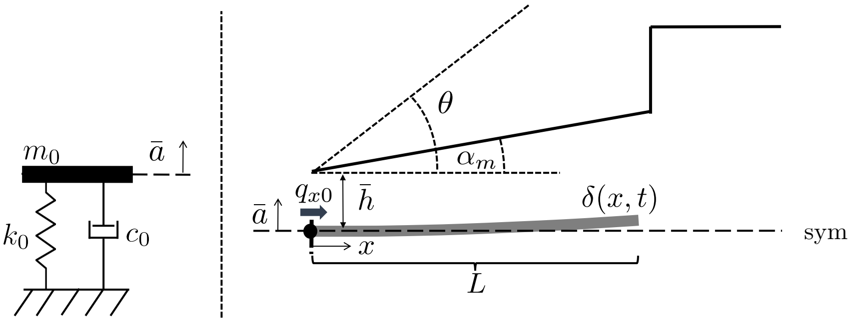

Figure 5.38: Illustration of spanwise quasi-1D geometry for comparison to experimental results.

Third is that the separation bubble over the diffusing channel walls effectively serve as a secondary diffuser boundary at an effective expansion angle of $\alpha_m$. The pressure distribution on the beam surface behaves as if the flow had been attached and expanding at an angle of $\alpha_m$. Because of separation characteristics of plane-asymmetric diffuser, we believe $\alpha_m \approx \theta_{\mathrm{cr}}$. Though this cannot be shown in experimental results, we assess critical flow rates over a range of $\alpha_m$, and discuss model results in the context of a range of effective angles simulated. In addition, in order to remain consistent with $h_0'^2 \ll 1$ criteria, we upper bound our results to $\alpha_m \leq \theta_{\mathrm{cr}} = 7$ [°], where $h_0 \approx 0.12$. The geometrical parameters in the simplified geometry are those of table 5.1, except the throat position $L_2 = 0$. The fluid, structural, and flexure properties are those of table 5.3 and the mean values in table 5.8.

### Compressibility

As shown in table 5.9 and described in section 5.4.3, critical flow regimes for flexures 2 and 3 are choked, while flexure 1 remains subsonic. Since throat Mach numbers are unity for the former two cases, and a relatively large expansion exists downstream of the throat, it is likely that a combination of shocks and expansions follow. The lack of detailed pressure measurements immediately downstream of the throat make it difficult to ascertain the actual flow regime, as another possibility exists where the flow continues to accelerate into the supersonic range. However, evident by the audible noise from the test section during flexure 2 and 3 runs as similar to that of flexure 1 runs, we do not believe this to be the case, nor the shocks to be particularly strong such that they extend a significant distance downstream of the throat. We believe it reasonable to assume that the flow becomes subsonic relatively quickly after bypassing the channel throat, and that the system expands as suggested in figure 5.38. However, these effects are not negligible and likely account in large part for quantitative discrepancies seen in the results shown in the next section when comparing experimental measured critical values to those predicted by the incompressible quasi-1D model.

In the flexure 1 case, where the flow remains subsonic, compressibility effects may be significant particularly if the structural response time scale is on the order of the sonic flow speed. However, the flutter instability gives rise to a response at $f_1 \sim 200$ [Hz], while the length based flow acoustic frequency is $f_a \sim 8.3\mathrm{E}3 \gg f_1$. This means that flow "information" in the form of an acoustic wave can travel multiple times the length of the cantilever, and that the flow has enough time to adapt to changes in the structure's shape. Hence, we believe that the effect of compressibility is likely localized near the throat and that its primary effects is *decreasing* the density of the fluid by $\approx 10\%$, consequently changing the mass ratio within that local region. Given the localization, limited density change, and the quasi-static behavior of structure relative to flow, we expect the incompressible model to be able to replicate flexure 1 experimental response well as compared to those of flexures 2 and 3.

These descriptions from values in table 5.9 are only valid for throat sizes near the equilibrium position of the beam; they are no longer valid once deflection amplitudes grow large at unstable flutter cases. The physics that drive the fluid-structure system in high amplitude cases may include a fluctuating Mach number, and significantly alter the flow regime and dynamics discussed here. These are not captured by the linear stability analysis in the subsequent model results.

### 5.5.2 Experimental Comparison to Spanwise Quasi-1D Model

The tool developed that has the ability to address most of the aforementioned issues, and more tractably be compared with experiments, is the incompressible quasi-1D model with spanwise leakage flow (derived and discussed in section 2.4).

As discussed in section 5.5.1, figure 5.38 shows the simplified model geometry consisting of a diffuser with angle $\alpha_m$ to account for flow separation. The geometrical parameters are those of table 5.1, except the throat position $L_2 = 0$. The fluid, structural, and flexure properties are those of table 5.3 and the mean values in table 5.8.

In the results to follow, we assess and discuss critical flow rates over a range of $\alpha_m$, with the hypothesis based on the idea that, if the true diffuser angle $\theta$ is large enough such that the flow is separated over most of its length, the resulting pressure profile on the beam surface is similar to that of a diffuser near the separation angle $\theta_{\text{cr}}$. Since $\theta = 19^\circ > \theta_{\text{cr}}$ in figure 5.2, we characterize the flutter boundary for the flextensional mode for diffuser angles $\alpha_m = [1-7]^\circ$ for flexure setting 1 and 3, and $\alpha_m = [2-7]^\circ$ for flexure settings 2 (the flextensional mode was stable $\alpha_m = 1^\circ$). The range of flow rates simulated is $q_{x0}$ =[0 - 500] [L/min]. Only the primary flexure mode is considered for comparison with experiments. The modeled cantilever beam modes are not relevant for experimental comparison due to the absence of material damping terms, which most likely dominate the stability of the physical beams [59], especially at higher modes. This is in contrast with the flexure mode, where we have explicitly accounted for material damping in the model and by measuring flexure properties in sections 5.3.1 and 5.3.2. Our retention of only the flexure mode is supported by the experimental results presented in section 5.4, where for the flow rates considered, only the flexure mode was excited.

Beginning with flexure setting 1, figure 5.39 shows the spanwise quasi-1D model results for the dimensional critical flow rates and frequency responses over $\alpha_m$, along with the corresponding mean experimental values from table 5.9. The stability boundary trend has a convex shape, with a $\alpha_m \approx 3^\circ$ representing the lowest critical flow rate over the range of diffuser angles tested. Both quasi-1D critical flow rate of 213 [L/min] and the critical frequency of 190 [Hz] at $\alpha_m = 7^\circ$ appear to replicate the experimental values of 208 [L/min] ans 187 [Hz] remarkably well. Figure 5.40 shows a representative mode 1 shape near the critical point at $\alpha_m = 7$ [°]. The mode shapes, both displacement and spanwise flow segments, are similar for all $\alpha_m$ values shown in figure 5.39. The beam shape agrees well qualitatively with the experimental flextensional mode in figure 5.29. This can be seen primarily from the dominant rigid body motion content, evident by the translation of the base. The leakage flow rate mode shows an almost linear trend from channel inlet to outlet, with flow direction switching from into-the-channel, or negative direction, at the inlet to out-of-the-channel, or positive, at the outlet. The inlet spanwise flow direction is opposite that of the inlet axial flow term and of the same magnitude. Hence, the model indicates that as flow enters the inlet axially, it leaves in the spanwise direction at the same time. This trend remains true for all three modeled flexure setting results, and highlights the importance of the leakage flow terms in addition to the axial flow boundary condition.

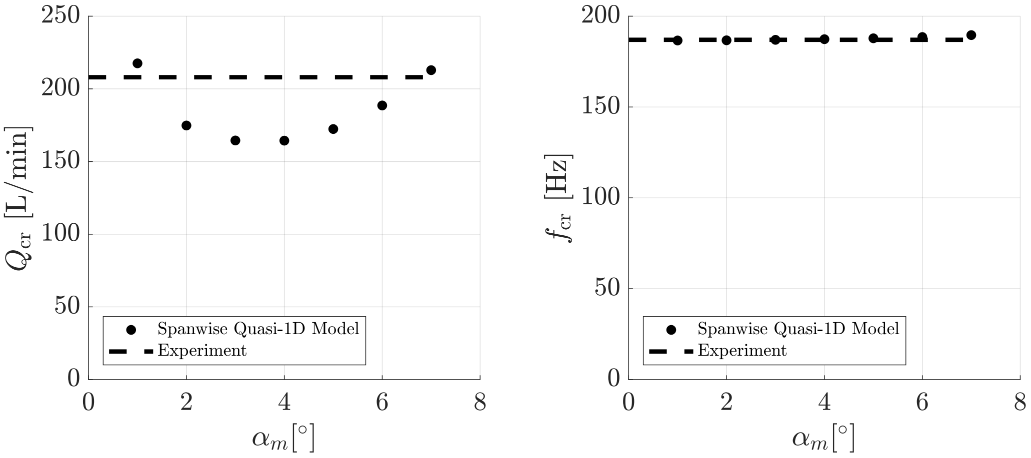

(a) Critical flow rate versus diffuser angle.

(b) Critical frequency versus diffuser angle.

Figure 5.39: Comparison between spanwise quasi-1D critical flow rate (left) and frequency (right) to experimental quantities for flexure setting 1 from table 5.5.

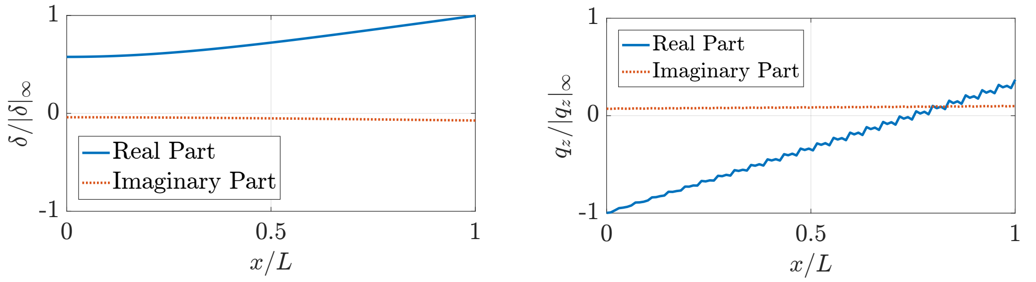

(a) Transverse displacement mode 1.

(b) Spanwise leakage flow rate mode 1.

Figure 5.40: Flexure setting 1 representative mode 1 plots of transverse displacement (left) and spanwise leakage flow (right) at $\alpha_m = 7$ [°].

Figure 5.41 shows results for flexure setting 2. The early time segment variant was chosen because voltage amplitudes in the data point near the bifurcation in figure 5.34 are $\sim$ 0.2 [V], well within the early time segment amplitude bound. Though the stability boundary convexity still remains, the comparison of values between experiments and model are no longer in good agreement. The frequency is overestimated by about 10%, and, if we keep the calibration of $\alpha_m = 7°$, we over-predict the critical flow rate by about 25%. A representative mode 1 shape is shown in figure 5.42 for both transverse displacement and spanwise flow. The flexure base displacement is evident though not as pronounced as that of flexure 1, but still reproduces the shape of the experimental result in figure 5.32 qualitatively well. The spanwise leakage flow is similar to results from flexure 1, with a linear trend and opposing flow directions between inlet and outlet spanwise flows, as well as inlet spanwise and inlet axial flows. Figure 5.43 shows critical property results for flexure 3, with figure 5.44 showing its representative mode 1 shape. These echo the descriptions of flexures 2: the convex shape of $Q_{\text{cr}}$ as a function of $\alpha_m$, with a model over-prediction of critical flow rate and frequency at $\alpha_m = 7$ [°]. Here, however, beam shape only replicates the base motion seen in flexure 3 experimental data in figure 5.35, missing the correct traveling wave form. The leakage flow rate mode shape is similar to those of flexures 1 and 2.

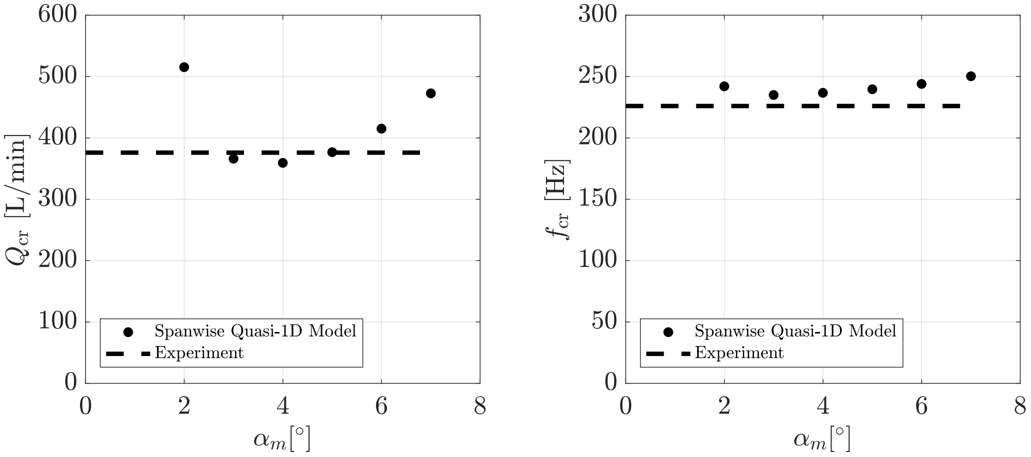

(a) Critical flow rate versus diffuser angle. (b) Critical frequency versus diffuser angle.

Figure 5.41: Comparison between spanwise quasi-1D critical flow rate (left) and frequency (right) to experimental quantities for flexure setting 2 from table 5.5.

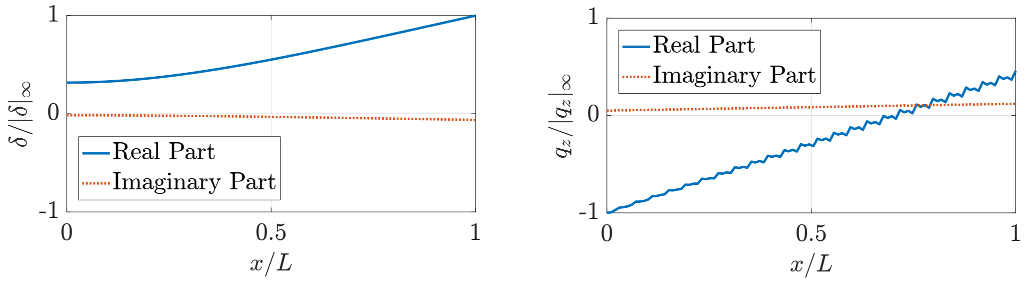

(a) Transverse displacement mode 1. (b) Spanwise leakage flow rate mode 1.

Figure 5.42: Flexure setting 2 representative mode 1 plots of transverse displacement (left) and spanwise leakage flow (right) at $\alpha_m = 7$ [°].

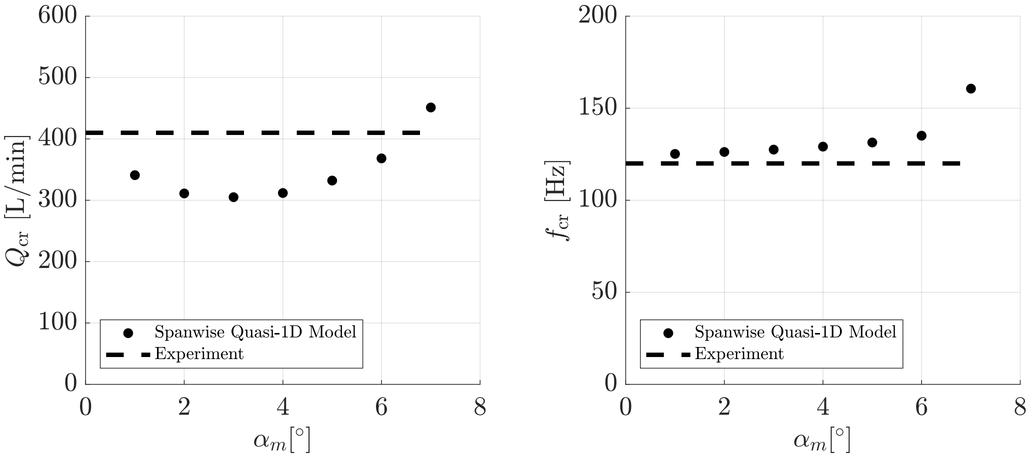

(a) Critical flow rate versus diffuser angle. (b) Critical frequency versus diffuser angle.

Figure 5.43: Comparison between spanwise quasi-1D critical flow rate (left) and frequency (right) to experimental quantities for flexure setting 3 from table 5.5.

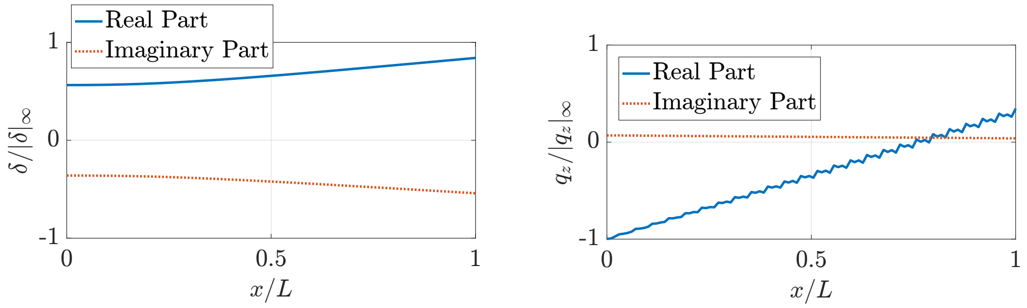

(a) Transverse displacement mode 1. (b) Spanwise leakage flow rate mode 1.

Figure 5.44: Flexure setting 3 representative mode 1 plots of transverse displacement (left) and spanwise leakage flow (right) at $\alpha_m = 7$ [°].

The lack of agreement between experiment and model results for cases of flexures 2 and 3 are expected primarily because compressibility effects cannot be neglected at their respective Mach numbers. This is also the case for flexure 1, although considerably less since its experimental Mach number is less than half the other two cases. The agreement between results however, particularly that of flexure 1, suggests that the model may capture a considerable portion of the relevant physics. This is in contrast to the quasi-1D model constrained to axial flow, where no aspect of the dynamics could be captured within the parameter space in the experimental geometry and material properties.

## *Chapter 6*

# CONCLUSIONS AND OUTLOOK

### 6.1 Conclusion

This thesis aims to elucidate the fluid-structure instability that drives the flextensional based flow energy harvester, primarily focused on the leakage-flow instability as a hypothesis.

Chapter 2 formulates this in quantitative terms by restricting the coupled fluid-structure equations through assumptions that define leakage-flow. The full equations are subsequently solved through a two-dimensional fluid-structure interaction direct numerical simulation algorithm in chapter 4, and the flutter instability onset and critical values compared to those predicted by the reduced order model derived. The agreement between FSI DNS and the quasi-1D model is remarkable for small channel gaps in a range of viscous and mass parameters tested. This holds even as the elastic-translating boundary condition is added to the system, along with a linear diffuser though to a lesser degree. Results indicate that the leakage-flow instability mechanism is a strong candidate as the primary source of fluid-structure instability for heavy beams in channels with gaps less than 15% of the beam length. This is valid for systems where the flow is approximately two dimensional.

Chapter 5 experimentally assesses the dynamics of the flextensional based flow energy harvester in air flow. Experiments characterize device mechanical properties first, then appraise the system dynamics in a flowing setting. Critical flow rates and frequencies are measured for three different flexures, with self-sustaining oscillations reached in tshe flextensional mode in all three tested cases. Furthermore, hysteresis is observed as the flow rate direction is reversed, indicating a bistable region and a subcritical Hopf bifurcation at the neutrally-stable point. Experimentally measured values for the flutter onset are then compared with predictions of the spanwise quasi-1D model developed in chapter 2. Results are encouraging: the model is able to predict the critical flow rates and frequency response of the first flexure setting, and is within a factor of 2 of flexure settings 2 and 3. The promising aspect of these predictions is that though many effects are not captured, including fluid compressibility, true frictional pressure loss, and flow separation, the crude geometry of a diffuser at its critical angle is able to estimate within reasonable bounds the stability properties of the experimental set up. This is in contrast with predictions from the quasi-1D model that only accounts for axial leakage-flow: no aspect of the dynamics, including the bifurcation type, was replicated for a wide range of parameters near those in the experimental set up. That distinction in itself indicates the importance of the spanwise flow, and three-dimensionality of the problem.

This work concludes that is it likely leakage-flow instability dominates the behavior and drives the dynamics of the fluid-structure interaction seen in the flextensional flow energy harvester system. More work is necessary to determine effects that are loosely approximated, such as flow separation, or entirely not accounted within the model, as compressibility. Yet the fundamental framework for reduced-order modeling is valuable for predicting the flutter onset and critical values in narrow channels, especially when beams are heavy relative to the fluid. Applications that fall under these parameter ranges will find a relevant tool-set in this work.

## 6.2 Outlook

Two broad tasks are suggested as a continuation of this thesis. The first is validation of the reduced order models through further experimentation, augmenting the model with more relevant physics as their importance becomes evident. Better flow instrumented flextensional energy harvester experiments are likely a good starting point. Measurements of effective spanwise flow, detailed velocity and pressure profiles over the beam surfaces, and more accurate assessment of flexure structural properties would help in quantifying or better estimating system unknowns. Another set of experiments where flexures reach the limit-cycle regime at a Mach number less than 0.1, then with gradually increasing Mach number values, would quantify the importance of compressibility in predicting stability boundaries. Lastly, a set of experiments where diffuser angle can be varied would elucidate the effect of flow separation on critical properties, especially when measurements suggested are implemented.

The second task is using the models developed in this work to assess and design new flow energy harvesters. One example is the convexity of the critical flow rate stability boundaries found as a function of diffuser angle in section 5.5. By understanding the variation of the minimum unstable flow rate in $\alpha_m$, more unstable, and perhaps more powerful, designs may be developed. Building an optimization algorithm constrained by the model dynamics in chapter 2 appears a logical next step. Iteration between model validation and the optimization is an obvious necessity, hence advancing both tasks simultaneously is seems like a sensible strategy.

# BIBLIOGRAPHY

[1] D. S. Herran and T. Nakata. “Design of decentralized energy systems for rural electrification in developing countries considering regional disparity.” In: *Applied Energy* 91.1 (2012).

[2] M. I. Yuce and A. Muratoglu. “Hydrokinetic energy conversion systems: A technology status review.” In: *Renewable and Sustainable Energy Review* 43 (2015), pp. 72–82.

[3] K. Sornes. “Small-scale water current turbines for river applications.” In: *Zero Emission Resource Organisation (ZERO)* (2010).

[4] S. Dudhani, A. K. Sinha, and S. S. Inamdar. “Assessment of small hydropower potential using remote sensing data for sustainable development in India.” In: *Energy policy* 34.17 (2006), pp. 3195–3205.

[5] A. Moschitta and I. Neri. “Power consumption assessment in wireless sensor networks.” In: *ICT-Energy-Concepts Towards Zero-Power Information and Communication Technology* (2014).

[6] M. Anyi and B. Kirke. “Evaluation of small axial flow hydrokinetic turbines for remote communities.” In: *Energy for Sustainable Development* 14.2 (2010), pp. 110–116.

[7] J. Algeroy et al. “Controlling reservoirs from afar.” In: *Oilfield Review* 11.3 (1999), pp. 18–29.

[8] E. Addiego-Guevara, M. D. Jackson, M. A. Giddins, et al. “Insurance value of intelligent well technology against reservoir uncertainty.” In: *SPE Symposium on Improved Oil Recovery*. Society of Petroleum Engineers. 2008.

[9] B. Yeten et al. “Decision analysis under uncertainty for smart well deployment.” In: *Journal of Petroleum Science and Engineering* 44.1 (2004), pp. 175–191.

[10] W. Tong. *Wind power generation and wind turbine design*. Wit Press, 2010.

[11] H. Guo et al. “Reliability analysis for wind turbines with incomplete failure data collected from after the date of initial installation.” In: *Reliability Engineering & System Safety* 94.6 (2009), pp. 1057–1063.

[12] *Life-limiting wear of wind turbine gearbox bearings: origins and solutions*. Vol. 4. Proceedings of European wind energy conference exhibition (EWEC 2010). 2010.

[13] X. Gao. “Vibration and flow energy harvesting using piezoelectric cantilevers.” PhD thesis. Drexel University, 2011.

[14] M. M. Bernitsas et al. "VIVACE (Vortex induced vibration aquatic clean energy): a new concept in generation of clean and renewable energy from fluid flow." In: *Journal of Offshore Mechanics and Arctic Engineering* 130.4 (2008), p. 041101.

[15] D. Zhu. *Vibration energy harvesting: machinery vibration, human movement and flow induced vibration*. InTech, 2011.

[16] A. Manbachi and R. S. Cobbold. "Development and application of piezoelectric materials for ultrasound generation and detection." In: *Ultrasound* 19.4 (2011), pp. 187–196.

[17] J. G. Smits, W. Choi, and A. Ballato. "Resonance and antiresonance of symmetric and asymmetric cantilevered piezoelectric flexors." In: *Ultrasonics, Ferroelectrics, and Frequency Control, IEEE Transactions on* 44.2 (1997), pp. 250–258.

[18] D. W. Allen. "Vortex-Induced vibration of deepwater risers." In: *Offshore Technology Conference*. Houston, 1998, pp. 1–7.

[19] K. Y. Billah and R. H. Scanlan. "Resonance, Tacoma Narrows bridge failure, and undergraduate physics textbooks." In: *Am. J. Phys* 59.2 (1991), pp. 118–124.

[20] L. Tang, M. P. Païdoussis, and J. Jiang. "Cantilevered flexible plates in axial flow: energy transfer and the concept of flutter-mill." In: *Journal of Sound and Vibration* 326.1 (2009), pp. 263–276.

[21] A. Khalak and C. H. K. Williamson. "Motions, forces and mode transitions in vortex-induced vibrations at low mass-damping." In: *Journal of Fluids and Structures* 13 (1999), pp. 813–851.

[22] M. J. Every, R. King, and D. S. Weaver. "Vortex-Excited Vibrations of cylinders and cables and their suppression." In: *Ocean Engineering* 9.2 (Jan. 1982), pp. 135–157. ISSN: 00298018. DOI: `10.1016/0029-8018(82)90010-5`. URL: `http://linkinghub.elsevier.com/retrieve/pii/0029801882900105`.

[23] T. Suzuki, T. Colonius, and S. Pirozzoli. "Vortex shedding in a two-dimensional diffuser: theory and simulation of separation control by periodic mass injection." In: *Journal of Fluid Mechanics* 520 (Dec. 2004), pp. 187–213. ISSN: 0022-1120. DOI: `10.1017/S0022112004001405`. URL: `http://www.journals.cambridge.org/abstract%5C_S0022112004001405`.

[24] M. P. Païdoussis. "Annular- and Leakage- Flow-Induced Instabilities." In: *Fluid-Structure Interactions: Slender Structures and Axial Flow, Volume 2*. Academic Press, 2003. Chap. 11, pp. 1221–1420.

[25] S. Sherrit et al. "Flow energy piezoelectric bimorph nozzle harvester." In: *SPIE Smart Structures and Materials + Nondestructive Evaluation and Health Monitoring*. International Society for Optics and Photonics. 2014.

[26] H. J. Lee et al. “Piezoelectric Energy Harvesting in Internal Fluid Flow.” In: *Sensors* 15.10 (2015).

[27] H. J. Lee et al. “Design and experimental evaluation of flextensional-cantilever based piezoelectric transducers for flow energy harvesting.” In: *SPIE Smart Structures and Materials + Nondestructive Evaluation and Health Monitoring*. International Society for Optics and Photonics. 2016.

[28] S. Sherrit et al. “Fluid flow nozzle energy harvesters.” In: *SPIE Smart Structures and Materials + Nondestructive Evaluation and Health Monitoring*. International Society for Optics and Photonics. 2015.

[29] E. B. Johansson. *Hydraulic instability of reactor parallel-plate fuel assemblies*. Tech. rep. Knolls Atomic Power Lab., Schenectady, NY, 1959.

[30] D. R. Miller. “Critical flow velocities for collapse of reactor parallel-plate fuel assemblies.” In: *Journal of Engineering for Power* 82.2 (1960), pp. 83–91.

[31] F. Inada and S. Hayama. “A Study on Leakage-Flow-Induced Vibrations.” In: *Japan Society of Mechanical Engineers International Journal Ser. 3, Vibration, Control Engineering, Engineering for Industry* 31.1 (1988), pp. 39–47.

[32] F. Inada and S. Hayama. “A study on leakage-flow-induced vibrations. Part 1: Fluid-dynamic forces and moments acting on the walls of a narrow tapered passage.” In: *Journal of Fluids and Structures* 4.4 (1990), pp. 395–412. ISSN: 10958622. DOI: `10.1016/0889-9746(90)90144-T`.

[33] H. Nagakura and S. Kaneko. “The stability of a cantilever beam subjected to one-dimensional leakage flow.” In: *Transactions of the 11th international conference on structural mechanics in reactor technology* (1991).

[34] S. D. Sommerfeldt and W. J. Strong. “Simulation of a player–clarinet system.” In: *The Journal of the Acoustical Society of America* 83.5 (1988), pp. 1908–1918.

[35] J. Backus. “Small-Vibration Theory of the Clarinet.” In: *The Journal of the Acoustical Society of America* 35.3 (1963), pp. 305–313.

[36] T. S. Balint and A. D. Lucey. “Instability of a cantilevered flexible plate in viscous channel flow.” In: *Journal of Fluids and Structures* 20.7 SPEC. ISS. (2005), pp. 893–912. ISSN: 08899746. DOI: `10.1016/j.jfluidstructs.2005.05.005`.

[37] G. A. Tetlow and A. D. Lucey. “Motions of a cantilevered flexible plate in viscous channel flow driven by a constant pressure drop.” In: *International Journal for Numerical Methods in Biomedical Engineering* 25.5 (2009), pp. 463–482.

[38] F. B. Tian et al. "Fluid–structure interaction involving large deformations: 3D simulations and applications to biological systems." In: *Journal of computational physics* 258 (2014), pp. 451–469.

[39] K. Shoele and R. Mittal. "Flutter instability of a thin flexible plate in a channel." In: *Journal of Fluid Mechanics* 786 (2016), pp. 29–46. ISSN: 14697645. DOI: `10.1017/jfm.2015.632`.

[40] P. Hidalgo, S. Jha, and A. Glezer. "Enhanced heat transfer in air cooled heat sinks using aeroelastically fluttering reeds." In: *Thermal Investigations of ICs and Systems (THERMINIC), 2015 21st International Workshop on*. IEEE. 2015, pp. 1–6.

[41] J. Cisonni et al. "The stability of a flexible cantilever in viscous channel flow." In: *Journal of Sound and Vibration* 396 (2017), pp. 186–202.

[42] C. Q. Guo and M. P. Paidoussis. "Stability of rectangular plates with free side-edges in two-dimensional inviscid channel flow." In: *Journal of Applied Mechanics* 67.1 (2000), pp. 171–176. DOI: `10.1115/1.321143`.

[43] S. Alben. "Flag flutter in inviscid channel flow." In: *Physics of Fluids* 27.3 (2015), p. 033603. DOI: `10.1063/1.4915897`.

[44] S. Alben. "Optimal flexibility of a flapping appendage in an inviscid fluid." In: *Journal of Fluid Mechanics* 614 (2008), pp. 355–380.

[45] X. Wu and S. Kaneko. "Linear and nonlinear analyses of sheet flutter induced by leakage flow." In: *Journal of Fluids and Structures* 20.7 (2005), pp. 927–948.

[46] K. Fujita and A. Shintani. "Flow-induced vibration of the elastic rod due to axial flow: unstable phenomena of continuous flexible rod as the axisymmetric body." In: *PVP Flow Induced Vibration* 389 (1999), pp. 199–206.

[47] K. Fujita and A. Shintani. "Axial Leakage Flow-Induced Vibration of the Elastic Rod as the Axisymmetric Continuous Flexible Beam." In: *Journal of Pressure Vessel Technology* 123.4 (2001), p. 421. ISSN: 00949930. DOI: `10.1115/1.1387442`. URL: `http://pressurevesseltech.asmedigitalcollection.asme.org/article.aspx?articleid=1458073`.

[48] K. Fujita and A. Shintani. "A consideration on pre- and post-instability of an axisymmetric elastic beam subjected to axial leakage flow." In: *Journal of Fluids and Structures* 23.3 (Apr. 2007), pp. 463–478. ISSN: 08899746. DOI: `10.1016/j.jfluidstructs.2006.08.016`. URL: `http://linkinghub.elsevier.com/retrieve/pii/S088997460600123X`.

[49] D. T. Akcabay and Y. L. Young. "Hydroelastic response and energy harvesting potential of flexible piezoelectric beams in viscous flow." In: *Physics of Fluids* 24.5 (2012).

[50] O. Doaré, M. Sauzade, and C. Eloy. “Flutter of an elastic plate in a channel flow: Confinement and finite-size effects.” In: *Journal of Fluids and Structures* 27.1 (2011), pp. 76–88.

[51] O. Doaré et al. “Effect of spanwise confinement on flag flutter: Experimental measurements.” In: *Physics of Fluids* (2011), pp. 1–4.

[52] A. Goza and T. Colonius. “A strongly-coupled immersed-boundary formulation for thin elastic structures.” In: *Journal of Computational Physics* 336 (2017), pp. 401–411.

[53] P. K. Kundu, I. Cohen, and D. R. Dowling. “Fluid Mechanics. The Science of Microfabrication.” In: Elsevier, 2012.

[54] Y. Shimoyama and Y. Yamada. “Experiments on the Labyrinth Packing.” In: 117 (1957), pp. 44–49. ISSN: 09168451. DOI: `10.1248/cpb.37.3229`.

[55] B. Lautrup. “Channels and Pipes.” In: *Physics of continuous matter: exotic and everyday phenomena in the macroscopic world*. CRC press, 2011. Chap. 16, pp. 564–265.

[56] B. Lautrup. “Addendum: Channel entrance flow.” In: *Physics of continuous matter: exotic and everyday phenomena in the macroscopic world*. CRC press, 2011.

[57] F. D. White. “Viscous Flow in Ducts.” In: *Fluid Mechanics*. Academic Press, 2008, pp. 375–389.

[58] D. J. Inman. “Distributed-parameter systems.” In: *Engineering vibration*. Vol. 3. Prentice Hall New Jersey, 2008. Chap. 6, pp. 464–538.

[59] H. T. Banks and D. J. Inman. “On damping mechanisms in beams.” In: *Journal of Applied Mechanics* 58.3 (1991), pp. 716–723.

[60] J. E. Sader. “Frequency response of cantilever beams immersed in viscous fluids with applications to the atomic force microscope.” In: *Journal of Applied Physics* 84.1 (1998), p. 64. ISSN: 00218979. DOI: `10.1063/1.368002`. URL: `http://scitation.aip.org/content/aip/journal/jap/84/1/10.1063/1.368002`.

[61] Cornelis A. Van Eysden and J. E. Sader. “Small amplitude oscillations of a flexible thin blade in a viscous fluid: Exact analytical solution.” In: *Physics of Fluids* 18.12 (2006), p. 123102. ISSN: 10706631. DOI: `10.1063/1.2395967`. URL: `http://scitation.aip.org/content/aip/journal/pof2/18/12/10.1063/1.2395967`.

[62] Cornelis A. Van Eysden and J. E. Sader. “Frequency response of cantilever beams immersed in viscous fluids with applications to the atomic force microscope: Arbitrary mode order.” In: *Journal of Applied Physics* 101.4 (2007), p. 044908. ISSN: 00218979. DOI: `10.1063/1.2654274`. URL: `http://scitation.aip.org/content/aip/journal/jap/101/4/10.1063/1.2654274`.

[63] L. Rosenhead. *Laminar boundary layers: an account of the development, structure, and stability of laminar boundary layers in incompressible fluids, together with a description of the associated experimental techniques*. Clarendon Press, 1963.

[64] S. H. Strogatz. *Nonlinear dynamics and chaos: with applications to physics, biology, chemistry, and engineering*. CRC Press, 2018.

[65] M. D. Süli E. "Newton-Cotes formulae." In: *An introductioin to numerical analysis*. Cambridge University Press, 2003. Chap. 7, pp. 200–223.

[66] K. Taira and T. Colonius. "The immersed boundary method: a projection approach." In: *Journal of Computational Physics* 225.2 (2007), pp. 2118–2137.

[67] T. Colonius and K. Taira. "A fast immersed boundary method using a nullspace approach and multi-domain far-field boundary conditions." In: *Computer Methods in Applied Mechanics and Engineering* 197.25 (2008), pp. 2131–2146.

[68] A. Goza et al. "Accurate computation of surface stresses and forces with immersed boundary methods." In: *Journal of Computational Physics* 321 (2016), pp. 860–873.

[69] S. Liska and T. Colonius. "A fast immersed boundary method for external incompressible viscous flows using lattice Green's functions." In: *arXiv preprint arXiv:1604.01814* (2016).

[70] A. Goza and T. Colonius. "A strongly-coupled immersed-boundary formulation for thin deforming surfaces, with application to elastic beams." In: *arXiv preprint arXiv:1610.01115* (2016).

[71] A. J. Goza. "Numerical methods for fluid-Structure interaction, and their application to flag flapping." PhD thesis. California Institute of Technology, 2018.

[72] M. A. Criesfield. *Non-linear finite element analysis of solids and structures, vol. 1*. Wiley, New York, 1991.

[73] X. Yang et al. "A smoothing technique for discrete delta functions with application to immersed boundary method in moving boundary simulations." In: *Journal of Computational Physics* 228.20 (2009), pp. 7821–7836.

[74] S. Turek and J. Hron. "Proposal for numerical benchmarking of fluid-structure interaction between an elastic object and laminar incompressible flow." In: *Fluid-structure interaction*. Springer, 2006, pp. 371–385.

[75] R. Bhardwaj and R. Mittal. "Benchmarking a coupled immersed-boundary-finite-element solver for large-scale flow-induced deformation." In: *AIAA journal* 50.7 (2012), pp. 1638–1642.

[76] K. Shoele and R. Mittal. "Computational study of flow-induced vibration of a reed in a channel and effect on convective heat transfer." In: *Physics of Fluids* 26.12 (2014). ISSN: 10897666. DOI: `10.1063/1.4903793`.

[77] P. J. Schmid. "Dynamic mode decomposition of numerical and experimental data." In: *Journal of fluid mechanics* 656 (2010), pp. 5–28.

[78] A. Towne, O. T. Schmidt, and T. Colonius. "Spectral proper orthogonal decomposition and its relationship to dynamic mode decomposition and resolvent analysis." In: *Journal of Fluid Mechanics* 847 (2018), pp. 821–867. DOI: `10.1017/jfm.2018.283`.

[79] K. K. Chen, J. H. Tu, and C. W. Rowley. "Variants of dynamic mode decomposition: boundary condition, Koopman, and Fourier analyses." In: *Journal of nonlinear science* 22.6 (2012), pp. 887–915.

[80] J. H. Tu et al. "On dynamic mode decomposition: theory and applications." In: *arXiv preprint arXiv:1312.0041* (2013).

[81] J. L. Lumley. "The structure of inhomogeneous turbulent flows." In: *Atmospheric turbulence and radio wave propagation* (1967).

[82] J. L Lumley. *Stochastic tools in turbulence*. Academic Press, New York, 1970.

[83] L. Sirovich. "Turbulence and the dynamics of coherent structures. I. Coherent structures." In: *Quarterly of applied mathematics* 45.3 (1987), pp. 561–571.

[84] N. Aubry et al. "The dynamics of coherent structures in the wall region of a turbulent boundary layer." In: *Journal of Fluid Mechanics* 192 (1988), pp. 115–173.

[85] O. T. Schmidt, T. Colonius, and G. A. Bres. "Wavepacket intermittency and its role in turbulent jet noise." In: *55th AIAA Aerospace Sciences Meeting*. 2017, p. 0686.

[86] O. T. Schmidt. "An efficient streaming algorithm for spectral proper orthogonal decomposition." In: *arXiv preprint arXiv:1711.04199* (2017).

[87] P. Welch. "The use of fast Fourier transform for the estimation of power spectra: a method based on time averaging over short, modified periodograms." In: *IEEE Transactions on audio and electroacoustics* 15.2 (1967), pp. 70–73.

[88] S. C. Kak. "The discrete Hilbert transform." In: *Proceedings of the IEEE* 58.4 (1970), pp. 585–586.

[89] G. Rigas et al. "Experimental sensitivity analysis and control of thermoacoustic systems." In: *Journal of Fluid Mechanics* 787 (2016).

[90] A. Orchini, G. Rigas, and M. P. Juniper. “Weakly nonlinear analysis of thermoacoustic bifurcations in the Rijke tube.” In: *Journal of Fluid Mechanics* 805 (2016), pp. 523–550.

[91] S. Etikyala and R. I. Sujith. “Change of criticality in a prototypical thermoacoustic system.” In: *Chaos: An Interdisciplinary Journal of Nonlinear Science* 27.2 (2017), p. 023106.

[92] J. Sirohi and I. Chopra. “Fundamental understanding of piezoelectric strain sensors.” In: *Journal of intelligent material systems and structures* 11.4 (2000), pp. 246–257.

[93] *MatWeb*. `http://matweb.com/search/DataSheet.aspx?MatGUID=b8d536e0b9b54bd7b69e4124d8f1d20a&ckck=1`. Used for aluminum and steel properties. Accessed: 2018-06-30.

[94] *Boston Piezo Optics Inc.* `https://www.bostonpiezooptics.com/ceramic-materials-pzt`. Used for PZT-5H properties. Accessed: 2018-06-30.

[95] J. Canny. “A computational approach to edge detection.” In: *IEEE Transactions on pattern analysis and machine intelligence* 6 (1986), pp. 679–698.

[96] S. Sherrit et al. “Miniature piezoelectric shaker mechanism for autonomous distribution of unconsolidated sample to instrument cells.” In: *Industrial and Commercial Applications of Smart Structures Technologies*. Vol. 7290. International Society for Optics and Photonics. 2009, 72900H-1 –72900H-9.

[97] M. J. Moran and H. N. Shapiro. *Fundamentals of engineering thermodynamics*. John Wiley & Sons, 2004.

[98] D. G. Hirsch. “An Experimental and Theoretical Study of Active Flow Control.” PhD thesis. California Institute of Technology, 2017, pp. 103–105.

[99] H. J. Kaltenbach et al. “Study of flow in a planar asymmetric diffuser using large-eddy simulation.” In: *Journal of Fluid Mechanics* 390 (1999), pp. 151–185.

[100] H. Lan, B. F. Armaly, and J. A. Drallmeier. “Turbulent Forced Convection in a Plane Asymmetric Diffuser: Effect of Diffuser Angle.” In: *Journal of Heat Transfer* 131.7 (2009), p. 071702.

[101] O. Törnblom, B. Lindgren, and A. V. Johansson. “The separating flow in a plane asymmetric diffuser with 8.5 opening angle: mean flow and turbulence statistics, temporal behaviour and flow structures.” In: *Journal of Fluid Mechanics* 636 (2009), pp. 337–370.

[102] V. Chandavari and S. Palekar. “Diffuser angle control to avoid flow separation.” In: *Int. J. Tech. Res. Appl* 2.5 (2014), pp. 16–21.

*Appendix A*

# TWO DIMENSIONAL MODEL COEFFICIENTS

The following are the coefficients from equation 2.64, with $x_1$ and $x_2$ as dummy integration variables,

$$M_{\text{fi}} = \rho_f \left[ \left( \int_0^L \frac{\int_0^{x_2} g_i(x_1)\, dx_1}{h_e(x_2)}\, dx_2 \right) \frac{\int_0^x \frac{1}{h_e(x_2)}\, dx_2}{\int_0^L \frac{1}{h_e(x_2)}\, dx_2} - \left( \int_0^x \frac{\int_0^{x_2} g_i(x_1)\, dx_1}{h_e(x_2)}\, dx_2 \right) \right] \tag{A.1}$$

$$\begin{aligned} C_{\text{fi}} = \rho_f\, q_{x0} \Bigg\{ & \frac{\zeta_{\text{out}}}{h_e(L)^2} \left( \int_0^L g_i(x_1)\, dx_1 \right) \left( \frac{\int_0^x \frac{1}{h_e(x_2)}\, dx_2}{\int_0^L \frac{1}{h_e(x_2)}\, dx_2} \right) + \left( \frac{f_0}{2} + \frac{q_{x0}\, \eta}{4} \right) \left[ \int_0^L \frac{\int_0^{x_2} g_i(x_1)\, dx_1}{h_e(x_2)^3}\, dx_2 \left( \frac{\int_0^x \frac{1}{h_e(x_2)}\, dx_2}{\int_0^L \frac{1}{h_e(x_2)}\, dx_2} \right) - \int_0^x \frac{\int_0^{x_2} g_i(x_1)\, dx_1}{h_e(x_2)^3}\, dx_2 \right] + \\ & 2\xi_x \left[ \int_0^x \frac{\left( \int_0^{x_2} g_i(x_1)\, dx_1 \right) \frac{\mathrm{d}}{\mathrm{d}x_2} h_e(x_2)}{h_e(x_2)^3}\, dx_2 - \int_0^x \frac{g_i(x_2)}{h_e(x_2)^2}\, dx_2 + \left( \int_0^L \frac{g_i(x_2)}{h_e(x_2)^2}\, dx_2 - \int_0^L \frac{\left( \int_0^{x_2} g_i(x_1)\, dx_1 \right) \frac{\mathrm{d}}{\mathrm{d}x_2} h_e(x_2)}{h_e(x_2)^3}\, dx_2, \right) \left( \frac{\int_0^x \frac{1}{h_e(x_2)}\, dx_2}{\int_0^L \frac{1}{h_e(x_2)}\, dx_2} \right) \right] \Bigg\} \end{aligned} \tag{A.2}$$

$$\begin{aligned} K_{\text{fi}} = \rho_f\, q_{x0}^2 \Bigg\{ & \xi_x \left[ 3 \int_0^x \frac{g_i(x_2) \frac{\mathrm{d}}{\mathrm{d}x_2} h_e(x_2)}{h_e(x_2)^4}\, dx_2 - \int_0^x \frac{\frac{\mathrm{d}}{\mathrm{d}x_2} g_i(x_2)}{h_e(x_2)^3}\, dx_2 + \left( \int_0^L \frac{\frac{\mathrm{d}}{\mathrm{d}x_2} g_i(x_2)}{h_e(x_2)^3}\, dx_2 - 3 \int_0^L \frac{g_i(x_2) \frac{\mathrm{d}}{\mathrm{d}x_2} h_e(x_2)}{h_e(x_2)^4}\, dx_2 \right) \left( \frac{\int_0^x \frac{1}{h_e(x_2)}\, dx_2}{\int_0^L \frac{1}{h_e(x_2)}\, dx_2} \right) \right] + \\ & \frac{3\, f_0}{4} \left[ \int_0^L \frac{g_i(x_2)}{h_e(x_2)^4}\, dx_2 \left( \frac{\int_0^x \frac{1}{h_e(x_2)}\, dx_2}{\int_0^L \frac{1}{h_e(x_2)}\, dx_2} \right) - \int_0^x \frac{g_i(x_2)}{h_e(x_2)^4}\, dx_2 \right] + \left( \frac{\zeta_{\text{in}}\, g_i(0)}{h_e(0)^3} + \frac{\zeta_{\text{out}}\, g_i(L)}{h_e(L)^3} \right) \left( \frac{\int_0^x \frac{1}{h_e(x_2)}\, dx_2}{\int_0^L \frac{1}{h_e(x_2)}\, dx_2} \right) - \frac{\zeta_{\text{in}}\, g_i(0)}{h_e(0)^3} \Bigg\} \end{aligned} \tag{A.3}$$

$$T_{\mathrm{f}i} = \rho_f \, q_{x0} \left\{ \left[ \frac{\zeta_{\mathrm{in}}}{h_e(0)^2} + \frac{\zeta_{\mathrm{out}}}{h_e(L)^2} \right] \left( \frac{\int_0^x \frac{1}{h_e(x_2)} \, dx_2}{\int_0^L \frac{1}{h_e(x_2)} \, dx_2} \right) - \frac{\zeta_{\mathrm{in}}}{h_e(0)^2} + 2\xi_x \left[ \int_0^x \frac{\frac{\mathrm{d}}{\mathrm{d}x_2} h_e(x_2)}{h_e(x_2)^3} \, dx_2 - \int_0^L \frac{\frac{\mathrm{d}}{\mathrm{d}x_2} h_e(x_2)}{h_e(x_2)^3} \, dx_2 \left( \frac{\int_0^x \frac{1}{h_e(x_2)} \, dx_2}{\int_0^L \frac{1}{h_e(x_2)} \, dx_2} \right) \right] + \right.$$
$$\left. \left[ \frac{f_0}{2} + \frac{q_{x0}\eta}{4} \right] \left[ \left( \frac{\int_0^x \frac{1}{h_e(x_2)} \, dx_2}{\int_0^L \frac{1}{h_e(x_2)} \, dx_2} \right) \int_0^L \frac{1}{h_e(x_2)^3} \, dx_2 - \int_0^x \frac{1}{h_e(x_2)^3} \, dx_2 \right] \right\} \tag{A.4}$$

The following are the coefficients from equation 2.65,

$$B_{qi} = -\frac{\int_0^L \frac{\int_0^{x_2} g_i(x_1)\,dx_1}{h_e(x_2)}\,dx_2}{\int_0^L \frac{1}{h_e(x_2)}\,dx_2} \tag{A.5}$$

$$D_{qi} = \frac{q_{x0}}{\int_0^L \frac{1}{h_e(x_2)}\,dx_2}\left[2\xi_x\left(\int_0^L \frac{\left(\int_0^{x_2} g_i(x_1)\ dx_1\right)\frac{\mathrm{d}}{\mathrm{d}x_2}h_e(x_2)}{h_e(x_2)^3}\,dx_2 - \int_0^L \frac{g_i(x_2)}{h_e(x_2)^2}\,dx_2\right) - \left(\frac{f_0}{2} + \frac{q_{x0}\,\eta}{4}\right)\left(\int_0^L \frac{\int_0^{x_2} g_i(x_1)\ dx_1}{h_e(x_2)^3}\,dx_2\right) - \right.$$
$$\left. \frac{\zeta_{\text{out}}}{h_e(L)^2}\left(\int_0^L g_i(x_1)\ dx_1\right)\right] \tag{A.6}$$

$$E_{qi} = \frac{q_{x0}^2}{\int_0^L \frac{1}{h_e(x_2)}\,dx_2}\left[\xi_x\left(3\int_0^L \frac{g_i(x_2)\ \frac{\mathrm{d}}{\mathrm{d}x_2}h_e(x_2)}{h_e(x_2)^4}\,dx_2 - \int_0^L \frac{\frac{\mathrm{d}}{\mathrm{d}x_2}g_i(x_2)}{h_e(x_2)^3}\,dx_2\right) - \frac{3\,f_0}{4}\left(\int_0^L \frac{g_i(x_2)}{h_e(x_2)^4}\,dx_2\right) - \frac{\zeta_{\text{in}}\,g_i(0)}{h_e(0)^3} - \frac{\zeta_{\text{out}}\,g_i(L)}{h_e(L)^3}\right] \tag{A.7}$$

$$G_q = \frac{q_{x0}}{\int_0^L \frac{1}{h_e(x_2)}\,dx_2}\left[2\,\xi_x\left(\int_0^L \frac{\frac{\mathrm{d}}{\mathrm{d}x_2}h_e(x_2)}{h_e(x_2)^3}\,dx_2\right) - \left(\frac{f_0}{2} + \frac{q_{x0}\,\eta}{4}\right)\left(\int_0^L \frac{1}{h_e(x_2)^3}\,dx_2\right) - \frac{\zeta_{\text{in}}}{h_e(0)^2} - \frac{\zeta_{\text{out}}}{h_e(L)^2}\right] \tag{A.8}$$

## *Appendix B*

# DISCRETE DELTA FUNCTION COEFFICIENTS

$$\psi_h^{(3),***}(r) = \frac{1}{h}\begin{cases} 0.4167E-1\left(\frac{|r|}{h}\right)^4 + (-0.1389+0.3472E-1A_8)\left(\frac{|r|}{h}\right)^3 + (-0.7122E-1-0.5208E-1A_8+0.2406A_5)\left(\frac{|r|}{h}\right)^2 + \\ \quad (-0.2406A_5-0.3792+0.1013A_8)\left(\frac{|r|}{h}\right) + 0.8019E-1A_5-0.4196E-1A_8+0.6486 & \frac{|r|}{h} \leq 1 \\ -0.625E-1\left(\frac{|r|}{h}\right)^4 + (0.4861-0.1736E-1A_9)\left(\frac{|r|}{h}\right)^3 + (-1.143175026+0.7813E-1A_9-0.1203A_6)\left(\frac{|r|}{h}\right)^2 + \\ \quad (0.8752+.3609A_6-0.1548A_9)\left(\frac{|r|}{h}\right) - 0.2807A_6+0.8228E-2+0.1150A_9 & 1 \geq \frac{|r|}{h} \leq 2 \\ 0.2083E-1\left(\frac{|r|}{h}\right)^4 + (0.3472E-2A_7-0.2639)\left(\frac{|r|}{h}\right)^3 + (1.2144-0.2604E-1A_7+0.2406E-1A_4)\left(\frac{|r|}{h}\right)^2 + \\ \quad (-0.1203A_4-2.4493+0.7263E-1A_7)\left(\frac{|r|}{h}\right) + 0.1523563211A_4+1.8432-0.7306E-1A_7 & 2 \geq \frac{|r|}{h} \leq 3 \\ 0 & \text{otherwise} \end{cases}, \tag{B.1}$$

$$A_4 = \sin^{-1}\left[\frac{\sqrt{3}}{2}\left(2\left(\frac{|r|}{h}\right)-5\right)\right] \tag{B.2}$$

$$A_5 = \sin^{-1}\left[\frac{\sqrt{3}}{2}\left(2\left(\frac{|r|}{h}\right)-1\right)\right] \tag{B.3}$$

$$A_6 = \sin^{-1}\left[\frac{\sqrt{3}}{2}\left(2\left(\frac{|r|}{h}\right)-3\right)\right] \tag{B.4}$$

$$A_7 = \sqrt{60\left(\frac{|r|}{h}\right) - 71 - 12\left(\frac{|r|}{h}\right)^2} \tag{B.5}$$

$$A_8 = \sqrt{1 - 12\left(\frac{|r|}{h}\right)^2 + 12\left(\frac{|r|}{h}\right)} \tag{B.6}$$

$$A_9 = \sqrt{36\left(\frac{|r|}{h}\right) - 12\left(\frac{|r|}{h}\right)^2 - 23} \tag{B.7}$$

## *Appendix C*

# MODELING AND SIMULATION PARAMETER TABLES

Table C.1: Table of parameters for constant channel flow simulations with varying $\hat{m}$ and and $\hat{k}$.

| Case # | $\hat{h}$ | $\hat{h}^2 Re_L$ | $Re_L$ | $\Delta x^*$ | $\hat{h}_{\text{corr}}$ | $\hat{m}$ | $\hat{k}$ | $\max_{\hat{m}} \left[\Delta \hat{k}\right]$ | $\max_{\hat{m}} [\Delta \lambda_{\text{Re}}]$ | $\max_{\hat{m}} [\Delta \lambda_{\text{Im}}]$ |
|---|---|---|---|---|---|---|---|---|---|---|
| 1 | 0.0250 | 0.5000 | 800 | 0.00125 | 0.0228 | [100 – 2] | [0.01 – 50] | 1.495 | 1.140 | 0.944 |
| 2 | 0.0500 | 0.5000 | 200 | 0.00250 | 0.0457 | [100 – 1] | [0.04 – 50] | 0.810 | 1.582 | 1.253 |
| 3 | 0.0500 | 1.2500 | 500 | 0.00250 | 0.0457 | [100 – 1] | [0.01 – 2.5] | 0.470 | 0.769 | 1.524 |
| 4 | 0.0500 | 2.5000 | 1000 | 0.00200 | 0.0466 | [100 – 1] | [0.01 – 2.5] | 0.533 | 0.789 | 2.171 |
| 5 | 0.1250 | 0.5000 | 32 | 0.00625 | 0.1143 | [100 – 1] | [0.0008 – 40] | 0.375 | 0.622 | 0.695 |
| 6 | 0.1250 | 1.2500 | 80 | 0.00313 | 0.1197 | [100 – 1] | [0.008 – 40] | 0.294 | 0.723 | 1.05 |

Table C.2: Table of parameters for constant channel flow simulations at $\hat{m} = 100$ and varying $\hat{h}^2 Re_L$ and $\hat{k}$.

| Case # | $\hat{h}$ | $\hat{h}^2 Re_L$ | $Re_L$ | $\Delta x^*$ | $\hat{h}_{\text{corr}}$ | $\hat{k}$ | $\Delta\hat{k}$ | $\Delta\lambda_{\text{Re}}$ | $\Delta\lambda_{\text{Im}}$ |
|---|---|---|---|---|---|---|---|---|---|
| 1 | 0.05 | 0.1 | 40 | 0.0025 | 0.04575 | [0.7 – 80] | 0.920 | 0.057 | 0.158 |
| 1 | 0.05 | 0.5 | 200 | 0.0025 | 0.04575 | [0.7 – 80] | 0.920 | 0.280 | 0.356 |
| 1 | 0.05 | 1 | 400 | 0.0025 | 0.04575 | [0.02 – 10] | 2.242 | 0.021 | 1.107 |
| 1 | 0.05 | 1.5 | 600 | 0.0025 | 0.04575 | [0.02 – 10] | 2.242 | 0.131 | 2.669 |
| 1 | 0.05 | 2 | 800 | 0.0025 | 0.04575 | [0.02 – 5] | 1.540 | 0.010 | 0.849 |
| 1 | 0.05 | 2.5 | 1000 | 0.0025 | 0.04575 | [0.02 – 5] | 1.540 | 0.007 | 0.839 |
| 1 | 0.05 | 3 | 1200 | 0.0017 | 0.04711 | [0.01 – 2.5] | 0.770 | 0.015 | 0.623 |
| 1 | 0.05 | 3.5 | 1400 | 0.0017 | 0.04711 | [0.01 – 2.5] | 0.770 | 0.071 | 0.465 |
| 1 | 0.05 | 4 | 1600 | 0.0013 | 0.04779 | [0.01 – 2.5] | 0.770 | 0.103 | 1.565 |
| 1 | 0.05 | 4.5 | 1800 | 0.0013 | 0.04779 | [0.01 – 2.5] | 0.770 | 0.105 | 0.019 |
| 2 | 0.125 | 0.1 | 6.4 | 0.0063 | 0.11429 | [0.08 – 50] | 2.041 | 0.324 | 0.535 |
| 2 | 0.125 | 0.5 | 32 | 0.0063 | 0.11429 | [0.08 – 50] | 1.329 | 0.034 | 0.922 |
| 2 | 0.125 | 1 | 64 | 0.0063 | 0.11429 | [0.01 – 2.5] | 0.770 | 0.013 | 0.624 |
| 2 | 0.125 | 1.5 | 96 | 0.0063 | 0.11429 | [0.01 – 2.5] | 0.770 | 0.011 | 0.609 |
| 2 | 0.125 | 2 | 128 | 0.0063 | 0.11429 | [0.01 – 2.5] | 0.770 | 0.003 | 0.599 |
| 2 | 0.125 | 2.5 | 160 | 0.0063 | 0.11429 | [0.01 – 2.5] | 0.770 | 0.003 | 0.598 |
| 2 | 0.125 | 3 | 192 | 0.0063 | 0.11429 | [0.01 – 2.5] | 0.770 | 0.002 | 0.596 |
| 2 | 0.125 | 3.5 | 224 | 0.0063 | 0.11429 | [0.01 – 2.5] | 0.770 | 0.002 | 0.595 |
| 2 | 0.125 | 4 | 256 | 0.0063 | 0.11429 | [0.01 – 2.5] | 0.770 | 0.002 | 0.595 |
| 2 | 0.125 | 4.5 | 288 | 0.0063 | 0.11429 | [0.01 – 2.5] | 0.770 | 0.002 | 0.594 |
| 2 | 0.125 | 5 | 320 | 0.0063 | 0.11429 | [0.01 – 2.5] | 0.770 | 0.001 | 0.594 |
| 2 | 0.125 | 5.5 | 352 | 0.0063 | 0.11429 | [0.01 – 2.5] | 0.770 | 0.035 | 2.001 |
| 2 | 0.125 | 6 | 384 | 0.0052 | 0.11616 | [0.01 – 2.5] | 0.770 | 0.001 | 0.592 |
| 2 | 0.125 | 6.5 | 416 | 0.0052 | 0.11616 | [0.01 – 2.5] | 0.770 | 0.001 | 0.056 |
| 2 | 0.125 | 7 | 448 | 0.0045 | 0.11735 | [0.01 – 2.5] | 0.770 | 0.001 | 0.056 |
| 2 | 0.125 | 7.5 | 480 | 0.0045 | 0.11735 | [0.01 – 2.5] | 0.770 | 0.001 | 0.057 |
| 2 | 0.125 | 8 | 512 | 0.0039 | 0.11837 | [0.01 – 2.5] | 0.770 | 0.097 | 2.319 |
| 2 | 0.125 | 8.5 | 544 | 0.0039 | 0.11837 | [0.01 – 2.5] | 0.770 | 0.027 | 2.057 |
| 2 | 0.125 | 9 | 576 | 0.0035 | 0.11905 | [0.02 – 5] | 1.540 | 0.006 | 0.101 |
| 2 | 0.125 | 9.5 | 608 | 0.0035 | 0.11905 | [0.02 – 5] | 1.540 | 0.008 | 0.117 |

Table C.3: Table of cases for constant channel flow simulations and moving boundary conditions with varying $\hat{m}_{\mathrm{bc}}$ and $\hat{k}$ at $\hat{m} = 5$.

| Case # | $\hat{h}^2 Re_L$ | $Re_L$ | $\hat{m}$ | $\hat{h}$ | $\hat{m}_{\mathrm{bc}}$ | $\hat{k}_{\mathrm{bc}}$ | $\Delta x^*$ | $h_{\mathrm{corr}}$ | $\hat{k}$ | $\Delta\hat{k}$ | $\lambda_{\mathrm{Re}}$ | $\lambda_{\mathrm{Im}}$ |
|---|---|---|---|---|---|---|---|---|---|---|---|---|
| 1 | 0.5 | 32 | 50 | 0.125 | 1800 | 0.1 | 0.006 | 0.114 | [ 0.42 - 41.67 ] | 0.375 | 0.213 | 0.497 |
| 1 | 0.5 | 32 | 50 | 0.125 | 500 | 0.1 | 0.006 | 0.114 | [ 0.42 - 41.67 ] | 0.375 | 0.210 | 0.499 |
| 1 | 0.5 | 32 | 50 | 0.125 | 100 | 0.1 | 0.006 | 0.114 | [ 0.42 - 41.67 ] | 0.375 | 0.179 | 0.507 |
| 1 | 0.5 | 32 | 50 | 0.125 | 50 | 0.1 | 0.006 | 0.114 | [ 0.42 - 41.67 ] | 0.375 | 0.146 | 0.510 |
| 1 | 0.5 | 32 | 50 | 0.125 | 10 | 0.1 | 0.006 | 0.114 | [ 0.42 - 41.67 ] | 0.251 | 0.101 | 0.373 |
| 1 | 0.5 | 32 | 50 | 0.125 | 9 | 0.1 | 0.006 | 0.114 | [ 0.83 - 83.33 ] | 0.275 | 0.064 | 0.393 |
| 1 | 0.5 | 32 | 50 | 0.125 | 8 | 0.1 | 0.006 | 0.114 | [ 0.83 - 83.33 ] | 0.225 | 0.077 | 0.346 |
| 1 | 0.5 | 32 | 50 | 0.125 | 7 | 0.1 | 0.006 | 0.114 | [ 0.83 - 83.33 ] | 0.500 | 0.025 | 0.026 |
| 1 | 0.5 | 32 | 50 | 0.125 | 5 | 0.1 | 0.006 | 0.114 | [ 0.83 - 83.33 ] | 12.375 | 0.007 | 0.395 |

Table C.4: Table of cases for elastically-mounted rigid beam in a diffuser. Parameters $\hat{m}_{\mathrm{bc}}$ and $\alpha[°]$ are varied.

| Case # | $Re_L$ | $\hat{h}^2 Re_L$ | $\hat{m}_{\mathrm{bc}}$ | $\hat{h}$ | $\hat{k}_{\mathrm{bc}}$ | $\Delta x^*$ | $h_{\mathrm{corr}}$ | $\alpha[°]$ | $\Delta\alpha[°]$ | $\Delta\lambda_{\mathrm{Re}}$ | $\Delta\lambda_{\mathrm{Im}}$ |
|---|---|---|---|---|---|---|---|---|---|---|---|
| 1 | 400 | 6.25 | 10 | 0.125 | 0.1 | 0.0031 | 0.1197 | [ 0.1-10 ] | 1 | 0.053 | 0.039 |
| 1 | 400 | 6.25 | 1 | 0.125 | 0.1 | 0.0031 | 0.1197 | [ 0.1-10 ] | 1 | 0.096 | 0.042 |
| 1 | 400 | 6.25 | 0.1 | 0.125 | 0.1 | 0.0031 | 0.1197 | [ 0.1-10 ] | 1 | 0.110 | 0.032 |

Table C.5: Table of cases for cantilever beam in a diffuser. Parameters $\alpha[^\circ]$ and $\hat{k}$ are varied.

| Case # | $Re_L$ | $\hat{h}^2 Re_L$ | $\hat{m}$ | $\hat{h}$ | $\alpha[^\circ]$ | $\Delta x^*$ | $h_{\mathrm{corr}}$ | $\hat{k}$ | $\Delta\hat{k}$ | $\Delta\lambda_{\mathrm{Re}}$ | $\Delta\lambda_{\mathrm{Im}}$ |
|---|---|---|---|---|---|---|---|---|---|---|---|
| 1 | 200 | 0.5 | 50 | 0.05 | 1 | 0.0025 | 0.04575 | [ 50 - 0.1 ] | 0.4625 | 0.0663 | 0.1591 |
| 1 | 200 | 0.5 | 50 | 0.05 | 2 | 0.0025 | 0.04575 | [ 50 - 0.1 ] | 0.2056 | 0.051 | 0.105 |
| 1 | 200 | 0.5 | 50 | 0.05 | 4 | 0.0025 | 0.04575 | [ 50 - 0.1 ] | 0.0533 | 0.0296 | 0.0375 |
| 1 | 200 | 0.5 | 50 | 0.05 | 6 | 0.0025 | 0.04575 | [ 5 - 0.04 ] | 0.0175 | 0.0086 | 0.0243 |
| 2 | 400 | 6.25 | 50 | 0.125 | 1 | 0.003 | 0.1197 | [ 0.8333 - 0.0417 ] | 0.0877 | 0.0251 | 0.2922 |
| 2 | 400 | 6.25 | 50 | 0.125 | 2 | 0.003 | 0.1197 | [ 0.8333 - 0.0417 ] | 0.0668 | 0.0181 | 0.2511 |
| 2 | 400 | 6.25 | 50 | 0.125 | 4 | 0.003 | 0.1197 | [ 0.8333 - 0.0417 ] | 0.0509 | 0.0074 | 0.2029 |
| 2 | 400 | 6.25 | 50 | 0.125 | 6 | 0.003 | 0.1197 | [ 0.8333 - 0.0417 ] | 0.0388 | 0.0048 | 0.1704 |

## *Appendix D*

# APPENDIX TO EXPERIMENTAL STUDY OF FLEXTENSIONAL FLOW-ENERGY HARVESTER

## D.1 Flextensional Response to Fluid Flow Experimental Procedure

The following is the procedure for running an individual flowing test:

1. Flexure is assemble onto its fixed base, and into the test section;
2. Wires are sealed from the test section rear;
3. Vacuum grease and rubber tape are placed around the top of the flow path to minimize leakage paths other than those established in figure 5.2a;
4. Test section window is closed and bolted;
5. Electronics and data acquisition system are turned on;
6. Lab air valve is opened, while needle valve remains closed;
7. Needle valve is slowly opened to less than 5 [L/min];
8. Flow rate is increased in increments of ~ 50 [L/min], but adapted near critical points, and held for at least 20 seconds, after which video data is taken. A manual time stamp is added to the video data set;
9. Step 8 is repeated through the critical point until a maximum flow rate near 450 [L/min] has been reached;
10. Flow rate is decreased in increments of ~ 50 [L/min], but adapted near critical points. Video data is taken after 20 seconds of constant flow;
11. Step 10 is repeated through the critical point until a minimum flow rate is reached, near 20 [L/min].
12. The lab air valve is closed first, to ensure no air pressure remains between the lab valve and needle valve section, then the needle valve is closed;
13. The test section window is removed and the flexure dynamic test is carried out, as described in section 5.3.2.